



HAL
open science

Development and evaluation of an intraoperative beta imaging probe for radio-guided solid tumor surgery

Sara Spadola

► **To cite this version:**

Sara Spadola. Development and evaluation of an intraoperative beta imaging probe for radio-guided solid tumor surgery. Medical Physics [physics.med-ph]. Université Paris Saclay (COMUE), 2016. English. NNT : 2016SACLS257 . tel-01500096

HAL Id: tel-01500096

<https://theses.hal.science/tel-01500096>

Submitted on 2 Apr 2017

HAL is a multi-disciplinary open access archive for the deposit and dissemination of scientific research documents, whether they are published or not. The documents may come from teaching and research institutions in France or abroad, or from public or private research centers.

L'archive ouverte pluridisciplinaire **HAL**, est destinée au dépôt et à la diffusion de documents scientifiques de niveau recherche, publiés ou non, émanant des établissements d'enseignement et de recherche français ou étrangers, des laboratoires publics ou privés.

NNT : 2016SACLS257

THESE DE DOCTORAT
DE
L'UNIVERSITE PARIS-SACLAY
PREPAREE A
L'UNIVERSITE PARIS-SUD

ÉCOLE DOCTORALE N°576 (PHENIICS)
particules hadrons énergie et noyau : instrumentation, image, cosmos et simulation

Spécialité de doctorat : Imagerie médicale et radioactivité

Par

Mme SPADOLA Sara

**Development and evaluation of an intraoperative beta imaging probe
for radio-guided solid tumor surgery**

Thèse présentée et soutenue à Orsay, le 27 septembre 2016 :

Composition du Jury :

M. Riccardo Faccini, Professeur, Sapienza Università di Roma, Rapporteur
M. Thomas Patzak, Professeur, Université Paris-Diderot, Rapporteur
M. Bruno Espagnon, Professeur, IPN Orsay, Président du jury
M. Stéphane Palfi, Professeur, Hôpitaux Universitaires Henri-Mondor, Examineur
M. Yves Charon, Professeur, Université Paris-Diderot, Directeur de thèse
M. Laurent Ménard, Maître de Conférences, Université Paris-Diderot, Co-directeur de thèse

Acknowledgments

I would like to thank all the people who contributed in some way to the work described in this thesis.

First and foremost I express my special appreciation and thanks to my thesis director Laurent Ménard, who have supervised me during these last three years. I would like to thank him, Marc-Antoine Verdier and Yves Charon for encouraging my research and for allowing me to grow on both the scientific and personal plane. Their advices on research and on my career have been priceless.

The results described in this thesis work were accomplished with the help and support of fellow labmates and collaborators. I am grateful to Laurent Pinot et Cédric Esnault for having helped me numerous times with the experimental set-up. I'm also indebted to Albertin Dubois, Françoise Bouvet-Lefebvre and Alexandre Liège for their support and availability to solve all the informatics issues.

I like to acknowledge all the members of IMNC for the nice time spent together and their support during those years. I would like to specially thank Christiane Robin for her kind helpfulness in the moment of needs, like when I broke my ankle, as well as Olivier Seksek, Nathalie Arlaud, Fred Pain and Hirc Gurden for their friendliness and encouragement to pursuit my objectives, and the PhD students of the laboratory for the funny moments spent together.

Finally, I would like to acknowledge friends and family who supported me during this time. First of all I would like to thank mamma Delizia, papà Massimo and le mie sorelline Nastasia and Eleonora for their love and support. A great thank to Amaury Hornbeck, who stayed to my side during the last and harder months of my thesis. Thanks to Héloïse Beutier, Yan Chelminski, Renata Coura, Camilla De Rossi, Amandine Gnaedinger, Emilie Gontran, Valérie Guiraud, Carlo Mancini, Imma Martinez, Cécile Peucelle and Antonella Tramontana; they were there for me whenever I needed, helping me to get through this period with the smile and lots of great memories. A special thank goes as well to Javier Byford and his family for their friendship and their help with the correction of the English of this thesis.

Contents

Introduction	9
1 Intra-operative imaging for oncological surgery	13
1.1 Cancer treatment	14
1.1.1 Evolution of cancer management	15
1.1.2 Oncological surgery	19
1.1.2.1 Clinical impact of surgery for the treatment of solid tumors	20
1.1.2.2 Interventional imaging techniques	23
1.2 Radio-guided cancer surgery	28
1.2.1 Radioactive tumor labelling	29
1.2.1.1 Constraints on the radiotracer choice	29
1.2.1.2 Particular radiotracers	30
1.2.1.3 Metabolic radiotracers	31
1.2.1.4 Monoclonal antibodies radiotracers	32
1.2.2 Intraoperative detection devices	33
1.2.2.1 Detection performance parameters	33
1.2.2.2 Cerenkov light imaging	35
1.2.2.3 Gamma detection	36
1.2.2.4 Beta detection	43
1.2.3 Clinical applications	49
1.2.3.1 Cerenkov light imaging	49
1.2.3.2 Gamma counting and imaging probes	50
1.2.3.3 Beta counting and imaging probes	55
1.3 New β intraoperative imaging devices based on SiPMs	57
2 Beta imaging probes for intraoperative tumor resection	59
2.1 Challenges and constraints of intraoperative positron detection	59
2.2 Radiation interactions	60
2.2.1 β interaction mechanisms	61
2.2.1.1 Collision loss	61
2.2.1.2 Range and absorption of β particle	63
2.2.1.3 Backscattering of low energy β	64
2.2.1.4 Annihilation	64
2.2.2 Interactions of gamma rays	64
2.2.2.1 Photoelectric effect	64
2.2.2.2 Compton effect	65
2.2.2.3 Gamma rays attenuation	66
2.3 Indirect radiation detection: scintillators and photodetectors	67
2.3.1 Scintillators and scintillation phenomenon	67
2.3.1.1 Organic scintillators	68
2.3.1.2 Inorganic scintillators	70

2.3.1.3	Light collection and scintillator mounting	71
2.3.2	Photodetection systems	72
2.4	Influence of the γ noise background on the positron detection	75
2.4.1	Nature and origin	76
2.4.2	Strategies for noise minimization	77
2.5	The miniaturized β imaging probes	80
2.5.1	Design of the probe	80
2.5.2	The scintillator choice	81
2.5.2.1	Material nature and geometry	81
2.5.2.2	Optical coating and light shielding	83
2.5.3	The photodetection device	84
2.5.3.1	Operation principles of SiPM	85
2.5.3.2	SiPM intrinsic characteristics and drawbacks	88
2.5.3.3	Advantages and drawbacks of SiPMs for the development of intraoperative beta probe	94
2.5.4	Readout electronics	95
2.5.4.1	Electronic characteristics	98
2.5.4.2	Acquisition software	101
2.5.5	Image reconstruction algorithms	101
3	Development and optimization of the positron imaging probes	107
3.1	Characterization of the photodetection system	107
3.1.1	Experimental set-up	107
3.1.2	SiPM gain	108
3.1.3	Response uniformity	110
3.1.4	Temperature influence	111
3.2	Optimization and performances of the single scintillator probe	112
3.2.1	Measurements of the imaging performances	112
3.2.2	Simulation study	114
3.2.3	Comparison of scintillator materials and thicknesses	115
3.2.3.1	Energy response and sensitivity	115
3.2.3.2	Spatial performances	117
3.2.4	Influence of the light spreading window	119
3.2.5	Influence of optical coating and light shielding	119
3.2.6	Sensitivity to the background noise and tumor detectability	121
3.2.7	Focus on the optimal configuration	123
3.2.7.1	Overvoltage optimization	123
3.2.7.2	Spatial performances	125
3.2.7.3	Correction of temperature dependance	126
3.2.8	Comparison of reconstruction methods	128
3.2.8.1	Standard barycenter method	128
3.2.8.2	Iterative position weighted barycenter method	128
3.2.8.3	Analytical model fitting method	129
3.2.8.4	Neural network method	130
3.3	Optimization and performances of the dual scintillator probe	131

3.3.1	Scintillators discrimination	134
3.3.1.1	Automatic clustering	134
3.3.1.2	Overvoltage and electronic gain optimization	136
3.3.1.3	Events discrimination method with cut	136
3.3.1.4	Influence of light guide thickness	137
3.3.1.5	Focus on the optimal configuration	137
3.4	Towards the clinical prototype	140
3.4.1	Development of a new miniaturized readout electronics	140
3.4.2	Mechanical housing design	141
4	Pre-clinical evaluation of the probe performances	143
4.1	Experimental protocol	143
4.1.1	Estimation of positron sensitivity	143
4.1.2	Spatial resolution performances	144
4.1.3	Phantoms geometry and uptakes	145
4.1.4	Evaluation of tumor detectability	146
4.2	Spatial and sensitivity performances	149
4.2.1	Sensitivity and minimal detectable activity	149
4.2.2	Spatial response	151
4.3	Tumor detectability evaluation	152
4.3.1	Influence of background noise	152
4.3.2	Influence of radiotracer uptake in tumor	154
4.3.3	Detectability of small tumors	156
4.4	Discussion and conclusions	157
	Conclusions and prospectives	161
A	Résumé	163
A.1	Imagerie per-opératoire pour guider l'exérèse des tumeurs solides	163
A.2	Les imageurs β per-opératoires	163
A.2.1	Principe de détection des sondes β	164
A.2.2	La tête de détection	164
A.2.3	Le photodecteur et l'électronique d'acquisition	165
A.3	Développement et optimisation des sondes positon	166
A.3.1	Caractérisation du système de photodétection	167
A.3.2	Optimisation et performances de l'imageur avec un scintillateur unique	167
A.3.2.1	Mesures des performances d'imagerie	167
A.3.2.2	Etude par simulations Monte-Carlo	168
A.3.2.3	Choix de la configuration optimale	168
A.3.2.4	Focus sur la configuration optimale	170
A.3.3	Optimisation et performances de l'imageur avec deux scintillateurs . .	172
A.3.4	Présentation du prototype clinique	174
A.4	Evaluation préclinique des performances de la sonde	175
A.5	Conclusions	176

Bibliography

179

Introduction

Cancer is a large family of diseases characterized by abnormal cell growth with the potential to invade or spread to other parts of the body. This group of disease represents one of the leading cause of mortality worldwide. Many treatments strategies have been developed during the years to face the different cancerous pathologies. The major ones are surgery, radiotherapy and chemotherapy. Depending on the nature and development of the disease, the treatment may be curative. Surgery is a key step in the treatment of solid tumors, that grow as solid masses of tissues and have distinct structure from surrounding tissues. The accurate removal of a tumors is one of the major factor influencing the patient prognosis. The challenge is to precisely define the margins of the tumor mass in order to remove while preserving as much as possible the healthy surrounding tissues.

Surgery is usually planned for each patient images basis obtained with a Computed Tomography (CT) or Magnetic Resonance Imaging (MRI). Those techniques provide morphology and anatomic information allowing to characterized the tumor size, texture and vascularization. However, those images are acquired before the operation and are difficult to associate to the patient anatomy during the surgery. More generally, performances and ergonomics of pre-operative imaging technologies are not suited to accurately define the extend of a tumor lesion or di detect small tumors. In that context, intraoperative detection devices are useful tools to guide the surgeon in the accurate resection of the tumor lesion. Many devices have been developed based on different imaging techniques such as interventional ultrasounds, optical imaging, interventional MRI or radioguided imaging probes. Their aim is to provide real time evaluation of the tumor resection margins. The use of specific tumor-seeking radiotracers coupled with miniaturized sensors is more and more studied. Compared to anatomical imaging tools, *in situ* localization of tissues labeled with functional tracers provides higher sensitivity and specificity. Therefore, they are more suitable for the localization of small tumoral uptakes. Radioguided surgery protocols, using γ probes have proven usefulness utility for tumor resection in different pathologies. The development of new specific radiotracers labeled with positron emitters and initially dedicated to Positron Emission Tomography, has created a renewed interest for radioguidance methods. As a result, several gamma counting probes specially dedicated to the detection of the of high energy gamma rays produced by the annihilation of positrons in tissue have been developed lately. However, the high penetration of γ rays strongly decreases the sensitivity and spatial selectivity of such probes and requires the use of mechanical or electronic collimation in order to remove the contamination coming from areas of non-specific accumulation of the radiotracer. Meanwhile, the intraoperative detection of positron is still rarely used today despite the intrinsic advantages that presents compared to the detection of γ rays. The short range of β particles of a few millimeters in tissues allows to remove the contamination of non specific uptake areas, improving the spatial resolution and the signal-to-noise ratio of the detection process. Due to this short range, no collimation system is required, allowing the development of compact detection system with very high sensitivity. The detection of β particles is therefore particularly promising technique to provide the surgeon useful information about

the resection margins and the control of the surgical cavity after resection.

In this context, the imaging and modelization in neurobiology and cancerology laboratory (IMNC UMR 8165) based in Orsay, France, has been developing a new generation of miniaturized intraoperative β probes based on Silicon Photomultipliers photosensors (SiPM). The SiPM presents the advantageous feature of being extremely compact and present performances comparable to that of the photomultipliers based on the vacuum technology. The project SONIM (Nouvelles SONdes miniaturisées pour la détection de particules chargées en Imagerie Moléculaire) has been initiated in a previous thesis [Hudin 2013], during which characterized the performances of SiPM as photodetectors for intraoperative beta detection of radiolabeled tumor tissue and aims develop two new prototypes of miniaturized positron imaging probes and to evaluate their ability to perform in real time tumor localization and post-operative control of the surgical cavity. The work characterized the performances of SiPM as photodetectors for intraoperative beta detection of radiolabeled tumor tissue. This manuscript is divided in four main chapters.

The first chapter presents the general clinical context of cancer therapy and especially the role of medical imaging in cancer treatment. Surgical procedures and the major tools developed to improve efficiency in the resection of solid tumors are described, by presenting different clinical pathologies for which the surgery plays a key role. Furthermore, the different intraoperative imaging technologies available nowadays for guided surgery are presents with a particular focus on radioguided imaging techniques. A state of the art of γ and β detection modalities is described, showing the interest for their use in an operating room, for different clinical applications.

The second chapter will make a general presentation of the fundamentals of interaction between radiation and matter. The basic components of a detection system based on the indirect detection of the radiation through the coupling of a scintillator to a photodetector will be detailed. The nature and origin of the γ background noise in the positron detection and the different strategies that can be used to minimize it will be detailed. The design of two miniaturized imaging probe prototypes and detection components choices are also detailed, including the photodetection device based on a SiPM array. Then, the readout electronics are presented (components, characteristics, parameter optimization etc.). Finally, the imaging reconstruction algorithms which were tested during this work are described.

The third chapter introduces the detection system characterization and optimization for the two configurations of the imaging probe. Different designs of the positron imaging probes, including scintillator material and thickness, light spreading window and optical reflector, were investigated with Monte Carlo simulations and measurements. Their impact on the probes performances were optimized in terms of positron sensitivity, gamma ray noise reduction, spatial resolution, distortion and uniformity of response. The effect of different reconstruction algorithm on spatial performances is also studied. Finally, the dedicated miniaturized electronic readouts and mechanical housing designed to obtain a fully operational intraoperative probe in the operating room will be presented.

The fourth chapter presents the global performances of the first prototype probe in a

preclinical study using radioactive phantoms. This study allowed to evaluate the β sensitivity and the ability of detecting small radiotracer uptake in presence of a high background noise.

In conclusion, we resume and comment performances and limits of the two intraoperative imaging probes and give some perspectives that could guide the future improvements and implementation of the probe in a clinical environment.

Intra-operative imaging for oncological surgery

Cancer is the second leading cause of death in the world after cardiovascular disease. In 2012 in Europe there were 3.7 million new cancer cases, 1.9 million cancer deaths and 9.7 million people living with cancer [Ferlay *et al.* 2013]. The word cancer comes from the Greek word *karkinos*, used by the physician Hippocrates (460-370 B.C.) to describe carcinoma tumors. Nevertheless, he was not the first to observe this disease; the world's oldest recorded case of cancer hails from ancient Egypt in 1500 BC [Sudhakar 2010]. Nowadays the word cancer, medically known as *malignant neoplasm*, describes a class of diseases characterized by unregulated cell growth. Different factors can cause this disease, from genetic predisposition to environmental factors that can directly damage genes or combine with existing genetic faults within cells. In humans over 200 different cancers are known. Tumors are classified by the type of cell that is initially affected. Normal cells in the body follow a preordained path of growth, division and death. The programmed cell death is called *apoptosis*. Unlike regular cells, tumor cells do not experience programmatic death and instead continue to grow and divide. This leads to a mass of abnormal cells that grows out of control. When a cell is mutated, the mutation can be transmitted to the daughter cells, which in turn continue to mutate and duplicate in an uncontrolled way. The uncontrolled proliferation of cells can lead to benign or malignant disease. If not treated in time, both may harm the patient and could lead to death.

Benign tumors do not invade neighboring tissues or spread throughout the body, although some types can still produce a negative health effects as well as degenerate into cancerous tumors. Therefore, the patients may be cured with only local treatment with a high rate of survival.

Malignant tumors, on the other hand, can invade the organs near its primary site and may also spread to more distant parts of the body through the lymphatic system or blood stream. When cancer cells break away from the primary (original) tumor and travel to other places in the body, another tumor may form. The new occurrences of disease thus generated are referred to as *metastases*. The secondary tumor is of the same type as the primary tumor. Metastatic tumors are very common in the late stages of cancer and are more difficult to treat.

Cancer is classified in five broad groups by the type of cell it originates from. *Carcinomas* originate from epithelial cells and begin in tissue linings in the inner or outer surfaces of the body. *Sarcomas* arise from mesenchymal cells so they are made of cells located in bone, cartilage, fat, connective tissue, muscle and other supportive tissue. Common malignancies, such as breast, colon and lung cancer, are almost always carcinoma. *Lymphomas* are tumors that develop from lymphatic cells while *leukemia* begins in the bone marrow and often

accumulates in the blood stream. *Adenomas* are cancers arising in the thyroid, the pituitary gland, the adrenal gland and other glandular tissue. With the exception of leukemia, most tumors grow as solid masses of tissue with a distinct structure, and we refer to them as *solid* tumor. Many diverse treatment strategies have been developed, throughout the years, to face the varied cancerous pathologies.

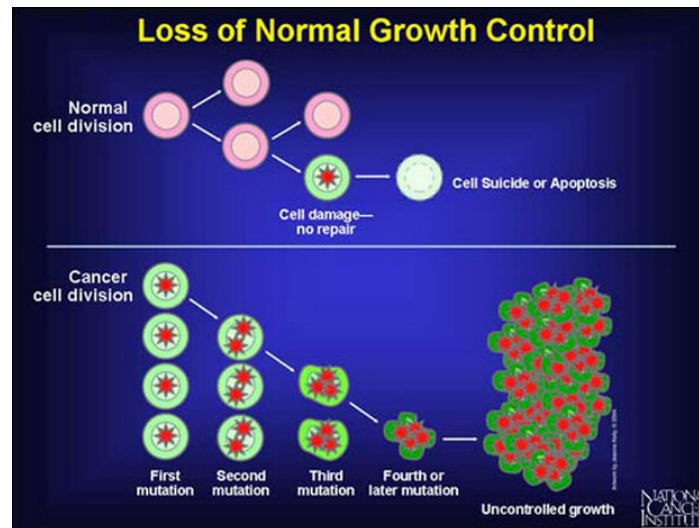


Figure 1.1 – Cell growth in normal cells (top) and cancer cells (bottom).

1.1 Cancer treatment

The goal of cancer treatment is to "cure" the cancer, or prolong survival in patients with the advanced disease, while preserving the highest possible quality of life in both the short and long term. Today, two main therapeutic strategies are available to treat solid tumors malignancies: locoregional and systemic treatments. A combination of these two type of therapy is frequently used.

Locoregional treatments are restricted to a localized region of the body and aim to control primitive tumors or macro-metastasis. This is commonly obtained by surgery and/or radiotherapy. The surgery consist in the ablation of the tumor (primary or secondary) in association or not to the biopsy of the lymph node that could have be invaded by the cancerous cells. Radiotherapy is performed by the local irradiation of the organ and/or of the anatomical area containing the tumor. An irradiation of the lymphatic node can be as well associated.

Systematic treatments are complementary to locoregional ones. They consists in the administration to the patient of a systematic drug treatment that diffuses in the whole body, throughout the blood stream, with the intent to kill cancerous cells and so to reduce primary tumors (in case they were not previously treated), and to eliminate metastasis and tumor focal area too small or of too complex access to be treated with a locoregional method. Systematic treatments aim to a general control of cancer by reducing the risk of recurrence or

development of metastasis. Chemotherapy, hormonal therapy and immunotherapy are the treatments allowing this kind of control.

Presently, the therapeutic strategy is designed personally for each patient thanks to the collaboration of multiple specialized doctors (surgeon, oncologist, radiotherapist, pathologist, radiologist). Typically, the choice of the optimal therapy is determined by the compromise between the benefit and the risk related to the patient health status, the nature of the cancer (histological type, interested organ, tumor size, infiltration to the nearby organs and lymph node, eventual metastasis presence) and the toxicity and morbidity risk of the treatment.

The actual approach to cancer treatment results from more than a century of technologies and the evolution of biomedical knowledge. In the following sections, the key innovations and breakthroughs in the field of cancer management will be synthetically presented, starting from the surgical approach, since that was the first and only effective treatment during the first decades of the 19th century, till the introduction and technological progresses in radiotherapy to finish with the more recent systemic drugs therapies. The development and worldwide access of structural and then molecular imaging, that allows accurate staging, localization and treatment monitoring of malignancies, had been an important driver for the development of all these treatments methods.

1.1.1 Evolution of cancer management

Management of cancer has drastically evolved in the last few decades. From the turn of the century up to the end of the second World War, thanks to the invention of anesthesia in 1846, surgery had been the primary method of treatment against cancer.

Surgery evolution

At the beginning of the 20th century, based on the belief that cancer spread outward by infiltration from the original site of generation, Halsted and Handley formulated their hypothesis, in which *en block* dissection was considered mandatory to improve loco regional control and mortality rates for carcinoma of the breast [Halsted 1907]. Accordingly, extended procedures were devised for other malignancies, like colorectal cancer. Data collected between 1900 and 1950 report an increase of survival rates of cancer patients treated with surgery alone from near 0 to approximately 30 % in the US. Although radiotherapy was already available during this period, it caused such toxicity at its early stage that it had no impact on the overall survival of patient and scientific articles in the 1920s and 1930s questioned the utility of this new technique [DeVita 1983]. While Halsted and Handley were developing their radical operations, Stephen Paget formulates his 'seed and soil' theory, according to which metastasis processes do not occur by chance but, rather, that metastasis development can take place only if there is an affinity between the originally tumor cells and new organ microenvironment. This concept has been confirmed by numerous publications thanks to the techniques of modern cellular and molecular biology almost a hundred years later [Ribatti *et al.* 2006] and represented a breakthrough for the understanding of tumor disease. One of the important notions in the last decades has been the growing awareness

that locoregional recurrence is not the main cause of a deadly prognosis: metastatic disease spreading to vital organs is the major cause of patient's morbidity and death. Indeed, when radical surgery is necessary to obtain locoregional control, the patient is not likely to benefit from it in terms of survival if the metastatic disease disseminates to the vital organs. This understanding of metastasis became a key element in recognizing the limitation of cancer surgery. As a consequence, it began the tendency to perform more restricted radical surgery in order to put more emphasis on systematic treatment, in locally advanced tumors, and to give high importance to accurate lymph node staging.

Originally, due to the unavailability of accurate imaging devices, the treatment was planned when the patient had already reached the surgeon in operating theatre for an "exploration surgery". Starting from the 1970s, not only the existing imaging techniques, mainly based on X-ray radiation, saw a large improvement but new radiographic tools like ultrasound, computerized tomography (CT), and magnetic resonance (MRI) became also widely available [Scatliff & Morris 2014]. Those techniques provide anatomic and morphologic information allowing non-invasive *in vivo* characterization of the tumor size, texture and vascularization. Overlapping of morphologic and anatomic images allows a more complete overview significantly improving the accuracy of the diagnosis and preoperative staging. As general rule, operability is now judged before-hand and individual planning treatments are carefully planned and discussed in advance. Surgical procedures have also evolved thanks to the development of new excision tools, like electrocautery or ultrasonic cavitation device (combination of an ultrasound probe with a suction device), minimally-invasive techniques for imaging of internal organs such as endoscopy, laparoscopy and natural orifice transluminal endoscopic surgery [Wang *et al.* 2015, Arezzo *et al.* 2015] or computer-assisted technologies including simulation-based surgical training, planning, navigation, augmented reality, teleoperation and robot-assisted surgery. Navigation, which is often used during brain tumor surgery, allows to accurately define the real spatial position of the surgical tools in the operative wound in agreement with the planning developed from preoperative images of the tumor and surrounding healthy tissue. The improvement of topical anesthesia has allowed to perform brain tumor procedures while the patient is awake and sedated. In this way, the neurosurgeon can map the areas around the tumor by electrostimulation, consisting in the electrical stimulation of nerve tissues and the recording of the neural electrical activity, while questioning the patient to precisely locate the functional areas of the brain and avoid them during resection of tumoural tissues [De Witt Hamer *et al.* 2012]. Finally, among the latest innovation introduced in the operation room, the robot-assisted surgery allows telemanipulated or computer controlled minimally-invasive surgical procedures. Several robot systems have been developed for specific applications, such as the da Vinci (bariatric surgery, gastrectomy for cancer, gynecological oncology etc.), NeuroMate (neurological surgery) or Thor-aCAB surgical system (cardiovascular procedures) [Ficarra *et al.* 2007, Goldberg *et al.* 2015, Ishikawa & Watanabe 2015]. The use and further development of these new techniques aims to reduce the overall postoperative morbidity (by enhancing the accuracy, safety and ease of use of surgical procedures), hospital stay and treatment costs while improving survival rate and one's quality of life.

Other therapeutic approaches

The main challenge in radiotherapy treatments, from the first attempt of treating cancer with x-ray radiation in 1896, is to deliver controlled dose distribution to the tumor mass while sparing the surrounding healthy tissues. Advances in imaging techniques, computer technologies, radiation physics and radiobiology have led to rapid development in this field. An example is represented by intensity-modulated radiotherapy (IMRT) that was first introduced in 1960s. IMRT provides highly conformal dose distribution by the modulation of the radiation beam intensity using static or dynamic collimators [Nakamura *et al.* 2014]. In 1990s, with the introduction of inverse treatment-planning procedures, the quality of radiotherapy treatment has seen further improvement. A personalized treatment plan can be developed specifically for each patient to achieve an uniform dose distribution on the tumor target while minimizing the dose to the surrounding healthy tissues (Fig. 1.2). Another radiotherapy technique, that has been increasingly used worldwide over the last 20 years, is the stereotactic body radiotherapy (SBRT) [Martin *et al.* 2014]. SBRT refers to the precise irradiation of an image-define extra-cranial lesion, by delivering a high total radiation dose using a small number of fractions. In order to deliver safely large radiation fractions, the treatment system has to be able to produce uniform dose on target volume and steep dose gradient between the gross tumor target and the organs at risk. Inter- and intra-fraction movement of the target as to be take into account by image guidance to ensure that the dose deliver is perfectly matching the patient anatomy. SBRT treatment can be delivered successfully using a conventional gantry-based linear accelerator with appropriate image guidance based on a cone-beam computed tomography system and motion management techniques. However, a new special platform has been developed to allow greater non-coplanar beam arrangements with greater accuracy, such as, for example, the CyberKnife robotic stereotactic radiosurgery system (Accuray) or the Vero SBRT system (BrainLab) [Oppenlander & Porter 2014]. Furthermore, hadrontherapy, which uses irradiating beams of charged particles (protons and other ions, such as carbon). Inversely to X-rays that gradually and mainly exponentially loss energy in tissues, the hadrons deposit almost all of their energy in a sharp peak at the end of their path, in the so-called Bragg Peak. This allows to obtain high conformal treatments, providing efficient sparing of the healthy tissues surrounding the targeted tumor. As a result, handron therapy presents the clear advantages over external radiotherapy in improving both local control of very aggressive tumors and providing a lower tissues toxicity [Lodge *et al.* 2007]. Finally, a last innovative radiotherapeutic techniques which relies on a multidisciplinary approach, deserves to be quoted: the targeted radionuclide therapy. High-affinity radiopharmaceuticals, such as free radionuclides or radiolabeled peptides or antibodies, are transported in blood stream after injection and target molecules on the surface of the tumor cells. The radioactive decay of the radionuclide (β and α emitters) will then cause significant damage to the cancer cells with minimal damage to healthy tissues. This technique represents a further step towards personalized treatment and increase of the overall therapeutic efficiency. However, tangible therapeutic outcomes have been yet demonstrated only for therapy of hematological malignancies [Gudkov *et al.* 2016].

In the same way, new adjuvant treatments have also undergone impressive development in the past years. Gene therapy is probably the most promising field. We can distinguish

different therapy approaches such as immunotherapy and gene transfer. Immunotherapy includes all treatments aiming to stimulate or support the immune system to attack the tumor cells [Wurz *et al.* 2015]. The potential of cancer immunotherapy is known since the 1890s when William Coley showed that the injection of killed bacterial cultures had curative effects in cancer patients. However, first attempt to develop effective therapeutic vaccines and antibodies against solid tumor have been often unsuccessful. An increased knowledge of the mechanism of cancer reaction to immune system and the identification of tumor-associated antigens had led to the development and therapeutic successes of monoclonal antibody in 2013 and gave a renewed interest for anti-cancer immunotherapy. The gene transfer is a new treatment modality that delivers a foreign gene into patient cancerous cells, as a drug, to cause cell death or slow the growth of cancer [Herweijer & Wolff 2003]. Ideally, gene therapy should allow to treat primary and disseminated tumors with a minimal effect on normal cells, which would represent its main and most innovative advantage in comparison to the standard chemotherapy. So far, gene therapy failed or reported limited success in cancer therapy. Nevertheless, experts keep optimistic advice for future advances of this therapeutic mode [Das *et al.* 2015].

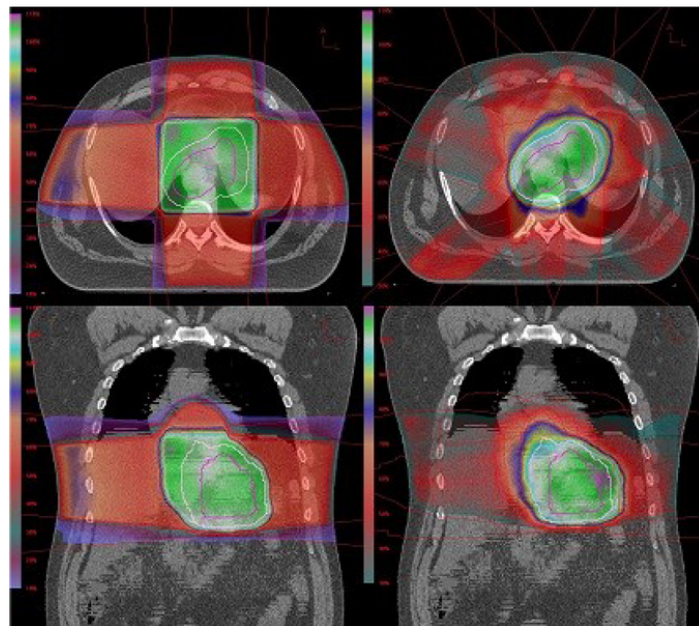


Figure 1.2 – Coronal and axial images of dose distribution for a 3D conformal radiotherapy plan (3D-CRT) plan (left) and IMRT (right) for esophageal cancer [Ling *et al.* 2014]. 3D-CRT utilized X-ray beams traversing the body, creating both entrance and exit doses; as a result the organs at risk are also exposed to radiation. IMRT, using multiple beam angles with modulated intensity, escalates dose at the target while sparing surrounding normal tissues.

Imaging contribution

The concept of medical imaging was born nearly 120 year ago with the discovery of X-ray by Rontgen. From this moment on, it has undergone remarkable developments. In a cen-

tury, we passed from the radiological planar representation of X-ray attenuation of tissues to the detection of submillimetric structures or to the quantification of molecular concentrations. CT scanner and MRI, became largely available respectively during 1970s and 1990s, are medical imaging technologies used to obtain anatomical and structural data on tissue. We can also have access to information regarding metabolism, blood flow, regional chemical composition and absorption of the interest tissues thanks to the functional imaging techniques. Among those, we can distinguish some specific functional sequence of MRI, so called functional MRI (fMRI) and multiple nuclear imaging techniques such as gamma camera scintigraphy, Photon Emission Tomography (PET) and Single Photon Emission Computed Tomography (SPECT). Alongside screening programs aiming for the early diagnosis of cancer, all those imaging techniques plays also a fundamental and complementary role in the treatment of cancer. First of all, they allow to perform the tumor diagnosis, providing information on the location, size, shape and the stage of the malignancy. The medical imaging, together with other specific analysis results (e.g. biopsies, blood analysis etc.), are then consulted and evaluated from a multidisciplinary approach to choose the best therapeutical approach. The availability of detailed information on the biochemical nature of the tumor, its precise localization and delineation allows to plan an individualized and custom treatment that presents the optimal balance between the curative purpose and the undesired side effect such as unaesthetic scar, mutilations, or functional deficit. If surgery is included in the treatment planning, several imaging technologies can be used to guide it. For example, pre-operative MRI images can be used to localize brain lesions, define their extension and obtain functional information to define the eloquent surrounding area. To enhance the accuracy of the surgical procedure, some intraoperative imaging technologies such as interventional ultrasounds [Volders & Haloua 2016], optical imaging [Keereweer *et al.* 2013], interventional MRI [Hall & Truwit 2008] or radioguided imaging probes [Povoski *et al.* 2009], are available to provide a real time visual feed-back on the tumor resection margins. These technics and their clinical applications will be described in more details in the following sections. After surgery, imaging is used to control the quality of the excision and assess the following therapeutical steps. The radiation treatment planning uses imaging techniques to define the optimal dose distribution before treatment, patient position control during the treatment, and more recently, to guide tumor irradiation [Vargo & Beriwal 2014, Hsieh *et al.* 2016]. In chemotherapy, imaging is used for therapeutic monitoring and to predict prognosis. To date, PET imaging is the reference technique for therapeutic follow-up because it allows an accurate and early evaluation of metabolism and volume evolution of treated tumors [Ishiba *et al.* 2015, Zaniboni *et al.* 2015].

Despite the various adjuvant therapeutical approaches and the numerous technological advances, in part described above, surgery remains the primary treatment for solid tumors. In this chapter, we are going to focus on the surgical treatment of solid tumors and on the tools that have been developed to guide the surgeon in the operation room.

1.1.2 Oncological surgery

The excision surgery represents, in most of cases, the first therapeutic step recommended for solid tumor treatment. Depending on the pathology and the staging, two approaches

can be adopted. When solid tumors are discovered in an early stage (small size tumors and well-defined boundaries, no metastasis or involvement of lymph nodes), conservative surgery may be performed. This approach aims to complete removal of the tumoral tissues while preserving as much as possible the surrounding healthy tissues to achieve low morbidity and recurrence rate together with good esthetic results or preservation of organs functionality. On the other hand, when surgery is recommended for voluminous lesions conservative treatment is not allowed and radical treatment is performed: thyroidectomy, mastectomy or gastrectomy represents a few examples. In this scenario, the possibility of a complete excision of malignancies, to reduce recurrence probability, has to be balanced with the risk of higher morbidity and poorer quality of life. In this context, intraoperative detection devices could be useful tools for guiding the surgeon in the accurate resection of the tumor lesions. They allow real-time visualization of tumors locations and boundaries during surgery and inspection of the surgical bed after resection and/or imaging of specimen from the resected tissues in order to control the tumor resection margins. If tumoral residuals are found, the surgeon can continue the operation until complete removal is achieved or sensitive structures are touched. In this way, recurrence and re-operation rate can be sensibly reduced.

1.1.2.1 Clinical impact of surgery for the treatment of solid tumors

Surgery is used both to obtain a therapeutic locoregional control of the cancer and accurate staging of the malignancy.

The surgeon has to perform an excision that removes all the gross tumor area plus a safety *margin* around it to ensure that eventual infiltrated or migrated cells are as well removed. A non-resected tumor mass, called *residual* tumor, may occasionally regrows resulting in a tumor *recur*. The resection margins are distinguished in *positive*, if residual tumor cells are present, or *negative*, if no trace of disease is detected. Depending on the tumor location and extension, sentinel lymph node or the entire nodal station may be excised as well to control the spread of the disease. The histopathological analysis of the extracted tissues and/or the lymph nodes is used for the cancer staging. The resection quality is classified according to the residual disease status (called 'R' factor). The denomination R0 refers to no gross or microscopic residual disease, R1 to microscopic residual malignancies (microscopically positive surgical margins but no gross residual disease) and R2, to grossly evident disease residual. Therefore, the histologic study and classification of the surgical specimens allows to predict the risk of locoregional and metastatic recurrence. These are key points that will influence the choice of the strategy to apply for the adjuvant treatment, if needed. In summary, the surgical treatment can improve survival and quality of life and provides the information to plan complementary therapies. These treatments can be curative or only palliative when patients have advanced cancer or widespread disease.

In the following paragraphs, the attention will be focused on a few selected malignancies for which surgery represents a milestone of curative treatment.

Breast - Breast cancer is the most frequent malignant tumor in women. Around 25% to 35% of these cancers are not palpable at the diagnosis. This stage distribution at diagnosis is mainly due to the wide spread use of mammography for screening and diagnosis together

with the awareness of women. Breast cancer at low stages is associated to a good prognosis: the 5-year survival rate for women diagnosed with localized breast cancer is 98.6%. However, the survival reduces to 83.8% for regional stage and to 23.3% for distant stages. In addition to the stage, the patient survival depends on tumor grade, hormone receptor status and human epidermal growth factor receptor 2 (HER2) status. Surgical treatment for breast cancer involves mastectomy or, for most women diagnosed at early stage, breast-conserving surgery (BCS). This surgery consists of removing the whole tumor plus several millimeters of normal tissues around it. These margins are grossly measured during surgery but until now, no standardized definition has been provided [Angarita *et al.* 2014]. The margin status is microscopically evaluated at the edges of the resected specimen. The majority of woman with early stage breast cancer who undergoes BCS receives complementary adjuvant treatments (radiotherapy and/or chemotherapy and/or hormonal therapy) to improve disease-free and overall survival. The goal of breast conserving treatment is to completely remove the cancer while obtaining low morbidity and good or excellent cosmetic results. However, BCS is also associated with a higher risk of locoregional recurrence than for mastectomy [Fisher *et al.* 2002]. Among others biological components, the strongest predictor of local recurrence is the status of surgical margin [Leong *et al.* 2004, Park *et al.* 2000]. Local recurrence from positive margin is indeed 2 to 3 times greater than with a negative margin [Mullen *et al.* 2012]. After breast-conserving surgery, positive margins are found in 15% to 47% of breast cancer patients and 20% to 81% of ductal carcinoma in situ patients [Angarita *et al.* 2014]. Generally, management of positive margins includes re-excision or mastectomy, depending on the extent of the positive margins and the remaining healthy breast tissues. However, re-excision may result in poor cosmetic results, improved morbidity, increased medical cost and patient stress. The factors that most significantly predict the risk of local recurrence are younger age, higher tumor grade and presence of microcalcifications on mammography and accuracy of lesion burden delineation. Preoperative imaging, such as mammography and ultrasound, and in some cases MRI, allows to define disease boundaries and helps to plan the surgical treatment. However, some lesions are difficult to visualize or occult with mammography. MRI can potentially overcome this limitation, but has a high rate of false-positive requiring supplementary biopsy to confirm the surgical plan [Lehman *et al.* 2009, Houssami *et al.* 2008]. Ultrasound presents a low capability to depict microcalcifications, especially when they are located inside echogenic and fibroglandular breast tissues, and in situ carcinoma.

In women with early-stage breast cancer, the regional lymph node status is one major prognostic factor. Axillary lymph node dissection has been a standard component in the routine of breast cancer management to improve disease control. However, axillary clearance may cause lymphedema, nerve injury and shoulder dysfunction. Sentinel lymph node biopsy is now accepted as a standard of care to perform axillary staging in early breast cancer patients [Senkus *et al.* 2013]. The role of sentinel lymph node in clinical management of breast cancer and other pathologies will be described in more details in Section 1.2.3.2.

Glioma - Gliomas are a group of central nervous system neoplasms that develop in the brain or the spine. Gliomas make up approximately 30% of all brain and central nervous system tumors and 80% of all malignant brain tumors. Gliomas are classified by cell type, grade and localization. A main distinction is made between low-grade gliomas and high-grade gliomas. Low-grade gliomas are rare and compared to high-grade gliomas are heterogeneous,

slowly growing, less aggressive and by consequence associated with a better prognosis. Conversely, high-grade gliomas are highly vascular and infiltrative tumors and are therefore associated with a low survival, usually inferior to ~ 15 months. Depending on the glioma classification, a combination of surgical, radiation therapeutic and chemotherapeutic approaches is used to guarantee an optimal survival and outcome. The goal of surgery is to relieve symptoms and eliminate or control the tumor. The accuracy and extension of the surgical resection are believed to be a key factor to achieve a promising prognosis in neurological oncology [Carpentier 2008, Gil-Robles & Duffau 2010]. Low grade gliomas are usually associated to a better prognosis, however the 5-year survival percentage ranges from 42% to 92% [Sanai & Berger 2008]. Whatever the grade, the largest extent of resection has to be obtained without causing damages to the surrounding functional brain parenchyma (such as speech or balance). The main challenge that the surgeon has to face to perform total or near total resection is the intraoperative lack of information about the margins status and the eventual proximity of eloquent tissue limiting possible resectable area. Traditionally, excision of brain tumors relies on the neurosurgeon's ability to identify slight variation in cortical topography. However, even experienced surgeon may be enable to detect those irregularities. For this reason, preoperative images obtained with ultrasounds, CT, MRI [Rössler *et al.* 2005] or PET [Kaschten *et al.* 1998] can be used to guide the surgeon action. Nevertheless, the brain parenchyma becomes distorted during surgery because of loss of cerebrospinal fluid, oedema and tumor resection. This phenomenon is called brain shift. As a result, preoperative images becomes less reliable during operation, limiting as well the efficiency of neuronavigation [Barbosa *et al.* 2015]. Electrical stimulation of the brain is used in combination with awake craniotomy to guide the tumor resection. This technique allows to map the cortical area involved in motor, sensory, language, and cognitive function located within the tumor or along its margins. The intraoperative stimulation mapping procedure is nowadays an essential procedure in glioma resection and different approaches are available [Hamer *et al.* 2012, Szelényi *et al.* 2010].

Pancreas - Diagnosis of pancreatic cancer is associated to a poor prognosis. Large number of studies had highlight the aggressive nature of these tumors and their high local recurrence rate in combination with early metastasis spread. Complete surgical resection, associated with adjuvant treatments such as chemotherapy, is currently the only curative treatments for pancreatic cancer. However, only a minority of patients is suitable for resection of pancreatic cancer [Hackert *et al.* 2009]. This depends on the localization of the tumor. If it is located in pancreatic areas adherent to or involving adjacent vascular structures, vascular reconstruction can be performed but with limitations [Varadhachary *et al.* 2006]. Pancreatic cancer surgery is performed only when high probability to completely remove all cancerous cells can be achieved (radical resection), since non-radical resection does not improve survival but rather seems to be related to higher morbidity and mortality [Barugola *et al.* 2009]. The 5-year survival rate for patients treated with surgery ranges from 61% to 16%, for patients with stage I and stage IV pancreatic neuroendocrine tumors (National Cancer Data Base). Preoperative imaging modalities such as CT and MRI are generally used for assessment of pancreatic tumor resectability (R0 margin classification). However, the efficacy of these techniques is limited due to difficult differentiation between necrosis, fibrosis and edematous tissue from malignant tumor cells, especially after neoadjuvant therapy [Buchs *et al.* 2010,

Cassinotto *et al.* 2013]. Combined use of endoscopic ultrasound and laparoscopic ultrasonography improves the accuracy of resectability evaluation [Mortensen *et al.* 2011]. Despite this evaluation, microscopic residues (R1 resection) are reported in 75% of cases, resulting in local recurrence and poorer overall survival [Verbeke *et al.* 2006, Esposito *et al.* 2008]. The association of preoperative functional and anatomical images could enhance surgical planning. However, translation of those images to the operating room is difficult due to the change in patient position, tissues swelling after surgeon manipulation and lack of sensitivity for subcentimetric lesion. Visualization and delineation of pancreatic cancer during surgery would greatly improve accuracy of resection [Handgraaf *et al.* 2014].

Thyroid - Thyroid cancer count 3.8% of all new cancer cases in US and its incidence, particularly in women, is rapidly raising [SEER 2014]. The most common type of thyroid cancer is the papillary thyroid tumors, which are the most common endocrine malignancy, slow-growing and highly curable, the follicular and the medullary tumors. Therapeutic management consists in surgery, whose extension depends on the staging, followed by radioiodine therapy for ablation of thyroid remnants and micrometastasis or residual of tumor disease. Most of the patients receive a total (84%) or partial (15%) thyroidectomy [NCDB 2011]. Total thyroidectomy is associated with a increased frequency of surgical complications such as recurrent laryngeal nerve injury and permanent hypocalcemia [Kebebew & Clark 2000]. However, this radical surgery applied to papillary thyroid cancer bigger than 1 cm allows to reduce recurrence risk and improve long-term survival [Bilimoria *et al.* 2007]. Even by combining total thyroidectomy with radioiodine remnant ablative therapy as initial therapeutic strategy, locoregional neck recurrence occurs in nearly 5% to 20% of this patients. The additional application of radioiodine ablative therapy alone does not show adequate control of disease recurrence [Mazzaferrri & Kloos 2001]. Therefore, total resection of thyroid tissues is fundamental to improve patient's survival. Surgery outcome relies once again on accurate preoperative imaging, which enables complete visualization and delineation of the primary tumor. Ultrasound is the most important imaging modality in the evaluation of thyroid cancer while CT and MRI are of interest for cases of invasive and bulky tumors. Functional imaging with PET or PET-CT may also be useful for recurrent cancer not visible on anatomic imaging [Yeh *et al.* 2015].

1.1.2.2 Interventional imaging techniques

When a therapeutic surgical excision of the tumor can be performed, no matter the implied pathology, its success depends directly from the accurate localization and complete ablation of the malignant tissues. Depending on the intervention site, the surgeon can guide the operative procedures relying either on anatomical reference or, when this is in not possible, uses extemporaneous exams of tissue samples, like the frozen-section analysis. The histopathological analysis of the samples requires a significant processing and evaluation time that significantly extend the time of the surgery. Even though this method is commonly performed for resection margin assessment, it has been shown that for some pathologies it has low sensitivity in evaluating final resection margin status [Nelson *et al.* 2013] [Moncrieff *et al.* 2015]. The limitation of this extemporaneous exams is connected to the limited and unrepresentative tissue sampling. Various other protocols have been developed

to guide the surgery and improve it in terms of accuracy, safety and duration. First, the surgeon can use diagnostic images, such as CT or MRI images, that have been previously acquired to plan the surgery. These images help to determine the localization of the tumor lesion. However, for some pathologies, the surgery itself induces modification of the anatomy making the previously acquired images of difficult interpretation to localize the malignancies (*i.e.* brain shift, see 1.1.2.1). More generally, performances and ergonomics of pre-operative imaging technologies are not suited to accurately define the extend of a tumor lesion. Most detection challenges appear with small size lesions, when the lesion has not clearly delimited margins or is localized in an anatomical region difficult to access.

Different intraoperative imaging technologies have been developed to help the surgeon exploring the resection bed and evaluate the possible presence of tumor residual during surgery. These information can be used to perform more extent resection and potentially improve prognosis. These intraoperative tools are used in operating room from more than 20 years for different pathologies interventions (breast cancer, colorectal cancer, thyroid, brain tumors, etc.) We can identify two categories of intraoperative imaging technologies that are currently in clinical use. The first includes standard anatomic imaging systems adapted for intraoperative use, such as ultrasounds, interventional MRI or X ray imaging. The second one relies on the combination of radioactive or optical tumor seeking agents with miniaturized detection systems.

In the following paragraphs will be presented the physical principles, characteristic and limits of three of the main non-isotopic intraoperative imaging modalities: MRI, ultrasounds and optical imaging. Since radioguided imaging is the focus subject of this thesis, it will be described in detail with its clinical applications in Section 1.2.

Interventional magnetic resonance imaging - Magnetic resonance imaging allows to obtain images of the distribution of the hydrogen atoms present inside the organism. This is obtained by placing the patient into a static intense magnetic field (typically between 1.5 and 3 Teslas) which has the effect of aligning the magnetic dipole moment (spin) of the atomic nuclei. The spin acquires as well a precise moment around the static field axis, at the Larmor frequency. If radiofrequency excitation pulse of this frequency is sent, the nucleus undergoes a resonance effect and the spins are moved through the plan transverse to the static magnetic field. When the excitation pulse end, the spins return to their equilibrium position along the direction of the static field in a so-called relaxation time, emitting a pulse at the Larmor frequency that can be registered by specific antennas. The relaxation time depends on the molecular local agitation and therefore the tissue nature. The contrast also depends on the proton density (water distribution) and a possibly, on the presence of contrast agent, that modifies the relation time.

MRI allows to obtain high-resolution images with high contrast between soft tissues. Spatial resolution is directly proportional to the field strength. Intraoperative MRI aims to a real-time assessment of tumor resection [Kubben *et al.* 2011, Senft *et al.* 2011]. Nowadays, the most common clinical application for intraoperative MRI are the brain tumor surgeries. A recent study focused on glioblastomas treatment showed that intraoperative MRI allows to realize total tumor resection in 96% of cases (23 on 24 patients) compared to 68% in the



Figure 1.3 – Excision surgery performed with a low magnetic field MRI (PoleStar N-20, 0.15 T).

control group that underwent a standard microsurgery [Senft *et al.* 2011]. Intraoperative MRI can be performed with an open low-field MRI scanner placed in (from 0.2 to 1.0 Teslas) (see Fig. 1.3) [Blanco *et al.* 2005] or a parallel stationary high field MRI scanner placed in the adjacent room [Martin *et al.* 2000]. The open magnets configuration is more suitable for a bed-side type of interventional procedures than a closed system and despite its low magnetic field the image quality is sufficient for interventional use. However, both approaches have the drawbacks of additional operation time, equipment size and high cost.

Ultrasound imaging - Ultrasonography measures the reflection properties of ultrasounds (amplitude, echo time, resonant frequency, etc. . .) at the interface between two medium of different densities and mechanical properties. Ultrasound probes use a piezoelectric transducer, able to produce a sound wave ranging from 1.5 to 50 MHz and to detect its echo. The sound is focused by the transducer, producing an arc-shape sound wave that travels into the body and come into focus at a desired depth. The sound wave is partially reflected or scattered from small structures. Images are reconstructed from the returned sound wave echoes that vibrates the transducer, which turns the vibrations into electrical pulses. The ultrasound image resolution is inversely proportional to the frequency of the emitted wave.

In the past decades, medical ultrasound has undergone major improvements and has become an indispensable imaging modality, thanks to its flexibility and non-invasive character. Moreover, due to continuous improvements in image quality and 3D image visualization as well as the availability of blood flow information via the Doppler effect, ultrasonography is progressively achieving a greater role in radiology, cardiology, image-guided surgery and therapy. Tumors generally have higher density than healthy tissues and therefore produce stronger echoes. Intraoperative ultrasound imaging helps to determine the surgical entrance and to guide tumor resection thanks to the *in situ* real-time estimation of the size, shape and localization of the lesion. Ultrasonography has been used to evaluate tumor resectability and the identification of metastases in pancreatic tumors [Puri *et al.* 2016], brain tumors [Unsgaard *et al.* 2006], breast tumors [Ramos *et al.* 2013],

hepatic tumors [D'Hondt *et al.* 2011] and colorectal tumors [Greif *et al.* 2010]. Ultrasound imaging is inexpensive, safe and of easy repeatability. However, its use is limited by low spatial resolution for deep sited lesion and the interpretation of the ultrasound images depends on the operator experience [Rygh *et al.* 2008].

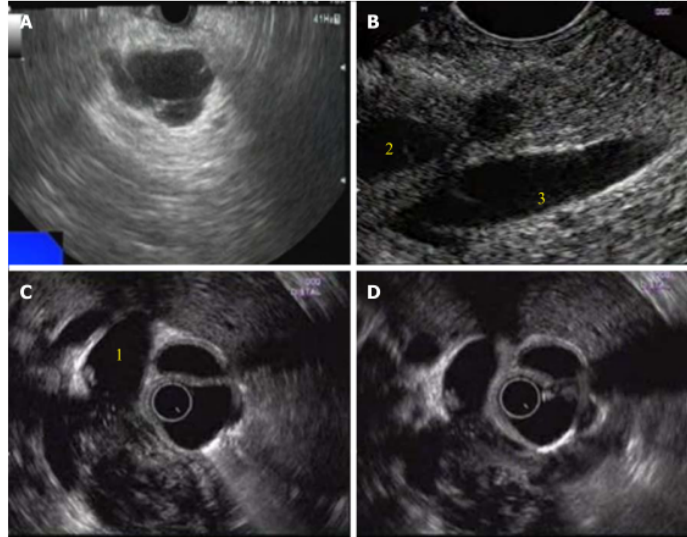


Figure 1.4 – Endoscopic ultrasound showing mass lesion in pancreas [Puri *et al.* 2016].

Optical imaging - Optical detection measures the main parameters (intensity, spectrum, polarization, etc.) characterizing the origin (fluorescence, bioluminescence, etc.) and path of the light into tissues. Optical imaging technologies have the interesting features of providing multiparametric functional information on the analyzed tissue, contrarily to ultrasound and MRI that provide more anatomic and structural information. Further advantages of optical detection are the lack of ionizing radiation, capability of long-term observations and the relatively easy setup. Among the various existing optical detection technologies only the fluorescence is used today for detection of cancerous lesions during surgery. The clinical potential of other techniques, like the Raman spectroscopy [Cals *et al.* 2015] or optical imaging of intrinsic signal [Prakash *et al.* 2009] are still under investigation.

In general, *in vivo* fluorescence imaging is based on the illumination of target tissues with a light source emitting a specific wavelength that can excite the endogenous (autofluorescence) or exogenous fluorophores. When they subsequently return to their basal energy state, the fluorophores emit photons with specific wavelength. The recent availability of sensitive, small and low cost digital imaging systems has enabled the use of real-time digital fluorescence imaging in surgical guidance application. The imaging systems are mostly based on charged-coupled device (CCD) and complementary metal-oxide-semiconductor (CMOS) low-noise and high-sensitivity imaging sensors associated to an excitation light source.

Endogenous fluorescence detection allows to measure the properties of those organism's molecules that emits sufficient fluorescent light to be detected *in vivo* (some aromatic amino

acid, elastin, collagens, NADPH, flavin adenine dinucleotide, lipid components and porphyrins). The concentration and properties of different fluorophores is linked to the biochemistry, physiology and histological organization of the tissues. Cancerous tissues can be discriminated from the health ones thanks to their different optical signature (intensity, spectral distribution, life time of the fluorescent endogenous) [Marcu 2012]. The **imaging of exogenous fluorescence** uses molecular tracers that are not naturally present in the body. The principal molecules used are the indocyanine green (ICG, excitation: 800 nm, emission 850 nm) and the 5-Aminolevulinic acid (5-ALA). The ICG is water soluble and fixes on humane albumin. It had shown good performance for the detection of brain tumors [Haglund *et al.* 1996] and hepatic tumors [Abo *et al.* 2015] and has the advantage of having excitation and emission light in a range where tissues absorption is low. Last years have seen the successful introduction in clinics of indocyanine green for the sentinel lymph node biopsy of various kinds of tumors [Aoyama *et al.* 2011, Jewell *et al.* 2014, Xiong *et al.* 2014, Verbeek *et al.* 2014]. This imaging technique allows to visualize in real-time lymphatic drainage pathways thanks to transcutaneous/transmesenterial fluorescence readout with near-infrared imaging systems. The 5-ALA is a non-fluorescent prodrug that stimulates the synthesis and the consequent accumulation of fluorescent porphyrins preferentially in mitochondria-active tissues such as tumors. Intraoperative use of 5-ALA is an accepted method that allow to enhance glioma visualization under blue light and thus more complete resection leading to increased survival [Stummer *et al.* 2006]. Other fluorescent dyes, such as the fluorescein, that cumulates in cerebral areas where the blood-brain barrier is damaged are clinical available. The study performed by [Acerbi *et al.* 2014] showed that intravenous administration of fluorescein during surgery of high grade glioma is safe and allows a high rate of complete resection (achieved in 16 cases on 20). Figure 1.5 shows the view of the surgical cavity obtained with the dedicated microscope used during surgical procedure.

New fluorescent dyes, excitable in the visible to near-infrared wavelengths, are under development expanding the possible applications of fluorescence imaging at both cellular and systemic levels [Etrych *et al.* 2016]. However, fluorescence imaging method have some major drawbacks. Although fluorescent intensity is directly proportional to the fluorochrome concentration, it is strongly affected by tissue depth and the optical properties of the surrounding tissue [Ntziachristos *et al.* 2005]. For example, high tumor vascularization (high hemoglobin concentration) will reduce the signal because of the increase absorption of photons by the intervening tissues. Moreover, the exogenous tracers cause a cutaneous sensibility of the patients, that have to stay indoor for several days.

Anatomic imaging technologies present some useful features allowing to lead the surgeon gesture on the basis of tissues structures, but have limited efficiency for the detection of small tumors foci or tumor margins, especially when they are infiltrated. On the other hand, fluorescence imaging allows to access to cancerous tissues functional information thanks to the molecular targeting. However, the number of tracers allowed in clinical routine is still very limited. In that context, the intraoperative detection methods based on radiolabeled tumor detection are integrated in reliable and well-established clinical protocols.

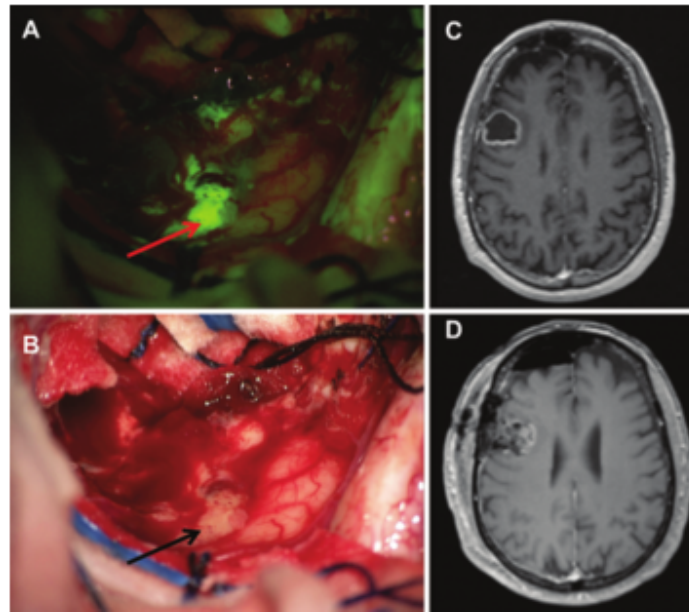


Figure 1.5 – Intraoperative view during resection of a right frontal glioblastoma; the 5-ALA fluorescent tumor area to resect is pointed by a red arrow (A). The same view is shown with a white light illumination where tumor tissues are indicated by black arrows (B). Preoperative axial T1-weighted MR image with contrast agent (C). Postoperative (48 h) contrast MR image showing a complete tumor resection (D) [Acerbi *et al.* 2014].

1.2 Radio-guided cancer surgery

The concept of radioguided surgery was born in 1949, when Selverstone *et al.* used a Geiger-Muller tube to detect the β^- radiation emitted from the ^{32}P , intravenously injected to 33 patients suspected of brain tumor [Selverstone *et al.* 1949]. However, this first metabolic radiotracer was put aside due to high irradiation of the patient. From the sixties, the development of new nuclear imaging modalities, such as the gamma camera and the single photon emission tomography (SPECT), stimulated the development of new gamma-emitting radiotracers. The availability of these radiotracers led to the conception and development of dedicated intraoperative probes [Povoski *et al.* 2009, Tsuchimochi & Hayama 2013]. Along with the development of positron emission tomography (PET) and the associated β^+ emitting radiopharmaceuticals in the 1970s, came also a renewed interest for the design of β^- intraoperative probes. More recently, research in target radionuclide therapy lead to the development of an increasing number of α , β^- and Auger electrons emitting pharmaceuticals. This had open the prospective of using β^- radiotracers instead of β^+ radiotracers for intraoperative imaging [Collamati *et al.* 2015a]. Radioguided surgery of cancer and sentinel lymph nodes is now a well-established clinical practice. The efficiency of the intraoperative radio-guidance in terms of sensitivity and specificity relies on the association between the miniaturized detection device, the nuclides and the tumor-seeking agent. We present in the following sections (1.2.1 and 1.2.2) the main characteristics and diversity of radiotracers and intraoperative probes used in radioguided operative cancer surgery.

1.2.1 Radioactive tumor labelling

The radiopharmaceuticals generally used for radioguided surgery are a chemical combination of a biological compound, which targets specific biochemical receptors or is metabolized by cells, with a radioisotope for radiolabeling. They exist as well radioactive nucleus that can be used alone as tracers, like ^{204}Tl , ^{123}I or ^{125}I . The great variety of molecules that can be synthesized allows to observe many different biological processes. We can distinguish two targeting mechanisms. The first one consists in the use of particular radiotracers that have negligible interaction with molecules in the body and whose non-specific uptake depends mainly on their diffusion properties (see Section 1.2.1.2). The second method uses analogs of molecules that participate to the target biological process (peptide, amino acids, antibodies, neurotransmitter, etc.) (see Section 1.2.1.3). These radiotracers can be used to label tumor cells that show specific physiological or metabolic anomalies.

1.2.1.1 Constraints on the radiotracer choice

The choice of the radioisotope associated to the ligand molecule is limited by constraints of different natures. It exists chemical constraints concerning the production of the couple tumor seeking agents labeled compound and physics constraints associated to the detection optimization and limitation of patient exposure.

Chemical constraints - First of all, the radiotracer uptake in the tumor must be as specific as possible. The specificity of a radiotracer is defined by the ratio between radiotracer uptake in tumor and healthy tissue. A high specificity improves the tumor detectability with external or intraoperative imaging devices. The radiotracer must also not interfere into the physiology or the metabolism of the observed process. In that context, the high sensitivity of radioisotopic imaging allows the injection of very low amount of radiotracer (nanomole concentrations), thus minimizing any pharmacological effect. Furthermore, the chemical bond between tracer and radionuclide has to be stable *in vivo* in order to ensure a good uptake of the radionuclide in the target area while limiting its diffusion into the body, causing lost in sensitivity and specificity as well as potential toxicity. Finally, the rapid systemic clearance of unbounded radiotracers is also critical to achieve high contrast imaging.

Physic constraints - The radiations emitted by the radionuclide have to show specific characteristics in order to be detected without producing collateral damage for the patient. The energy of the radiation must be high enough to travel through the tissue and enter the detector, but in the meantime be low enough to be stopped inside it and detected. For γ emitters that has to ideally range between 100 and 300 keV. This energy range is optimal for external detection and it limits as well patient irradiation and distal contamination generated by scattered photons. For β^+ emitters, the radionuclides must be selected with a low energy (less than 1 MeV) in order to limit the dose to the patient. The physical half-life of the radionuclide should be compatible with the *in vivo* pharmacokinetics of the tumor seeking agent [Zhou *et al.* 2013]. Half-life must be longer than the time required for the preparation of the pharmaceutical, its delivery to the clinic, its injection, the uptake in the tumor and the imaging protocol. For example, the short half-life of ^{11}C ($t_{1/2}=20$ min), ^{13}N ($t_{1/2}=10$

Isotope	Half-life	Radiation	Energy (keV)	Production
^{11}C	20.3 min	β^+ (100%)	385.7	Cyclotron
^{18}F	110 min	β^+ (97%)	250	Cyclotron
^{64}Cu		β^+		
^{68}Ga	67.6 min	β^+ (89%)	836	Generator
		γ	1077,34	
^{124}I	100.3 h	β^+ (%)	370	
^{99m}Tc	6 h	γ	141	Generator
^{201}Tl	73 h	γ	167, 71	
^{111}In	67.9 h	γ	245, 172	Generator
^{90}Y	64.8 h	β^-	933.5	Generator
^{131}I	8 d	β^-	181	Fission
		γ	360	
^{177}Lu	6.7 d	β^-	149,112, 48	Reactor
		γ	321, 208, 113	

Table 1.1 – *Most common radionuclides used in diagnostic imaging and radiotherapy which are currently or has potential to be used for radioguided surgery. Decay properties and the production mode are presented. For β emitters, the energy represented is the mean energy of the β spectra.*

min) and ^{15}O ($t_{1/2}=2$ min) is not suitable for radioguided surgery application. In addition, the radionuclide should be ideally produced at low cost, readily available and easy to combine with the tracer. Table 1.1 presents the most common radionuclides relevant for the radiolabeling synthesis of radiopharmaceuticals for diagnostic imaging and radio guidance. We present as well some β^- radionuclides, actually used for radiotherapeutic purpose, that presents decay properties interesting for intraoperative detection applications.

A large number of radiotracers has been developed satisfying more or less strictly the above cited constraints. In the following three sections are presented different approaches used to target cancerous cells.

1.2.1.2 Particular radiotracers

Particular radiotracers are used to observe the diffusion of molecules inside the body. The most common ones are the colloids labeled with ^{99m}Tc (antimony trisulphide, albumine, rhenium sulphide). These molecules do not interact with the organism; they are just passively transported by body fluids. The principal feature of colloid radiotracers, that determines their ability to diffuse inside structures of interest, is their size. These radiotracers are essentially used for sentinel lymph node identification (see Paragraph 1.2.3.2), detection of non-palpable lesions and more generally for lymphatic and blood perfusion imaging. In the first application, the radiotracer is injected in the ill organ or directly into

the malignancy, often under ultrasound or radiological guidance. The particle dimension has to be small enough to ensure uniform dispersion of the colloids, allowing their transfer from the interstitial injection site to the lymphatic channels and nodes. However, too small particles could penetrate the capillary membranes and diaphragms outside the lymphatic system degrading image contrast. Therefore, the ideal size for colloid ranges from 20 nm to 100 nm [Wilhelm *et al.* 1999].

1.2.1.3 Metabolic radiotracers

Another strategy for tumor labeling consists in the use of radiopharmaceutical targeting the metabolic activity of cells. Several of them have found a place in clinical routine.

The **^{18}F -fludeoxyglucose** is a glucose analog with the positron-emitting radioisotope ^{18}F that substitutes the normal hydroxyl group at the 2' position into the glucose molecule. When this radiotracer is absorbed, phosphorylation prevents the glucose from being released again from the cell. Indeed, the absence of the 2' hydroxyl group prohibits the ^{18}F -FDG from undergoing further glycolysis: after phosphorylation the ^{18}F -FDG is transformed into ^{18}F -FDG-6-phosphate and remains blocked inside the cell. Fast metabolism cells, such as those of brain, heart or a malignant tumor, are glucose avid and, thereby, accumulate FDG at a higher rate than other cells. ^{18}F -FDG allows to measure malignancy on the basis of increased glucose uptake. This one of the few radiotracers approved by U.S. Food and Drug Administration for clinical PET imaging in oncology, together with ^{18}F -Sodium-fluoride, used for imaging of bones to identify osteogenic activity, and the N^{13} -Ammonia, used for imaging of the myocardium. ^{18}F -FDG is now frequently used for diagnosis and management of cancer patient as well as a standard to which confront new PET radiotracers in development for clinical use. More recently, it has started to be used for radioguided surgery of colorectal cancer [Shestakova *et al.* 2006], breast cancer [Hall *et al.* 2007], thyroid cancer [Kim *et al.* 2011], melanoma [Povoski *et al.* 2008] or lymphoma [Povoski *et al.* 2015].

Somatostatin and its analog **octreotide** are used in combination with ^{111}In (^{111}In -pentetreotide) or with ^{68}Ga (as ^{68}Ga -DOTATATE and ^{68}Ga -DOTATOC). These molecules are hormones inhibitors. These radiotracers allow fast tumor localization, blood clearance and renal excretion. They are currently used to image neuroendocrine tumors, some digestive system tumors and meningioma that overexpress somatostatin receptors. They have also been used for radioguided surgery of pathologies cited above [Kaemmerer *et al.* 2012] [Hall *et al.* 2015]. Somatostatin analogs have been also conjugated with the β^- emitters ^{177}Lu and ^{90}Y for clinical practice of target radionuclide therapy of pancreatic tumor [Sansovini *et al.* 2013]. A feasibility study showed the potential of targeting meningioma and high grade glioma with ^{90}Y -DOTATOC for radioguided surgery [Collamati *et al.* 2015b].

Among the metabolic tracers used during surgery, we can also cite the **hydroxy-methylene-diphosphonate** (HMDP) or **methylene-diphosphonate** (MDP) labelled with ^{99m}Tc to measure the osteoblastic activity. These radiotracers are commonly used for the detection of bones tumor or metastasis, like the osteoid osteoma [Colton & Hardy 1983]. The meta-iodobenzylguanidine (MIBG), labeled with ^{131}I or ^{123}I , is a physiologic analog of norad-

renaline. It binds to adrenergic tissue allowing to target and to detect endocrine tumors, pheochromocytomas and neuroblastomas [Shimotake *et al.* 2005].

Furthermore, other radiotracers that have not still been used, show potential for radioguided surgery. This is the case of **choline** or **fluorocholine** labeled with ^{11}C or ^{18}F , respectively. Choline is the precursor for biosynthesis of phospholipids in the cell membrane and enters into the cell through choline transporters. Choline is used for synthesizing phosphatidylcholine. Choline kinase activity is significantly over-expressed in tumor cells. These radiotracers are particularly interesting for tumors with low glucose consumption for which ^{18}F -FDG is not effective. ^{18}F -choline or fluorocholine is anyway a better candidate for imaging applications thanks to longer half-life of ^{18}F compared to ^{11}C . Several studies showed that choline imaging allows to detect prostate cancer, glioblastomas, meningioma and gliomas [Fuccio *et al.* 2011, Mertens *et al.* 2012]. The ^{18}F -**fluoro-L-phenylalanine** (^{18}F -DOPA) is a tracer of the transport of dopamine, a neurotransmitter which plays a major role in reward-motivated behavior as well as motor control and control of various hormones release. ^{18}F -DOPA is taken up into cancer cells by amino acid transporters which are over-expressed in cancer. ^{18}F -DOPA mostly undergoes decarboxylation and increased activity of L-DOPA decarboxylase is a tracer of neuroendocrine tumors of the central nervous system. Finally, **O-(2- ^{18}F -fluoroethyl)-L-tyrosine** (^{18}F -FET) is a promising ^{18}F -labeled amino acid analog that is taken up by transport system L but is not incorporated into proteins. ^{18}F -FET allows specific labeling of gliomas. The use of both ^{18}F -Choline and ^{18}F -DOPA are authorized to be placed on sale in France.

1.2.1.4 Monoclonal antibodies radiotracers

A third way of targeting cancerous cells, for imaging or therapeutic purposes, is through the use of monoclonal antibodies. Monoclonal antibodies (mAb) are proteins produced by the B lymphocytes of the immune system in response to foreign proteins, called antigens. Antibodies work as markers, binding to the antigen so that antigen molecules can be recognized and destroyed by phagocytes. Monoclonal antibodies can be targeted against antigens expressed on the surface of tumor cells or against antigens expressed within the extracellular environment around the cell. A large variety of monoclonal antibodies has been identified to target different tumor types. Among those, the most intensely investigated and clinically evaluated for applications in radioimmunoguided surgery is the TAG-72 (Tumor Associated Glycoprotein 72) and the CEA (CarninoEmbryonic Antigen) which target antigen expressed by epithelial tumors (breast, colon, lung), or as well PSMA (Prostate-Specific Membrane Antigen) for targeting prostatic cancer. These monoclonal antibodies radiotracers have been used for radioguidance during surgery for colorectal cancer [Mayer *et al.* 2000, Agnese *et al.* 2004], renal tumor [Strong *et al.* 2008], thyroid cancer [Bartolazzi *et al.* 2008] and breast cancer [Scollard *et al.* 2011]. Furthermore, $^{99\text{m}}\text{Tc}$ -Tilmanocept is a new agent that has been recently approved for guiding sentinel lymph node biopsy in several solid tumors [Wallace *et al.* 2013, Agrawal *et al.* 2015]. Tilmanocept has high specificity for the CD206 receptors which are present on the surface of macrophages and dendritic cells residing in sentinel lymph node. This is the first target specific radiotracer for sentinel lymph node cells.

The principal drawback of the immunological approach is the relatively long time (a few days to a few weeks) needed after injection to attend the optimal uptake of the tracer in tumor tissues. For this reasons, the radionuclides associate with antibodies (^{123}I , ^{131}I , ^{111}In) have relatively long half-life compared to the one used for diagnostic imaging. To reduce irradiation of the patients, the circulatory half-life of the antibodies has to be reduced. This can be done through pre-targeting. This approach consists in two steps: in a first step, the tumor is pretargeted with an unlabeled antibody construct and in the second step this construct is targeted with radiolabeled small molecules. This results in a more rapid clearance of the radioactivity from normal tissues due to the fast pharmacokinetics of the small molecules as compared to the antibodies [van de Watering *et al.* 2014].

1.2.2 Intraoperative detection devices

If surgery protocol foresees the use of an intraoperative miniaturized probe for detection of radiolabeled malignancies, the patient is injected with the appropriate radiotracer before the surgery. The time of administration (which ranges from several minutes to few hours) is chosen in order to maximize the uptake into tumor cells and will depend on the modality of assimilation of the molecular tracer in tissues. Radioguided detection is usually performed in three steps. First of all, the surgeon explores the surgical field with the detection probe before incision to localize the uptake areas of the radiotracer. Secondly, during tissue excision, the intraoperative detection device is used to control in real time the resection margins. Finally, the quality of the excision is evaluated by the analysis of the residual activity in the extracted tissues or in the surgical bed. Due to the wide range of surgical procedures and available radiotracers, different types of intraoperative probes have been developed for the detection of γ , β^+ or β^- emitting radiotracers. The detection of positron and electrons can be direct or indirect, with the detection of Cerenkov light emitted by the charged particles passing through tissues.

1.2.2.1 Detection performance parameters

Several parameters can be used to define the performances of an intraoperative detector. The optimization of these parameters usually implies many trade-offs in the design of the detector.

Spatial selectivity represents the volume of tissue observable with the probe. It is described by the width of the sensing cone out of which the radiation or the particle is being detected at a defined distance. Spatial selectivity depends as well on the average path of radiations or particles in tissues. γ rays detectors are able to detect signals coming from tissues localized in deep (the attenuation length of water at 140 keV is 6.5 cm), but in return are also sensitive to background noise generated from distal non-specific uptake areas. Inversely, due to the short free path of β inside tissues (of the millimeter order for positrons emitted by ^{18}F), these particles are not suitable for detection of tumors located deep inside the patient. However, this short range allows to remove a large part of the biological background noise and thus, improve the signal-to-noise ratio. Moreover, β particles can be detected in the operative wound with small and low weigh detectors because no collimation

is needed (see Section 1.2.2.4). The interaction mechanisms of γ rays and β particles in the energy range of clinical radiotracers will be presented in details in Section 2.2.

Sensitivity represents the ability to detect incident radiation (γ or β) for a given energy range. It is usually expressed as the number of counts detected per second and per MBq of source activity (cps/MBq). It depends on the intrinsic detection efficiency of the detector and its geometry, which defines the acceptance solid angle between the detector entrance window and the radioactive source. This solid angle, which is inversely proportion to the square distance between the probe and the source, is the main restricting factor to γ probe sensitivity for the localization of in deep-seated malignancies (see Section 1.2.2.3). The second factor that strongly influences the sensitivity of γ detectors is the collimation system used to select the radiations coming from the tissues according to their incident angles. The sensitivity of β detectors is more specifically influenced by the strong absorption of β particles inside tissue interposing between the source and the detector.

Spatial resolution defines the ability of the detection probe to accurately localize the position of a radioactive point source, as well as to separate and distinguish close point sources. For the imaging probes, this is usually estimated from the full width at half maximum (FWHM) of a point source image. For counting probes, the spatial resolution is equal to the lateral spatial selectivity.

Energy resolution defines the capability of the detector to discriminate between emitted radiations with different energies. It depends mainly on the number of information carriers (photons and/or electron-hole pairs) generated inside the detection volume for a given energy deposition. Energy resolution is a key feature for detection of γ radiations. A high energy resolution allows to discriminate primary photons from scattered photons (generated by Compton effect). This allows to improve the image **contrast**, which reflects the ability to distinguish the activity within the target issue from that of the background activity coming from the surrounding healthy tissues. The energy resolution does not concern the beta detection.

Sensitivity is a key feature for intraoperative imaging since it directly defines the detectability of the tumor tissues and the minimum time needed to detect them. Intraoperative detection of small tumor foci depends as well on the ability to reject background noise coming from the non-specific uptake of the radiotracer. For γ detection probes, background noise rejection can be optimized by improving the design of the collimation system or the energy resolution. In the case of positron detection, the background noise comes from the high energy γ (511 keV) generated by the annihilation of β^+ in tissues. This noise can be minimized through an accurate choice of material and dimension of the sensing volume or actively removed by using dedicated rejection devices (see Section 1.2.2.4 and Section 2.4.2). Beyond the detection performances, many design features of the intraoperative probe may be important for the surgeon. First of all, the weight, shape and ergonomics of the probe are key features to facilitate the exploration of the surgical wound and reduce the distance between the detector and the analyzed tissue, in order to improve sensitivity and spatial resolution. In that context, wireless technologies could help to further enhance the ergonomics of intraoperative detectors used in radioguided surgery [CrystalPhotonicsGermany 2016]. Secondly, audible signal and/or digital display associated to the spatial distribution of the counting rate are important tools to provide to the surgeon the critical information needed to

perform real-time localization of the radiolabeled tumor foci [Tsuchimochi & Hayama 2013]. Lastly, versatility of the system by using interchangeable detection head, interchangeable collimator, removable shielding or user-adjusted energy windows for different radiotracers can help to extend the scope of intraoperative devices.

1.2.2.2 Cerenkov light imaging

Cerenkov luminescence was first described by the Russian scientist P. A. Cherenkov in 1934. This initial observation consisted in the blue light emissions, which can be seen in water basin when radioactive decay is taking place inside it. Cerenkov radiation is produced when a charged particle travels a dielectric medium with a velocity that exceeds the speed of light in this medium. The charged particle induces a local polarization of the medium along its path, and radiation is emitted during the return to a steady state. Production of Cerenkov light is a threshold effect and the number of photons emitted depends on the velocity and thus, the energy of the particle and on the refractive index of the medium as described by the Franck and Tamm theory. In 2009, Robertson *et al.* demonstrated that detection of Cerenkov luminescence emitted by β emitters can be potentially used for optical detection in a clinical setting [Robertson *et al.* 2009]. In particular, they showed that β^+ emitting radiotracer (precisely ^{18}F) used for PET imaging are sufficiently energetic to produce Cerenkov luminescence. The minimum energy required for a β to produce Cerenkov radiation in tissues (refraction index between 1.36 and 1.45) is indeed around 260 keV. Most of the positron radiotracers exhibit higher β^+ endpoint energy.

The finding of Robertson *et al.* was validated by [Liu *et al.* 2010]. They evaluated the Cerenkov light yield produced by some β^+ emitters such as ^{18}F and ^{64}Cu and β^- emitters such as ^{90}Y , ^{131}I and ^{177}Lu . They showed that higher energy beta particles generated stronger optical signal and should be preferred to improve detection and imaging sensitivity. For example, ^{18}F (positrons end point energy of 633 keV) produces 1.4 Cerenkov photons per decay (in water) while ^{90}Y (β^- with endpoint energy of 2.28 MeV) can produce up to 57 photons per decay in water [Mitchell *et al.* 2011]. Liu *et al.* also performed some *in vivo* imaging experiments on mice using different radiopharmaceuticals to target glioma, bones, thyroid and prostate cancer. Following these preliminary studies, various devices for planar or tomographic preclinical imaging using Cerenkov luminescence have been developed [Li *et al.* 2010a, Spinelli *et al.* 2011]. The interest of this new imaging technique has been also evaluated for image-guided surgery application [Holland *et al.* 2011, Liu *et al.* 2012, Song *et al.* 2015]. In that context, Cerenkov imaging offers the intrinsic advantages of intraoperative optical imaging devices (easy set-up, low cost, high spatial resolution) without the limit of the restricted availability of fluorescent tracers. Nevertheless, the physical properties of Cerenkov radiation imply many constraints on the detection. First of all, the low number of generated photons imposes the use of high sensitive devices and high uptake inside target tumor tissues in order to enhance the image contrast. A recent study conducted by [King *et al.* 2015] compared the performances of a Cerenkov luminescence imaging device with a β radioluminescence imaging device, incorporating a scintillator with a γ -rejection method to perform β imaging. King *et al.* showed with phantom experiments that the β -radioluminescence imaging device allow to obtain a sensitivity 560 folds greater than that of the Cerenkov light imaging. Furthermore, Cerenkov radiation is emitted

in a continuous spectrum that ranges from the near ultraviolet through the visible spectrum, with a distribution that is inversely proportional to the square of the wavelength. Therefore, a large fraction of Cerenkov light produced *in vivo* is emitted in the ultraviolet region. In this range, the photons are strongly absorbed by the tissues due to the hemoglobin (absorption coefficient is 0.5 and 2 mm⁻¹ for grey matter and heart tissues, respectively), meaning that the detected signal comes mainly from tissues surface. Conventional planar Cerenkov light imaging cannot give any information about under skin tissue. Moreover, scattering of photons inside tissues further degrades the spatial resolution. Liu *et al.* and Song *et al.* propose endoscopic imaging as option to reduce optical signal loss in tissue absorption and scattering through a minimally invasive technique. In their study on a mouse model, Liu *et al.* found that the sensitivity limit of their system was 45 kBq (1.2 μCi)/300 μl with ¹⁸F-FDG. This implies that if the system were used for head and neck tumors of the oropharynx an intravenous injection of 2.1 GBq would be necessary for a 70 kg patient in order to visualize a 300 μg tumor within a 5 minutes scan. This activity is 5 to 10 times higher than the dose required for a PET standard exam. Another option to reduce the effect of tissue absorption would be to shift the Cerenkov emission from UV to the red wavelength region. Cerenkov light can be used to excite a fluorescent agent and generates an emission in the longer-wavelength region. For example, quantum dots have a large Stokes shift, they can be easily excited by Cerenkov light, and the resulting optical emission is shifted to longer wavelengths which are more suitable for deep tissue imaging [Dothager *et al.* 2010]. The wavelength shift can also be obtained by coupling the radionuclide with fluorescent nanoparticles or other fluorophores [Thorek *et al.* 2013b, Li *et al.* 2015].

1.2.2.3 Gamma detection

Gamma detectors, and especially counting probes, are the only radiation detectors that have been used in clinical routine within the operating room for more than 20 years. They are either designed for detection of middle-energy radiations ranging from 20 to 360 keV, corresponding to the SPECT dedicated radiotracers or for the high-energy 511 keV γ rays produced by the PET radiotracers. We can distinguish between two types of detector: the counting and the imaging probes.

Gamma counting probes - Many γ counting probes are commercially available with different shapes dedicated to various clinical applications (Fig. 1.6). Most of them look like straight or tilted pencils. Gamma probes dedicated to laparoscopy are equipped with a longer handle, up to 50 cm, in order to be able to fit through a trocar. All these counting probes give real-time information about the number of events detected inside the detector head, which can be displayed on a monitor and/or be converted into a sound signal allowing the surgeon to scan the surgical wound looking for radiolabeled tumoural foci. Some examples of γ commercially available counting probes are presented in Table 1.2.

The counting probes are compact monopixel detectors. They consist of a detection head built around a scintillation or semiconductor ionization detector enclosed by lateral shielding in order to stop all radiations coming from the probe sides [Mariani *et al.* 2010, Heller & Zanzonico 2011]. The probe spatial selectivity, which directly affects the resolution, is furthermore improved by implementing a collimator placed at the tip of the detector



Figure 1.6 – (Left) From the bottom to the top gamma counting probes for laparoscopic use and a shorter version, high sensitivity probe, articulatable hand held probe, probe dedicated to the detection of high energy gamma rays produced by positron emitters and wireless probe. (Right) Wireless gamma counting probe with its Bluetooth connected control module (manufactured by Crystal Photonics Germany) [CrystalPhotonicsGermany 2016].

to select the direction of incoming radiations. The length and aperture dimension of the collimator define the acceptance cone. The improvement of the lateral spatial selectivity allows to reduce the background noise contamination coming from the distal non-specific radiotracer uptake area. To further optimize the noise rejection, an energy discrimination can be used to identify and discard the Compton events scattered inside tissues. The efficiency of the discrimination depends on the energy resolution of the detector itself. The collimator is usually removable and its geometry may be adapted to the surgical application. This choice is the result of the compromise between spatial selectivity and sensitivity. High selectivity is needed to discriminate fine structures, implying the use of longer and narrower collimators. Conversely, the collimator can be removed to quickly explore a larger field of view. The counting probe CarolIResis incorporates a retractable collimator that allows to tune the probe performances without removing the collimator [Mathelin *et al.* 2006a]. The geometry of the collimator and the lateral shielding should also be adapted to the energy of the incident radiation. The probes dedicated to the detection of 511 keV γ rays produced by positron emitting radiotracers have thicker shielding and therefore a larger diameter and higher weight (Fig. 1.6).

Two main detection technologies are used for the development of gamma counting probes: scintillation detector and semiconductor ionization detectors. In the first category, the detection of the γ ray is indirect. The detection system is composed of an inorganic scintillator coupled to a photon detection device. The most commonly employed crystals are the thallium-activated sodium iodide (NaI:Tl), the thallium-activated cesium iodide (CsI:Tl), the samarium-activated lutetium ortho-oxysilicate (LSO) and the bismuth germanate (BGO). These crystals have high atomic number and offer a good compromise between γ absorption and scintillation light yield (38 and 54 photon/keV for the NaI:Tl and CsI:Tl, respectively). A photosensor device such as a photomultiplier tube or a silicon photodiode, is used to enhance

Probe name	Energy range (keV)	Detector	FoV (mm)	Sensitivity (cps/MBq)	Spatial resolution (mm)	Energy resolution (%)
EuroProbe CdTe	20-364	CdTe	∅11	3200	15 at 1 cm	12
NeoProbe 2000	27-364	CdZnTe	∅14	3000	15 at 1 cm	7
C-Track	27-364	CdZnTe	∅11	2800 (contact)	18 at 1 cm	21
CaroliReS Probe	27-364	YAP:Ce	∅10	13500	8.5-13.7	56
Navigator GPS	37-364	CdTe	∅14	-	13	21
High energy PET Probe	511	NaI	∅12	39000	8	-
CXS-OP-SZ	140-522	CsI+PIN	∅15	20000 (contact)	17 at 1 cm	16
EuroProbe CsI	110-1000	CsI:Tl	∅16	4500	21 at 1 cm	29

Table 1.2 – Characteristics and performances of several gamma counting probes for radioguided surgery.

the produced visible light and to convert it into an electrical pulse. The energy resolution of the detector depends both on the crystal properties, the photosensor quantum efficiency at the wavelength of the scintillation light and the light collection efficiency between the scintillator and the photosensor (optical coupling and coating). For conventional detectors in which a photosensor is directly coupled to the crystal in the probe housing, the energy resolution is around 10-15% at 140 keV. Scintillators materials and characteristics and photosensors commonly used for intraoperative scintillation-based detection probes are presented and discussed in details in Section 2.3.1 and 2.3.2, respectively.

The second detection technology is based on the direct detection of the radiation using semiconductor ionizing detectors at room temperature, such as cadmium telluride (CdTe) or cadmium zinc telluride (CdZnTe). These are high density crystalline materials with relatively high atomic number, which allow the absorption of medium-energy γ by photoelectric effect. The photoelectron created by the interaction of the radiation in the lattice ionizes the atoms of the crystal producing free electron-hole pairs. Under the influence of an electric field, these pairs drift toward the collection electrodes generating a current signal. The number of electrons produced per unit of energy deposited in semiconductor detectors is far greater than the number of photons produced inside scintillator detector, thus allowing a better energy resolution (around 5% at 140 keV). The main drawback of these detectors is connected to the technical limitation of growing crystals with sufficient purity for thicknesses superior to 5 mm. Defects can trap the electrons produced by radiation and thus reduce the charge collected. For this reason, the sensitivity of semiconductor detectors is lower than that of scintillator detectors for energies superior to 200 keV. Both detection systems present advantages and disadvantages. Scintillation detector-based probes have a relatively low cost and high sensitivity especially for medium- to high- energy γ . Main drawbacks include bulkiness and poorer energy resolution and thus worst noise rejection. Semiconductor-based

probes are compact and have excellent energy resolution and scatter rejection. Their main disadvantage is the lower sensitivity, especially for medium- to high- energy photons.

The main limitation of γ counting probes consists in their low spatial selectivity due the important path of γ radiations in tissues (mean free path from 4 to 24 cm for γ of energy ranging from 140 keV to 511 keV). This type of probe is by consequence sensitive to the non-specific uptake of the radiotracers, which can degrade or even compromise the detection of small tumors. This may happen when tumors are located close to the radiotracer injection site or to organs with high natural affinity with the radiotracer, such as bladder or when the difference between radiotracer uptake in tumoral and healthy tissues is low. Moreover, the spatial distribution of the background noise is generally highly inhomogeneous and the detection efficiency is strongly dependent on the positioning of the probe compared to the non-specific uptake structure (inclination, distance). The development of miniaturized γ imaging devices allows to overcome these limitations. A miniaturized γ -camera provides a two-dimensional spatial distribution of the radiotracer and therefore discriminate the background noise from the tumor signal and thus, to improve the detection signal-to-noise ratio which is a key parameter for radioguided surgery.



Figure 1.7 – Surgeon positioning the sterile-wrapped head of the γ -camera Sentinella[®] (S102, Oncovision) using a laser pointer (A,B) and the relative image of a sentinel lymph node (C). Miniaturized portable gamma cameras eZ-scope[®] (Anzai) (D) and Compact Gamma Camera (CGC) from Bugby et al. (E).

Camera Name	Collimator +Detector	FoV (mm)	Energy range	Sensitivity (cps/MBq)	Spatial resolution (mm)	Energy resolution (%)
TReCam	Para+LaBr:Ce +MA-PMT	50×50	^{99m} Tc	300	0.9 at contact	11.3
eZ-SCOPE® (Anzai)	Para or PH+ CdZnTe	32×32	71-364 keV	184	2.0 at 1 cm	8.6
MinicamII® (Eurorad)	Para+CdTe	40×40	30-200 keV	200 at 1 cm	2.46 (theoretical)	5-7
Sentinella 102® (Oncovision)	PH+CsI:Na PSPMT	40×40	71-364 keV	90-900 at 1 cm	5.4-8.2 at 3 cm	15.9
Intraoperative γ -camera (GE Healthcare)	Para+CdZnTe	40×40	40-200 keV	100 at 5 cm	5 at 5 cm	8
SSGC clinical-type (Tsuchmochi)	Para+CdTe	44.8×44.8	550 keV max.	150	1.6 at contact	6.9
IP Gardian 2 (Li-Tech)	Para+CsI:Tl +MAPMT	49×49	^{99m} Tc	210	2.2 intrinsic	20
CarolIReS (IPHC)	Para+GSO +MAPMT	50×50	-	1000	10 at 3 cm	45 (⁵⁷ Co)
NodeView (IMI)	NaI:Tl +PSPMT	50×50	-	270	1.8 at 0.6 cm	12
Bugby <i>et al.</i> (CGC)	PH+CsI:Tl CCD	40×40	-	214	1.28	58 (⁵⁷ Co)

Para = Parallel collimator, PH= Pin-hole collimator.

Sensitivity, spatial resolution and energy resolution are presented for a source of ^{99m}Tc (140 keV)

Table 1.3 – Characteristics and performances of some miniaturized gamma cameras dedicated to radioguided surgery.

Gamma imaging probes - The last twenty years have seen the development of miniaturized γ probes for radioguided surgery as complementary devices to counting probes. These miniaturized cameras are generally based on the basic design of the large field of view γ camera first developed by Anger in 1951 [Anger 1958]. The detection principle consists of the association of a collimator and a position sensitive detector in order to obtain the position of interaction of the incident γ ray, and thus the real-time distribution of the tumor-seeking radiotracer in the target tissues. The development of compact, low weight, robust and easily handled intraoperative cameras was made possible through the numerous technological evolutions concerning the photodetector [Tsuchimochi & Hayama 2013]. To date, several miniaturized gamma cameras are available on the market (see Fig. 1.7). Their field of view ranges from 20 to 100 cm² for a total weight of less than 4 kg. These portable systems can be directly held by the surgeon on contact with the tissue or mounted on an articulated arm for stable positioning, like in the case of Sentinella (Oncovision) shown in Figure 1.7. A sample of these devices is presented in Table 1.3. Unlike γ counting probes, the interest of γ -camera for radioguided surgery is still under evaluation.

As for counting probes, γ -cameras are equipped with a shielding and a collimation system. The collimator choice is a crucial step because it largely influences the spatial performances of the camera (spatial resolution and sensitivity) as well as its weight, dimension and handling. Parallel hole collimators and pinhole collimators are typically used for miniaturized

γ -camera. A parallel hole collimator is made of tungsten or lead plate drilled with holes perpendicular to the collimator surface. This type of collimator realizes a planar projection of the spatial distribution of the radiotracer on the detector with a magnification 1:1. The diameter and length of the holes determine the acceptance angle of the incident rays, and thus the sensitivity of the collimator. The minimal septal thickness is defined by the energy of the radiation that has to be detected. The septa thickness is usually set to allow less than 5% of off-axis photons to pass through the collimator. The magnitude of the spatial resolution loss is directly proportional to the diameter width of the collimator holes and inversely proportional to the hole length. An improvement of spatial resolution can be obtained at the cost of a degraded sensitivity. A pinhole collimator consists of a plate with a single hole (Fig. 1.7, E). The radiotracer distribution image is projected upside-down through the hole on the detector with a magnification depending on the distance between the aperture and the object. The sensitivity of a pinhole collimator improves proportionally with the diameter aperture while the spatial resolution degrades. Maximum magnification, that is the smallest field of view, is obtained when the pinhole is close to the object and decreases as the pinhole is moved further away. This property makes the pinhole collimators particularly suitable to image small, anatomical structures with high resolution.

As for the counting probes, the two main detection strategies used for γ -cameras are semiconductor ionizing detectors and scintillator detectors.

The miniaturized detectors based on the direct detection of γ rays are generally based on pixelated arrays of semiconductor elements operating at room temperature such as CdTe, CdZnTe and less frequently, mercuric iodide (HgI₂). The signal produced in each pixel is usually processed by application-specific integrated circuit (ASIC)-based readout electronics. The intrinsic spatial resolution of a semiconductor array is directly defined by the pixel's size. A small pixel size also allows to reduce the impact of charge trapping by impurities in the crystal. Theoretically, any pixel size is possible but too small pixels suffer for a greater statistical uncertainty in the counts per pixel and implies as well the use of a more complex and therefore expensive electronics. Semiconductor detectors provide better energy resolution than scintillation detectors and allow the fabrication of small, light and more portable camera (e.g. the eZ-scope weight 0.8 kg without collimator, Fig. 1.7). However, as for the counting probes, the main drawback of the semiconductor detector is their low sensitivity for medium and high-energy γ .

Scintillation detector-based cameras combines an inorganic scintillator and a position sensitive detector, which provides the position of the incident γ ray interaction point inside the scintillator from the spatial distribution of the scintillation light. In order to control the spread of the scintillation light on the photosensor, which strongly impacts the intrinsic spatial performances of scintillation-based detectors, the scintillators can be produced as continuous block or pixelated arrays [Pani *et al.* 2002]. The light distribution on the photosensor can also be tuned by inserting a light spreading window between the scintillator and the position sensitive detector. Pixelated scintillators have the advantage of producing a more uniform response on the whole surface, which allows to reduce the distortion effects due to the deformation of the light distribution caused by the light absorption or reflection by the

continuous scintillator edges. However, pixelized scintillators impose a compromise between spatial resolution (defined by the pixel size), detection efficiency (dead areas introduced by the crystal segmentation) and energy resolution (photon absorption due to multiple reflections inside one pixel). The most commonly used scintillators for miniaturized γ cameras are NaI:Tl, CsI:Tl, CsI:Na, Yap:Ce, GSO or, more recently, LaBr:Ce, which thanks to its high light yield (63 photons/keV) and density (5.08 g/cm^3) allows to obtain excellent imaging performances (see Section 2.3.1.2).

The first photodetector used to develop miniaturized γ cameras had been the position sensitive photomultiplier tube (PS-PMT). This and other similar technologies of photodetector, such as multi-anode PMT (MAPMT) or MicroChannel PMT (MCPMT), allow to determine the position of incidence of the photon on the photocathode. This information is obtained thanks to the use of multi-anodic structures, associated to multi-channel electronic readout, allowing to access to the charge collected by each individual pixel and therefore, to the scintillation light distribution, enhancing image reconstruction performances. The structures and characteristics of the most commonly used PMT-based photodetectors in intraoperative medical imaging are presented and discussed in Section 2.3.2. The development of these compact position sensitive detectors had contributed to the development of miniaturized γ cameras some of which are now commercialized (Table 1.3) [Fernández *et al.* 2004, Mathelin *et al.* 2006a, Salvador *et al.* 2007, Trotta *et al.* 2007, Trotta *et al.* 2008, Netter *et al.* 2009]. Different position reconstruction methods have been proposed to optimize the imaging performances such as the barycenter squared [Pani *et al.* 2009], maximum likelihood [Lee *et al.* 2002], neural network [Marone *et al.* 2009] or light distribution fitting [Cornelio *et al.* 2011], which are described in more details in Section 2.5.5. Other photodetectors have been employed for the development of miniaturized γ -cameras but in a more marginal way. We can quote the silicon photodiodes PIN arrays [Gruber *et al.* 1998], the Intensified Position-Sensitive Photodiode (IPSD), which couples a micro-channel plate image intensifier tube to a position-sensitive diode [Pitre *et al.* 2003] or the arrays of silicon drift detectors [Busca *et al.* 2010]. Recently, Bugby *et al.* proposed an handheld small field of view γ -camera using a pinhole collimator focusing the γ rays on a CsI:Tl scintillator joined to an electron multiplying Charge-Coupled Device (EMCCD) technology [Bugby *et al.* 2014] (Fig. 1.7). In CCD image sensor, the pixels consist of p-doped Metal-oxide-semiconductor (MOS) capacitors. When the capacitor array is irradiated, the photosensitive region of CCD pixels (an epitaxial layer of silicon) accumulates an electric charge proportional to the intensity of the incident light. Then, a control circuit permits the transfer of the content of each capacitor to its neighbor, operating in the so-called shift register. The last captor of the array transfer its charge to a charge amplifier in order to convert it into a voltage. In electron multiplying CCDs, the signal is further amplified compared to standard CCD thanks to the use of an additional electron multiplication stage. These photosensors have a dark count rate that strongly increases with temperature. Thus the prototype of Bugby *et al.* incorporate a cooling system which increases probe dimensions. Finally, the recent appearance of Silicon PhotoMultipliers (SiPM), developed and fine-tuned during the last fifteen years, allowed the development of new miniaturized γ -cameras with excellent performances and improved compactness [Majewski *et al.* 2011, Yamamoto *et al.* 2011, Dinu *et al.* 2015]. The photodetector techno-

logy will be presented in details in Section 2.5.3.1.

1.2.2.4 Beta detection

Even though the first radioguided surgery was performed in 1949 with a β^- emitting radionuclide, this detection method was left aside during many years and its use is still today marginal. However, the recent emergence of promising specific tumor-seeking agents labeled with positron or electron emitters is giving rise to a renewed interest for radioguided surgery using beta probes. Intraoperative beta detection presents intrinsic advantages over gamma detection to improve accuracy and sensitivity of tumor localization during surgery. The main advantage is the improved spatial selectivity due to the short range of beta particles in tissue compared to the attenuation length of γ rays for a given energy. For example, the maximum range inside water of positrons emitted from a ^{18}F nucleus ($E_{max} = 650$ keV and $\bar{E} = 240$ keV) is of the order of 1 mm [Levin & Hoffman 1999], as will be described in Section 2.2. This short range allows to avoid contamination coming from non-specific uptake of the radiotracer and thus, to improve the tumor signal-to-noise ratio. Moreover, the short range of β particles in soft tissue is also perfectly suited to inside-body localization of tumor with small and low weight detectors, both because no collimation is needed but also because β particles can be successfully absorbed in small volume detectors (1 mm thick plastic scintillator is enough to absorb all energy). Therefore, the intrinsic sensitivity of β detection is from one to three orders of magnitude higher than that of γ detection. The sensitivity of a γ probe for a radioactive source placed on contact with the detector ranges from 3 to 40 cps/kBq compared to more than 100 cps/kBq for a β probe (see Tables 1.3 and 1.4). However, the short range of β particles requires to put the detector in contact with the target tissues and so to be made as compact as possible in order to be introduced in the operative wound or to be used in an endoscopic system [Shimazoe *et al.* 2011]. β detection is also of no use for the localization of deep-seated tumors.

The advantages and constraints of β detection are complementary to the ones of γ detection. Detection of γ rays allows the localization of deep seated malignancies. However, its poor spatial selectivity and sensitivity makes it unsuitable for the inspection of resection margins and detection of small cancerous foci. On the other hand, β detection is of no value for localization of deep-seated tumors or if interposing tissues are present, but it can provide real-time information about the tumor extend, the assessment of reasonable surgical resection margins and the post-operative control of the surgical cavity, leading to a complete resection of the tumor while preserving as much as possible the surrounding healthy tissues.

Design of intraoperative β counting probes - As for γ detection, β counting probes have the shape of a pencil to be easy to handle and to be inserted in narrow surgical cavities. Some examples of β probes developed in the last years are presented in Table 1.4 and Figure 1.8.

In contrast to monoenergetic γ rays, β disintegrations are characterized by a continuum energy spectrum that goes from 0 up to 500 keV or 2 MeV for the radionuclides commonly used in nuclear medicine imaging (see Table 1.1). Aside their compactness, the ability to detect low energy β particles is one of the key features of β probes because it directly impacts their sensitivity.



Figure 1.8 – Image of the intraoperative β counting probe developed by Camillocci *et al.* with a screen to display in real-time the counting rates (A) and image of the wireless Beta Probe from IntraMedical Imaging (B).

Due to their low range in matter, electrons and positrons can be directly detected in silicon semiconductor ionizing sensors with thin and low density semiconductor ionizing sensors such as silicon. The low Z of silicon limits the undesirable effect of backscattering of the charged particles inside the detector (see Section 2.2.1.3). Silicon semiconductor detectors are usually build around a p-n junction with the thinnest boundary possible in order to limit the energy lost by incident charged particles and a thick enough depletion area to completely absorb their energy [Raylman & Wahl 1996, Raylman & Hyder 2004]. However, semiconductor sensors are presently highly sensitive to temperature, requiring a cooling system, and the absence of intrinsic gain, which make them unsuitable for the development of miniaturized intraoperative β probes. Many β sensitive probes also propose the use of an indirect detection through scintillation light. Due to their low effective atomic number and density, organic scintillators, mainly composed of carbon, oxygen and hydrogen, are good candidate for the detection of charged particles in small volumes while being relatively insensitive to γ rays. Among the organic scintillators, plastic ones are frequently used due to their low cost and simplicity of manufacture into almost any desired size or shape (see Section 2.3.1.1). The scintillator is usually coupled with photomultiplier tubes. Due to the bulkiness of PMTs, light is usually guide to the photosensor throughout a light guide made, for example, with optical fibers [Daghighian *et al.* 1994, Raylman & Wahl 1994]. A major problem of the optical fibers is that only a small fraction of the light emitted from the scintillator, which has random orientation, would actually be transmitted down the fiber causing sensitivity degradation, especially for low-energy beta particles [Hoffman *et al.* 1999]. Semiconductor devices, such as avalanche photodiodes or surface barrier detectors, are small enough to be directly coupled with the scintillator. However, their low intrinsic gain, that avoids the detection of

Probe name	γ noise rejection	Detector	FoV (mm)	Sensitivity (cps/kBq)	Spatial resolution (mm)
Yamamoto <i>et al.</i>	Coincidence	Plast. scint. +BGO+PMT	$\varnothing 8$	2.6 (at 5 mm)	11 (at 5 mm)
Raylman <i>et al.</i> (probe)	Subtraction	Silicon (IISD)	$\varnothing 16.5$	195 (at 1 mm)	-
Raylman <i>et al.</i> (endoscope)	Subtraction	Silicon (SBD)	$\varnothing 3$	195 (at 1 mm)	3 (at 0.5 mm)
Beta Probe (Intra Medical)	Subtraction	Plast. scint. +PMT	$\varnothing 5.5$	108 (contact)	10 (contact)
Beta Probe (Silicon Instrumental)	-	Silicon	$\varnothing 16$	243 (at 1 mm)	8 (at 1 mm)
Beta Probe CSX-OP- β (Crystal Gamma Probes)	-	pin-photodiode	$\varnothing 12$	20 (contact for ^{68}Ga)	8 (at 6 mm)
Camillocci <i>et al.</i>	-	P-terph. scint. +PMT	$\varnothing 5$	-	2.8 (at 0.35 mm)

Plast. scint. = Plastic scintillator. P-terph. scint. = P-terphenyl scintillator.

Table 1.4 – Characteristics and performances of some beta counting probes dedicated to radioguided surgery.

light levels lower than a few dozen photons, limit their usefulness. In that context, development of silicon photomultipliers has made available compact photosensors with intrinsic gain equivalent to vacuum photomultipliers (see Section 2.5.3). A few prototypes of β counting probe are based on this new technology [Mester *et al.* 2011, Solfaroli Camillocci *et al.* 2016].

If β sensitivity is the most important parameter to detect small tumor labeled with positron emitters within acquisition times compatible with the surgery duration, the ability of the probe to reject the background γ noise is also crucial to improve the tumor signal-to-noise ratio and thus, the detectability of the lesions. Indeed, together with the positron signal, the β probe will detected as well a background noise originating from the 511 keV annihilation γ rays. Its origin and nature is discussed in details in Section 2.4. The intensity of the noise contamination will depend on the localization of the targeted area: it will be more important in proximity of non-specific uptake structures, such as brain, kidney or bladder. Two different methods can be followed to reduce the background noise. The first one consists in a passive reduction of the γ rays contamination by optimizing the choice of the materials and geometry of the detector. The second option relays on the active rejection of the noise, for which different strategies can be proposed: coincidence detection of a positron with one of its annihilation γ using a phoswich scintillator [Hoffman *et al.* 1998, Yamamoto *et al.* 2004, Yamamoto *et al.* 2005] or subtraction of the gamma contamination estimated with an additional detector shielded to positrons. [Daghighian *et al.* 1994, Raylman & Hyder 2004]. Both methods will be described in details in Section 2.4.2.

A further solution to avoid the γ background noise consists in the use of β^- -emitting radiotracers. This option is gaining interest thanks to the recent development of molecular therapy radiotracers, that can efficiently and selectively delivers β^- emitters to the tumor. These tracers create essentially no γ contamination, since bremsstrahlung contribution is negligible (0.1% emission probability) [Solfaroli Camillocci *et al.* 2016]. Camil-

lacci *et al.* have developed a β^- counting probe prototype based on a sensitive cylinder of organic scintillator (p-terphenyl) coupled to a photomultiplier tube through optical fibers [Solfaroli Camillocci *et al.* 2014] (see Fig. 1.8). Since no rejection method is needed, the external dimensions of the prototype are compact. A further advantage of this technic consist in the reduced irradiation of the patient and of the medical staff.

Beta imaging probes - Compared to counting devices, intraoperative β imaging should greatly facilitate the fast mapping of the radioactive distribution of the tumor-seeking tracers in the surgical cavity, and improve the tumor signal-to-noise ratio by providing a spatial discrimination between true signal and background noise. This should enable to further increase the impact of β detection for radioguided tumor surgery. The first attempt to realize a β imaging probe prototype is nearly 20 years old and many other prototypes have been developed in recent years (Table 1.5). However, no β imaging probe has yet been evaluated in theater block. As shown in the Table, the sensitive surface of β imaging probes is generally less than 5 cm², because extreme compactness is a key feature for shallow detection inside narrow surgical cavity (see Figure 1.9). As for β counting devices, direct or indirect detection technologies can be implemented to develop β imaging probes.

The cameras based on direct β detection use silicon detectors based on heterojunctions (p-n junction where layers are made of different semiconductor materials). Evolution of silicon detection technologies has led to the manufactory of pixelized detectors of various pixels and array geometries. The main challenge connected to the use of this detector is the readout of a large number of pixels. Some groups have proposed the intraoperative use of detectors initially designed for autoradiography and based on arrays of pixels smaller than 100 μm [Visvikis & MacDonald 1998, Russo *et al.* 2008]. These geometries allow to achieve excellent spatial resolution, on the order of 200 μm , at the cost of a complex readout electronics needed to manage the great number of pixels. However, such very high spatial resolution is usually not suited to the real accuracy of the operative procedures. The detector developed by Russo *et al.* uses a single-particle counting unit based on a silicon pixel bump-bonded to the Medipix2 readout circuit. The 300 μm thick silicon detector consists of 256 \times 256 square pixels of 55 μm pitch, connected one by one to an electronic channel. Medipix2 allows to store a maximum of number of counts per pixel that a dedicated serial electronic interface read out to reconstruct the image. However, the size of the electronic card greatly increases the external dimensions of the detector (35 \times 55 mm²), making it not suited to insertion inside narrow surgical cavities. Visvikis *et al.* propose a probe based on a CCD. This technology is characterized by a dark counting rate that strongly increases with the temperature, imposing the use of a high detection threshold which degrades the β detection efficiency (from 75 cps/kBq to 27 cps/kBq between 20 °C and 37 °C). This temperature sensitivity is a major drawback for intraoperative application and can be only corrected using a Peltier module put in direct contact to the detector, which loses its compactness. Others research groups use silicon arrays with pixels of approximately 1 \times 1 mm² which requires a much simpler readout electronics [Tornai *et al.* 2002, Huh *et al.* 2005]. Other silicon technologies are available for β direct detection and could potentially be used for the development of intraoperative cameras. Among the interesting devices, we can quote CMOS sensors (Complementary Metal-Oxyde Semiconductor) that integrate a part of the electronic signal

Probe	γ noise rejection	Detector	Sensible area (cm ²)	Sensitivity (cps/kBq)	Spatial resolution (mm)
Gamelin <i>et al.</i>	-	Fiber scintillator +PSPMT	0.27	3 (at 1.5 mm)	-
Levin <i>et al.</i>	-	CaF ₂ :Eu BGO+PMT	1.2	230 (contact)	0.5
Liu <i>et al.</i>	Coincidence	Plastic scintillator GSO+MAPMT	2.5	78 to 194 (contact)	2
Stolin <i>et al.</i>	-	Plastic scintillator +SiPM	1.7	108 (contact)	2.5
Heckathorne <i>et al.</i>	-	Plastic scintillator +SiPM	1.5	360 (contact)	2.1
Russo <i>et al.</i>	-	Silicon +Medipix2	1.98	377	0.23 (at contact)
Sabet <i>et al.</i>	Subtraction	CsI:Tl LYSO:Ce+SiPM	1.3	-	0.8
Thacker <i>et al.</i>	-	M.C.CsI:Tl +EMCCD	2.7 or 6	-	0.05
Tipnis <i>et al.</i>	-	M.C.CsI:Tl +CCD	25	216 (contact)	-
Bogalhas <i>et al.</i>	Subtraction	Fiber scintillator+ PMMA+MCPMT	2.3 or 5	217	1.6 (contact)
Visvikis <i>et al.</i>	-	CCD	0.98 or 4.4	75	0.132 or 0.176 (contact)
Yamamoto <i>et al.</i>	Coincidence	CaF ₂ :Eu +PSPMT	3.1 or 12.5	0.5 et 0.8	-
Hudin <i>et al.</i>	Subtraction	Plastic scintillator GSO:Ce+SiPM	1.6	340 (contact)	0.5

Table 1.5 – Characteristics and performances of some intraoperative positron imaging probes.

processing directly inside the silicon close to the junction or position sensitive avalanche photodiodes (PSAPD). The first has already been implemented for brachytherapy dosimetry [Caccia *et al.* 2004] and the second one has been coupled to microfluid chips (designed for cell incubation or other biological applications) for *ex vivo* imaging of cellular radiotracers uptake [Dooraghi *et al.* 2013]. Whatever the silicon technology, the temperature sensitivity and the complexity of the electronic readout makes still difficult the use of β direct detection with silicon detectors for intraoperative applications.

Most of the detectors developed for β imaging are based on the coupling between a scintillator and a position sensitive photomultiplier devices (MAPMT or PSPMT) through optical fibers. The use of a light guide allows to export the detection system removing all voltage and current sources from the surgical cavity and reducing the overall probe dimensions. For example, the probe developed at IMNC, which is built around clear and plastic scintillating fibers held in an close packed annular arrangement around the excision tool in order to detect and remove the radiolabeled tumors at once (Fig. 1.9) [Bogalhas *et al.* 2009]. Gamelin *et al.* also propose an hybrid endoscopic device, which integrates an optical coherence tomography imaging probe, allowing identification of pre-neoplastic changes thanks to

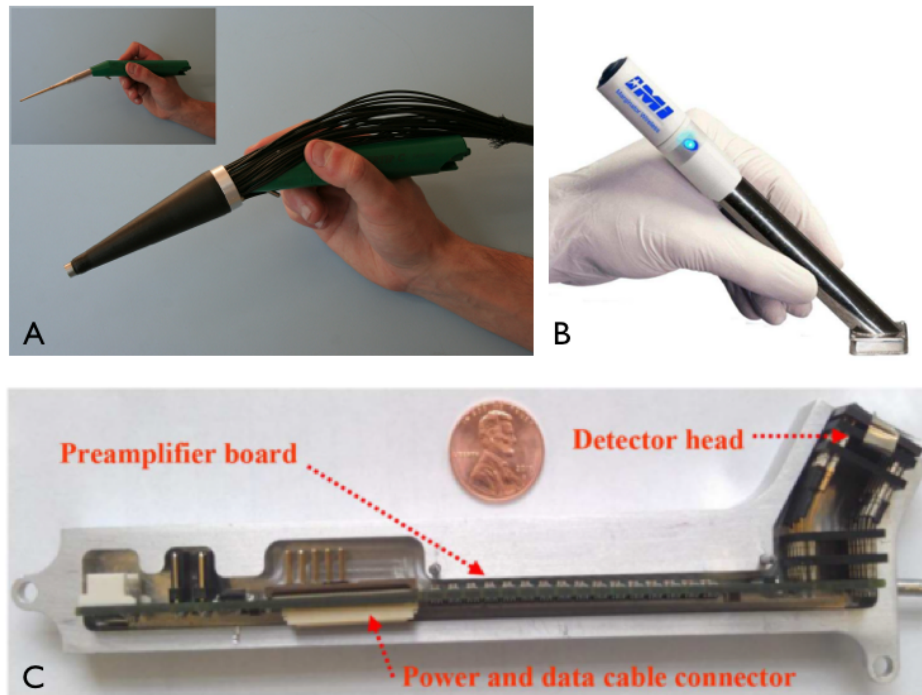


Figure 1.9 – Intraoperative β imaging probes: annular imaging probe enclosing an excision tool [Bogalhas *et al.* 2009] (A), Marginator (IntraMedical Imaging) (B) and prototype of a SiPM-based probe [Sabet *et al.* 2015](C).

its high resolution, with several scintillating fibers for mapping positron activity in tumor foci [Gamelin *et al.* 2009]. However, as for the counting probes, the use of long optical fibers drastically reduces the collected scintillation light and thus the β sensitivity. The direct coupling between scintillators and small photosensors, such as MAPMT, allows to partially overcome this issue, but the size of the probe is still increased [Liu *et al.* 2003]. The use of scintillation materials, such as $\text{CaF}_2:\text{Eu}$ [Yamamoto *et al.* 1997, Hoffman *et al.* 1999] or CsI:Tl [Tornai *et al.* 2001], with a light yield compared to plastic scintillator also contributes to sensitivity improvement. These scintillators have the added benefit of growing into a microcolumnar structure and therefore present a high degree of light channeling, which potentially improves spatial resolution by reducing the light spreading on the photosensor [Tornai *et al.* 2001, Singh *et al.* 2013, Sabet *et al.* 2015].

A further improvement of the detector sensitivity can be achieved using semiconductor photosensors which feature a detection efficiency much higher than that of photomultipliers (>40%). For example, EMCCD provide higher sensitivity to low light fluxes compared to CCD due to their internal gain. However, these devices can only measure the integral of the electron signal created by the activity distribution with no distinction between single β events. Because no reconstruction of the interaction point of the detected event inside the scintillator can be implemented based on their charge distribution, a highly focused scintillation light is needed at the output of the crystal in order to achieve a high spatial resolution. In that context, Thacker *et al.* proposed to couple an EMCCD to a microcolumnar CsI:Tl

scintillator through a flexible fiber optic bundle [Thacker *et al.* 2008, Singh *et al.* 2009]. In this device, the external bulky EMCCD can be equipped with a cooling system, which permits to avoid the drawback of temperature sensitivity encountered, for example, with the probe developed by Visvikis *et al.* [Visvikis & MacDonald 1998]. The emergent technology of silicon photomultipliers also introduces new interesting features for scintillator-based intraoperative β imaging probes, such as compactness, low weight, simplicity of implementation, versatility and robustness, while ensuring high detection efficiency, typically superior to the one of vacuum technology phototube and comparable gain (from 10^5 to 10^6). Moreover, silicon photomultipliers are suitable for use at room temperature and can be directly coupled to the scintillator. Among the alternative photosensors that have been developed and implemented during the last ten years, Silicon Photomultipliers (SiPM) have the potential to fulfill most of the needs to achieve efficient intraoperative β detection (high signal-to-noise ratio, compactness, low weight, simplicity of implementation and versatility) and to notably impact the performances of future intraoperative devices. This approach has been initially proposed by Heckathorne *et al.* [Heckathorne *et al.* 2008] and Stolin *et al.* with a prototype designed to be directly put on the surgeon fingertip [Stolin *et al.* 2010].

Hudin *et al.* [Hudin *et al.* 2012a] also developed two β imaging probes with different background subtraction methods. More recently, Sabet *et al.* proposed a similar approach with a β imaging probe built around a pixelated CsI:Tl scintillator optically glued to a continuous LYSO:Ce directly coupled to a 4×4 SiPM array (Fig. 1.9) [Sabet *et al.* 2015].

Most of β imaging probes integrate the rejection of the γ background noise by using coincidence detection [Hoffman *et al.* 1999] or subtraction [Bogalhas *et al.* 2009] [Gamelin *et al.* 2009]. Their advantages and drawbacks will be discussed in more details in Section 2.4.2.

1.2.3 Clinical applications

The intraoperative detection techniques described above have found multiple clinical applications for guiding operative procedures during tumor resection or sentinel lymph node biopsy.

1.2.3.1 Cerenkov light imaging

Cerenkov light imaging was first used in clinical routine for radiation therapy monitoring in order to visualize in real time the dose delivery during external beam [Jarvis *et al.* 2014] or internal radiation therapy [Spinelli *et al.* 2013] (Fig. 1.10). The work of Spinelli *et al.* has shown that Cerenkov imaging can be used for monitoring the biodistribution of β emitters such as ^{90}Y and ^{177}Lu in superficial organs, even if they demonstrated its feasibility only in the context of therapeutic doses. At the same time, Thorek *et al.* ran a first clinical trial of Cerenkov light imaging for patients undergoing a routine ^{18}F -FDG PET/CT scan [Thorek *et al.* 2013a]. In order to visualize deep-seated tumors, the study required the use of an ultra-sensitive photodetection device and strict restrictions on the ambient light. They were able to establish a correlation between the uptake value measured from PET and the counting rate per area on the Cerenkov light imaging. More specifically, they were able to

detect a Cerenkov light signal in lymph nodes with local activity as low as 0.05 MBq/ml localized 1.6 ± 0.5 cm under the skin. This preliminary study demonstrated that Cerenkov light imaging can be performed with diagnostic doses of ^{18}F -FDG when using a sensitive optical equipment. On the other hand Hu *et al.* presented a human pilot trial that validated the feasibility of Cerenkov light imaging endoscopy (Fig. 1.10) [Hu *et al.* 2015]. Cancerous lesions of the gastrointestinal tract are usually superficial and easily reachable by endoscopy, bypassing the disadvantage of Cerenkov radiation limited penetration. Moreover, the gastrointestinal tract is a totally dark environment which avoid the interference of the Cerenkov luminescence with ambient light. Finally, Gootendors *et al.* are currently performing a first woman clinical trial for breast-conserving surgery with intraoperative use of ^{18}F -FDG Cerenkov luminescence imaging of tumor excision margins and sentinel lymph node (SLN) metastases [Grootendorst & Purushotham 2015]. Wide local excision specimens and sentinel lymph nodes were imaged immediately after excision with an investigational Cerenkov light imager specimen analyzer (Lightpoint Medical Ltd, UK). SLNs were successfully identified and increased Cerenkov light radiance was observed on primary tumors and metastatic sentinel lymph nodes compared to negative SLNs. These preliminary studies on Cerenkov light imaging show promising results even though the β sensitivity of this techniques in hundreds of times lower than that obtained with a scintillator-photosensor based device (see Section 1.2.2.2). More clinical data needs also to be collected to validate the efficiency of this technique for intraoperative imaging.

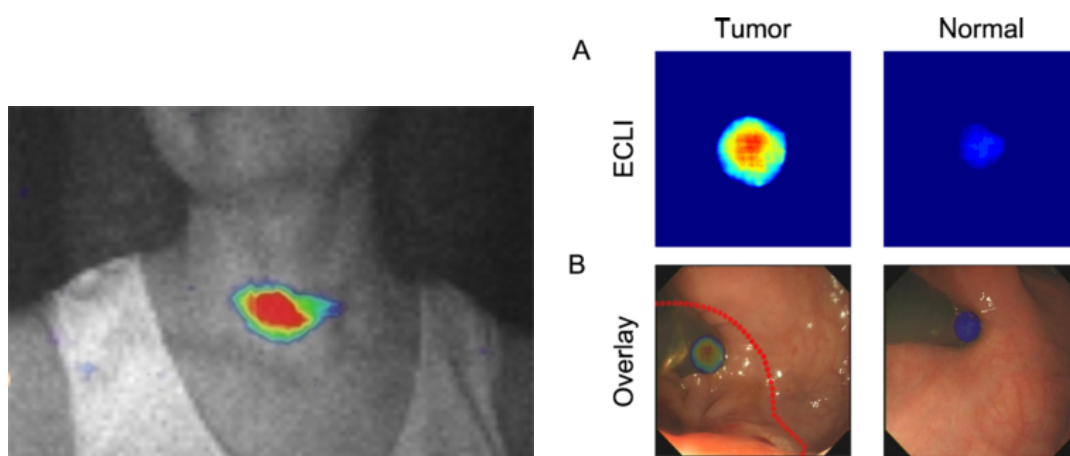


Figure 1.10 – Images of two human applications of Cerenkov light imaging. (Left) Overlapping of the Cerenkov image of the thyroid (in color) on the photographic image of a patient injected with a therapeutic dose of ^{131}I [Spinelli *et al.* 2013]. (Right) Patient injected with ^{18}F -FDG PET diagnostic dose. **A** Cerenkov luminescence image of cancerous and normal tissues. **B** Endoscopic Cerenkov light images matching with white-light photographs [Hu *et al.* 2015].

1.2.3.2 Gamma counting and imaging probes

Radioguided surgery protocols, using γ counting probes or miniaturized γ cameras, are successfully integrated in the clinical routine for SLN biopsy and their utility for tumor resection has been demonstrated for different pathologies. Furthermore, it presents a great

potential of improvement thanks to the regular development of new specific radiotracers. Radioguidance allows to perform less invasive surgery and provides the surgeon vital information for the localization of occult or difficult access tumors.

Sentinel lymph node biopsy - Sentinel lymph node concept was first introduced in clinic by Cabanas in 1977. In his study, he investigated the dissemination of cancerous cells through lymphatic system by lymphography on a group of patients affected by penile cancer [Cabañas 1977]. He showed that dissemination followed an orderly progression, spreading first to regional lymph node, then to the next echelon of lymph nodes and so on, since the flow of lymph is directional. Cabanas remarked the existence of a lymph node that is first invaded by tumor cells, denominating it sentinel lymph node. According to his study, histopathological analysis of the sentinel lymph node should allow to predict tumor dissemination and therefore accurately plan the strategy of excision for the lymphatic echelon. Successive studies presented similar conclusions for other pathologies for which the lymphatic route is a principal way to metastasize from their original focus (breast, melanoma, head and neck, prostate, colorectal, uterus) [Veronesi *et al.* 1999, Shoaib *et al.* 2001, Meads *et al.* 2014]. The sentinel lymph node biopsy consists in collecting only one, or more often 2 to 3, lymph nodes minimizing the surgical act and thus, the post-operative morbidity. The histologic analysis of a small number of nodes also provides accurate cancer staging [Veronesi *et al.* 2006, Holl *et al.* 2009, Sadeghi 2015]. This is a fundamental information for directing the multidisciplinary approach to therapy. The axillary dissection is performed only if the biopsy shows the involvement of the removed lymph nodes. In order to perform the biopsy, surgeons have to identify with certainty the sentinel lymph node during surgery. In 1993, Krag *et al.* and Alex *et al.* were the first to propose the use of radioactive labeling and a gamma counting probe for intraoperative detection of breast cancer and malignant melanoma sentinel lymph nodes [Krag *et al.* 1993, Alex *et al.* 1993]. The protocol, used nowadays as routine clinical practice, consists of the injection around the primary tumor site of a radiotracer (radiocolloid marked with ^{99m}Tc) followed by the localization and extirpation of the sentinel lymph node using an intraoperative handheld gamma probe. Aside gamma probe detection, the second main technique implemented in clinical practice is the visual blue dye method. This method consists in the injection of blue dye around the primary tumor site and attend for it to diffuse into the lymphatic system. The surgeon follows the blue-stained lymphatic vessels until they enter into a blue-stained lymph node. The combination of the two techniques is used as well. A meta-analysis study showed that identification rates of sentinel lymph node in breast carcinoma and melanoma patients are high for both biopsy techniques: 85/84% for the blue dye alone and 94/99% for the radiocolloid alone [Niebling *et al.* 2016]. The combination of the two techniques allows a high identification rate (95/98%) and a lower false negative rate than each of the technique alone. However, several studies have reported a steady increase in SLN identification rate with use of radiocolloid alone thanks to the training of surgeons on the radioguided protocol. Further drawbacks of the blue dye method are the eventual increase of tissue damages compared to radioguided surgery due to the visual tracing down of the blue stained lymphatic vessels through the sentinel lymph node and the risk of allergic reaction.

Sentinel lymph node biopsy is the main protocol in radioguided surgery. To date, this

procedure is used worldwide in clinical routine and has become the reference for staging melanoma, breast cancer [Veronesi *et al.* 1999] and prostate cancer [Holl *et al.* 2009]. The use of gamma counting probes also shows promising results for vulvar and cervical cancers, with a sentinel lymph node identification rate reported of 93-100% and 80-100%, respectively [Povoski *et al.* 2009]. The results are less promising for the esophagus cancer and parotid glands [Povoski *et al.* 2009]. The high rate of false negative observed in these pathologies is due to the complex and extensive lymphatic network causing the diffusion of metastasis directly from the primary tumor to the second lymph node stage (skip metastasis). The utility of radioguide SLN biopsy of thyroid cancer is still unclear. However, the few available studies performed with ^{99m}Tc -radiocolloids report a successful localization ranging from 78% to 100% [Povoski *et al.* 2009]. Finally, this method can be difficult to implement for those pathologies having deeply located lymphatic chains or when the first lymph nodes are located too close to the injection site, such as for thyroid cancer [Rettenbacher *et al.* 2000], head and neck [Kovács *et al.* 2005] or gynecological malignancies [Levenback *et al.* 2009].

When used as a complementary tool to counting probes, the interest of intraoperative γ -cameras has been evaluated for SLN biopsy of various pathologies, such as breast cancer [Zavagno *et al.* 2008], melanoma [Sim *et al.* 1986] [Albertini *et al.* 1996] and others cutaneous malignancies [Stoffels *et al.* 2012], oral cavity squamous cell cancer [Sieira-Gil *et al.* 2015], prostate [Vermeeren *et al.* 2011], head and neck [Kovács *et al.* 2005] or urological [Vermeeren *et al.* 2009] cancers. Many of these studies first evaluated the performances of miniaturized γ -camera to replace the pre-operational lymphoscintigraphy [Goto *et al.* 2005, Vidal-Sicart *et al.* 2011, Kerrou *et al.* 2011]. In fact, the real benefit of this technique for the patients is sometimes contested since it implies an additional time and cost of the protocol, requiring a nuclear medicine department and the availability of a wide field of view γ -camera. The study performed with the miniaturized γ -camera POCI, including 162 patients with a breast cancer, reported detection of more SLNs with the handle imaging probe than with preoperative lymphoscintigraphy in 36 % of patients, equal number for 34% of them and fewer SLNs in 25% of patients [Kerrou *et al.* 2011]. Moreover, the acquisition time achieved with POCI (< 10 min in 84% of the patients) was shorter than that of lymphoscintigraphy (mean 15.7 ± 3.4 min). The preliminary results obtained with a new miniaturized γ -camera TReCam on 15 breast cancer patients undergoing SNOLL procedure showed a perfect concordance between the tumor localization obtained with the γ probe and the pre-operative lymphoscintigraphy. TReCam allowed the visualization of 53.3% of the sentinel lymph node detected with the lymphoscintigraphy and it was considered of easy use for all patients [Bricou *et al.* 2015]. These studies and those conducted with other devices demonstrate that miniaturized gamma-camera can reliably replace standard large field of view γ -camera while reducing the logistical problems linked to the lymphoscintigraphy [Kerrou *et al.* 2011]. The final goal is to extend the use of the sentinel lymph node protocol to clinical centers without nuclear medicine department. Miniaturized gamma camera could also be used easily in different locations such as nuclear medicine departments, operating rooms, as well as the patient's room.

During sentinel lymph node biopsy, various studies have also demonstrated that intraoperative imagers, used in addition to counting probes, facilitated the identification of deep-seated lymph nodes, placed in the vicinity of the injection site or at anatomical area difficult

to access (inframammary or inner mammary lymphatic chain). Those lymph nodes, that cannot be identified a γ counting probe due to its reduced spatial selectivity, could lead to an increased risk of false-negative and therefore tumor recurrence [Mathelin *et al.* 2006b]. Vidal-Sicart *et al.*, conducted a study on patients with lymph nodes of difficult localization for various pathologies (melanoma, breast cancer and gynecologic cancer). They reported an increased excision rate of lymph nodes from 75% to 95% thanks to the combined use of a γ counting probe and a portable γ camera [Vidal-Sicart *et al.* 2010]. The improvement in sentinel lymph node identification increases the probability of extracting the metastatic ones. The use of γ cameras have been reported as well for inspection of the surgical bed in order to control that no more radioactive lymph nodes are present [Motomura *et al.* 2005].

Localization and delimitation of tumor margins - The intraoperative tumor localization with a γ counting probe was first proposed by the neurosurgeon William Sweet in 1951 [Sweet 1951]. Five years later, Harris *et al.* published the first description of radioguided surgery for thyroid cancer where the γ radiation emitting by ^{131}I were detected with a CsI:Tl scintillation probe [Harris *et al.* 1956]. The seventies saw a fast development of radiotracers for SPECT imaging opening the way to new applications in radioguided surgery. In the early 1980s, intraoperative γ detection was introduced for the biopsy and/or resection of bones lesions [Ghelman *et al.* 1981] and rectal cancer with the immunoradiotracer ^{131}I -labeled anti-CEA [Aitken *et al.* 1984]. In the same decades, Ubhi *et al.* used intraoperative detection of ^{201}Tl -Cl during surgical treatment of hyperparathyroidism [Ubhi *et al.* 1984].

More generally, intraoperative imaging technologies for radioguided surgery of tumors is of great interest for small occult lesions that are difficult to visualize or are non-palpable during revision surgeries when anatomy is altered. Aside from the sentinel lymph node biopsy for breast cancer and melanoma, the most widely used application of γ detection probe is minimally-invasive radioguided surgery for primary hyperparathyroidism, a dysfunction of the parathyroid glands induced in nearly 96% of cases by a parathyroid adenoma, and thyroid cancer. The ^{131}I radionuclide can be used at the same time for ablative therapy and radioguided surgery [Rubello *et al.* 2007], while for patients with iodine-negative recurrent tumors the use of ^{99m}Tc -MIBI [Rubello *et al.* 2006], ^{99m}Tc (V)-DMSA [Adams *et al.* 2001] or also ^{18}F -FDG [Kraeber-Bodéré *et al.* 2005] had been proposed. For thyroid cancer, this approach allows systematic evaluation of the completeness of the surgical resection for recurrent or persistent diseases, especially in difficult anatomic area [Negele *et al.* 2006]. One of the most well described radioguided protocol in literature is also the radioguided occult lesion localization (ROLL) for non-palpable breast lesions. This technique required the intratumoral injection of a ^{99m}Tc -based agent, under stereotactic control or ultrasonography, allowing, tumor localization during excision. Monti *et al.* performed a study on 953 patients with histologically or cytologically proven breast cancer and reported successful lesion localization in 99.6% of cases [Monti *et al.* 2007]. Alternatively, Duarte *et al.* showed the feasibility of tumor delineation through radioguided intraoperative margin evaluation after intravenously injection of the radiopharmaceutical ^{99m}Tc -sestamibi into the patient. This technique allowed the removal of the primary tumor with histological free margins on 82.6% of patients (mean margin of about 5 mm) [Duarte *et al.* 2007]. This better tumor localization also allows to reduce the revision surgeries compared to the wire-guided standard technique [Lovrics *et al.* 2011].

Numerous studies are also reported for colorectal cancer. Most of them are based on the use of ^{125}I -labeled anti-TAG-72 monoclonal antibodies [Hladik *et al.* 2001, Tiernan *et al.* 2012]. It has been shown the ability to efficiently localize colorectal cancer-specific antigens with high detection rate (up to 97%) and also to identify occult lymph node metastases. Even if fewer reports are available, the interest of this radioguidance for resection margins assessment is currently under evaluation for brain tumors, such as high grade glioma, labeled with ^{99m}Tc -MIBI or ^{201}Tl [Bhanot *et al.* 2007, Serrano *et al.* 2005], or meningioma labeled with ^{111}In -DTPA-pentetreotide [Dammers *et al.* 2009]. Furthermore, other clinical studies are focused on the intraoperative localization of extra-cranial neuroblastoma on pediatric patients [Martelli *et al.* 1998], pheochromocytoma [Ricard *et al.* 1993] labeled with iodine-MIBG tracers, and neuroendocrine tumors targeted with ^{111}In -DTPA-D-Phe¹-octreotide [Adams & Baum 2000]. Radioguided surgery with γ counting probes has been only evaluated in a few studies for the osteoid osteoma [Etchebehere *et al.* 2004].

PET radiotracers have recently gained interest for radioguided surgery. For example, ^{18}F -FDG can be potentially used for localization and resection of all glucose-avid tumors. A few examples of feasibility studies have been realized by Essner *et al.* [Essner *et al.* 2001], Piert *et al.* [Piert *et al.* 2007, Piert *et al.* 2008] and Gulec *et al.* [Gulec *et al.* 2006, Gulec 2007] for different cancerous pathologies (thorax, digestive system, breast, ovary, head and neck, thyroid, melanoma and lymphomas). The intraoperative localization was performed with a high energy γ counting probe dedicated to the detection of 511 keV γ rays. Most of the studies describing ^{18}F -FDG intraoperative localization highlights the interesting possibility of associating it with a pre-operative PET/CT to identify the malignancies and a postoperative PET/CT scan to evaluate the quality of the surgery with the same radiotracer. The intraoperative counting probes are then used to confirm the localization and the excision of the lesions already identified. Moreover, their enhanced handling and spatial resolution compared to PET imaging optimize the identification of tumors or lymphomas that are small, occult or of difficult access. This multimodal approach has proven its efficacy for glucose-avid lesions, such as melanoma [Franc *et al.* 2005, Povoski *et al.* 2008], colorectal cancer with abdominal and pelvic recurrence [Sarikaya *et al.* 2007], recurrent ovarian cancer [Barranger *et al.* 2005, Cohn *et al.* 2008], breast cancer [Hall *et al.* 2007] and non-small cell lung cancer [Moffatt-Bruce *et al.* 2008]. Povoski, Cohn, Moffat-Bruce and Hall also propose in their study a further evaluation of the tumor margins on resected specimens using dedicated PET scanner.

The interest of miniaturized γ -cameras for intraoperative localization of lesions has been preliminary evaluated for non-palpable early breast cancers and parathyroid adenomas. Paredes *et al.* performed a protocol on 42 women consisting in preoperative lymphoscintigraphy, surgical excision of the lesion guided with a γ probe and afterwards images of the surgical bed and tumoral specimens with a portable γ -camera (Sentinella 102, Oncovision) in order to control the surgical resection margins and the absence of tumor residues. Congruence of 60% was found between the intraoperative images and the results of histopathological analysis. Furthermore, all images were successfully acquired within 5 minutes [Paredes *et al.* 2008]. More recently, Casella *et al.* evaluated on 20 patients the localization efficiency of a miniaturized γ -camera (IP Gurdian 2) for minimally invasive approach in

surgical treatment of primary hyperthyroidism. Patients were intravenously injected with Tc-sestaMIBI during the operation. Results showed that intraoperative use of the miniaturized γ -cameras allow to correctly localize pathological parathyroid glands (diagnostic accuracy of 98.2%) with higher reliability than the currently used pre-operative scintigraphy and intraoperative ultrasound [Casella *et al.* 2015]. Finally, few studies have been realized for bones tumors localization [Ménard *et al.* 1997, D’Errico *et al.* 2001]. In a recent one, conducted by Infante *et al.*, the surgery was performed after injection of ^{99m}Tc -hydroxy diphosphonate and the tumor nidus was localized in all of the twelve patients using the combination of a γ probe and a miniaturized γ -camera [Infante *et al.* 2015].

1.2.3.3 Beta counting and imaging probes

We show that the detection of β particles presents some interesting features, complementary to γ detection. Its high spatial selectivity and sensitivity make β detection particularly suitable to detect the presence of residual tumor sites in the resection bed of the gross tumor mass while minimizing the loss of normal tissue.

The potential interest of intraoperative β detection was mainly evaluated with preclinical investigations and a few clinical studies. The use of β counting probes has been proposed in association to the one of γ counting probes, mainly for the detection of malignancies labeled with ^{18}F -FDG. Animals usually underwent microPET scan before radioguided inspection and during post-mortem dissection. Strong *et al.* implanted athymic mice with one of four possible tumor cell lines (gastric, pancreas, squamous cell and breast cancer). This was the first study to demonstrate a strong correlation ($R = 0.8$) between high-energy γ detected by conventional PET imaging and β counts from the probe. Moreover, the study showed that β counts, compared to the detection of γ rays’ emissions, may improve real-time tumor localization [Strong *et al.* 2009]. Gonzales *et al.* evaluated the performances of high-energy γ and β probes (IntraMedical Imaging LLC) on nude rats inoculated with mesothelioma and lymphogenic mesothelioma tumor cells and injected with ^{18}F -FDG. The probes were able to locate during surgery all the suspicious lesions and lymph nodes identified on PET scan. Furthermore, lesions smaller than 1 cm, not identifiable on PET scan, have been detected intraoperatively and their malignancy was confirmed with pathological examination. It was also shown that the better sensitivity and spatial selectivity of the β probe provided better performances over the γ probe in detecting malignancies smaller than 1 cm diameter: the average tumor signal-to-noise ratio was 4.8 and 6.6 for the γ and the β probe, respectively [Gonzalez *et al.* 2011a, Gonzalez *et al.* 2011b]. More recently, Camillocci *et al.* propose the use of their intraoperative β^- counting probe with ^{90}Y -labeled peptides that shows a minimal uptake compatible with the detection of neuroendocrine tumors, meningioma and high grade gliomas [Collamati *et al.* 2015a]. The probe prototype was evaluated on *ex vivo* meningioma specimens from a patient injected with ^{90}Y -DOTATOC [Solfaroli Camillocci *et al.* 2016]. The preliminary results showed the ability of the probe to discriminate a tumor foci as small as 0.2 ml from the background activity within 1 s of acquisition time. In addition to the absence of γ background noise, a further advantage of this technique consists in the reduced irradiation of the patient and of the medical staff. Thanks to the low activity concentration needed for effective detection and to the short range of β^-

emitted by ^{90}Y , it was estimated that the dose absorbed from the surgeon hands and body would be respectively nearly 24 and 46 times smaller than the dose absorbed in a standard ^{99m}T -labeled tracer surgery [Solfaroli Camillocci *et al.* 2014].

Some clinical studies have been also conducted to evaluate the efficiency of β detection for intraoperative margin assessment. The potential benefit of positron counting probes has been demonstrated for melanoma in the neck [Essner *et al.* 2002] and recurrent melanoma [Franc *et al.* 2005], especially with challenging or altered anatomy. This last study was realized on 5 patients, injected with ^{18}F -FDG, using a high-energy γ rays and positron probe (PET-Probe; IntraMedical Imaging LLC). For eight of the 19 specimens identified by the probe, it was found an increased FDG uptake when compared with the surrounding tissues before resection. Only one of the 11 specimens that were not identified with the probe contained a melanoma. The probe yielded a sensitivity of 89% (8 of 9) and a specificity of 100%. Moreover, in 3 of the 5 patients, the probe allowed the detection of lesions non-visualized and non-palpable that were later confirmed as pathologic. A more complete study, performed by Piert *et al.*, evaluated the performances of a positron counting probe after ^{18}F -FDG injection on 17 patients with various histologically proven malignancies (gastric adenocarcinoma, thyroid cancer, breast cancer, malignant melanoma, colorectal cancer) [Piert *et al.* 2007]. In 16 out of 17 cases, the tumor tissues, identified with a pre-operative PET, were clearly detected with a tumor-to-background ratio of 6.6 ± 4.8 (mean \pm SD) well above the minimum of 1.5 needed to confidently discriminate tumor from normal surrounding tissues. The probe also allowed the localization of three additional tumor lesions that were not immediately apparent at surgery.

Several studies underlined the potential interest of the imaging to improve the performances of intraoperative beta detection such as higher signal to noise ratio, improvement of spatial selectivity without any loss of sensitivity and rapid detection of the surgical bed. However to date, only a few preclinical or clinical studies are available. The EMCCD-based device developed by Thacker *et al.* and SiPM-based imager of Sabet *et al.* have been evaluated on rabbits with tongue tumor [Singh *et al.* 2009, Sabet *et al.* 2015]. The EMCCD probe allowed to detect tumors with dimensions between 99 and 168 mm^2 and discriminate a minimal activity of 100 nCi/cm^3 [Singh *et al.* 2009]. The SiPM probe showed a sensitivity down to nano-curie activity concentrations. However, authors also reported the influence of probe orientation on background noise contamination.

The hybrid dual-modality device developed by Gamelin *et al.* have been also clinically evaluated for detection and characterization of ovary tissues labeled with ^{18}F -FDG [Gamelin *et al.* 2009]. Ten patients were recruited and a total of 18 normal, abnormal and malignant ovary specimens were evaluated *ex vivo* using this device. The study showed a positron count rate ratio of 7.5 or higher between malignant and normal ovaries and in accordance with the optical coherent tomography images [Yang *et al.* 2011]. More recently, Camillocci *et al.* propose the use of their intraoperative β^- detection probe with ^{90}Y -labeled peptides, which shows a minimal uptake compatible with the detection of neuroendocrine tumors, meningioma and high grade gliomas [Collamati *et al.* 2015a]. The β^- counting probe prototype was evaluated on *ex vivo* meningioma specimens from a patient injected with ^{90}Y -DOTATOC [Solfaroli Camillocci *et al.* 2016]. The preliminary results showed the abil-

ity of the probe to discriminate from the background activity a tumor foci as small as 0.2 ml within 1 s of acquisition time. In addition to the absence of γ background noise, a further advantage of this technique consists in the reduced irradiation of the patient and of the medical staff. Thanks to the low activity concentration needed for effective detection and to the short range of β^- emitted by ^{90}Y , it was estimated that the dose absorbed from the surgeon hands and body would be respectively nearly 24 and 46 times smaller than the dose absorbed in a standard ^{99m}T -labeled tracer surgery [Solfaroli Camillocci *et al.* 2014].

1.3 New β intraoperative imaging devices based on SiPMs

To date, intraoperative radioguided surgery for oncological applications is a well established technique, thanks to the use of γ counting and imaging probes used in many protocols dedicated to cancer treatment or staging. The development of new diagnostic or therapeutic β -emitting radiotracers has reinforced the interest for β intraoperative detection as a complementary technique able to extend the scope of radioguided surgery. It should allow an enhanced accuracy of the operative procedure especially, when trying to define the surgical resection margins. This thesis takes place in that context and provides continuity to the previous works made in the laboratory by Hudin *et al.* [Hudin 2013]. Its aim is to develop a fully operational small field of view β imaging probe based on the silicon photomultiplier technology and to evaluate its performances for the localization of small tumor residuals.

Beta imaging probes for intraoperative tumor resection

This thesis is part of the SiPMED project (Silicon PhotoMultiplier for bioMEDical Imaging), that was designed to develop a new generation of intraoperative imaging devices based-on the silicon photomultipliers technology. In that context, the objective of this study was the development of an intraoperative β probe to guide the surgical excision of solid tumors.

In this second chapter, we will first discuss the challenges and constraints of the positron detection that lead to the instrumental approach chosen for the development of the intraoperative probes. Then, we will present the physics of β particles for typical energies of clinical radiotracers as well as the physics of high energy γ rays generated by the annihilation of positron in tissue, which represents a background noise for our application. Then will follow a description of the characteristics of the detector major components. Because the radiation detection is based on the conversion of deposited energy into light, we will briefly present the scintillation mechanisms and materials and the photodetection systems available to readout this scintillation light. The nature and origin of the background noise will be discussed, together with the different detection approaches that have been developed for its rejection. Finally, the characteristics of the electronics and the image reconstruction methods used will be described.

2.1 Challenges and constraints of intraoperative positron detection

As previously mentioned in Chapter 1, positron detection, thanks to its intrinsic high spatial selectivity and sensitivity in the surgical cavity, has the potential to improve the accuracy and safety of the surgery for solid tumors. However, this detection modality imposes some instrumental constraints. Positron probe has to be compact, lightweight and easy to handle in order to perform detection in contact with the tissues. The probe sensitivity has to be high enough to permit the localization of tumor foci with low radiotracer uptake (on the order of several kBq/ml) within an acquisition time compatible with the surgical practice (a few dozen of seconds). The spatial resolution has to be adapted to the precision of the surgical gesture (of the order of the mm). However, achieve high spatial resolution allows to improve the tumor signal-to-noise ratio. Furthermore, to improve the tumor-to-background ratio and detection specificity, the probe must reduce the influence of the signal coming from the surrounding healthy tissues. For positron detection, the contamination signal arises from the annihilation γ and can be particularly large when the analyzed tissues are located

in proximity to non-specific radiotracer uptake areas, such as bladder, brain, kidneys, heart etc. Finally, the position of the target tumor should be easily correlated to its real position in the surgical cavity. This correlation may be more complicated for imaging or counting probes of large diameter.

The use of β imaging probes has several advantages compared to that of counting probes, actually used in the operating room [Piert *et al.* 2007]. First of all, the signal-to-noise ratio is improved since the signal can be better discriminated from the background noise based on their spatial distribution visualized on the same image. Secondly, the field of view of an imaging probe, that imposes no tradeoff between spatial selectivity and sensitivity, allows to analyze a larger tissue area at once, speeding up the exploration of the surgical cavity. In order to satisfy as much as possible the instrumental constraints listed above, we have developed two intraoperative imaging probes with a small field of view ($25.7 \times 25.7 \text{ mm}^2$) and based on different approaches to reduce the background noise contamination. For the first configuration, the background noise is reduced thanks to accurate choice of the material and the dimensions of the detection volume. For the second configuration, a system for the estimation and consequent subtraction of the γ background noise was implemented, at the cost of a more complex signal analysis and slightly increased dimensions.

Most of the β probes currently available or under development relies on a detection system based on scintillation materials [Daghighian *et al.* 1994, Tipnis *et al.* 2004] [Yamamoto *et al.* 2005]. The scintillation light can be transported with optical fibers, in order to place the photodetector outside the surgical cavity allowing to improve the compactness of the probe head [Tornai *et al.* 1996]. However, this configuration reduces the handling and degrades the light collection efficiency, and as consequence, the β detection sensitivity. The silicon photomultipliers (SiPM) characteristics and performances give the possibility to overcome the constraints imposed by the use of standard PMT, allowing the manufacture of counting and imaging probes that are more compact and with excellent detection sensitivity. A few prototypes of imaging probes based on this technology have been proposed [Heckathorne *et al.* 2008, Stolin *et al.* 2010, Hudin *et al.* 2012a, Sabet *et al.* 2015], but to our knowledge none have been already clinically tested.

2.2 Radiation interactions

The operating mode of any radiation detector basically depends on the interaction mechanism of the radiation to be detected with the material of the detector itself. Radiations can be classified in directly and indirectly ionizing. Charged particles (such as fast electrons and positrons) and uncharged particles (such as X-ray and γ -rays) are examples of the first and the second class, respectively. Beta particles can lose energy in a medium through collision, bremsstrahlung (braking radiation) and emission of Cerenkov radiation. However, at energy of a few MeV or less, typically encountered in clinical applications, the energy loss by radiation emission represents a relatively small fraction. This is the case, for example, of ^{18}F , one of the most commonly used positron radioisotope in clinical practice, which presents a continuous energy spectra with an end point at 633 keV. Therefore, the major interaction

mechanisms regarding β^+ are the elastic and inelastic collisions and at the end of their range, the annihilation, which produces two gamma rays at 511 keV. Main interactions regarding a γ ray with this energy are the photoelectric absorption and the Compton scattering. Pair production cannot take place below the energy threshold of 1.022 MeV (corresponding to the energy of the $\beta^--\beta^+$). The next sections will briefly present the nature and characteristics of the principal interaction modes for beta particles and gamma rays in the energy range characteristic of clinical radiotracers, as reported in literature [Knoll 2010]. In this case, the interactions result in the full or partial transfer of energy of the incident radiation to the electrons or nuclei of the atoms.

2.2.1 β interaction mechanisms

In general, charged particles passing through matter undergo energy loss and deflection from their incident direction. These effects are primarily caused by inelastic collision with atomic electrons of the material and elastic scattering from nuclei. Therefore, β particles moving through an absorption material follow a tortuous path (see Fig. 2.1). The large deviations in β trajectories are due to their mass identical to that of orbital electrons, with which they are interacting. A large fraction of their energy can be lost in a single interaction. The coulomb forces, which represent the main mechanism of energy loss for charged particles, are present for both positive and negative charged particles. Whether the interaction consists of a repulsive or attractive force between the incident particle and the orbital electron, the impulse and energy transfer for particles of equals mass are almost the same. Therefore, the tracks of positron and electrons in an absorber are similar and their energy loss and range are close for equal initial energy. However, positron significantly differs for annihilation radiation generated at the end of the positron track.

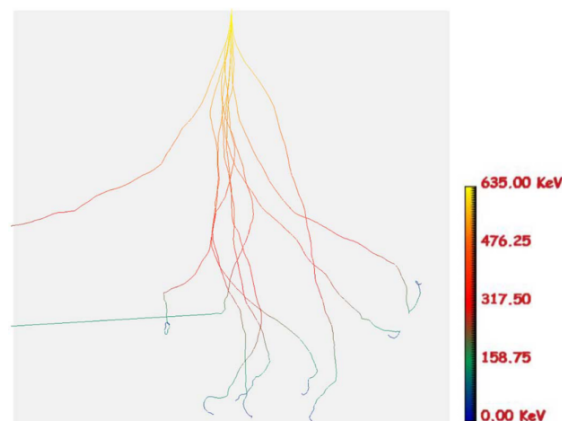


Figure 2.1 – Simulated range for β of 635 keV (end point energy of ^{18}F) in water [Sabet et al. 2015].

2.2.1.1 Collision loss

For the estimation of the energy collision loss of electrons and positrons, it has to be taken into account their small masses, their deflection, and for the electrons, their indistinguishab-

ility from the orbital electrons. The specific energy loss of fast electrons and positrons due to ionization and excitation, the so-called 'collisional losses', had been derived by Bethe in the following formula:

$$-\left(\frac{dE}{dx}\right)_c = 2\pi N_a r_e^2 m_e c^2 \rho \frac{Z}{A} \frac{1}{\beta^2} \left[\ln \frac{\tau^2(\tau+2)}{2(I/m_e c^2)^2} + F(\tau) - \delta - 2\frac{C}{Z} \right], \quad (2.1)$$

where for e^-

$$F(\tau) = 1 - \beta^2 + \frac{\tau^2}{8} - \frac{(2r+1)\ln 2}{(\tau+1)^2}, \quad (2.2)$$

and for e^+

$$F(\tau) = 2\ln 2 - \frac{\beta^2}{12} \left[23 + \frac{14}{\tau+2} + \frac{10}{(\tau+2)^2} + \frac{4}{(\tau+2)^3} \right]. \quad (2.3)$$

In the expression, r_e is the classical electron radius and m_e its rest mass, N_a is the Avogadro's number, A and Z are the atomic weight and atomic number of the absorber atoms, $\beta = v/c$, δ is the density correction factor and the shell correction factor C . The parameter I represents the average excitation and ionization potential of the absorber and τ the kinetic energy in $m_e c^2$ units.

In addition to the inelastic collisions with the electrons of the atoms, β particles passing through an absorber also undergo repeated elastic Coulomb scattering with nuclei. The stopping power of electrons in water as a function of energy is represented in Figure 2.2, clearly showing that the predominant process, for β below 1 MeV, is the collision loss.

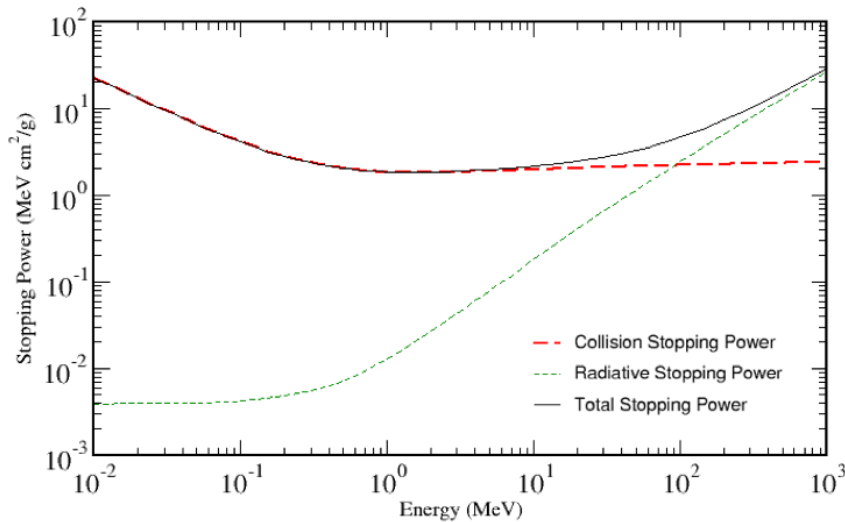


Figure 2.2 – Collision and radiative stopping power for β particles in water (NIST).

2.2.1.2 Range and absorption of β particle

The range of β particles in matter is generally really different from the calculated path length obtained from the integration of the formula 2.1, due to their susceptibility of being multiple scattered by nuclei. A difference between 20 and 400% can be found, depending on the material and the energy of β particles.

Because of their continuous energy spectra, the absorption of β -decay particles follows a nearly exponential behavior, which can be easily fit by:

$$I = I_0 e^{-\mu x} \quad (2.4)$$

where I and I_0 are the intensity of the flux with and without the absorber, respectively and x is the absorber thickness. The μ constant is known as the β^- absorption coefficient and is directly proportional to the end point energy of the β^- decay spectrum. Fig 2.3 shows the typical range of β particles as function of their energy in different materials. The maximum range of β particles emitted by ^{18}F (635 keV) is 2.3 mm, illustrating the shallow field of view of β detection. The use of positron emitters with higher energy allows to increase the thickness of the sensitive volume (maximum range of 3.8 mm for ^{11}C with an end point energy of 960 keV). This graph also shows that β particles can be efficiently absorbed in very thin detection materials, such as plastic scintillator. But on the other hand, this imposes the optimization of the nature and thickness of the materials around the detection volume (including optical coating of the scintillator, light shielding, mechanical housing, etc. . .).

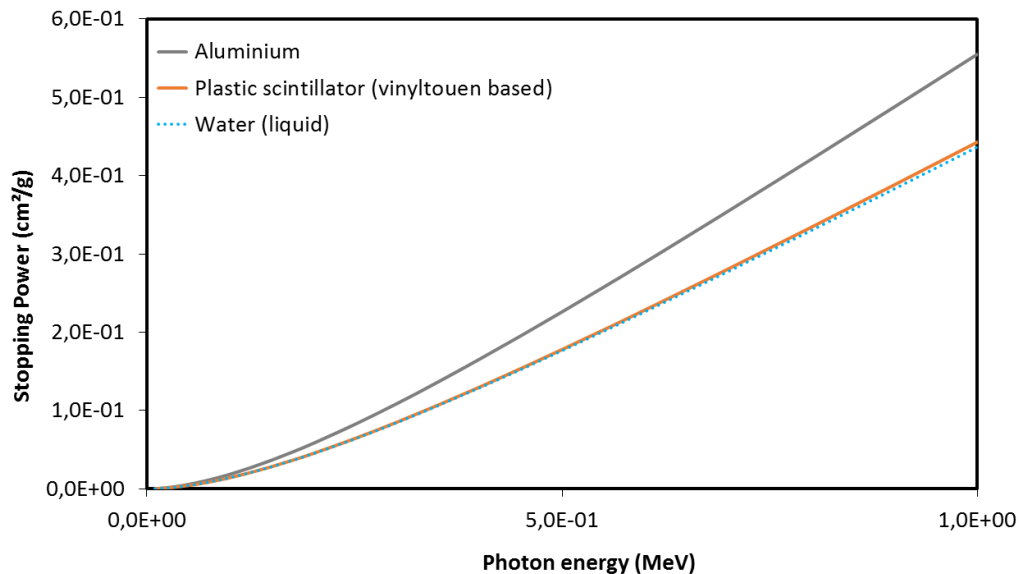


Figure 2.3 – Range of electrons as a function of the energy in a plastic scintillator ($\rho = 1.03 \text{ g/cm}^3$), water ($\rho = 1.00 \text{ g/cm}^3$) and aluminum ($\rho = 2.70 \text{ g/cm}^3$) (data from NIST database).

2.2.1.3 Backscattering of low energy β

The fact that β particles can undergo large-angle deflection along their tracks leads to the backscattering phenomenon. A beta entering the surface of an absorber can be sufficiently deflected so that it will re-emerge from the surface through which it is entered. Backscattering is most important for β with low energy and absorbers of high atomic number. This phenomenon also depends on the incidence angles. β particles entering at oblique angles to the absorber surface have a greater probability to be backscattered out than those entering perpendicularly to the surface. Depending on the geometry of the detector and the β energy, this phenomena may scatter out the particle before being able to produce a usable signal. For this reason, the materials surrounding the β detection volume must be carefully chosen in order to minimize the impact of backscattering on the β sensitivity.

2.2.1.4 Annihilation

When positron energy is very low, close to their mass energy and at the end of their range, they interact with electrons of the absorption material in the process of annihilation. The positrons annihilate with the absorber electrons producing two photons with an energy equal to the electron mass: 511 keV. In order to conserve the momentum, these two photons are always emitted in opposite directions. Since the annihilation γ rays produced are very penetrating compared to the β range, it can lead to the deposition of the energy far from the original positron track.

2.2.2 Interactions of gamma rays

The two major types of interaction that plays an important role in the production and detection of the γ ray background noise generated by the annihilation of positrons in tissue are the photoelectric effect and Compton scattering. All these processes cause the partial or complete transfer of the γ ray energy to the electrons of the absorber.

2.2.2.1 Photoelectric effect

The photoelectric effect is a mechanism by which photons can be absorbed by matter. If a photon has a slightly higher energy than the binding energy of the orbital electrons of the attenuator, the photoelectric effect can take place. The photon disappears, giving the electron sufficient energy to be emitted and ejected from the atom with a kinetic energy E_k given by:

$$E_k = h\nu - E_b \quad (2.5)$$

where $h\nu$ is the energy of the incident photon and E_b is the binding energy of the electron. The resulting atom is then a ionized atom with a vacancy in one of its bound shells. This vacancy is quickly filled through capture of a free electron from the medium or rearrangement of electrons from other shells of the atom. As consequence, one or more characteristic X-ray photons may be generated. In most cases, these X-rays have low energy and are reabsorbed close to original site. The photoelectric process is the predominant interaction mode for

gamma ray of relatively low energy.

The cross section decreases with increasing photon energy and is roughly described by:

$$\sigma_{ph} \propto Z^n (h\nu)^{-3.5} \quad (2.6)$$

with n ranging from 4 to 5 depending on the photon energy. Therefore, photoelectric absorption process is enhanced for absorber materials of high atomic number Z .

2.2.2.2 Compton effect

The Compton effect (incoherent scattering) represents a photon interaction with a loosely bound electron. The incident photon energy $h\nu$ is much larger than the binding energy of the orbital electron. The photon transmits part of its energy to the recoil electron and is scattered as photon with energy $h\nu'$ through a scattering angle θ . The angle ϕ represents the angle between the incident photon direction and the direction of the recoil electron.

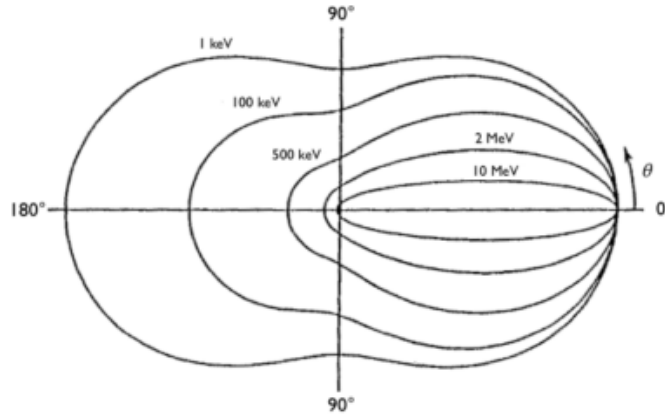


Figure 2.4 – Polar plot of the number of photons (incident from the left) which are Compton scattered into a unit solid angle at the scattering angle θ . The curve are represented for the reported initial energies [Knoll 2010].

To satisfy the conservation of momentum and energy, the scattered photon is emitted with energy (considering the electron as free):

$$h\nu' = \frac{h\nu_0}{1 + \frac{h\nu_0}{mc^2}(1 - \cos\theta)} \quad (2.7)$$

where $h\nu_0$ is the energy of the incident photon, m is the electron mass. The cross section of the Compton effect, σ_c depends linearly on the atomic number Z of the attenuator. The highest energy that can be deposited by Compton interaction, corresponding to the photon back-scattering ($\theta=0$), is called the Compton edge and for incident γ rays of 511 keV is

equal to 345 keV. The angular distribution of the scattered gamma rays is predicted by the *Klein – Nishina* equation for the different scattering cross section $d\sigma/d\Omega$:

$$d\sigma/d\Omega = r_0^2 \left[\frac{1}{1 + \alpha(1 - \cos\theta)} \right]^3 \left[\frac{1 + \cos^2\theta}{2} \right] \left[1 + \frac{\alpha^2(1 - \cos\theta)^2}{(1 + \cos^2\theta)(1 + \alpha(1 - \cos\theta))} \right] \quad (2.8)$$

where $\alpha = h\nu/m_0c^2$ and r_0 is the classical electron radius. Therefore, the angular distribution is not isotropic: for higher energy values the gamma rays have a strong tendency to forward scattering, as shown in Figure 2.4.

Figure 2.5 shows the cross sections of the photoelectron and Compton effects as a function of gamma ray energy for water and lead. It illustrates the relative importance of these two processes. At 511 keV, the interaction in water is dominated by the Compton effect. The γ noise impinging on the detector will therefore be composed of a large amount of low-energy scattered γ .

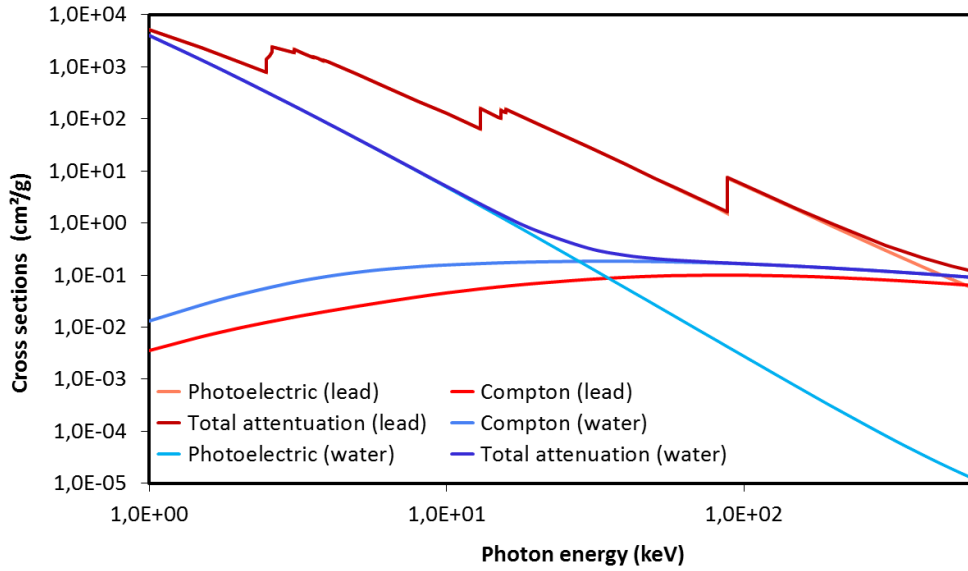


Figure 2.5 – Energy dependence of the Compton scattering and photoelectric absorption processes in water and lead (data extracted by XCOM database).

2.2.2.3 Gamma rays attenuation

The total probability of a γ radiation to interact in the absorber is the sum of the individual cross sections of the interaction mechanism. In the clinical context, the total cross section per unit path length μ is equal to the sum of the photoelectric absorption and Compton scattering interaction probability. This is more commonly known as *total absorption coefficient* and is simply the inverse of the mean free path of a photon. Therefore, it follows that the fraction of photons passing through a distance t is:

$$\frac{I}{I_0} = e^{-\mu t} \quad (2.9)$$

where I_0 is the number of incident photons. The average mean free path of γ rays of 511 keV in water is about 24 cm. Therefore, the background noise generated by positron annihilation may come from distal non-specific uptake areas of the radiotracer, which may lead to a strong contamination. Furthermore, the detection sensitive volume cannot be shielded from distal radiation without loss in detector compactness.

2.3 Indirect radiation detection: scintillators and photodetectors

The two main types of detectors available for the detection of particles and radiation quanta are scintillators coupled to a photodetection system and semiconductors. The next section will be focused on the principle of the indirect radiation detection, with a description of the two main scintillation light production mechanisms and the major classes of photodetection systems.

2.3.1 Scintillators and scintillation phenomenon

Scintillators materials present the property known as *luminescence*. A luminescent material converts the energy of an incident particle into a number of low energy photons, in the visible or near visible range. These photons are therefore easy to detect with photodetection systems. If the light is reemitted in a time inferior to 10^{-8} s the process is commonly called *fluorescence*. When the light is reemitted with a delay larger than a few microseconds the process is called *phosphorescence* or *afterglow*.

Scintillation is characterized by several parameters, such as the light yield, the decay constant and the radioluminescence spectrum. The light yield or quantum yield of scintillation is the amount of light quanta emitted by the scintillator per unit of energy deposited by ionizing radiation in the medium. This parameter is generally expressed in photon per keV or MeV.

The time evolution of the scintillation process may be described by a simple exponential decay of decay constant τ_d . The number of emitted photons at the time t , $N(t)$, can be described by the formula:

$$N(t) = \frac{N_0}{\tau_d} e^{-\frac{t}{\tau_d}} \quad (2.10)$$

where N_0 is the total number of photons emitted. For most scintillation materials, the finite rise time from zero to the maximum is usually much shorter than the decay time therefore is taken as zero in this expression for simplicity. In most cases, the reemission process exhibits a more complex decay, that is better described by the combination of two or more exponential decays. The radioluminescence spectrum is the wavelength distribution of the scintillation light when the medium is excited by ionizing radiations. It's generally composed of several emission bands, each characterized by their maximum λ_{max} and bandwidth $\Delta\lambda$ for a given

temperature.

In most of particle detection applications, an ideal scintillation material should present the following major characteristics: the ability to convert the radiation kinetic energy into detectable light with high efficiency, a light output proportional to the deposited energy, a short decay time to generate fast signal pulses and finally, transparency to its own fluorescence light. No material meets simultaneously all these criteria. Therefore, the choice of a scintillator is always a compromise among these and others factors. It exists a wide choice of scintillation materials, which can be divided into two main categories: the organic and inorganic scintillators. Inorganic scintillators, among all scintillators, have the highest light output and good linearity of response, which results in better energy resolution, but their response time is relatively slow. Organic scintillators are much faster, but emit less scintillation light. The target application influences the choice of the scintillation material. The inorganic scintillators, which have higher density and are composed of higher Z -value materials than organic scintillators are more suitable for γ ray detection and spectroscopy measurements. Conversely, the organic scintillators are generally preferred for timing measurements, and β and fast neutron detection. Due to their low density, organic scintillators have lower intrinsic sensitivity to γ radiations, which is the main noise component during positron detection. This subject will be further discussed in Section 2.4.

The basic mechanisms of light production and the scintillation characteristics will be synthetically discussed for the two types of scintillators, according to literature [Knoll 2010, Lecoq *et al.* 2006].

2.3.1.1 Organic scintillators

In organic scintillators the fluorescence arises from the transitions of the free valence electrons of a single molecule in the energy level structure. A wide group of organic scintillator is based on molecules with some symmetry properties, which presents the so called π -electrons structure. Energy can be absorbed by excitation of electrons into one of the excitation states. The ground state S_0 is singlet above which there is series of excited singlet states (S_1, S_2, \dots). A similar set of triplet electronic levels T_1, T_2, \dots are present as well (Fig. 2.6). The molecules of interest for scintillators have an energy spacing between S_0 and S_1 around 3 and 4 eV, while the spacing between the higher-lying states is usually smaller. Each of those electronic configurations is further subdivided into finer spaced levels corresponding to various vibrational states of the molecule. The typical energy separation between these states is about 0.15 eV. Since the thermal energy is inferior to the spacing between vibrational states, nearly all molecules at room temperature are in S_{00} state (lowest vibrational state of the ground state). The up forward arrows in Figure 2.6 represent the absorption of energy by the molecule. The higher singlet electronic state that are excited are quickly de-excited in the state S_1 through internal conversion, which emits no radiation. Furthermore, the excess of vibrational energy is quickly lost, generating in a negligibly short time a population of excited molecules in the state S_{10} . The majority of scintillation light is produced by the transition from the S_{01} state to the vibrational state of the ground electronic state. In organic scintillators, the fluorescence decay time is of the order of a few nanoseconds. This

is considered as the fast component of the emitted scintillation light. Sometimes, excited singlet state may as well be converted into triplet state by the so called 'intersystem crossing'. Because the life time of the T_1 state may be as much as 10^{-3} seconds, the de-excitation of the level T_1 to S_0 generates a delayed light emission named *phosphorescence*.

It can be assumed that only prompt fluorescence is observed and that the time profile of the light pulse should have a fast leading edge followed by a simple exponential decay. The scintillation light of organic scintillators is generally peaked in the blue region (400-450 nm), matching the common photodetection systems' spectral sensitivity. They are characterized by a light yield of a few thousand photons per MeV of absorbed energy. This value is lower than the one that can be obtained with inorganic scintillators. Organic scintillators may

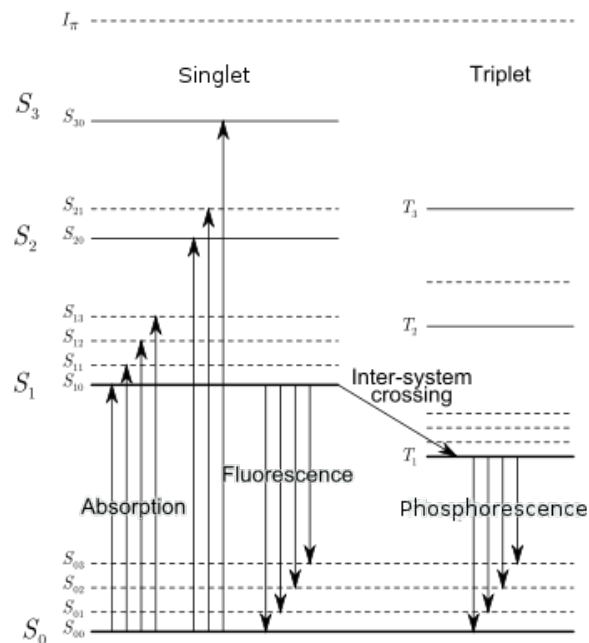


Figure 2.6 – Energy levels of an organic molecule with the π -electron structure.

be found in the form of pure crystals, such as anthracene and stilbene. They are durable but their scintillation efficiency depends on the orientation of the ionizing particle with respect to the crystal axis; this strongly limits their practical applications. Liquid organic scintillators may be produced by dissolving an organic scintillator in an appropriate organic solvent. The polymerization of an organic scintillator in a solvent allows to produce solid plastic scintillators. Thanks to the ease with which they can be fabricated, plastics scintillators are largely available in a wide selection of shapes and in large volumes for a low price. Some examples of organic material with their main characteristics are presented in Table 2.1.

Scintillator	Type	Density (g/cm ³)	Light yield (ph./keV)	λ_{max} (nm)	Decay constant (ns)
Anthracene	Crystal	1.25	40	448	30
Stilbene	Crystal	1.16	20	410	4.5
P-terphenyl	poli-crystal	1.23	35	400	3
NE-102	Plastic	1.02	25	423	2.4
NE-216	Liquid	0.89	31.2	425	3.5

Table 2.1 – *Properties of some commercially available organic scintillators [Knoll 2010, Angelone et al. 2014].*

2.3.1.2 Inorganic scintillators

The scintillation mechanisms in inorganic scintillator materials depend on the energy states determined by the crystal lattice of the material. In insulators or semiconductor materials, electrons can access only discrete energy bands, as show in Figure 2.7. The lower band, called the valence band, represents the electrons bounded to the lattice sites, while the conduction band represents the electron with energy sufficient to freely migrate throughout the crystal. It exists an intermediate band, named the forbidden band, that the electrons of a pure crystal cannot access. Energy absorption can result in the elevation of an electron from the valence to the conduction band, leaving a hole in the valence band. However, in pure crystals, the return of an electron to the valence band is an inefficient process for the photodetection because the typical gap width produces high energy photons that do not lie in the visible spectra. To enhance the probability of visible light emission, impurities, called 'activators', are usually added to inorganic crystals.

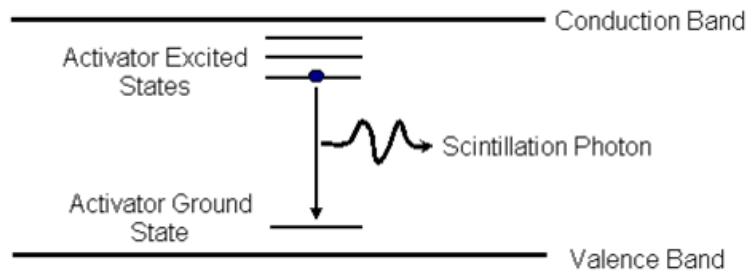


Figure 2.7 – *Energy band structure of an activated crystal scintillator.*

When a charged particle passed through the detection medium it forms a large number of electron-hole pairs by elevating electrons from the valence to the conduction band. The positive holes quickly drift to the impurity site, ionizing it. Meanwhile, the electrons are free to migrate throughout the crystal until they encounter the ionized activator site and drop into it. This creates neutral impurity configurations which have their own set of excited states within the forbidden band, as shown in Fig. 2.7. If the activator is properly chosen,

Scintillator	Density ($\text{g}\cdot\text{cm}^{-3}$)	Light yield (ph/keV)	Refractive index	λ_{max} (nm)	Decay constant (ns)	Hygroscopic
GSO	6.7	12.5	1.85	440	60, 400	no
NaI:Tl	3.7	43	1.85	415	230	yes
LaBr ₃ :Ce	5.1	63	1.9	380	16	yes
LaCl ₃ :Ce	3.9	49	-	330	20	yes
LYSO:Ce	7.1	32	1.8	420	41	no
GaGG:Ce	6.6	46	1.9	520	90	no
BGO	7.1	8.2	2.15	480	300	no

Table 2.2 – *Properties of some commercially available inorganic scintillators communally used for medical γ imaging [Lecoq et al. 2006, Knoll 2010].*

the excited configuration will very quickly de-excite to the ground state with the emission of photon in the visible range. The typical half-lives of such excited states are of the order of 10^{-7} seconds. The decay time of these states determines the time characteristics of the emitted scintillation light. One of the major consequence of luminescence through activator sites is that the crystal can be transparent to the scintillation light. However, inorganic crystals may present the undesired phenomena of afterglow. This consists in the delayed emission of phosphorescence light due to thermal excitation. The emission spectra is generally between the blue and ultra-violet region. The inorganic scintillators have the advantageous of high light yield and high density, which are all essential features for gamma detection. However, crystals growth may be complicated, limiting the possible shapes and maximum volume that can be manufactured, and increases the cost of inorganic scintillators. Furthermore, their light emission is influenced by temperature and they may be fragile, easily damaged by mechanical or thermal shock and hygroscopic, which requires to encapsulate the crystal into an air-tight housing.

Table 2.2 reports the major characteristics of some of the most commonly utilized scintillators for gamma rays medical imaging.

2.3.1.3 Light collection and scintillator mounting

Optical coating - In scintillator-based detector the goal is to collect the largest fraction of the light that is isotropically emitted from the energy deposited by the particle along its track. The efficiency of the light collection depends on the optical absorption within the scintillator and the losses at the scintillator surfaces. With the exception of large scintillators or particular materials, self-absorption is usually not significant. Since the scintillation light is isotropically emitted, only a small fraction of it will travel directly in the direction of the photosensor. To collect it, the remaining light must be reflected one or more times at the scintillator surface. Depending on the application, the light collection can be optimized by retrieving the light that escapes from the scintillator using a reflecting material at one or all scintillator surfaces, expect the one coupled with the photodetection system. Reflector can be either *specular* or *diffusive*. Specular reflectors act like perfect mirrors: the reflection angle is equal to the incidence angle. A polished metallic surface can be used as specular

reflector. On the other hand, the angle of reflection of perfect diffuse reflectors follows a Lambert's cosin law. Teflon or nanoparticles of TiO_2 or BaSO_4 can be used as diffuse reflectors. Absorbing coatings can also be used on edges of scintillators in order to improve image reconstruction in this area.

Optical coupling and shielding - Plastic or crystal scintillators are usually produced with at least one polished surface for the coupling with the photodetection device. The other surfaces can be polished or unpolished, depending on the specific detection needs. Although total internal reflection is preferable at reflecting surface, this effect must be minimized at the interface between the scintillator and the photodetector. Efficient coupling may be achieved for scintillators with refraction index fairly close to the one of the entrance window of the photodetector (typically glass, quartz or resin). In these cases, near-perfect coupling is obtained by filling the interface between the scintillator and the photodetection system with an optical coupling material, such as grease or thixotropic gel, with the same refraction index. The usefulness of scintillator of high refraction index is seriously hampered by the internal light reflection that traps a large fraction of the scintillation light within the scintillator itself.

Furthermore, all detection systems based on a scintillator coupled to a photodetector have to be shielded from ambient light. The entrance window of a β detector is usually covered with an opaque and thin metallic sheet or black plastic to allow the entrance of soft radiations (such as low energy beta particles, while shielding from visible photons).

Light guide - It is sometimes unadvisable or even impossible to directly couple the scintillator with the photosensor. Good light collection efficiency may be obtained by using a transparent solid, called light pipe, to mechanically couple these two components and guide the scintillation light. In the case of imaging systems, a light guide can be used to enlarge the light distribution reaching the photodetection surface. A larger number of photodetection units reached by scintillation light allow a more efficient reconstruction of the position of interaction of the radiation. The use of light guides is desirable as well when scintillation measurements are made in strong magnetic field and the photosystems have to be shielded from it, or to adapt the scintillator surface dimensions to the one of the sensitive photodetection. Light guides operate on the principle of total internal reflection. They are usually optically transparent solids with a relatively high refractive index to minimize the critical angle for the internal total reflection. The surfaces, depending on the applications, are generally highly polished and surrounded by a reflective or absorbing material depending on the applications requiring high light collection efficiency or efficient reconstruction of the interaction position.

2.3.2 Photodetection systems

The photodetector collects the scintillation light and converts it into a measurable electric current, with a charge proportional to the number of incident scintillation photons. A large set of photodetectors is actually available, based on two technologies: the vacuum technology and the semiconductor technology.

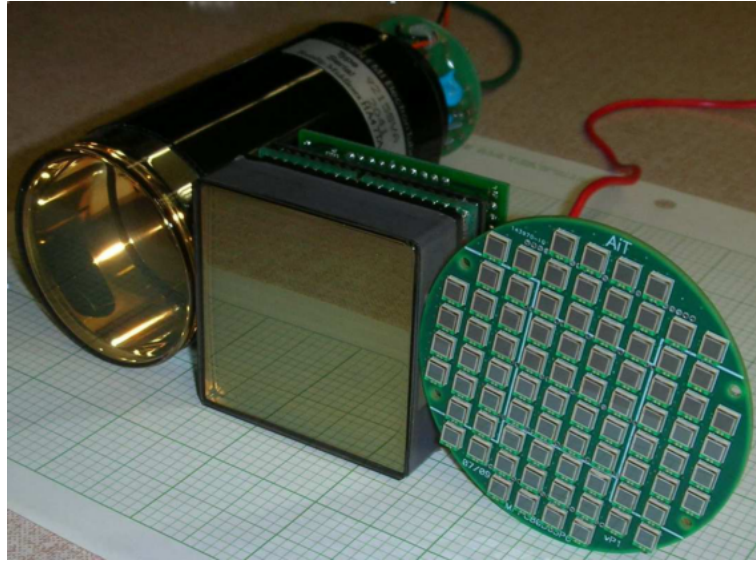


Figure 2.8 – Evolution of photodetectors technologies commonly used in intraoperative imaging. From the left to the right: a photomultiplier tube, a flat panel (MAPMT Hamamatsu) and a SiPMs array (Hamamatsu).

Vacuum-based system - Among the vacuum technology devices, the photomultiplier tubes (PMT) are today the most widely diffused. The PMTs are basically composed of a photocathode, allowing the conversion of the incident photons into electrons, so-called photo-electron, a multiple stages dynodes string, for the electrons multiplication and finally, an anode from which the final signal can be readout. The efficiency of the photoelectric conversion of the photocathode is expressed by the quantum efficiency, the ratio between the number of photoelectron released and the number of incident photons on cathode. The quantum efficiency depends on the wavelength of the incident light. PMT can be extremely sensitive to ultraviolet, visible and near-infrared light, depending on the type of material utilized for the photocathode. The dynodes string allows to amplify, in an avalanche process, the original photoelectrons created at the photocathode. The multiplied electrons are then collected at the anode, generating a measurable electric signal with a gain of the order of 10^6 , proportional to the number of incident photon on the photocathode. The detection efficiency, representing the probability of detecting an incident photons, is expressed as the product between the photocathode quantum efficiency and the collection efficiency of the dynodes.

Based on this operation mode, multiple PMTs structures have been developed in order to answer to the specific requests of different application fields (see Fig. 2.8). For example, there exist PMT providing the position of interaction of the incident photon on the photocathode (PSPMT, Position Sensitive PMT). These phototubes have a particular grid type dynode structure capable to confine the photoelectrons multiplication avalanche around the photon interaction position on the photocathode. The electrons avalanche is then collected on a crossed anode and read out by a network of resistances, that allows to reconstruct the centroid position of the light distribution using charge division from a reduced number of electronic channels [Soluri *et al.* 2006]. Other available technologies provide similar informations, such

as the MCPMT (MicroChannel PMT), which consists in a photomultiplier tube incorporating a microchannel plate instead of the conventional discrete dynodes or the HPMT (Hybrid PMT), which utilizes a photocathode coupled to a semiconductor electron detector. An alternative photomultiplier structure is the multi-anode photomultiplier tubes (MAPMT) which are made of multiple miniaturized photomultipliers placed side by side in a close-packed arrangement. Extremely compact MAPMTs (3 cm thickness and $5 \times 5 \text{ cm}^2$) composed of 8×8 or 16×16 elements are currently available (Flat panel H8500 and H9500, Hamamatsu).

The detection system based on the vacuum technology have been largely utilized during several decades. Their operational modes are mastered and they present fairly good performances. However, they need high supply voltage (of the order of the kV), they are fragile and bulky, and their performances degrades in presence of a magnetic field. Most of these drawbacks can be overcome with photomultipliers based on the semiconductor technology.

Semiconductor technology - Semiconductor detectors can be classified in three main categories: the photodiodes, the Avalanche PhotoDiodes (APD) and the SiPMs. All these technologies are based on the PN junction, employed in different conditions and operation modes.

Photodiodes are based on a PN junction or PIN structure, in which an electron-hole pair is created by an incident photon with sufficient energy. If the photon absorption occurs in the junction's depletion region, or in its proximity, the carriers are swept from the junction by the built-in electric field. A photocurrent, proportional to the number of incident photons, is then produced by the migration of the holes towards the anode and the electrons toward the cathode. They have high quantum efficiency, ranging from 60 to 90% in the visible spectra depending on the wavelength. However, because of their fairly low electronic gain, on the order of the unity, they are of difficult employment for light pulses less than hundreds of photons.

The APD are based on the same operational principle as photodiodes, but with higher voltage. An incident photon generates a finite number of electron-hole pairs, creating a current proportional to the number of incident photons. The typical gain of nearly 100 allows the detection of low light level till a dozen of photons. This is valid only if the bias voltage is below the breakdown voltage. If the voltage is higher than the breakdown voltage, the APD starts to work in Geiger mode and the device is referred to as Geiger-mode APD (GM-APD). In this bias condition, the electric field is so intense that a single carrier injected in the depletion region trigger a self-sustaining avalanche. The main limitation of the diode working in the Geiger-mode is that the output signal is the same regardless of the number of incident photons. Indeed, the output signal is rather a binary response. On the other hand, the gain is much higher: about 10^6 , which is comparable to the traditional PMT. This important gain allows to detect really low light levels, till the single photon.

In order to partially overcome the limitation of the GM-APD response, the diode can be segmented in tiny micro-cells, each working in Geiger-mode. These micro-cells are connected in parallel to a single output. Each micro-cell, when activated by a photon, gives rise to a current response, so that the output signal is proportional to the number micro-cells hit by a photon. This structure is called Silicon PhotoMultipliers (SiPM). These devices are sensitive to low light levels and present performances comparable or even superior to that of vacuum technologies [Dolgoshein *et al.* 2006]. They are able to detect luminous flux intensity as low

		Vacuum technology			Semiconductor technology		
		PMT	HPD	MC-PMT	PN,PIN	APD	SiPM
Detection efficiency	blue	30%	20%	20%	60%	50%	40%
	green-yellow	40%	40%	40%	80-90%	60-70%	25%
	red	<6%	<6%	<6%	90-100%	80%	10%
Time resolution /10pe		100ps	100ps	10ps	a few ns	a few ns	a few ps
Gain		10	3-8 10	10-10	1	200	10
Alimentation voltage		1 kV	20 kV	3 kV	10-100 V	100-500V	<100V
Used in magnetic field		<10 T	axial filed 4T	axial field 2T	insensible	insensible	insensible
Level of detectable signal		1 p.e.	1 p.e.	1 p.e.	100 p.e.	10 p.e.	1 p.e.
Mechanical features		fragile, bulky		compact	compact and robust		

Table 2.3 – Table comparing the typical performances of different photo detection technologies: photomultipliers tubes (PMT), hybrides photodiodes (HPD), micro-channels photomultipliers (MC-PMTS), photodiodes PIN, avalanche photodiodes (APD) and SiPMs [Hamamatsu KK 2006].

as a single photon thanks to a high signal-to-noise ratio (gain between 10^5 to 10^6), overcoming the important lack of internal gain of PN and PIN. SiPMs also have high temporal resolution (50-100 ps) and their detection efficiency is superior to that of most photomultipliers, in a range of wavelength going from the red to the blue ($\sim 40\%$ between 430 and 480 nm and 25% between 480 and 550 nm). Others SiPMs advantages are their high compactness (silicon substrate thickness inferior to 500 μm), robustness and insensitivity to the magnetic field up to 7 T [España *et al.* 2010]. The SiPMs can be easily assemble into arrays of different dimensions and shapes, allowing the development of a wide variety of dedicate detectors. Finally, the production of SiPMs has competitive price compared to other technologies. Table 2.3 summarizes and compares the SiPMs performances to that of others photodetectors.

2.4 Influence of the γ noise background on the positron detection

A generic detection system based on the indirect detection of β^+ is mainly constituted by an organic scintillator coupled through a light guide to a photodetection device. The scintillator is covered by a optical reflecting coating to optimize light collection and protected by a shielding to the ambient light. Finally, all these components have to be placed in a mechanical housing.

In a clinical environment, the β^+ radiotracer diffusing in the patient body emits positrons that at their turn annihilate in 511 keV γ rays generating a background noise. This noise degrades the detector signal-to-noise ratio, compromising the ability of the probe to detect small tumor uptake areas. In order to design a miniaturized detection system for which the background noise is minimized, we studied the origin, the nature and the intensity of this

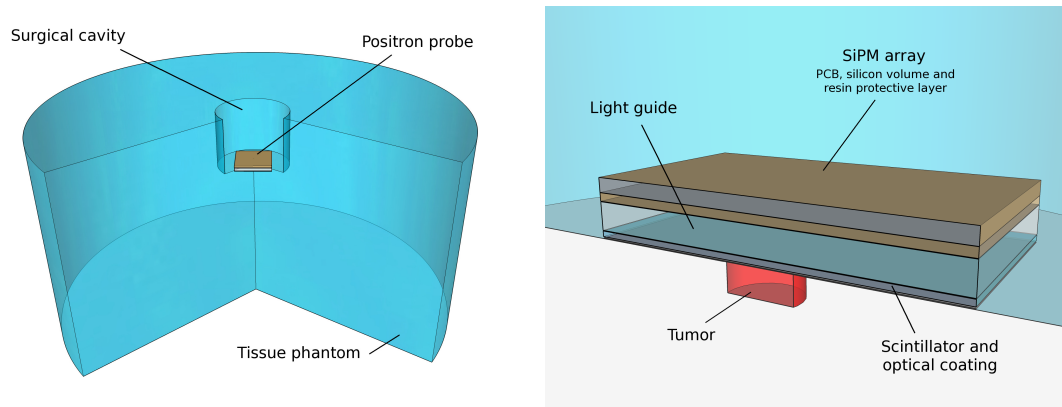


Figure 2.9 – Sectional views of the simulated geometries for the tissue phantom (left) and the positron imaging probe inside the surgical cavity (right). The aluminum mechanical housing of the probe has been removed for clarity.

background noise through Monte Carlo simulation.

2.4.1 Nature and origin

The positron annihilations give rise to a background noise whose primary component is the direct interaction of γ rays in the scintillator (initial 511 keV or Compton scattered photons). The γ rays also generate, by Compton interaction in the environment surrounding the scintillator, a second component of scattered electrons. Due to their low energy ($E_{max}=345$ keV corresponding to the Compton edge for 511 keV γ) and therefore short range, the Compton electrons able to interact inside the scintillator are produced in its vicinity. In order to estimate both noise contributions when the probe is settled in a clinical environment, the geometry of a typical detection head design, embedded in a surgical cavity, was fully modeled using a GATE Monte-Carlo simulation platform. All physics processes in which are involved β particles of energy within the ^{18}F spectra and the 511 keV annihilation γ rays were simulated with a range cut offset to 0.01 mm in all volumes. However, only β particles and γ rays radiation transport in the environment volumes and the detection probe were simulated (no propagation of scintillation light). The simulated detection head consisted of a small organic scintillator volume ($25.7 \times 25.7 \times 0.1$ mm³), a light guide (2 mm thick), coupled to a SiPMs array (including the resin protection layer and the silicon sensitive volume) mounted on a Printed Circuit Board (PCB). The detector entrance window was also covered with a 65 μm plastic reflective coating and a 10 μm thick aluminum sheet for light shielding. The detection system is covered on the sides and rear by a 1 mm thick sheet of aluminum in order to simulate the mechanical housing of the detection head (Fig. 2.9). The clinical environment was defined as a cylindrical tissue phantom of 15 cm radius and 15 cm height. The surgical cavity is simulated by a 5 cm diameter and 4 cm depth hole on the top of the cylinder as shown in Figure 2.9. The detector was placed at the bottom of the cavity.

The simulation results presented in Figure 2.10 shows that the majority of the scattered

electrons are created inside the tissue area placed right in front of the detector entrance window (46.5%), but also inside the light guide (24.7%), the optical coating (23%) and the light shielding (4%). The thickness and density of the materials right in front of the scintillator slightly influence the intensity of this noise component (see Section 3.2.5). On the other hand, the light guide thickness has no impact. The noise component rising from the gamma rays directly interacting in the scintillator is almost entirely produced inside tissues (more than 99.7%).

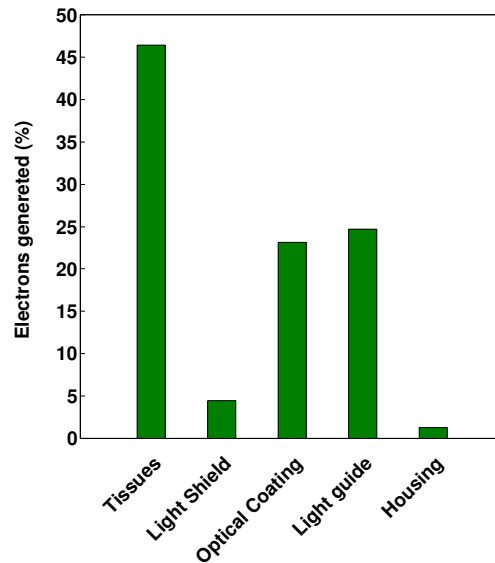


Figure 2.10 – Origin of the scattered electrons produced in the volumes surrounding the head detector (relative percentage normalized by the total electron noise). The light guide thickness is set to 2 mm. The scintillator is covered by a optical coating and an aluminum optical shielding.

2.4.2 Strategies for noise minimization

The number of incident γ rays interacting inside an absorber increases with its thickness. Therefore, the intensity of the gamma background contamination can be decreased by reducing the organic scintillator thickness. The results presented in Figure 2.11 were obtained for a detection system with the same components that the ones previously mentioned, but with a plastic scintillator thickness ranging from 0.05 mm to 0.5 mm. The intensity of the two components of these background noise contamination are plotted in Figure 2.11 as a function of the scintillation thickness. As expected, the gamma contribution is roughly inversely proportional to the scintillator thickness while the electron component is constant. As a result, the background noise is dominated by the scattered electrons for a thickness inferior to 0.1 mm. For a scintillator thickness ranging from 0.1 to 0.4 mm, the electron component increases from 22% to 48% of the total noise. Thus, reducing the thickness of the scintillator below 0.1 mm will have low impact on the background noise. These results suggest as well that the use of semiconductor devices, implementing very thin sensors would bring no sig-

nificant improvement in the development of positron probes with low noise contamination [Cappellini *et al.* 2008]. Conversely, an excessive reduction of the scintillator thickness will cause a degradation of the spatial performances and sensitivity due to the incomplete energy deposition. This effect can be partially offset choosing scintillation materials featuring high light yield.

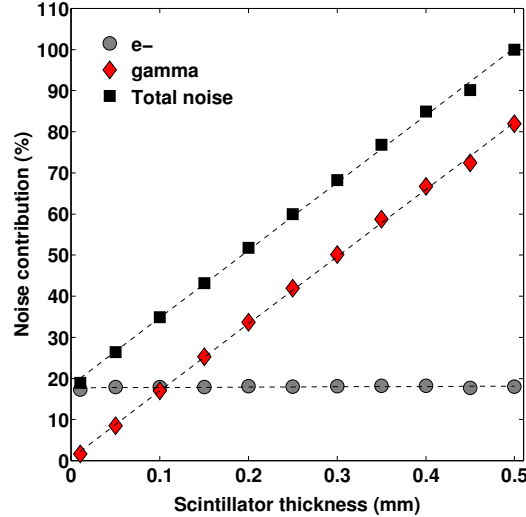


Figure 2.11 – Noise contributions (gamma rays, scattered electrons and total noise) as a function of the plastic scintillator thickness. All percentages are normalized by the total noise obtained for a scintillator thickness of 0.5 mm. The light guide thickness is set to 2 mm.

In Figure 2.12 are reported the energy spectra of particles interacting inside a 0.1 mm and 0.4 mm thick plastic scintillator when the positron probe is embedded in the surgical cavity on contact with a tumor disk. We can observe that the scattered electrons produce a signal that is almost indistinguishable from the one generated by the positrons. There is also no clear separation between positron and 511 keV γ ray. The end point energy of electrons spectra, corresponding to the maximum energy deposited within the thin scintillators, is closed to the 350 keV, Compton edge of the γ ray interaction. However, γ ray and β spectra exhibit sharper differentiation between 0 and 50 keV. Indeed, most γ rays are absorbed by the scintillator after diffusing in the surrounding tissues and so, are low energy events. Conversely, the small amount of β particles in the low energy region is due both to the shape of the emission energy spectrum of ^{18}F and the elastic backscattered diffusion and absorption of low-energy β particles in the optical coatings. Alongside its influence on the intensity of the background noise, we can also observe on Figure 2.12 that the reduction of the scintillator thickness affects the spectral distribution of the detected events which are shifted through lower energies. This effect limits the ability to remove a large amount of γ rays by applying an energy threshold while minimizing the loss of β sensitivity (see Section 3.2.3).

As briefly introduced in Chapter 1 (see Section 1.2.2.4), two main strategies have been

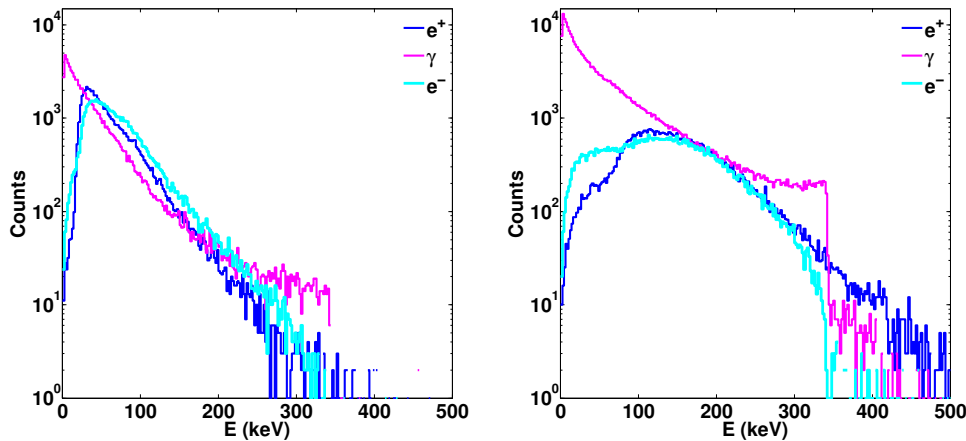


Figure 2.12 – Simulated energy spectra of particles interacting in a 0.1 mm (left) and 0.4 mm thick plastic (right). The probe is placed at the bottom of the surgical cavity at contact with tissues.

proposed to reduce the γ background noise contamination. The first method consists in the coincidence detection of a positron with one of its two annihilation γ rays. A phoswich detector, consisting in the coupling between a low-Z and low density organic scintillator, for positron detection, and a high Z stopping power inorganic scintillator, like BGO or GSO dedicated to high-energy γ detection, is typically used. The phoswich detector is read-out by a photodetector and the events originating from the two scintillators are discriminated by using pulse shape analysis based on the difference between the long decay time (on the order of few hundred ns) of inorganic scintillators compared to the short decay time of organic scintillators (about few dozen ns) [Yamamoto *et al.* 2004, Yamamoto *et al.* 2005, Hoffman *et al.* 1998]. When a β event interacts in the organic scintillator, a fast signal is observed. If a slow component, coming from the interaction of one of the annihilation γ rays in the inorganic scintillator is registered, within an appropriate time and energy window, the event is validated as true positron event. Events generating only fast or slow signals, corresponding to the interaction of γ rays in the organic or inorganic scintillators, will be discarded. However, if an annihilation photon is scattered in the organic scintillator through the inorganic scintillator, both components will be produced and this scattered event can be mistaken for a positron event. In order to minimize this assignment error, a high energy threshold must be used to reduce the amount of γ contamination, but at the expense of the positron sensitivity. Moreover, to obtain a good coincidence efficiency, the inorganic scintillation volume has to be high, reducing the probe compactness [Yamamoto *et al.* 2004, Yamamoto *et al.* 2005]. The second rejection method is based on the estimation of the γ rays contamination, by means of a second detection volume shielded from β particles. The γ signal can then be subtracted, after applying an appropriate weighting factor, in order to obtain the pure β signal [Daghighian *et al.* 1994, Raylman & Hyder 2004]. The two detection volumes can be readout by one or two detectors. When a single photodetection system is used, signals coming from the two scintillators are discriminated by using pulse shape information [Hoffman *et al.* 1998, Yamamoto *et al.* 2005, Sabet *et al.* 2015] or by analyzing charge spatial spread on the photosensor [Hudin 2013]. Hudin *et al.* developed two β imaging probes. The

first one is based on a stack of two SiPM arrays: the front detector is coupled to a continuous plastic scintillator while the rear one is coupled to a monolithic GSO scintillator both through a light guide. The image provided by the rear detector, shielded to β particles by the front one, is used to estimate the intensity of γ rays contamination. The second configuration consists of a continuous plastic scintillator and a pixelized LYSO scintillator separated by a light guide, mounted onto a single SiPM array. The events coming from the top continuous detector and the bottom pixelized one are discriminated from the analysis of the scintillation light distribution on the photosensor.

These subtraction methods allow to maintain the small dimensions of the probe, without sacrificing the β sensitivity, but its efficiency depends on the accurate choice of the weighting factor. However, this method presents the drawback of summing up the statistical counting errors from each detector, thereby decreasing the signal-to-noise ratio.

2.5 The miniaturized β imaging probes

During my thesis, I developed and optimized the performances of two detection configurations of an intraoperative positron imaging probe. This section is dedicated to the designs of these probes. Their different components will be described in details including the working principle of the SiPM array photodetection system, the readout electronics and the image reconstruction methods.

2.5.1 Design of the probe

Both configurations developed have been conceived to obtain extreme compactness and high sensitivity to positron. The first configuration is basically composed of a continuous organic scintillator coupled to a SiPMs array through a light guide (Fig. 2.13, left). It exploits a reduced sensitive volume as major solution to decrease the γ background noise. The light guide is used to optimize the spread of the scintillation light, which partially determines the accuracy of the position reconstruction.

The second configuration has been designed to actively reduce the influence of the background noise by estimating its contamination. The detector is composed of a stack of two scintillators separated by a light guide. The amount of γ contamination is estimated by the rear inorganic scintillator (" β -shielded" scintillator) shielded to β particles by the front organic scintillator (" β -sensitive" scintillator). A γ -free positron image is obtained by subtracting this contamination from the count rate distribution measured with the front detector after applying a suitable weighting factor. The light emitted from both scintillators is readout by the same SiPM array. Events originating from the front and the rear layers are discriminated from the analysis of the light distribution on the photosensor. The continuous nature of the organic scintillator and the light transmission through the light guide allows to create a wide light distribution on the SiPMs surface in contrast to that created from the inorganic scintillator that is in direct contact with the array. To further enhance the difference in light spreading, the β -shielded scintillator is pixelized. This scintillator pixelization allows to confine the light created inside the scintillator pixel itself, so that the light generated is strongly focused on a single SiPM. Thanks to those differences, the analysis of light distribution on

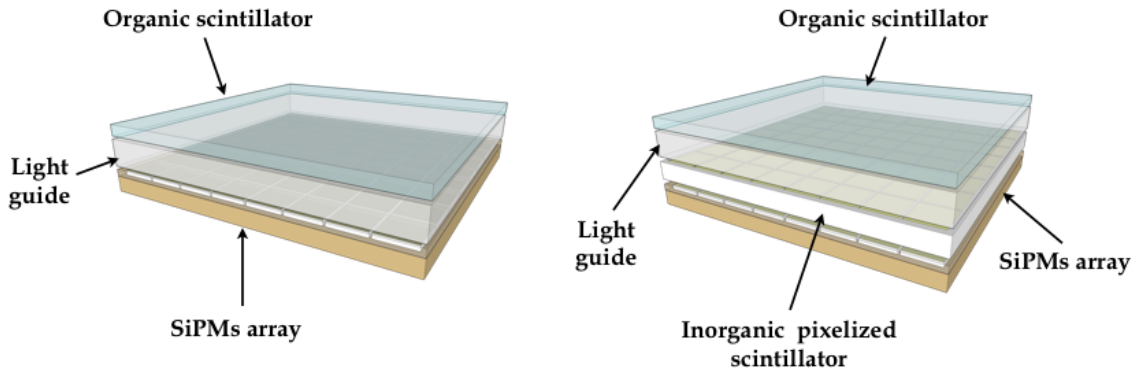


Figure 2.13 – Schematic representation of the design of the developed positron probes: the scintillation light produced by a single (left) and two scintillators is readout by a single SiPM array.

the SiPM array provides useful information for the discrimination between events interacting in β -sensitive and β -shielded scintillators.

Whatever the configuration, the sensitivity of the imaging probes depends mainly on the detection efficiency of the SiPMs as well as on the choice of the scintillation material and its thickness. Spatial response (resolution and distortion) strongly depends on spatial distribution of the scintillation light on the SiPM array. This distribution is influenced by the thickness and nature of the scintillation material, the light guide thickness, as well as by the optical coatings. Both configuration use a 8×8 SiPM array composed of $3 \times 3 \text{ mm}^2$ elements providing a field of view around $25 \times 25 \text{ mm}^2$. The SiPM array is described in details in the Section 2.5.3.

The optimization of the design of these configurations was focused on the choice of the material for the scintillating sensitive volume and optical coating, and on the geometrical features of the detection head (see Section 3.2). The double scintillator detection head geometry was mainly optimized in term of events discrimination (see Section 3.3).

2.5.2 The scintillator choice

The scintillator mission is to convert the energy deposited by the incident β particles and γ rays into a light pulse detectable by the photodetection system. The choice of the scintillator, its geometry and optical coatings are a crucial step in the optimization of the imaging probe design.

2.5.2.1 Material nature and geometry

Organic scintillators are perfectly suited to the detection of positrons thanks to their low Z and low density and their low intrinsic sensitivity to γ radiations. We chose, as reference scintillator, a standard plastic scintillator (EJ-212, Eljen Tech.) presenting a light yield of about 8 photons/keV with a maximum emission centered on the wavelength of 423 nm, well adapted to the maximum sensitivity of most commercially available SiPMs

(Table 2.4). The second scintillation material tested was the para-terphenyl or p-terphenyl (1,4-diphenylbenzene). This organic material is commonly used as a dopant for organic scintillators. P-terphenyl was selected for its high light yield of 27 photons/keV in the blue region [Angelone *et al.* 2014]. Its density is also slightly higher than that of the plastic material (1.23 g/cm^3 for p-terphenyl and 1.03 g/cm^3 for plastic). These properties allow to reduce the thickness of the scintillator material minimizing by consequence the background noise coming from the annihilation γ rays without compromising the amount of scintillation light and thus, β sensitivity and spatial performances. Both scintillators have decay constants lower than 3 ns (Table 2.4). Polycrystalline p-terphenyl (Proteus Tech.) is produced in the form of a compressed powder deposited on a polyester support, that works as a light guide (Fig. 2.14).

Different scintillator thicknesses (0.1 mm and 0.2 mm for the p-terphenyl scintillator and 0.2 and 0.4 mm for the plastic scintillator) were used for the single scintillator configuration, in order to find the optimal tradeoff between the energy deposited inside the scintillator by β particles and the γ background noise contamination. The spread of the scintillation light distribution at the SiPM array surface was studied for a light guide thickness of 1, 2 and 3 mm. The light guides were made in PMMA for the plastic scintillators and polyester for the p-terphenyl ones. The dimensions of all scintillators and light guides were fitted to the field of view of the SiPM arrays ($25.7 \times 25.7 \text{ mm}^2$).

The p-terphenyl was chosen for the β -sensitive scintillator of the double scintillators configuration. A thickness of 0.2 mm was used to increase the energy deposition and take into account the additional light loss introduced by the multiple optical interfaces. The detection of the γ background noise is done using a high density inorganic scintillator, in order to decrease the statistic fluctuations in the measurement of the γ contamination signal. Among all inorganic scintillators commercially available, LYSO:Ce appears to be the most suitable

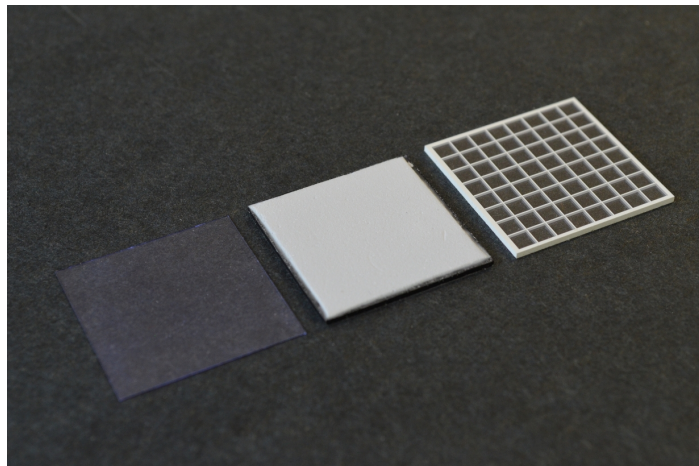


Figure 2.14 – Scintillators tested for the optimization of the intraoperative imaging probe. From the left to right: the plastic scintillator (EJ-212, Eljen Tech.), the p-terphenyl polycrystalline scintillator (Proteus Tech.) and the LYSO:Ce array with 8×8 pixels of $3 \times 3 \times 0.5 \text{ mm}^3$ separated by $200 \mu\text{m}$ of diffusing material (Hilger crystals).

Scintillator	Density (g/cm ³)	Light yield (ph/keV)	Refraction index	λ_{max} (nm)	Decay constant (ns)
EJ-212	1.02	8	1.58	423	2.4
p-Terphenyl	1.23	27	1.65	~420	3.0
LYSO:Ce	7.10	32	1.81	420	40

Table 2.4 – *Main characteristics of the scintillators evaluated for the two configurations of the intraoperative imaging probe.*

for the second pixelated scintillator. This scintillator presents a quite elevated light yield (32 photons/keV) and a fast decay time (40 ns) (Table 2.4). Compared to other fast inorganic scintillators with high density and high light yield, such as LaBr₃:Ce or LaCl₃:Ce [Pani *et al.* 2004], it has the advantage to be not hygroscopic, which allows its used without a protection housing and therefore facilitate the implementation in miniaturized imaging probe. LYSO:Ce is also easily manufactured in pixelated-scintillator structures. The major drawback of the LYSO:Ce is its intrinsic natural radioactivity due to the isotope ¹⁷⁶Lu, that is part of its chemical component, and emits β^- particles ($E_{max}=596$ keV). Its activity is about 39 cps/g on the energy range of 0 to 1.2 MeV. An alternative scintillator, not radioactive or hygroscopic, is the GSO, but it has lower light yield (about 10 photon/keV) and presents mechanical properties that do not allow its manufacture in scintillator arrays with the requested dimensions. GaGG:Ce scintillator overcomes both limitations of the GSO (light yield of 46 photon/keV). However, its maximum light emission is in the yellow range ($\lambda_{max}=520$ nm) and does not match the maximum sensitivity of most SiPM arrays. Moreover, GaGG:Ce presents a large absorption region between 400 and 480 nm, corresponding to the maximum emission peak of the p-terphenyl scintillator. Since the inorganic scintillator is place in contact with the SiPM, a large part of the p-terphenyl scintillation light would be absorbed by the GaGG:Ce, causing a drop of the probe sensitivity and a degradation of the spatial performances. Figure 2.15 presents the light transmission curves of the above cited inorganic scintillators compared to that of a PMMA light guide, that transmits more than 90% of light in the visible range. This graph clearly shows the inadequacy of the GaGG:Ce for the application. On the other hand, LYSO:Ce presents a transparency above 80% in the whole visible region. The pixelized LYSO:Ce was manufactured into an 8×8 array of 3×3×0.5 mm³ pixels separated by 200 μ m of diffusing material (Hilger crystals) (Fig. 2.14). This array matches the size and the gaps between the SiPMs into the array (see Section 2.5).

2.5.2.2 Optical coating and light shielding

The optical coating deposited on the top surface of the scintillators allows to enhance the light collection and distribution on the photodetector. Two types of optical coating have been tested experimentally. The ESR reflective coating (Enhanced Specular Reflector, 3M, $\rho = 1.35$ g/cm³) has a thickness of 65 μ m and an excellent reflection index ($\sim 95\%$ at 450 nm). The Teflon (PTFE, polytetrafluoroethylene) has a thickness of 75 μ m ($\rho = 0.46$ g/cm³) and can be assimilated to a perfect Lambertian diffuse reflector.

All surfaces were optically polished except the sides of the light guides and the plastic

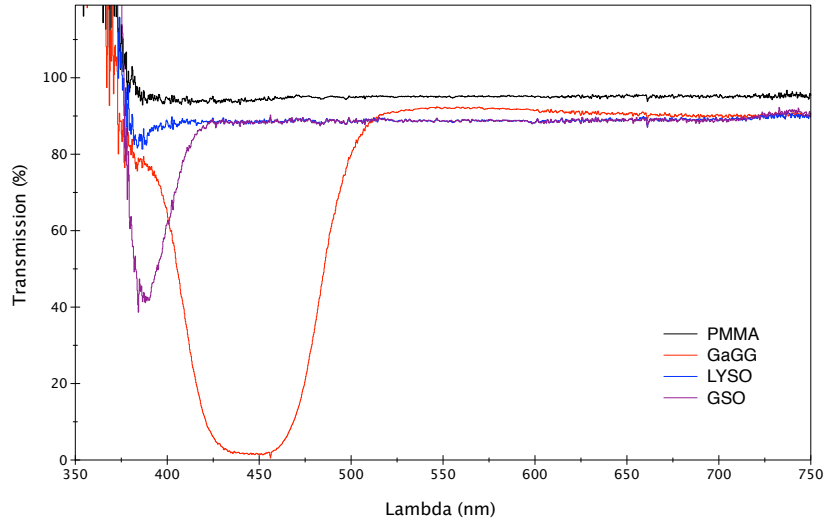


Figure 2.15 – Curve representing the percentage of transmitted light as a function of the wavelength for a few inorganic scintillators and the PMMA material. Measurements were made with a spectrophotometer coupled to an integrating sphere.

scintillators that were grounded and coated with a black absorbing paint. This allows an efficient truncation of the light distributions at the scintillator edges in order to reduce the image distortion in that region. A layer of optical coupling grease (BC-600, Bicon) was applied to all boundaries of plastic scintillators and only between the SiPM array and the light guide for the p-terphenyl ones because the p-terphenyl compressed powder is directly deposited on the light guide and is chemically sensitive to grease.

2.5.3 The photodetection device

The photons emitted by the scintillation materials are collected by with the SiPM array. We chose to implement the SiPMs produced by Hamamatsu. A 16-channels Through Silicon Via (TSV) SiPMs array (S12642-0404PA, Hamamatsu) was used for the single scintillator configuration (Fig. 2.16). TSV technology allows to reduce to 0.2 mm the dead-area in between the 3×3 mm² SiPMs. Four SiPM arrays were assembled together on a PCB in order to obtain a sensitive area of 25.7×25.7 mm² (space in-between the arrays of 0.5 mm). The double scintillator configuration is based on a 8×8 TSV SiPMs array with 3×3 mm² elements (S12642-0808PA, Hamamatsu) (Fig. 2.16). The gap between each pixel is 0.2 mm and the field of view is 25.4×25.4 mm². Each SiPM is composed by 3600 cells (GM-APD in parallel) of 50×50 μm².

The operational principle and main features of SiPMs will be synthetically described in the following sections. The focus will be put on the characteristics of the Hamamatsu SiPMs used. This part of the manuscript refers to the previous works of [Dinu *et al.* 2009] and [Hudin *et al.* 2012b].

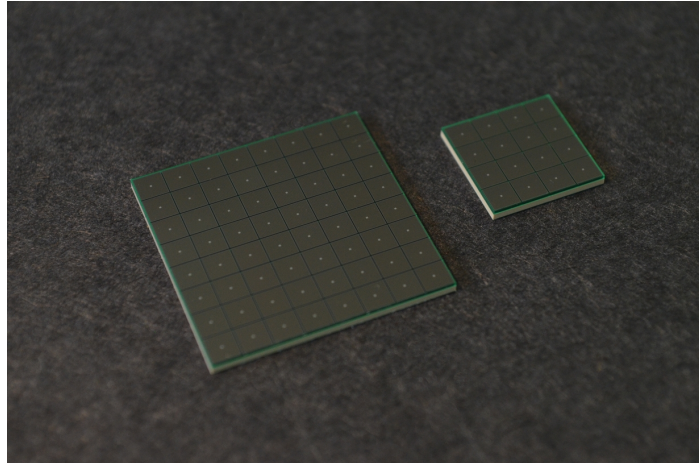


Figure 2.16 – 8×8 TSV SiPM arrays (left) and 4×4 TSV SiPM arrays (right) proposed by Hamamatsu, with $3 \times 3 \text{ mm}^2$ SiPMs composed of 3600 cells of $50 \mu\text{m}$ side dimension [Hamamatsu KK 2014].

2.5.3.1 Operation principles of SiPM

As previously mentioned, silicon photomultipliers are made of a matrix of cells interconnected in parallel on a common substrate of silicon (Fig. 2.17). These cells are composed of an avalanche photodiode working in Geiger mode (GM-APD) and a quenching R_Q . Multiple types of structures are available for SiPMs. In a conventional structure, each cell is made of highly doped silicon p-type substrate (p+), on which is settle an epitaxial layer (π) with a low p- doping. The junction is basically obtained by creating an n+ area on the surface of the epitaxial layer. Usually, a second p-type region is created underneath the n+ area. This allows to fix the breakdown voltage to a desired value. The final structure, composed of the overlapped layers p+, π , p and n+ is represented in Figure 2.17. When a voltage is applied to the cell, the epitaxial layer is associated with a low electric field and a drift region for the charges is created. On the other hand, the thin depletion area (smaller than a μm) that is created at the junction between the p and n+ areas is associated to an high electric field (3 to $5 \cdot 10^5 \text{ V/cm}$). This is called the avalanche region, where the charge multiplication takes place. The uniformity of the electric field within the pixel is guaranteed by a edge structure n- doped, called guard ring [Buzhan *et al.* 2001]. A layer of silicon oxide (SiO_2) is deposited on the surface to electrically decouple the cells and create an optical window to enhance the penetration of photon in the silicon. Finally, the cells are interconnected by a common aluminum strip through individual resistors of a few hundred $\text{k}\Omega$, called quenching resistor R_Q .

The evolution of the signal produced by a GM-APD can be described by the circuit model shown in Fig. 2.18. According to this model, the GM-APD, represented by the junction capacitance C_D , is connected in series with the quenching resistor R_Q . This capacitance is connected in parallel to a generator of voltage V_{BD} , which is the threshold voltage to trigger the Geiger avalanche process (BD goes for breakdown) and in series to the R_S resistor and the switch S . R_S includes both the resistance of the neutral region inside silicon as well as the space charge resistance ($R_S \sim 1 \text{ k}\Omega$). At the steady state, the switch is open and no

current pass through the circuit. The capacitance charges at $V_{bias} > V_{BD}$, where V_{bias} is the operating voltage. When an electron-hole pair is created nearby the p-n junction, the electron is drifted through the high-field region and there is a certain probability, known as turn-on probability, to initiate an avalanche discharge. The carrier initiating the discharge can either be photo-generated or thermally generated. In the case of Geiger mode ($V_{bias} > V_{BD}$), each created carrier can trigger multiple new avalanches, producing a number of electrons that grows exponentially (the electron gain is current-limited by the R_Q quenching resistance). In the circuit model, the switch S represents the trigger of a discharge. When the switch is closed (time t_0), C_D discharges through the series resistance R_S and the voltage V_{APD} drops to a value close to V_{BD} with a time constant τ_D equal to $R_S \cdot C_D$ (because $R_Q \gg R_S$). The discharged current is initially limited by the build-up of the avalanche process, which takes some dozens of ps. In this short time, the current I_{APD} throughout R_S rises to its maximum value, $I_{APD,0} = (V_{bias} - V_{BD}) / R_S$, and then decreases to the value I_0 , responding to the relation $I_0 = (V_{bias} - V_{BD}) / (R_S + R_Q)$. As V_{APD} and I_{APD} are decreasing, the voltage applied at the quenching resistance R_Q rises exponentially, together with the associated current I_{cell} (current through the diode). For $t=t_1$, the current I_{cell} reaches its maximum I_0 .

When the capacitance C_D is completely discharged, and R_Q is high enough, the diode current I_0 gets so low that a statistical fluctuation can quench the avalanche. The probability of such fluctuation becomes significant for diode currents below 10-20 μA . When this condition is satisfied, the average time needed to stop an avalanche is in the order of the ns. The total number of charges Q_{cell} generated during the avalanche is $C_D \cdot (V_{bias} - V_{BD})$. As the avalanche process is terminated ($t=t_1$), the S switch is open again, the current traversing the APD drops to zero and C_D recharges through R_Q up to the initial voltage V_{bias} ($t = t_2$) with a time constant $\tau_C = R_Q \cdot C_D$.

Each GM-APD composing the SiPM act as an individual elementary detector, with a binary response independent on the number of incident photons, as described above. Therefore, if n cells are activated at the same time, the charge measured at the SiPMs output is n times the charge produced by a single GM-APD. If the number of incident photons is

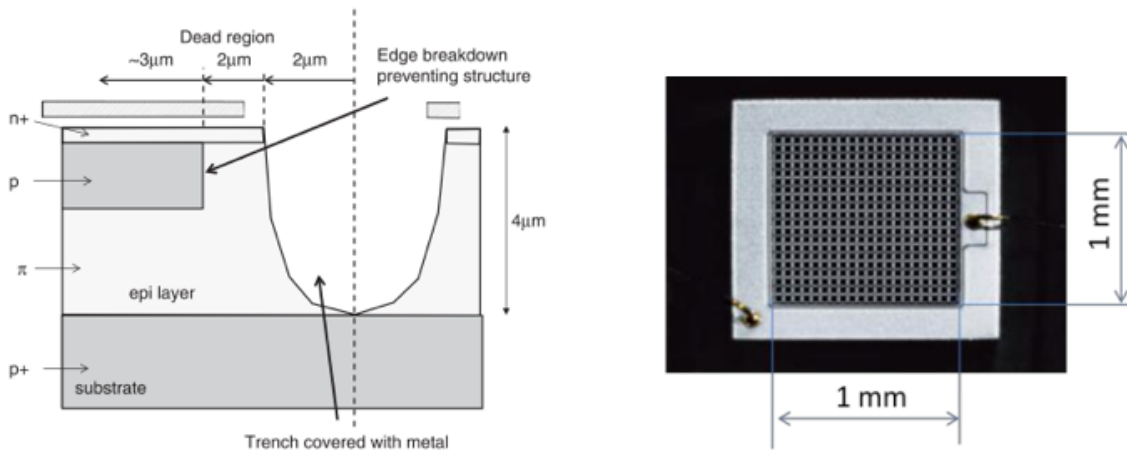


Figure 2.17 – Schematic representation of the border region of a conventional SiPM structure [Piemonte 2006] (left). $1 \times 1 \text{ mm}^2$ SiPM with 400 cells each of $50 \times 50 \text{ } \mu\text{m}^2$ from Hamamatsu (right) [Dinu et al. 2009].

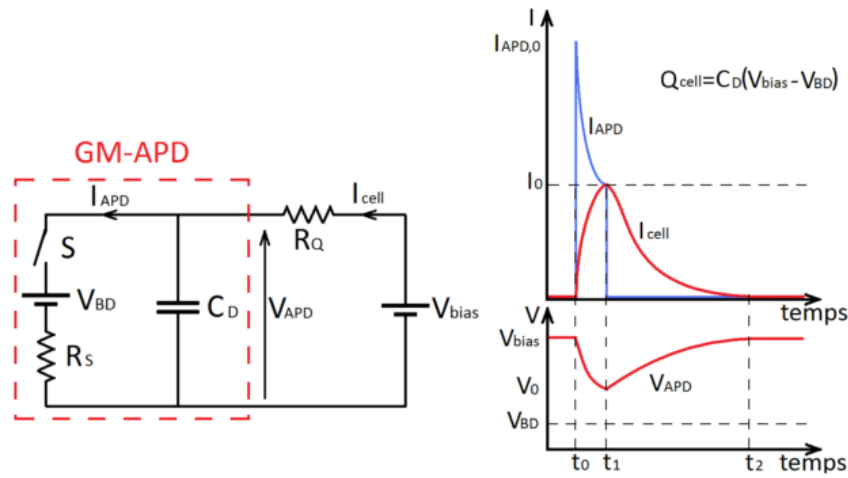


Figure 2.18 – Electric circuit equivalent of an APD in Geiger mode with quenching resistance (left) and the time evolution of the current and voltage passing through it (left) [Haitz 1964].

significantly inferior to the number of cells composing the SiPM, the probability that two photons interact simultaneously in the same cell is low. If this condition is satisfied, the SiPM behaves as an analogical device that generating a signal proportional to the light intensity (Fig. 2.19).

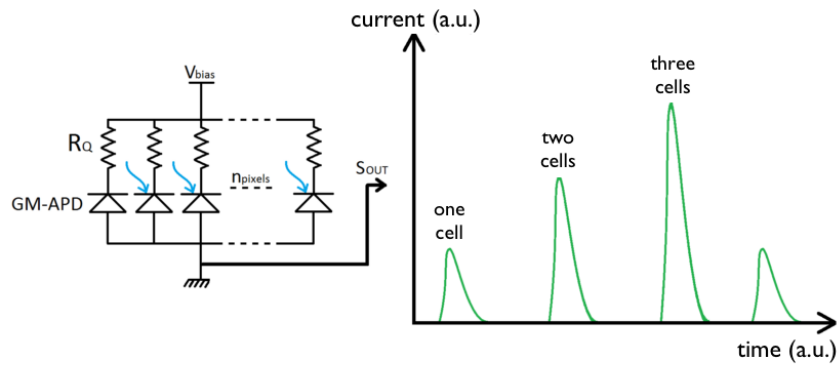


Figure 2.19 – Circuit model constituted of several cells connected in parallel. Each cell is composed of an APD connected in series with a quenching resistance [Hudin et al. 2012b].

The SiPM are produced by a large number of manufacturers, with various characteristics, from the dimensions of the cells to their organization in array. The SiPM are proposed with individual cells from $10 \times 10 \mu m^2$ to $100 \times 100 \mu m^2$. The dimensions of a SiPM ranges from $0.25 \times 0.25 mm^2$ to $9 \times 9 mm^2$ (CPTA/Photonique). For many applications, the small dimensions of these SiPMs represent a limitation. Larger sensitive area can be obtained by assembling together several SiPMs into an array. For example, Hamamatsu proposes arrays

of 4×4 , 8×8 and 16×16 SiPMs, each of 3×3 mm² (see Fig. 2.16). However, these SiPM arrays structure introduce dead areas in-between pixels (of 200 μm for Hamamatsu) and the breakdown voltage varies from one pixel to another.

2.5.3.2 SiPM intrinsic characteristics and drawbacks

The main intrinsic SiPM characteristics, such as gain, photon detection efficiency, dynamic range and thermal and correlated noises, are presented in details in the following paragraphs.

a) Gain

The gain is the number of charges created by a carrier during an avalanche process in a cell. It can be expressed by the relation:

$$G = \frac{Q_{cell}}{q_e} = \frac{C_D(V_{bias} - V_{BD})}{q_e} \quad (2.11)$$

where Q_{cell} is the maximum charge that can be accumulated in a cells, C_D the cell capacitance and q_e its elementary charge. If the breakdown voltage V_{BD} is considered as constant, the gain linearly depends on the bias voltage. Thus, the difference $V_{bias} - V_{BD}$, called overvoltage, plays an important role on the performances of the SiPM, as it will be developed in the following sections. However, the breakdown voltage, starting from which the avalanche processes are created, depends on the temperature and therefore, the gain as well [Buzhan *et al.* 2001]. In fact, when the temperature rises, the crystalline vibrations get more important and the primary carriers have a higher probability to interact with the crystalline network. As a consequence, the breakdown voltage rises. To compensate this effect, and maintain a constant gain, a higher bias voltage has to be applied. If each cell has a capacitance of about one hundred fF and an applied overvoltage of a few V, the gain of a SiPM is of the order of 10^6 , which is equivalent to PMT gain. Such an elevate gain allows to observe light signals of the other of one photo-electron.

b) Photon detection efficiency

The SiPM photon detection efficiency (PDE), represents the probability of an incident photon to be detected by the SiPM. The PDE can be considered as influenced mainly by three major factors, as described by the equation:

$$PDE = QE \cdot \varepsilon_g \cdot P_{01} \quad (2.12)$$

where QE is the quantum efficiency, ε_g is the so-called geometrical efficiency, that is the fraction of the total SiPM area which is effectively photosensitive and the factor P_{01} is the probability for a carrier created in the sensitive area to initiate a Geiger-mode discharge.

The quantum efficiency QE represents the probability for a photon to create a electron-hole pair in the active area of the detector. It is obtained by the product of two factors: the transmittance of the dielectric layer on the top of the silicon surface and the internal QE. Both factors depend on the wavelength of the incident light. The first one depends on the

incidence angle of the photon and can be optimized by implementing an anti-reflective coating. The second represents the probability for a photon that crosses the dielectric layer to generate a carriers pair in the active thickness of the silicon. The internal quantum efficiency generally ranges from 50% to 90% depending on the wavelength.

The trigger probability P_{01} depends directly on the bias voltage, because the ionization rate of the carriers increases with the electric field. It equally depends on the interaction point of the photon in the diode active area where the creation of the carriers takes place. The two carriers created by photogeneration travel in opposite directions and both contribute to the trigger probability. When a pair is created in the n+ terminal, the electron is directly collected while the hole is forced to cross the whole high-field region. Thus, the avalanche is triggered with a maximum probability by the hole. Likewise, when the pair is created in the p terminal, the situation is symmetrical and only electrons contribute to trigger the avalanches. In the central region both carriers contribute to initiate the avalanche but with different probabilities. Indeed, electrons have an ionization rate and a mobility higher than the holes in silicon (almost double for the ionization rate). Therefore, the trigger probability is maximum when the avalanche is triggered by an electron, that is when the photogeneration happens in the p region side of the junction, so that the electron has to cross the whole high-field region zone [Piemonte 2006]. The depth of the interaction of the incident photon depends on the wavelength. For the SiPM based on the structure type n+/p/ π /p+, which associates a n+ layer on a p+ substrate (see Sec. 2.5.3.1 and Fig. 2.17), only photons with a long wavelength above 500 nm (green and red) will be able to interact in the p-doped area. Blue/UV light (400-540 nm) has a small absorption depth in silicon (100-500 nm) and most of it is absorbed close to the cell surface, inside the n-p junction, where the probability to initiate an avalanche in the cell is particularly low. Indeed, this structure is optimal for green-red light detection. Inversely, the SiPMs based on a p/n+ structure (p layer on a n+ substrate) have a PDE optimized for the blue wavelength.

The geometrical efficiency or fill factor represents the ratio between the detector sensitive area and the total surface. This parameter mainly depends on the dead area surrounding the borders of the microcells. The design of the pixel and pitch layout depends on the passive quench elements and the bias voltage metal capacitance but also on the guard ring structures to prevent premature edge breakdown. The fill factor is variable from one SiPM to another depending on the size of the cell and the manufacturer. For the TSV SiPM array with $3 \times 3 \text{ mm}^2$ used for our imaging β probe the fill factor is equal to 62% [Hamamatsu KK 2014].

The variation of photon detection efficiency as a function of the light wavelength for the different GM-APD structures is presented in Figure 2.20. As shown in these graphs, SiPMs present a good PDE ranging from 20 to 50% comparable to that of the vacuum technology PMT (see Table 2.3).

c) SiPM dynamic range

The dynamic range is the range of light intensities for which the output signal of the SiPM is proportional to the input light signal. It is determined by the number of cells in a SiPM. The

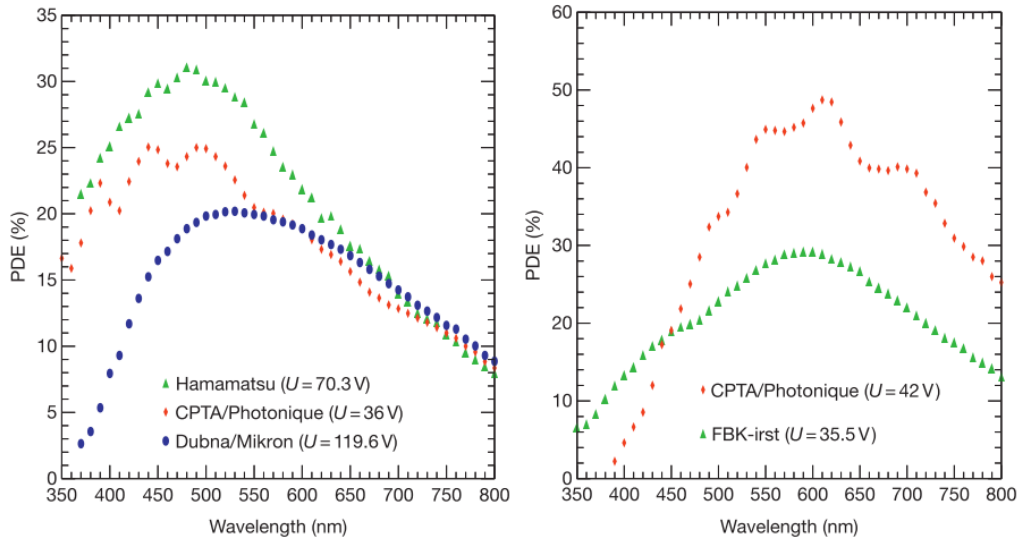


Figure 2.20 – Photon detection efficiency (PDE) as a function of the light wavelength with a GM-APD p -on- n structure for Hamamatsu ($V_{bias} = 70.3$ V), CPTA/Photonique ($V_{bias} = 36$ V) and Dubna/Mikron ($V_{bias} = 119.6$ V) (right) structure, measured at room temperature (left). PDE as a function of wavelength for a n -on- p structure produced by CPTA/Photonique ($V_{bias} = 42$ V) and FBK-irst ($V_{bias} = 35.5$ V), measured at room temperature [Musienko 2009].

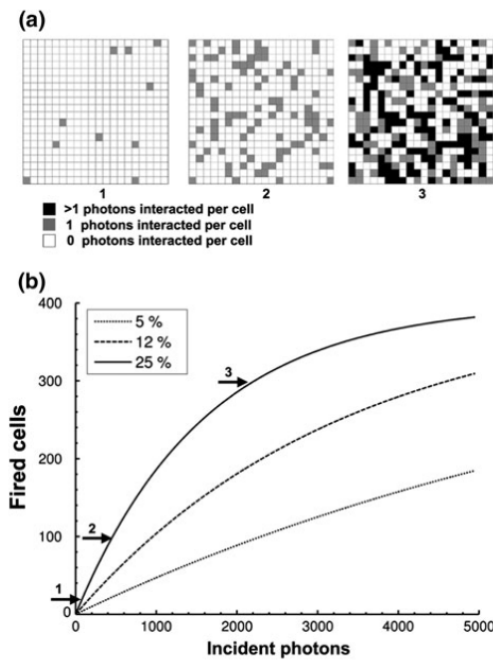


Figure 2.21 – Responses of a 400-cells SiPM calculated with the Eq. 2.13. (a) Representation of SiPM exposed at different light levels resulting (from left to right) in 10, 100 and 300 cells firing. The grey level represents the number of photons interacting per cell for a PDE of 25%. (b) Number of fired cells as a function of incident photons for different PDE values (5, 12 and 25%) [Roncali & Cherry 2011].

output signal is linear with light intensity only if no more than one optical photon interacts into a SiPM micro-cells at the same time. The main number of fired cells (N_f) after a light impulse can be approximately described by the following relation [Roncali & Cherry 2011]:

$$N_f = N_{cell} \left(1 - e^{-\frac{N_{ph} \cdot PDE}{N_{cell}}} \right) \quad (2.13)$$

where N_{ph} the number of optical photons incident on the SiPM surface and N_{cell} is the number of microcells in the SiPM. If the number of detected photons is small compared to the number of cells ($N_{ph} \cdot PDE \ll N_{cell}$), the output is linear as shown in Figure 2.21. However, this simplified model does not take into account the different noise sources and the recharge time of the SiPM. Other more complete models have been developed to simulate the SiPM response to different light sources as a function of their geometrical and physical characteristics [Van Dam *et al.* 2010]. The density of cells must be suited to the intensity of light that has to be detected. The SiPM chosen for our application is composed of 3600 cells (60×60 , 400×400 mm²). If we consider a maximum deposited energy by the β particles of about 500 keV in an organic scintillator with a light yield of 8 photons/keV (see simulations results in Section 2.4.2) and that this scintillation light is spread over ten SiPMs, the number of incident photons on a SiPM is 400. According to the formula 2.13, the corresponding number of fired cells is approximately 120, taking into account a SiPM with 3600 cells and a PDE of 40%. Therefore, the number of cells in our SiPMs overcome largely the maximum number of fired cell for the light levels investigated expected for our application.

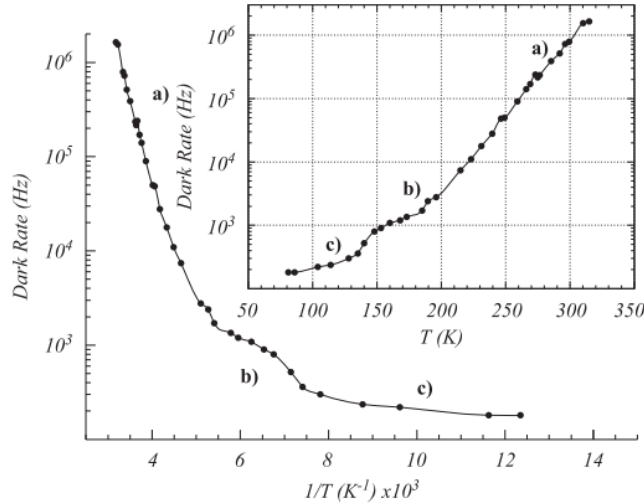


Figure 2.22 – Dark count rate as a function of the temperature at $\Delta V = 1.5$ V, for three trends: a) thermal effect, b) band-to-band tunneling, c) additional mechanism [Collazuol *et al.* 2011].

d) Dark count rate

In the absence of an external light signals, the electron-hole pairs in the silicon can be created by processes other than the photoabsorption. This effect is called dark noise and the processes responsible for it are thermal excitations and field-assisted excitations, called *tunneling* [Hurkx *et al.* 1992]. Each carriers pair, independently from their production mechanism, generate an avalanche which results in exactly the same output signal. The thermal energy of the carrier at room temperature is considerably smaller than the band gap. Therefore, thermal excitation in silicon can only take place in presence of impurities. Thermal excitation can be significantly reduced by cooling the system, but most effective is the improvement of the silicon purity during production. Tunneling is a quantum-mechanical phenomenon. Electrons, due to the influence of the electric field, have a certain probability for tunneling through the band gap to a state in the conduction band with the same energy. Differently from thermal excitation, which is possible without external bias voltage, this effect increases with the electric field or the applied voltage and cannot be reduced by cooling. The number of dark counts per second induced by these processes is referred to as dark count rate (DCR). This value increases with the number of cells, the volume of the depletion area, the number of impurities in the crystal, the temperature and the overvoltage (because the triggers probability increases with the bias). In common thermal conditions around 300 K, the thermal excitation is the dominate effect, while for temperatures below 200 K, the tunnel effect is the dominant noise component, as shown in Figure 2.22. At extremely low temperatures, the relation follows a different behavior, still under investigation [Collazuol *et al.* 2011]. A dark noise pulse produces a charge equivalent to a single photoelectron. The probability of two cells to be simultaneously fired by this process is negligible. The dark noise is a constraint especially for the detection of low light signals. At present, the available SiPMs have a mean DCR of the order of 100 kHz/mm² for a gain of $1.25 \cdot 10^6$, a detection threshold of 0.5 photoelectrons and a temperature of 20 °C [Hudin 2013].

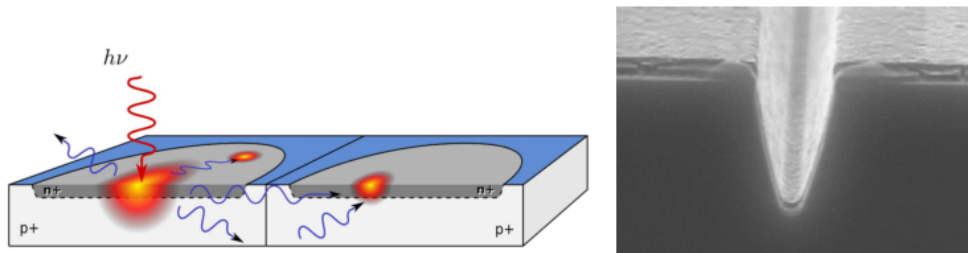


Figure 2.23 – Schematic representation of optical cross-talk between two adjacent cells: a secondary photon can traverse the junction and initiates an avalanche in adjacent cells (left) [Rech *et al.* 2008]. Optical tranches coated with metal to decrease the cross-talk probability (right) [Dinu 2013].

e) Correlated noise

The correlate noise corresponds to the noise generated by a primary avalanche, and can be produced by two effects: the after-pulsing and the optical cross-talk.

Optical interpixel cross-talk

The optical cross-talk is due to production of visible photons within a GM-ADP cell operated above breakdown voltage (approximately $3 \cdot 10^{-5}$ photons per charge carrier crossing the junction) [Lacaita *et al.* 1993]. Considering that the typical SiPM gain is of the order of 10^6 , about 30 photons can be emitted during an avalanche. These photons have a certain probability to propagate in the silicon and reach the neighboring cells not yet fired. Since their energy is greater than the one necessary to create an electron-hole pair, they can initiate a new avalanche (Fig. 2.23). These new avalanches are produced simultaneously to the primary one and are indistinguishable. Therefore, we measured an output signal with an amplitude corresponding to several fired cells instead of one (Fig. 2.24). To remove the cross-talk effect, metal coated trenches can be placed in between cells for optical isolation, as shown in Figures 2.17 and 2.23. The overall device cross-talk can be decreased using the optical trenches from about 20% below 3 %, thus to reduce the spacing between cells allowing to increase the fill factor up to 70% for the 50 μm size cells SiPM [McNally & Golovin 2009]. However, this solution does not completely remove the cross-talk due to the indirect photon propagation. Rech *et al.* showed that a substantial part of the optical cross-talk is caused by the reflection of photons on the bottom of SiPM, which cannot be stopped by the trenches [Rech *et al.* 2008]. The photons can also reach the neighboring cells through the protective resin of the SiPM or the scintillator coupled to it. This optical cross-talk phenomenon has a quadratic dependence from the overvoltage because the crosstalk probability is proportional to gain, that is the number of photons produced during the avalanche and to the trigger probability. Hence, a low overvoltage allows to limit the optical cross-talk. Its intensity is also inversely proportional to the distance between cells, which limits the maximum cells density of an array.

After-pulsing

The after-pulsing is the result of the capture of a charge carrier in an impurity, which is release after a time lapse, creating a second avalanche slightly delayed in time (from ns to μs). After-pulse probability increases quadratically from the applied overvoltage. However, for a temperature higher than 120 K, the after-pulse probability is almost independent from temperature [Collazuol *et al.* 2011]. If the delay between the primary avalanche and the releasing of the captured charge is short compared to the SiPM recharge time, the secondary avalanche will have a amplitude smaller than one photoelectron. This effect is clearly visible in Figure 2.24, where the amplitude of the after-pulses is sometimes inferior of a photoelectron.

f) Timing

The GM-APD timing resolution is defined as the time jitter between the effective moment of arrival of the photon at the sensor and the instant when the output current pulse is recorded. In GM-APD, the active pixel area and thickness of the depletion region are very small. This results in a very fast avalanche built-up (of a few tens of ps) and therefore, a fast response to the photoelectrons. The typical rise time of the pulse signal is of about 1 ns, and its decay time is determined by the time constant of the recharge $\tau_D = C_D \cdot R_Q$ (of a few tens of ns). Therefore, the recovery time of a single cell is inferior to 100 ns. For those applications that

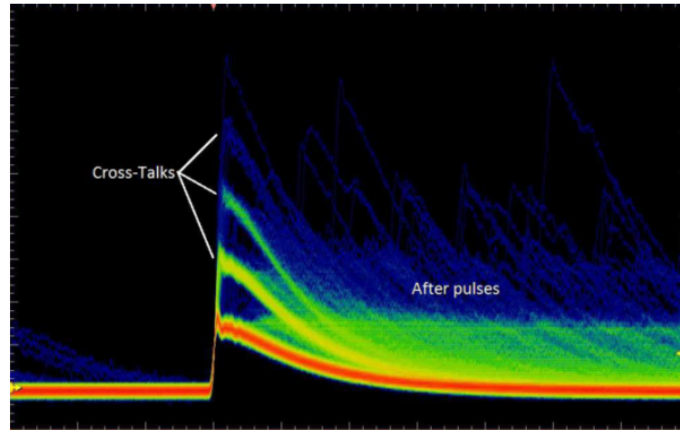


Figure 2.24 – Output signal of a SiPM, visualized on a oscilloscope: the after-pulse and cross-talk events are distinguishable [Dinu 2013].

needs a high detection rate (low dead time), as in the PET system, the most suitable SiPMs has small dimension pixels (low C_D) and low quenching resistance. However, the quenching resistance has to be high enough to efficiently quench the APD in the Geiger-mode.

2.5.3.3 Advantages and drawbacks of SiPMs for the development of intraoperative beta probe

As previously mentioned, Silicon Photon Multipliers detectors allow the detection and quantification of light signals with a large dynamic range down to the single photon level. SiPM can be organized in an array structure of parallel cells, each consisting of a Geiger-mode avalanche photodiode. The SiPM architecture, integrating a dense array of GM-APDs on the same substrate, overcomes the lack of proportionality of the single GM-APD and produces a current signal proportional to the number of incident photons. As the single GM-APD, the SiPM achieves a high gain ($\sim 10^5$ - 10^6), comparable to the vacuum technology PMT, and has the advantage to work with low voltage supplies (between 30 and 70 V depending from the technology) and have low power consumption. They exhibit good photon detection efficiency (~ 20 - 40%), peaked in the blue or green light region depending on the device technology. Furthermore, due to their high gain, they do not require complex electronic readout and benefit of a structure that is compact, light and rugged. These are key features when trying to increase the efficiency and reliability of intraoperative positron probes.

Main drawbacks of SiPMs for beta detection using scintillators concern the high dark count rate and the temperature stability. This is especially important for medical applications that foresee the use of SiPM photosensors at ~ 37 °C when the probe is introduced into the human body. The DCR increases with temperature, detector volume and bias voltage. The amplitude distribution of the dark count signal is strongly influenced by the correlated noise, which might artificially increase the mean charge output well above the single photoelectron level if the gain of the SiPM is high. This increased excess noise factor

can significantly hamper the detection of low-light events, such as produced by low-energy beta particles in plastic scintillators. Because the implementation of a cooling system is not possible for intraoperative detection applications, the minimization of the dark noise impact relies on a compromise between the SiPM features. A small pixel size decreases the DCR, but in return also decreases the PDE and increases the cross-talk probability (for a given gain) [Hudin *et al.* 2012b].

The temperature-dependent performances of the SiPMs is also a critical issue for the development of intraoperative probes. Because the temperature directly affects the breakdown voltage, all performances of the SiPMs are impacted by temperature variations, including gain, PDE and thermal and correlated noises. However, previous studies have shown that this influence can be accurately offset whatever the temperature by tuning the bias voltage as a function of the temperature variation, in order to maintain a constant overvoltage [Hudin *et al.* 2012b].

The SiPMs arrays from Hamamatsu were selected for our application because they provide the best compromise between gain, DCR, PDE, crosstalk probability and response uniformity among pixels. Table 2.5 summarizes the main features of the SiPMs assembled into the arrays used for the development of the intraoperative β probe.

Parameters	values
Spectral response range	320 to 900 nm
Peak sensitivity wavelength	450 nm
PDE (at 450 nm)	35%
DCR per 1 SiPM	$2 \cdot 10^3$ cps
Gain	$1.25 \cdot 10^6$
Breakdown voltage	65 ± 10 V
Temperature coefficient	60 mV/ $^{\circ}$ C

Table 2.5 – Main parameters of the Through Silicon Via (TSV) SiPMs arrays, with SiPMs of 3×3 mm² (series S12642) produced from Hamamatsu (for a temperature of 25 $^{\circ}$ C and an overvoltage of 2.4 V) [Hamamatsu KK 2014].

2.5.4 Readout electronics

The 64 SiPMs array are coupled to a miniaturized readout electronic based on a dedicated ASIC (Application-Specific Integrated Circuit). The signal treatment consists of an analog and a digital part. The acquisition system is made up of two EASIROC ASICs, fully analog, each connected to an Analog to Digital Convertor (ADC). The signal is then sent to a logic circuit (FPGA, standing for Field-Programmable Gate Array). The control of the digitization, acquisition and data transfer through the PC is done with a USB interface. The simplified bloc diagram of the device is presented in Figure 2.25.

EASIROC chip - Each EASIROC ASIC(Extended Analogue Silicon pm Integrated Read Out Chip) has 32-channels front-end electronics dedicated to the SiPM detectors gain trimming and readout [Callier *et al.* 2012]. It has been developed by the Pole Omega in LAL. The

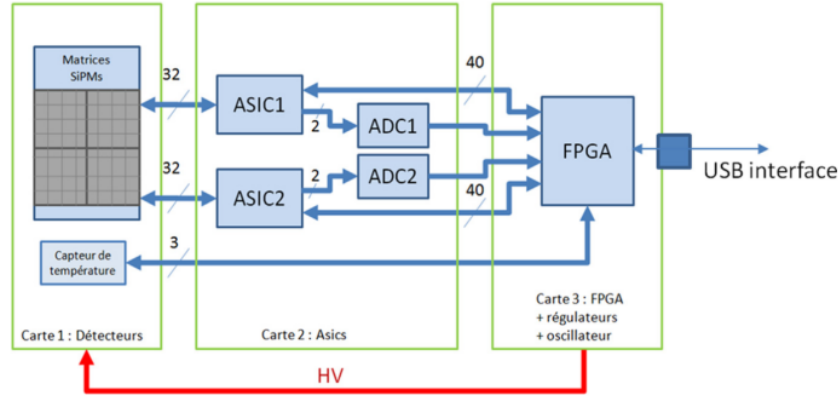


Figure 2.25 – Block diagram of the photodetector composed of a SiPM array coupled to the readout electronics. Two ASICs allow the gain trimming and readout of the 64 channels that are digitized by a two-channels ADC and then transmitted to the FPGA [Dinu et al. 2015].

diagram of a single channel of the ASIC is schematically represented in Fig. 2.26. The SiPM cathode is connected to the high voltage V_{HT} , delivered by the Keithley (model 2611A). The output signal at the SiPM anode is converted to a voltage thanks to 50Ω resistance. To individually adjust the bias voltage of each channel, the ASICs have an 8-bit DAC (Digital to Analog Converter), connected to the SiPM anode, allowing to provide a programmable low power input V_{DAC} ranging from 0 to 2.5 V (with a step of 10 mV). The voltage applied to the SiPM is then equal to $V_{bias} = V_{HT} - V_{DAC}$.

Each EASIROC channel embeds two variable-gain preamplifiers that can be independently programmed. Both low gain and high gain preamplifiers can be tuned on 4 bits, to perform the requested dynamic range from 160 fC to 320 pC (160 fC corresponds to the SiPM signal of one cell, for a gain of 10^6). The amplified signals are then sent into two slow shaper circuits. These circuit integrate and shape the signal with a time constant $\tau_{s-shaper}$ adjustable on 8 values (3 bits) from 25 to 175 ns. The amplitude of the slow shaper output signal is then proportional to the charge generated by the event. At the same time, the slow shaper preamplifier output signal is sent to a fast shaper of time constant $\tau_{f-shaper} = 15$ ns. This new signal is then compared with a threshold (common to the 32 channels and tunable on 10 bits) thanks to a discriminator. The signals of the 32 channels produced as output from the discriminator are sent into a logical 'or' for the 32 channels. Thus, if one of the channels signals exceeds the threshold, the slow shaper signal is put on 'hold' using a track and hold cell in order to register the integrated charge of the signal. The delay between the trigger and the hold signal is adjustable on 6 bits (from 0 to 160 ns, with a 2.5 ns step) depending on the shaping time of the signal. The analog data are digitized using a two-channels ADC (12 bits, 2 Msamples/s) and then transmitted to an FPGA (Altera Cyclone III).

FPGA and USB communication - The FPGA allows an easy programming of all the parameters of the ASIC. It organizes the informations relative to each event (time of the event, number of fired pixels, values of the collected charge) and save digital data in a buffer before to be transferred through an USB communication port (USB 2.0 High spec, 480 Mbits/s). The power consumption of the readout electronics is 4.48 mW/channels and

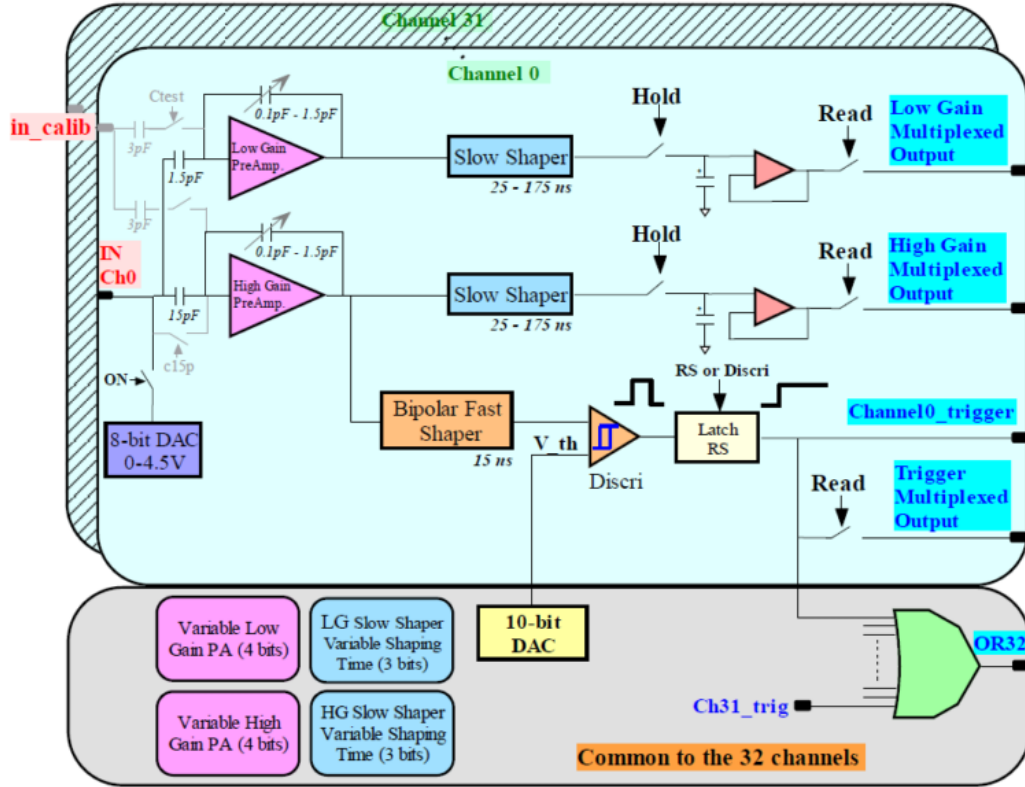


Figure 2.26 – Simplified diagram of a single channel of the EASIROC chip. An input DAC allows the adjustment of the SiPM high voltage on 2.5 V. Two voltage sensitive preamplifiers allow the adjustment on a dynamic range from 160 fC to 320 pC, followed by a trigger line made of a fast shaper and a discriminator. Two variable slow shapers and two Track and Hold blocks permits the charge measurement [Callier *et al.* 2012].

155 mW/chip.

The readout electronics was used in various embodiments depending on the measurements. The characterization of the SiPM gain was done by using a 32-channels test board including the EASIROC chip (see Section 3.1). All other measurements were done with the electronic modules designed and produced at LAL for the miniaturized γ camera based on SiPM arrays, called MAGICS (Miniaturized Gamma Imager for Cancer Surgery) [Dinu *et al.* 2015]. This 64-channel readout electronics is composed of three PCBs (Printed Circuit Boards) showed in Figure 2.27, including all components described above, that can be overlapped into a compact configuration. Finally, a new miniaturized readout electronics board was specifically developed during my thesis in order to meet the requirements of intraoperative positron detection (see Section 3.4.1). Main efforts were focused on the compactness and weight of the board, that should be integrated inside the handle of the probe, while maintaining good performances of the full system in terms of noise and reduced electronic cross-talk.

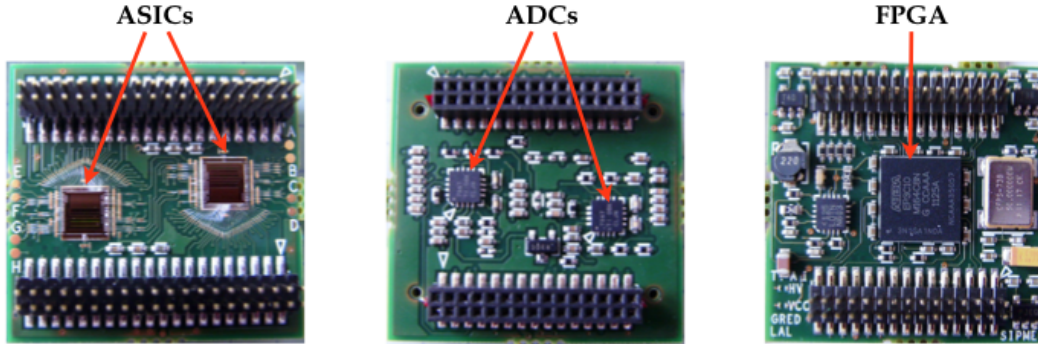


Figure 2.27 – From the left to the right: front side of the ASICs board with the two EASIROCS ASICs, back side of the ASICs board with the two ADC (12 bits, 2 Msample/s) and front side of the FPGA board with the ALTERA Cyclone III FPGA.

2.5.4.1 Electronic characteristics

The different parameters of the readout electronics are tunable through the FPGA, in order to adapt and optimize its performances to the detected signals. In the following paragraphs will be presented its main characteristics.

Trigger threshold - The threshold of the trigger is adjusted by a DAC of 10 bits, common to the 32 channels of the ASIC, and can supply a voltage ranging from 1.1 to 2.4 V with a 1.3 mV pitch (Fig. 2.28). This represents the voltage range for which the fast shaper signal amplitude is linear. To trigger signals of small amplitude, a continuous voltage is added at the output of the preamplifier. This voltage creates a continuous level on the signal, which shifts the electronic noise pedestal to 900 mV closed to the minimal voltage of the trigger threshold.

The trigger threshold level was adjusted according to the measurement. It was set at a level of 0.5 photoelectron (1.24 V for a preamplifier gain of 100 fF and a SiPM gain of $1.25 \cdot 10^6$) for the measurements of the SiPM gain performed with a pulsed LED source and an external trigger, or at a threshold around fifteen photoelectrons (1.37 V for a preamplifier gain of 1 pF and a SiPM gain of $1.25 \cdot 10^6$) for the acquisition with an internal trigger, in order to obtain a dark count rate low enough to avoid the dead time (typically less than 10 dark counts per second and per SiPM).

Individual adjustment of the SiPMs bias voltage - The 8-bits DAC connected to the SiPM anodes allows to accurately adjust the bias voltage V_{bias} delivered to the SiPMs, channel by channel. This feature is essential to obtain a uniform response over the SiPM array, but as well to compensate the influence of the temperature by maintaining a constant overvoltage on each channel during the system operation, making it independent of temperature variation (section 3.1.4 and 3.2.7.3). The tuning of the applied voltage between 0 and 2.5 V is obtained using a 8-bit DAC dedicated to each detector power line (accuracy of 10 mV). Figure 2.28 shows the linear relation between the voltage adjustment and the

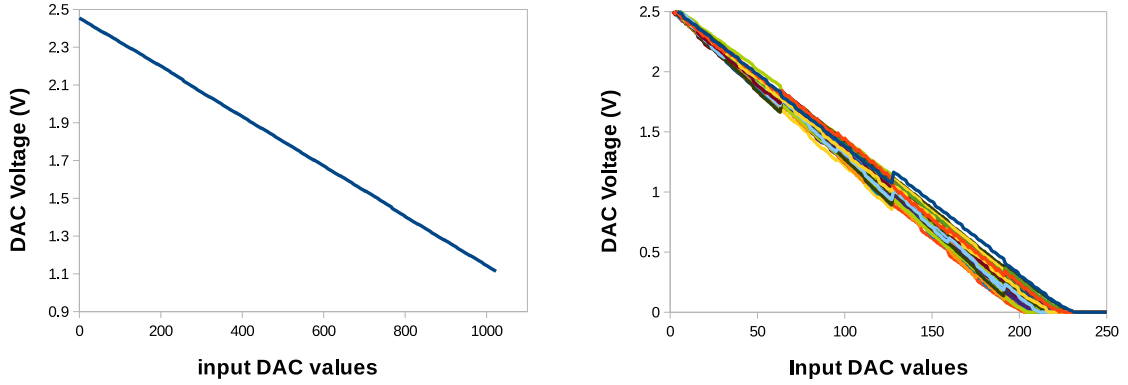


Figure 2.28 – Trigger threshold as a function of the 10-bits DAC values, common for all the 32 channels of one ASIC (left) and applied voltage tuning values for the SiPMs bias voltage as a function of the 8-bit DAC values for the 32 channels of one ASIC (right).

DAC values for some of the 64 channels. The DAC response is uniform among the different channels with a maximum standard deviation for the DAC input value of 0.09 V. The mean value of the DAC slope is -10.9 ± 0.1 mV/bin.

Gain, dynamic and linearity - The gain of the preamplifiers is proportional to the ratio between the input capacitance (1.5 and 15 pF for the low and high gain respectively) and a compensation capacitance on 4 bits ranging from 100 fF and 1.5 pF. This allows to obtain a voltage gain from 1 to 15 for the low gain preamplifier and from 10 to 150 from the high gain preamplifier. The dynamic range for a SiPM gain of about 10^6 goes from 1 to 93 photoelectrons and from 9.3 to 625 photoelectrons for an input capacitance of 100 fF and 1.4 pF, respectively.

Time constant and delay - The integration time constant of the slow shaper is set to optimize the signal to noise ratio of the detected signals. Thus, it is adapted to the timing characteristics of the signals generated by the SiPM array. A time constant too short window not allow a correct estimation of the developed charge but on the other hand a too long time constant would increase the electronic noise and fluctuation due to the integration of the dark noise events. The duration of the detected signal is given by the convolution of the SiPM cells recharge time and decay time of the scintillator. The time constant associated to the SiPM cells recharge time of the S12642-0404PA and S12642-0808PA arrays is of about 30 ns and the decay time constant of the scintillators variates from about 3 ns for the organic scintillators to 40 ns for the LYSO. Therefore, we have chose to use a common integration time constant $\tau_{slow-shaper}$ of 50 ns.

Once the integration time constant is defined, the delay between the trigger and the transmission of the logic signal 'hold' has to be adjusted so that the slow shaper signal is maintained at its maximum and the registered value is proportional to the charge created

by the detected event. The optimal delay was estimated by enlightening the array with a pulse LED source (470 nm). The optimal delay is defined as the value allowing to measured the maximum charge output (maximum position corresponding to the peak of the LED spectrum). The optimal for the delay parameter is obtained around 80 ns.

System dead time - The digitalization, treatment and transfer of data from the ASICs to the computer through the ADC, the FDGA and the USB generate a dead time during which the acquisition system is unable to detect any event. This dead time may become critical in the case of the detection of a small radiolabeled tumor inserted into an environment highly radioactive due to the non-specific radiotracer uptake. In these conditions, the dead time can strongly hamper the detection capability of the probe. The data relative to a single event are transferred right after the detection and treatment by the ASIC. One source of dead time is the data transfer through the USB which is non-compressible and last about 18 μs . A second source of dead time is due to the digitalization of the analogue signals that is equal to 43 μs for the 64 channels. The acquisition mode is characterized by a *non-paralyzable*

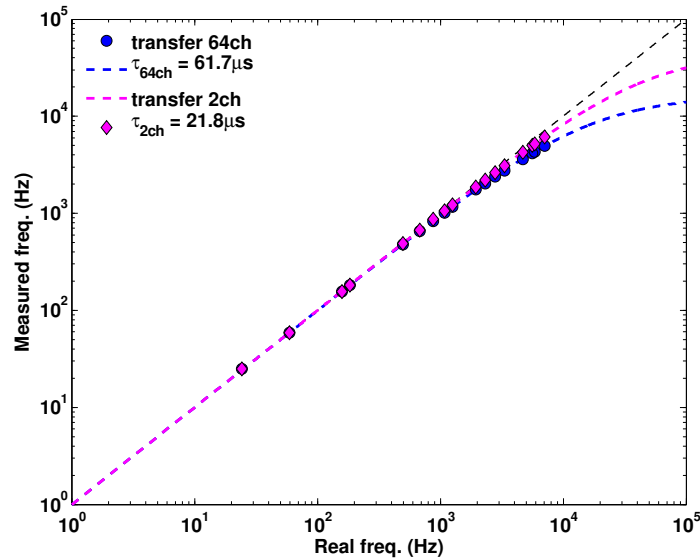


Figure 2.29 – Dead time of the acquisition electronic for the transfer of 2 and 64 channels. Random signals are sent to one channel of the electronics. The frequency of the acquired signals is represented as a function of their real frequency. The non-paralyzable model of the dead time is adjusted on each experimental curve.

behaviour, meaning that an event happening during the dead time τ of the electronic is simply lost but do not extend the duration of dead time. For an increasing event rate the detector will reach a saturation rate equal to the inverse of the dead time. The measured frequency can be expressed as a function of the real events frequency and the duration of the dead time τ as follows:

$$F_m = \frac{F_r}{1 + F_r \cdot \tau} \quad (2.14)$$

The signal digitalization of the whole array channels generate most of the dead time, but can be reduced by treating and transferring for each detected event only information relative to a few selected and not the whole 64 channels. This is done using a digital threshold on the charge collected from each SiPM and allowing the data transfer only for channels exceeding it. The effect of the number channels digitalized and transferred channels on dead time is shown in Figure 2.29. When only two channels are registered, corresponding typically to a thermally generated event, the dead time is close to the USB transfer time, while in case of transfer of all channels it's close to the sum of the digitalization plus the transfer time. For example, for 1 kHz frequency the error on the number of detected events compared to the real events is of about 2% and 6%, in case of the transfer of only 2 channels or all 64 channels, respectively [Hudin 2013].

2.5.4.2 Acquisition software

The monitoring of the ASIC through the FPGA, as well as the data acquisition and storage, are controlled thanks to a software developed with Labview and based on the acquisition program provided by the Pole Omega.

The control parameters of the electronics are transmitted to the ASIC by tuning the input parameters of an internal buffer, called slow-control. It allows to adjust all the parameters previous described (preamplifier gain, shaping time, trigger level, setting of the 8-bit DAC for the overvoltage homogeneity, etc.), or to disable certain channels or circuit of the ASIC, depending on the user needs. The slow-control is transmitted to the ASIC through the FPGA. The parameters setting of the FPGA are as well controlled by the acquisition software, allowing to choose the acquisition mode (internal or external trigger) or the delay between the trigger and the hold signal. Furthermore, it is possible to define a digital threshold on the charge values for the 32 channels controlled from each ASIC. This allows to reduce the amount of unnecessary data and thus, to significantly decrease the dead time associated to the data transfer (see Paragraph 2.5.4.1).

The software retrieves the data (channel number, output charge expressed in bins and acquisition time), organizes and registers them in a list-mode file, event by event. Finally, it allows to control the SiPM bias voltage through a power supply (Keithley 2611A), to register the current through the array and the temperature as a function of time, thanks to the temperature sensors placed behind the SiPMs array (see Fig. 3.28), and to control the movement of the motorized platforms used to perform the analyze of the spatial and energy response of the β detection device (see Section 3.2.1 and Fig. 3.1).

2.5.5 Image reconstruction algorithms

Signal treatments allows to reconstruct the position of interaction of the β or γ radiation event as well as their deposited energy from the charge values measured on the 64 channels of the SiPM array (Fig. 2.30). Multiple algorithms have been developed to reconstruct the position of interaction starting from a discrete charge distribution. The choice of the reconstruction algorithm, that depends on the detector design, may significantly influence its spatial performances. Image reconstruction methods can mainly be grouped in two families:

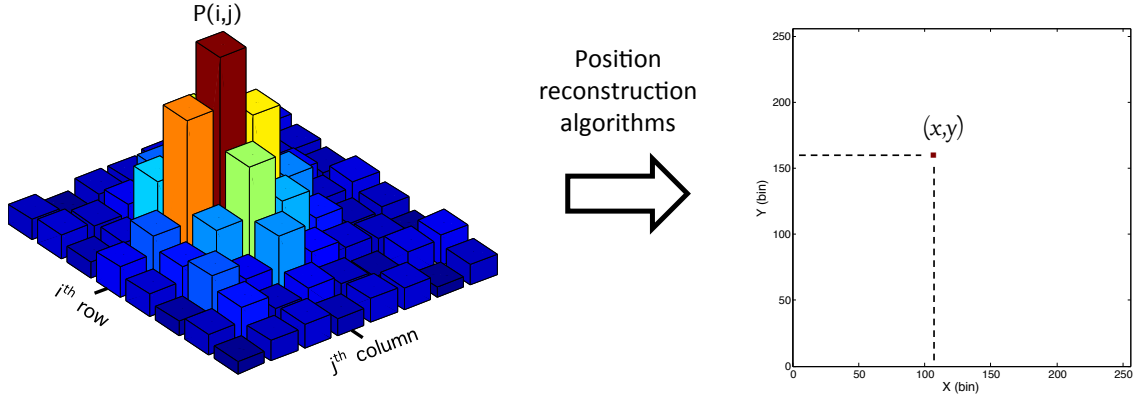


Figure 2.30 – Charge distribution over the 64 SiPMs of the array generated by one event (left). Reconstruction of the interaction position (X, Y) and energy E of the incident event on the detector (right).

not supervised and supervised methods. The first family do not need any information about the detector response while the second requires an accurate preliminary characterization of the spatial response on the whole field of view.

Various algorithms have been tested during my thesis. However, in the following paragraphs, we will only introduce the ones providing the best spatial performances. All codes were implemented with the MATLAB software.

Barycenter method - The simplest method, proposed by Anger in 1958, consists in calculating the center of gravity, or barycenter, of the distribution of the detected charge [Anger 1958]. For a regularly spaced $m \times n$ array of SiPMs, the position of interaction (x, y) of an event is obtained with the following formula:

$$(x, y) = \frac{\sum_{i=1}^m \sum_{j=1}^n P_{i,j} \cdot (i, j)}{\sum_{i=1}^m \sum_{j=1}^n P_{i,j}} \quad (2.15)$$

where $P_{i,j}$ is the signal amplitude of the SiPM at the position (i,j) corresponding to the i^{th} row and the j^{th} column of the array. The advantage of this standard method is the short calculation time, allowing to analyze in real time an high number of events. However, one limit with the conventional center-of-gravity is that all the SiPMs in the array are treated with the same importance, independently from the position of the incident event. This can degrade the efficiency of the reconstruction if the signal level or the signal-to-noise ratio between pixels are different. For example, when an event interacts in proximity of the detector edges, the tails of the light distribution are cut off and /or deformed generating a distortion of the image, more accentuated near the edges. To reduce the influence of the light distribution tails and the inhomogeneity of the background noise level, a threshold can be applied on the charge value registered by the SiPMs before the calculation of the barycenter of the charge distribution.

Other alternative methods have been developed implementing a weighting of pixels signals before event position calculation. For example, [Pani *et al.* 2009] and [Netter *et al.* 2009] proposed to apply a quadratic weighting factor to the pixels values (weighted barycenter method). This weighting allows to increase the weight of the pixels corresponding to the centre of the charge distribution compared to the tails. It has been applied to γ -cameras based on multi-anode photomultiplier tubes, in order to improve the position accuracy of the reconstruction [Pani *et al.* 2011]. However, this method is not suitable for our application. In fact, the thin organic scintillators produce a small amount of light that spreads on a small number of pixels. The application of a quadratic weighting factor reduces further the width of this charge distribution. As a result, this algorithm produces strongly non-uniform response depending on the interaction position of the event.

Iterative position weighted barycenter method - Another approach proposed to weight the SiPM signal is the iterative position weighted barycenter method. The SiPM signals are weighted according to their distance to the calculated point of interaction in the scintillator. Whenever a new position is calculated, the weighting factor changes. The calculation becomes therefore an iterative process. The weighting factor can be estimated with an empirical function [Chapuis *et al.* 2002] or a Gaussian function [Baker & Moallem 2007]. In this iterative method, the estimation of the new position (x_{new}, y_{new}) is given by the equation 2.16 for which the weighting factor is calculated with the formula 2.17.

$$(x_{new}, y_{new}) = \frac{\sum_{i=1}^m \sum_{j=1}^n w(i, j) \cdot P_{i,j} \cdot (i, j)}{\sum_{i=1}^m \sum_{j=1}^n P_{i,j}} \quad (2.16)$$

$$w(i, j) = e^{-\frac{(j-x_{old})^2 + (i-y_{old})^2}{2\sigma^2}} \quad (2.17)$$

where (x_{old}, y_{old}) is the previous position estimate, σ is the standard deviation of the Gaussian function centered on (x_{old}, y_{old}) and $P_{i,j}$ is the signal value of the pixel in the i^{th} row and j^{th} column [Liu & Goertzen 2013]. After each iteration step, the algorithm uses the new estimated position as the centroid of the Gaussian function. The iteration is stopped when distance between the updated and previous position reaches a user defined minimum value. Liu *et al.* propose a minimum distance of approximately 1% of the distance between the centers of two adjacent SiPMs [Liu & Goertzen 2013].

Analytical model fitting methods - Another group of algorithms consists in fitting a reference function describing the scintillation light distribution on the charge distribution measured by the array. The fitting process is realized thanks to an iterative algorithm based on the method of the non-linear least squares. The fitting process is computationally expensive due to the multiple parameters allowed to vary. Several reference functions of the scintillation light distribution reaching the photodetector have been defined starting from empirical observations (Gaussian, Cauchy, Scrimber-Baker) [Ling *et al.* 2008, Fabbri *et al.* 2011]

or theoretically calculated [Li *et al.* 2010b]. One of the most commonly used function in literature to describe the theoretical light distribution of the light reaching the photodetector is the Scrimger-Baker distribution function [Scrimger & Baker 1967]. For a continuous scintillator:

$$I(x, y) = \frac{I_0}{((x - x_0)^2 + (y - y_0)^2 + h^2)^{\frac{3}{2}}} \quad (2.18)$$

where h is the distance between the point of scintillation light emission and the photodetector surface.

Neural network - The artificial neural networks are a family of mathematical models inspired by biological neural networks. Various models of networks have been developed during the last years and their basic structure, represented in Figure 2.31, consists of neurons, grouped in layers and of the connections in between them.

The 'Rosenblat multilayer perceptron' network was one of the first to be developed and its simple structure allows fast calculation time. This network is a feedforward model where a set of input data is mapped onto a set of appropriate outputs, thanks to multiples layers of nodes and, except for the input ones, each node is a neuron (or processing element). Each node of each layer is fully connected to the next one. Thus, the information is transmitted from layer to layer per packages. The number of inputs are linked by a set of one or more layers of 'hidden' nodes, which are at their turn connected to a number of output nodes, chosen according to the required informations. Each of the nodes in the hidden layer is associated to a non-linear activation function, whose weights are optimized through a supervised learning process, which requires a knowledge of the desired output for each input. Thus, the neural network method requires a priori calibration step of the detector on its whole field of view. The study of [Marone *et al.* 2009] showed that the application of neural networks is a promising technique for reconstruct the position of interaction of events creating a signal shared on multiples photosensors. They demonstrated that good results may be obtained with a single hidden layer.

The neural network allows to translate the charge distribution recorded on the 64 photosensor pixels into the event position of interaction (x, y) . Therefore, the used network consists of 64 input nodes and two nodes on the output layer with a single hidden layer of nodes. The number of nodes N in the hidden layer is one of the network parameters that can be optimized. Each of the neuron of the hidden layer $h_j \forall j \in [1, N]$ has value:

$$h_j = a^H \left(\sum_{i=1}^{I=64} q_i \cdot w_{ij} + b_j^H \right) \quad (2.19)$$

where w_{ij} is the weight of the connection between the i^{th} input node and the j^{th} hidden neuron, b_j^H is the threshold of the j^{th} hidden neuron and a^H is the activation function of the hidden layer. Analogous relations concern the two nodes in the output layer. The parameters of the network are optimized thanks to a learning process. The learning process starts with some random weights associated to neurons connections. As first step, the training charge distribution input is propagated through the network. The output reconstructed

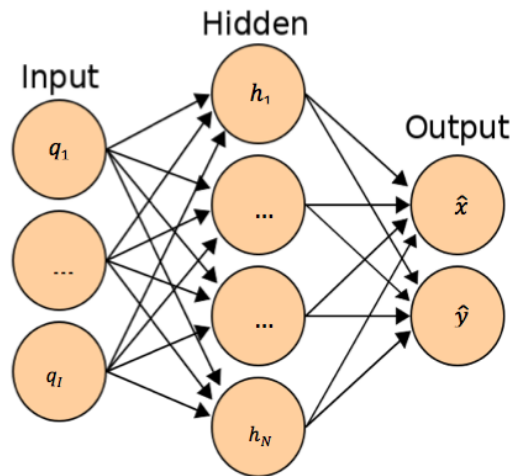


Figure 2.31 – Schematic representation of a basic neural network structure.

position (x,y) of interaction, resulting from the values of the weights and thresholds, will be more or less close to the real position (x_0,y_0) . During the learning process, the weights and thresholds parameters are modified so that the mean square error between the reconstructed and real event position is minimized [Collobert *et al.* 2012]. The loop during which the connection parameters are modified is called an epoch of the learning process. The learning process is stopped either when the parameters variation do not change anymore the results between two successive epochs or by user choice. After that the training is successfully concluded, the neural network allows real time reconstruction of event position of interaction [Marone *et al.* 2009].

Finally, other position reconstruction methods have been proposed, such as the statistical methods of maximum-likelihood [Lerche *et al.* 2011] and the nearest neighbors [Beekman & Schaart 2010]. However, they require an important calculation time and therefore are not suitable for real time image reconstruction.

Development and optimization of the positron imaging probes

In this Chapter, we will present the development of the two probe prototypes. First will be discussed the characterization of the performances of the photodetection system based on a SiPMs array. Then will be presented the optimization of the design of the two intraoperative probes based on measurements and simulations. In particular a detailed characterization of the optimal configuration for the single scintillator prototype will be given, including thickness and scintillator material, optical coating and light shielding. The influence of the bias voltage and temperature as well as the image reconstruction algorithm on its performances will be specially discussed. The optimization of the dual scintillator probe will be also presented by focusing our study on the events discrimination between the two scintillators. In the final part of this Chapter, we will describe the specific mechanical and the dedicated miniaturized electronics board developed for the positron imaging probe.

3.1 Characterization of the photodetection system

This section will first describe the experimental set-up used for the characterization of the photodetection system. Then we will present the characterization of the gain and uniformity of the response of the SiPM array. Finally, the influence of the temperature on the SiPM array performances and the method developed to allow an effective correction of this temperature effect will be discussed.

3.1.1 Experimental set-up

The experimental set-up is composed of a Keithly 2611A stabilized source-meter (Keithly Instruments Inc.) able to supply the SiPMs with a continuous voltage up to 200 V and with a step of 5 mV. The bias voltage is driven by the acquisition software (see Section 2.5.4.2). The Keithly also displays the leakage current of the SiPMs with an accuracy of 2 nA in the range from 10 to 100 μ A. The SiPMs array and the electronics boards are placed into a climatic chamber (Fisher Bioblock), where temperature is maintained constant with an accuracy of ± 0.1 °C in the range between -10 and +50 °C. Figure 3.1 shows a view of the inside of the climatic chamber. The temperature on the SiPMs is monitored thanks to a temperature sensor placed on the back of the PCB on which they are mounted (see Fig. 3.28).

The SiPMs array was enlighten with a blue LED source (470 nm) emitting light pulses with a duration of 50 ns. The LED is placed at about 25 cm from the detector and covered



Figure 3.1 – Photography of the experimental set-up: 3-axis motorized platform and the EASIROC board inside the climatic chamber.

with a light diffuser window to ensure an uniform irradiation of the SiPM array. The number of photons incident on the SiPM array surface is controlled and reduced using a neutral density filters. The logical signal controlling the LED is sent to the external trigger of the readout electronics in order to remove the dark noise events. Others parameters of the readout electronics were set according to the data presented in Section 2.5.4.1.

3.1.2 SiPM gain

For the measurement of the gain, the SiPMs array was connected to the EASIROC board (16 channels were analysed at the same time). All measurements were performed at a controlled temperature of 20°C. The average intensity of the light pulses was set around a level corresponding to 5 photoelectrons. The intrinsic gain of the SiPMs was measured from the spectrum of the LED source for each channel of the array, on which we can clearly distinguish the peaks generated by the photoelectrons and corresponding to one, two, three, etc. fired cells, as shown in Figure 3.2. The photoelectron peaks positions are evaluated by fitting a multiple gaussian function on the experimental spectrum on each channel:

$$F(x) = \sum_{i=1}^N A(i) \cdot e^{-\frac{(x-p-(i-1)\cdot g)^2}{2\cdot\sigma_i^2}} \quad \text{with} \quad \sigma_i^2 = \sigma_0^2 + (i-1) \cdot \sigma_1^2 \quad (3.1)$$

where $A(i)$ is the amplitude of the i^{th} peak, p is the pedestal of the electronic noise (first peak of the spectra), g is the separation between two adjacent peaks, which corresponds to the intrinsic gain of the SiPM. The variable σ_i is the standard deviation of the i^{th} gaussian peak, that depends on σ_0 , the standard deviation of the pedestal, and on σ_1 , associated to

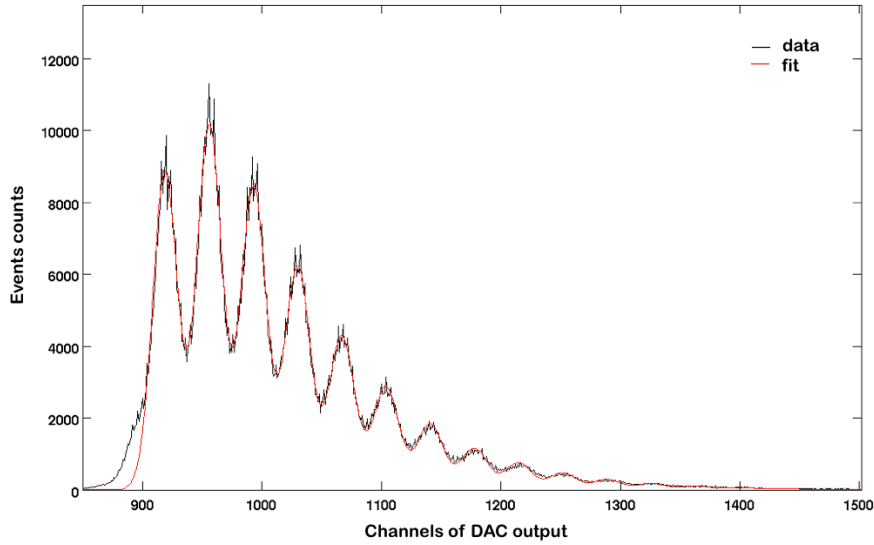


Figure 3.2 – Light spectrum obtained with a SiPM and photopeaks gaussian fit overlapped.

the signal fluctuations due to the inhomogeneity in the intrinsic gain among the SiPMs cells.

The EASIROC test board uses a decoupling resistor of $34.5\text{ k}\Omega$ between the high voltage input and the SiPM cathode of each SiPM, which, due to the current circulating through the array (from 0.3 to $2.7\ \mu\text{A}$), causes a drop of the bias voltage V_{bias} applied on the SiPMs. Therefore, the measured gain variation as a function of the overvoltage is not linear. However, since the leakage current is measured by the source-meter, the equivalent voltage drop can be estimated and the value of the applied voltage corrected.

The results presented in the Section 3.1 refer to the four 16-channels TSV SiPMs arrays (S12642-0404PA, Hamamatsu) used for the single scintillator configuration (Fig. 2.16). Similar results were obtained for the 64-channels SiPMs array (S12642-0809PA, Hamamatsu). The gain curve for all the 64 channels, corrected for the leakage current, are presented as a function of the applied bias voltage in Figure 3.3. The average gain for an overvoltage of 1.6 V , corresponding to a V_{bias} of 66.1 V , is $(7.25 \pm 0.25) \cdot 10^5$. Since the gain increases linearly as a function of the overvoltage $\Delta V = V_{bias} - V_{BD}$ (see Section 2.5.3.2), the breakdown voltage V_{BD} is extracted for each SiPM by fitting the gain variation as a function of the bias voltage with a linear relation and by extrapolating the bias corresponding to a unity gain. The average value of V_{BD} on the 64 SiPMs is $63.80 \pm 0.03\text{ V}$, where the error represents the standard deviation. These results highlight that the array response is intrinsically almost uniform thanks to the selection, by the manufacturer, of the SiPMs assembled in each array. It is possible to further improve the response uniformity with a fine tuning of the delivered supply voltage on each SiPM in order to offset breakdown voltage differences and thus, to obtain equivalent gains.

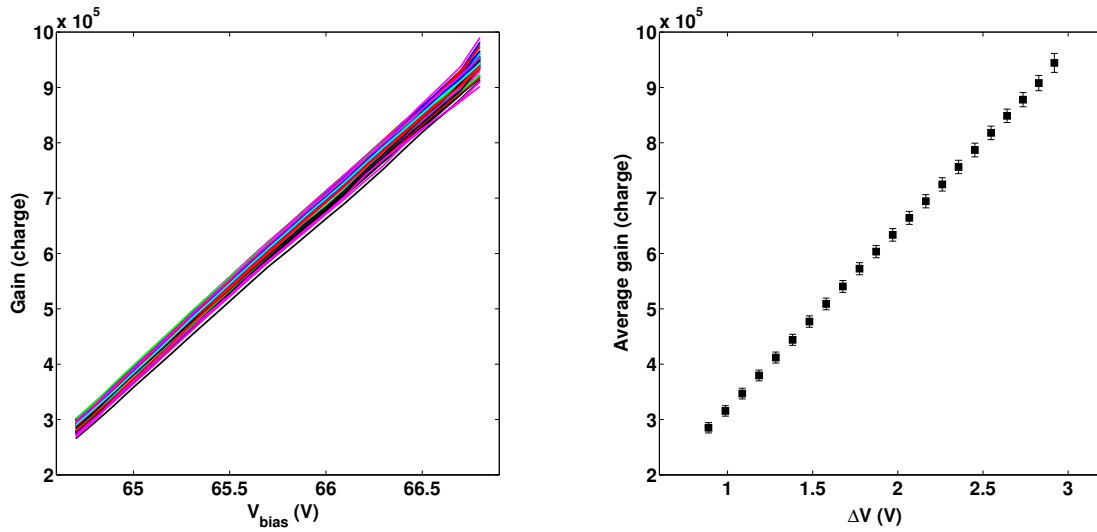


Figure 3.3 – Gain of the 64 SiPMs of the array as a function of the bias voltage (left). Mean value of the gain (corrected for the leakage current) as a function of the overvoltage ΔV . The error bars represent the standard deviations of the gain over the 64 SiPMs. Measurements were done at a temperature of 20°C .

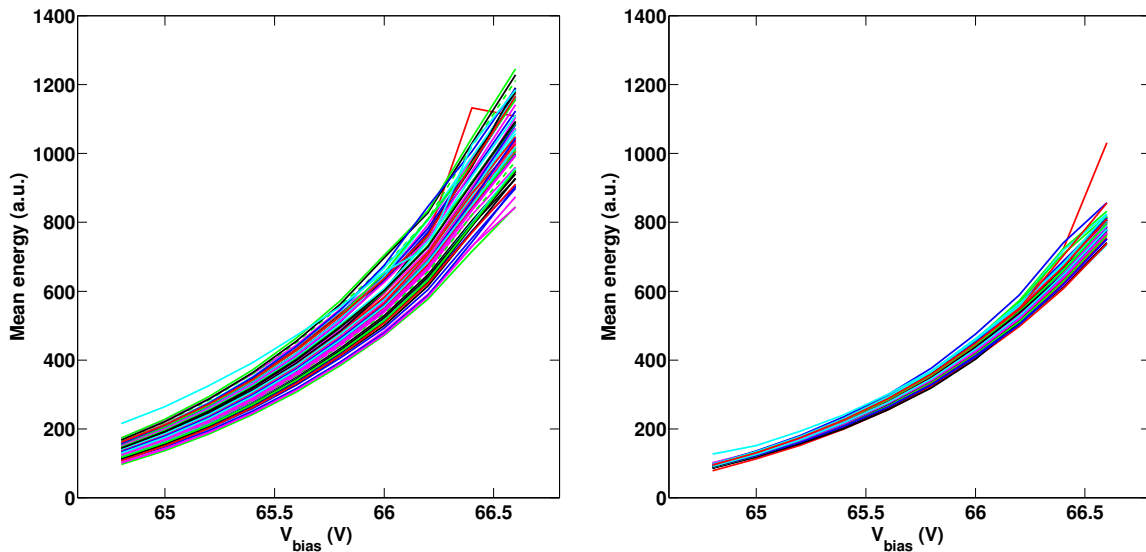


Figure 3.4 – Mean charge response of the 64 SiPMs to a pulse LED source as a function of the bias voltage (corrected for the leakage current), without (left) and after uniformity correction (right). Measurements were done at a temperature of 20°C .

3.1.3 Response uniformity

The SiPMs array was connected to the electronic board developed for the camera MAGICS, which allows the simultaneous readout of the 64-channels (see Section 2.5.4). The response uniformity of the array was improved thanks to a fine tuning of the 8-bits DAC,

one for each ASIC channel (see Section 2.5.4.1). An experimental set up equivalent to the one described in Section 3.1.1 was used with this board. However, the higher electronic noise of the MAGICS board does not allow a distinction between the single photoelectrons. Therefore, the mean energy of the light spectrum is used to estimate the SiPM response, in place of the individual photopeaks values used in Section 3.1.2. To improve the accuracy on this measurement, the amount of incident light was increased to an average intensity corresponding to around 50 photoelectrons by tuning the neutral density filters. Figure 3.4 presents the mean charge of the LED spectra as a function of the applied bias voltage before uniformity correction (same DAC value for all channels). The charge response does not depend linearly on bias voltage mainly due to the increasing probability of cross-talk and afterpulses. After DAC adjustment, the standard deviation of the response over the 64 SiPMs decreases by 70% for an overvoltage of 1.6 V (Fig. 3.4).

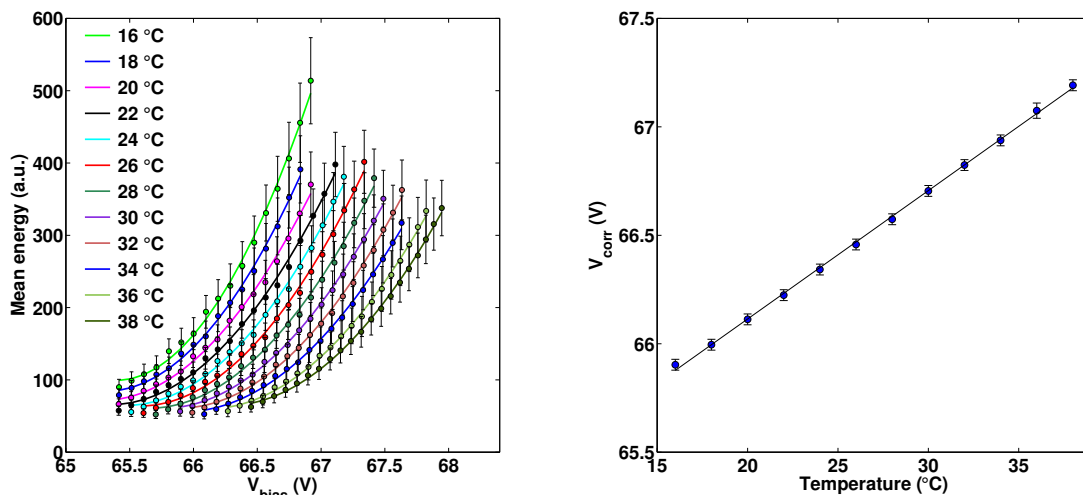


Figure 3.5 – Mean charge of the LED spectra as a function of the bias voltage for 12 different temperatures (left). Values of the bias voltage correction allowing to obtain a constant SiPM overvoltage (reference voltage and temperature set to 67.5 V and 20°C) (right). The error bars represent the response uniformity over the SiPMs array.

3.1.4 Temperature influence

Our intraoperative imaging probes conceived for *in situ* detection in surgical cavities may undergo rapid temperature variations. Therefore, the temperature dependance of SiPM gain was evaluated in order to develop a temperature correction method.

The temperature influence on the detector performances was evaluated for the single scintillator detection head set into the mechanical housing (see Section 3.4.2) and connected to the MAGICS electronic board. The goal was to estimate the temperature dependence of the SiPMs array in its final environment. The aluminum light shielding was removed to enable photons coming from the pulse LED source to reach the SiPMs array. The detector

response, estimated from the mean charge of the LED spectra, was evaluated as a function of the overvoltage in the temperature range between 16 and 38°C with a step of 2°C (Fig. 3.5). As expected, the charge response drops with temperature according to the decrease of the breakdown voltage and thus, the overvoltage, which directly impacts gain, photon detection efficiency, and crosstalk and afterpulses probabilities of SiPMs (see Section 2.5.3.2). However, this variation can be compensated by accurately tuning the bias voltage as a function of the temperature in order to maintain a constant overvoltage. Figure 3.5 shows the voltage correction that should be applied to the SiPM in order to keep the mean charge of the LED spectra to a constant value over temperature. The reference bias voltage and temperature are set to 67.5 V and 20°C. The voltage correction is extrapolated for any temperature from a linear fit on the experimental values (slope of 0.07 V/°C). The validation of this temperature-compensated method will be presented in Section 3.2.7.3.

3.2 Optimization and performances of the single scintillator probe

This section is dedicated to the characterization and optimization of the intrinsic performances of the imaging probe based on a single scintillator (Fig. 3.6). This is done in terms of spatial performances (resolution and distortion) and sensitivity. As described in Chapter 2, these features directly depend on the number of scintillation photons detected, and thus, on the nature and geometry of the scintillator, whose influence is presented in Section 3.2.3. Spatial performances depend also on the spatial spread of scintillation light on the SiPM array which is influenced by the thickness of the light guide and the nature of the optical coating covering the scintillator (see Section 3.2.4 and 3.2.5). Following this optimization study, the performances of the optimal design of the imaging probe will be presented in Section 3.2.7 as a function of the temperature and bias voltage, that influences their detection features of the SiPMs (gain, detection efficiency and thermal and correlated noises) and therefore the charge distribution generated for each scintillation light pulse. Finally, the choice of the image reconstruction method to further improve the device performances will be discussed in Section 3.2.8.

3.2.1 Measurements of the imaging performances

The field of view of the various detection head designs was scanned using a β -emitting ^{204}Tl source collimated by a 0.5 mm diameter hole. The source was mounted on a 3-axis motorized platform (see Fig. 3.1), with a 2 μm resolution. Due to the symmetry of the detector, only one eighth of the field of view (FoV) was scanned with a step of 800 μm , covering a triangular region going from the center to within 850 μm of the detector edges. The whole experimental set-up was placed in the climatic chamber at the controlled temperature of 20 °C. The response uniformity correction of the SiPMs array, described in Section 3.1.3, was implemented. For these measurements, the trigger level of the readout electronics for each detected event was set to a minimum charge collected on the SiPM with the highest charge of about 15 photoelectrons, in order to reduce the total dark count rate down to 1 kHz and thus, avoid any dead time. Other parameters of the readout electronics were

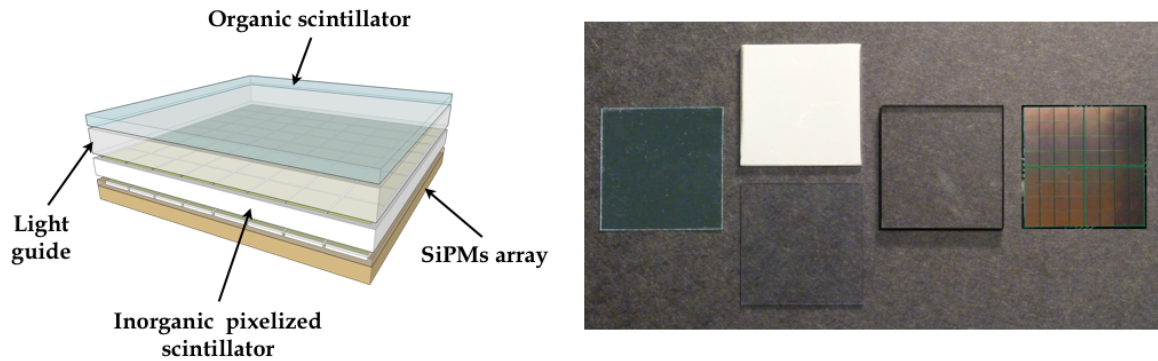


Figure 3.6 – Design of the single scintillator configuration of the positron imaging probe (left). Components of the positron imaging probe (right and starting from left): specular reflector coating, *p*-terphenyl scintillator (up) and plastic scintillator (down), light guide and 64-channel SiPMs array.

set according to the data presented in Section 2.5.4.1. The measurements relative to each detection head configuration were also performed by applying an electronic gain adapted to the signal dynamic and an optimal bias voltage on the SiPM array. This optimized voltage, in terms of spatial performances and sensitivity, was estimated following an experimental protocol described in more details in Section 3.2.7.1.

The charge distribution of the events provided by the SiPMs array is first corrected, channel by channel, by subtraction of the electronic pedestal value. The optimization study of the detector design was conducted by using the image reconstruction algorithm based on the standard barycentre method. The (x,y) position of the β or γ interactions in the scintillator is calculated from the standard centroid of the distribution of the total output charge provided by the SiPMs array after a charge subtraction (see Section 3.2.8.1). This subtraction reduces the influence of the light distribution tails and the fluctuation of the electronic noise. Events with signal on two or less pixels after charge subtraction, which mostly correspond to thermic noise events, are discarded. The optimal charge subtraction in terms of spatial performances was found to be corresponding to 8 photoelectrons for all detector configurations (see Section 3.2.8.1). Source position and FWHM are calculated from the Gaussian fit on the projection of the positions peaks along the x and y directions. The deviation from the spatial linearity, known as spatial bias, is estimated as the absolute difference between the reconstructed position, corrected for the linear compression effect measured in the central region, and the mechanical source position. Spatial resolution along x and y directions is estimated from the FWHM corrected for the local bias and deconvoluted by the diameter of the collimator hole. The average and standard deviation of the spatial performances over the FoV are estimated separately within the central region (from -11.2 to 11.2 mm on x and y directions) and the detector edges corresponding to the half of the outermost pixels. For the spatial uniformity measurements, a ^{22}Na source positioned at about 30 cm from the detector surface was used to obtain an uniform irradiation. The integral and differential uniformity values were estimated, removing the edge pixels and smoothing the image with a 3×3 pixel gaussian filter, according to the NEMA protocol

[National Electrical Manufacturers Association 2012]. The integral uniformity is calculated by the difference between the maximum and the minimum pixel values in the whole image divided by their sum:

$$IU = \frac{C_{max} - C_{min}}{C_{max} + C_{min}} \times 100 \quad (3.2)$$

The differential uniformity (DU) is calculated for each pixel in a similar manner, but with C'_{max} and C'_{min} being the maximum and the minimum pixel values in a 'plus sign'-shaped kernel, which consists of the central pixel in (i,j) and two pixels in each direction $(i\pm 2; j\pm 2; \text{nine pixels total})$. DU is reported as the worst case (highest value) within the central detector area.

The positron sensitivity of each detector head design was estimated from the uniform irradiation with the ^{22}Na source, whose energy spectrum for positrons is close to that of the common PET isotope ^{18}F . Simulation showed that the 511 keV and 1274 keV γ rays flux originating from the ^{22}Na source represents less than 2% of the total detected events (see Section 3.2.2). The relative β sensitivity of each detector head design is defined as the number of events detected in the central region of the FoV normalized by the number of events detected with the reference configuration combining a 0.2 mm thick p-terphenyl scintillator coupled to a 2 mm light guide. Only events with an energy (total output charge) above a threshold of 32 photoelectrons, corresponding to a total dark count rate on the SiPM array of 1 Hz, are taken into account.

3.2.2 Simulation study

As discussed previously in Section 2.4, the γ background noise, arises both from the direct interaction of annihilation γ inside the scintillator and from Compton electrons generated in the material surrounding the scintillator and then scattered in it. In order to estimate both noise contributions and their influence on small tumor detectability when the probe is settled in a clinical environment, the geometry of the various detection head designs, embedded in a surgical cavity, were fully modelled using the GATE Monte-Carlo simulation platform. As described in Section 2.4.1 we simulated only radiation transport of in the phantom and detection probe. No light propagation was simulated due to the complexity of reproducing optical interfaces close to that of the experimental detector. The phantom was modified adding a focal area of tumor tissue with different sizes (2 mm thick cylinder of diameters 3, 5 and 7 mm) placed at the bottom of the phantom cavity. The detector was placed inside the cavity in direct contact with the tumor foci. Three activities concentration ratios of ^{18}F -labeled radiotracers between tumorous and healthy tissues were considered (2:1, 4:1 and 8:1).

The simulated position of particles interaction is calculated considering the centroid of the energy deposition along the particle track inside the scintillator. In order to take into consideration the effect of scintillation light transmission and diffusion we used the experimental energy spectra and charge distribution at the SiPM array obtained for each detection configuration. The simulated energy response of each detector configuration was first converted in photoelectrons by convolving the energy deposition by the mean number of photoelectrons detected per each deposited keV. This conversion number was estimated from the ratio

between the mean value of the experimental and simulated spectra obtained for a central irradiation of the field of view of the imaging probe with a ^{22}Na source. The total charge collected for each simulated event was then distributed over the 64 SiPMs according to the average charge distribution. This average charge distribution, characteristic of each detector configuration, was measured from the irradiation of the central region of the detector with the ^{22}Na source. Finally, the simulated energy spectra were reconstructed after applying for each event the charge thresholds associated with the electronics trigger and the charge subtraction associated with the position reconstruction (including the rejection of events with two or less pixels).

The detectability of the tumor volume was quantified for each detection head design by calculating the tumor peak-to-valley ratio (Peak-Valley) from the simulated image. The Peak-Valley is defined as the ratio between the mean number of detected interactions inside a circular region of interest (ROI) on the tumor image and that detected on a normal tissue region (see Section 4.1.4).

The reliability of the GATE physics and material compounds was validated by implementing a preliminary simulation modeling of the detector heads in the experimental set-up in which they were tested (including the metallic box containing the detectors and the read-out electronics, the breadboards, the source mechanical support, the motorized platform and the climatic chamber walls) (Fig. 3.1). For the validation, the detector surface was uniformly irradiated with a ^{22}Na source. Simulations and measurements were made with and without a 1 mm thick shielding of aluminum placed between the source and the detector. The first configuration roughly corresponds to an irradiation with γ rays and their subsequent Compton electrons and the second one to a pure flux of positron particles (small contamination of Compton electrons and γ rays). We showed that the ratios between the number of events detected experimentally with and without shielding differ from the simulated ones only of 2 to 5%, for the different detection head configurations.

3.2.3 Comparison of scintillator materials and thicknesses

The influence of the material and thickness of the organic scintillator on the sensitivity and spatial performances of the positron imaging probe was studied by setting the thickness of the light guide (2 mm) and the nature of the optical coating (specular reflector).

3.2.3.1 Energy response and sensitivity

Thanks to the higher light yield and density of p-terphenyl compared to plastic material, the amount of scintillation light collected on the SiPM array is enhanced, even for a very thin layer of material. The energy spectra obtained for the different scintillator configurations with an uniform irradiation of a ^{22}Na source are represented in Figure 3.7. The mean energy of the ^{22}Na spectrum measured with the 0.1 mm thick p-terphenyl scintillator is close to the value obtained with the 0.4 mm thick plastic and 1.8 times higher than the value obtained for 0.2 mm one (Table 3.1).

Scintillator thickness (mm)	\bar{E} (ph. e^-)	r_q	Experimental sensitivity (%)	Simulated sensitivity (%)
p-terphenyl				
0.1	422	0.75	94.4±1.0	98.7±0.7
0.2	882	0.54	100.0±1.1	100.0±0.7
plastic				
0.2	247	0.52	73.5±0.9	73.1±0.5
0.4	424	0.34	81.6±0.9	91.9±0.6

Table 3.1 – The relative β sensitivity and mean deposited energy (\bar{E}) are estimated from an uniform irradiation with a ^{22}Na source. Experimental and simulated β sensitivities are normalized by the highest sensitivity value, obtained with the 0.2 mm thick p-terphenyl configuration coupled to a 2 mm light guide. r_q is the ratio between the charge of the SiPM with the highest charge and the charge of the surrounding SiPMs calculated from the mean charge distribution measured with the ^{22}Na irradiation. For all measurements, the scintillator was covered with an enhanced specular reflector.

The high light yield of p-terphenyl ensure an elevate positron sensitivity for both 0.2 and 0.1 mm scintillator thicknesses (reduction of only 5.6% passing from 0.2 to 0.1 mm thickness) and allows to obtain a significantly higher sensitivity than the plastic material (Table 3.1). As an example, the 3.6 higher light collection achieved with the 0.2 mm thick p-terphenyl scintillator compared to the plastic one results in an improvement of the β sensitivity by more than 36%. This increase is mainly due to the stronger impact of the electronic trigger on low energy β event (the mean number of β events remove after charge subtraction during image reconstruction is less than 2% whatever the detection head). Moreover, for an nearly equal mean energy, the 0.1 mm thick p-terphenyl scintillator allows a β sensitivity that is still 13.5% higher than that of the 0.4 mm thick plastic scintillator. This can be explained by the difference in the scintillation light distribution. The 0.4 mm plastic scintillator generates a wider light distribution with longer tails compared to the 0.1 mm thick p-terphenyl as illustrated by the r_q values reported in Table 3.1. This parameter is calculated as the ratio between the charge of the pixel with the highest charge and the charge of the surrounding pixels of the SiPMs array, calculated from the mean charge distribution measured with a ^{22}Na irradiation. The difference in the r_q value is mainly due to the surface condition of the scintillators (smooth for plastic and rough for p-terphenyl) and the nature of their coupling with the optical coating (grease for plastic and air for p-terphenyl). The impact of the charge threshold associated with the electronic trigger increases with the width of the charge distribution resulting in a lower β sensitivity measured with the plastic scintillators. This effect is well reproduced by the simulations that show the same sensitivity ranking between the detector configurations (Table 3.1). Figure 3.7 shows the overlapping of the experimental and simulated energy spectra obtained for the 0.1 mm thick p-terphenyl scintillator. The effect of the charge threshold applied on simulated spectra is visible at low energies and matches with the slope present on the experimental one. The differences between the two spectra at high energy are due to the afterpulses and optical crosstalks that have not been included in simulations. This correlated noise induces a fluctuation of the charge multiplication process (excess noise factor), which no longer follows a Poissonian distribution. The

trigger level of the readout electronics is set as a function of the amplitude distribution of the dark count signal of the SiPMs array that is also strongly influenced by the correlated noise [Hudin *et al.* 2012b]. Thus, recent improvements aiming to reduce the thermal and correlated noise of SiPMs arrays at high gain should help to improve the sensitivity of future positron imaging probes. Simulations show that a decrease of the trigger level from 15 to 10 photoelectrons would improve the relative β sensitivity of the 0.2 mm thick plastic configuration from 73.1% to 85.9% compared to that of the 0.2 mm thick p-terphenyl scintillator.

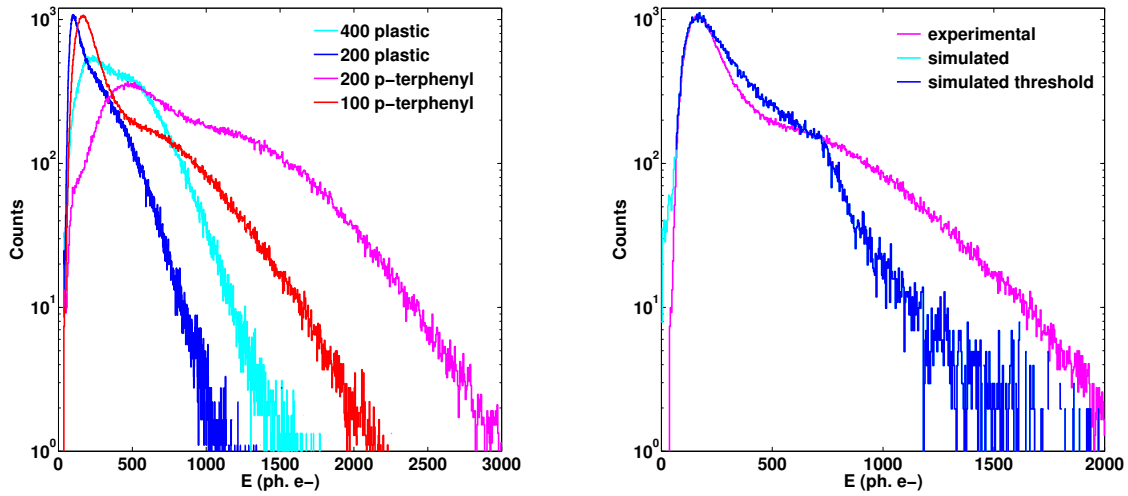


Figure 3.7 – Energy spectra of a ^{22}Na source obtained in the detector central region, for different scintillator configurations (left). The experimental spectra measured with the 0.1 mm thick p-terphenyl is overlapped to the simulated one after conversion to photoelectrons and application of the charge threshold associated with the electronic trigger and the charge subtraction related to the image reconstruction.

3.2.3.2 Spatial performances

The spatial performances of the different detection heads are presented in Table 3.2. P-terphenyl scintillators exhibit much better spatial resolution than plastic ones, in both central and periphery regions while the bias is comparable in the center and slightly improved on the detector edges (Fig. 3.9). This is due to the higher amount of scintillation light collected on the SiPM array with p-terphenyl. For an equivalent scintillator thickness of 0.2 mm, the p-terphenyl material allows an improvement of 50% for the spatial resolution on the whole field of view and of 27% for the bias on the detector edges. The higher scintillation light collection obtained with p-terphenyl compared to plastic scintillator also provides a more homogeneous response on the overall field of view for equivalent light guide thickness. This is reflected by the lower values of the integral and differential uniformities, as shown in Figure 3.8, as well as the lower standard deviation of bias and spatial resolution

Scintillator thickness (mm)	Spatial Res. (mm)		Bias (mm)		Unif.(%)		
	centre	edge	centre	edge	IU	DU	
p-terphenyl	0.1	0.64±0.06	0.96±0.35	0.05±0.04	0.35±0.34	40	25
	0.2	0.57±0.08	0.76±0.23	0.05±0.04	0.36±0.34	33	20
plastic	0.2	1.04±0.10	1.50±0.46	0.07±0.07	0.48±0.41	41	29
	0.4	0.82±0.12	1.21±0.40	0.07±0.07	0.50±0.44	31	16

Table 3.2 – Spatial performances of the different detection head designs. The mean values and standard deviation of the spatial resolution (FWHM) and bias calculated over all testing positions, are given separately for the central and edges areas. Integral (IU) and differential (DU) uniformities were estimated on the whole field of view from the uniform irradiation with a ^{22}Na source. For all measurements, the scintillator is covered with an enhanced specular reflector and coupled to a 2 mm thick light guide.

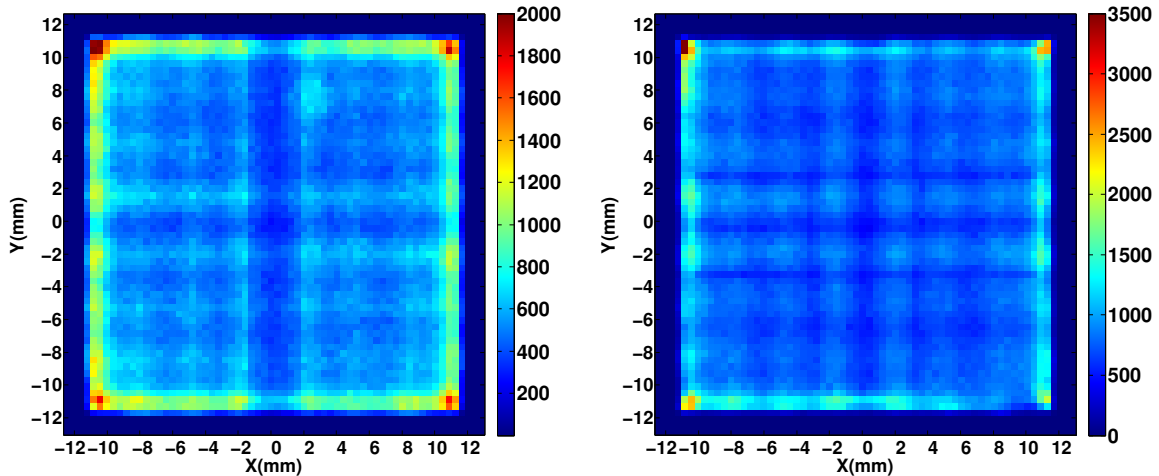


Figure 3.8 – Images obtained from the uniform irradiation of the detector with a ^{22}Na source. The detection head is composed of a 0.2 mm thick plastic scintillator (left) or 0.2 mm thick p-terphenyl (right) coupled to a 2 mm thick light guide. For the two configurations, the scintillator is covered with an enhanced specular reflector.

(Table 3.2). In fact, when sparse scintillation light is produced, the charge subtraction applied before centroid calculation strongly reduces the weight of the light distribution tails and makes the width of the charge distribution artificially thinner and thus more dependent on the discretized nature of the photosensor. The mean number of fired pixels when irradiating with a ^{22}Na source the central region of the 0.2 mm thick p-terphenyl or plastic scintillators coupled to a 2 mm light guide is 20 and 8.5, respectively.

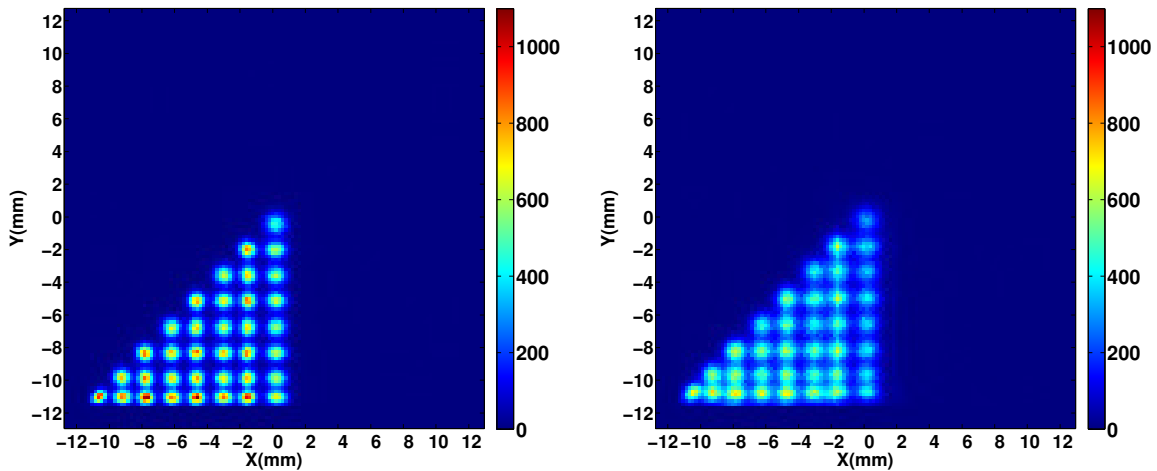


Figure 3.9 – Image of a scan of one eighth of the FoV with a ^{204}Tl collimated source (0.5 mm diameter) obtained with a detector configuration coupling a 0.1 mm thick p-terphenyl (left) and 0.2 mm thick plastic scintillator (right) to a 2 mm thick light guide. The spots on the images are spaced 1.6 mm apart in both directions.

3.2.4 Influence of the light spreading window

The influence of the thickness of the light guide was investigated with the 0.1 mm thick p-terphenyl scintillator. The best compromise in terms of spatial resolution, bias and uniformity for a thin scintillator coupled to a SiPMs array with $3 \times 3 \text{ mm}^2$ elements is obtained with a 2 mm thick light spreading window (Table 3.3). A too thin light guide discretizes the light response of the SiPMs array, leading to high bias and strong spatial inhomogeneities especially in the central region of the detector. These effects are clearly visible on the image obtained with a light guide of 1 mm shown in Figure 3.10. The increase of the light guide thickness improves the response uniformity but degrades the spatial resolution and bias towards the center in the periphery detector region, due both to the spread of the light distribution and its more important truncation by the absorbing edges (Fig. 3.10, right). However, unlike plastic scintillators, the broadening of the light distribution has no impact on the positron sensitivity achieved with p-terphenyl scintillators due to the higher scintillation light collection (Table 3.3).

3.2.5 Influence of optical coating and light shielding

The amount of scintillation light collected and its distribution on the SiPMs array strongly depend on the nature of the optical coating covering the scintillator as well as the light guide thickness. Two optical coatings were evaluated for single scintillator-light guide configuration (0.1 mm p-terphenyl with 2 mm thick light guide): an enhanced specular reflector (ESR) and a PTFE diffusing coating (see Section 2.5.2.2). The results are presented in Table 3.4. The nature of the optical coating covering the scintillator shows only a slight impact on the spatial performances. However, the much lower density of the PTFE allows to detect nearly 10% more β events than with ESR.

Light guide (mm)	Spatial Res. (mm)		Bias (mm)		Unif.(%)		Sensitivity (%)	\bar{E} (ph. e ⁻)
	centre	edge	centre	edge	IU	DU		
1	0.66±0.09	0.97±0.37	0.22±0.15	0.30±0.27	80	65	92.8±1.0	465
2	0.64±0.06	0.96±0.35	0.05±0.04	0.35±0.34	40	25	94.4±1.0	422
3	0.94±0.12	1.43±0.53	0.07±0.07	0.48±0.40	30	18	93.3±1.0	319

Table 3.3 – Spatial performances obtained for the 0.1 mm thick *p*-terphenyl coupled with light guide (LG) of increasing thickness. The average values of the spatial resolution (FWHM) and bias calculated over all testing positions with a ²⁰⁴Tl source are given separately for the central and edges areas. The errors correspond to the standard deviation of the parameter in the area considered. Integral (IU) and differential (DU) uniformities were estimated on the whole field of view from the uniform irradiation with a ²²Na source. The sensitivity and mean deposited energy (\bar{E}) are estimated from ²²Na uniform irradiation. The sensitivity is normalized by the sensitivity value obtained with the 0.2 mm thick *p*-terphenyl configuration coupled to a 2 mm light guide. For all measurements, the scintillator was covered with an enhanced specular reflector (ESR).

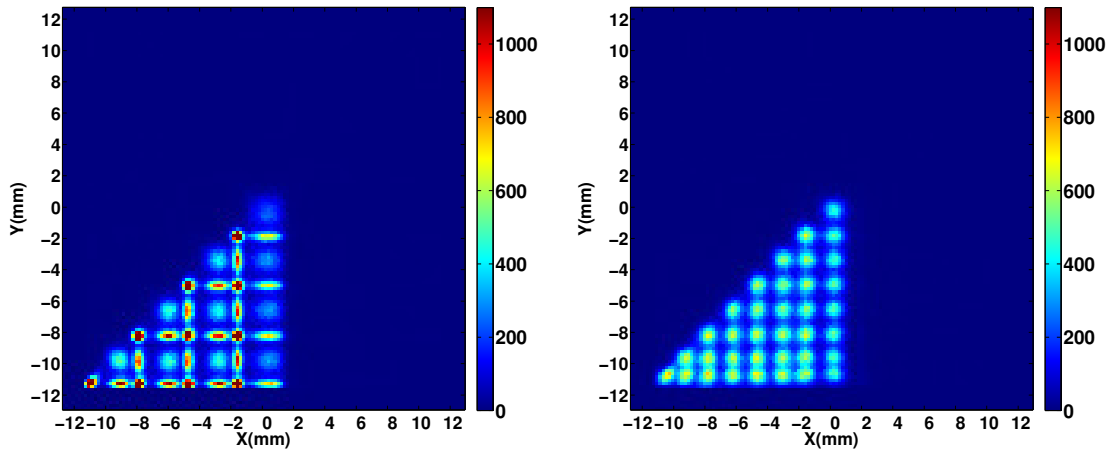


Figure 3.10 – Image of a scan of one eighth of the FoV with a ²⁰⁴Tl collimated source (0.5 mm diameter) obtained with a detector configuration coupling a 0.1 mm thick *p*-terphenyl scintillator to a 1 mm (left) and a 3 mm thick light guide (right). The spots on the images are spaced 1.6 mm apart in both directions.

Simulations show that this loss of sensitivity is mainly due to the larger absorption of low energy β particles by ESR as a consequence of its higher density. Conversely, the percentage of backscattered events is not impacted by the higher density of the ESR coating. When a 65 μm thick layer of ESR is simulated, we observe a reduction of positron sensitivity of almost 18% (17.2% and 0.8% of absorbed and scattered events, respectively) compared to a loss of sensitivity of 6.5% (5.8% and 0.7% of absorbed and scattered events, respectively) with the 75 μm thick PTFE. This increase of sensitivity achieved with the PTFE coating compared to the ESR one is close to the experimental value.

The addition of a light shielding in front of the optical coating further reduces the fraction of low energy radiation entering in the sensitive volume. The influence of the materials composing the detector entrance window has been evaluated through Monte-Carlo. Alongside the aluminum, others less dense materials could also be used, such as a black plastic

Optical coating	Spatial Res. (mm)		Bias (mm)		Unif.(%)		Sensitivity (%)	\bar{E} (ph. e ⁻)
	centre	edge	centre	edge	IU	DU		
ESR	0.64±0.06	0.96±0.35	0.05±0.04	0.35±0.34	40	25	90.4±1.0	422
PTFE	0.75±0.07	1.15±1.13	0.06±0.05	0.40±0.40	39	25	100.0±1.1	409

Table 3.4 – Spatial performances obtained for the detection head coupling a 2 mm thick light guide with a 0.1 mm thick p-terphenyl scintillator and covered with a specular reflector (ESR) or a diffusing (PTFE) optical coating. The average and standard deviation of the spatial resolution (FWHM) and bias calculated over all testing positions with a ²⁰⁴Tl source are given separately for the central and edges areas. Integral (IU) and differential (DU) uniformities were estimated on the whole field for view from the uniform irradiation with a ²²Na source. The relative β sensitivity and mean deposited energy (\bar{E}) are estimated from an ²²Na uniform irradiation. The sensitivity is normalized by the highest value measured with the PTFE optical coating.

polyvinyl fluoride (PVF) film, which is 3 times lighter but in return has to be at least 5 fold thicker than the aluminum sheet to properly shield from ambient light. For the simulations, the thickness of the light shielding was set to 10 μm and 50 μm , for the aluminum and PVF material, respectively. Simulations show that the materials placed between the source and the scintillator not only influence the positron signal but also the scattered electron noise component due to Compton interaction in the environment surrounding the scintillator. Thicker or denser materials stop more positrons and Compton electrons created in the tissue but at the same time give rise to more electrons coming from the optical coatings or light shielding. Conversely, the intensity of the γ noise component is not significantly influenced by these material choices since their volume remains globally small. Therefore, a trade-off between thickness and density of the optical coating and shielding has to be made to maximize the number of positrons interacting in the scintillator while minimizing the scattered electron noise. Among the four simulated combinations of the light shielding and optical coating components, the association of a 10 μm thick aluminum and a 75 μm thick PTFE offers the best trade-off, between positron sensitivity and scattered electron noise. The positron signal is only reduced by 9% and the global noise contamination is increased by 8% compared to the configuration without shielding and optical coating (Fig. 3.11). While the noise contamination remains comparable, the positron signal is reduced of nearly 5.5% for the combination between PTV and PTFE and 10.6% for the combination between aluminum and ESR, when compared to the association of aluminum and PTFE.

3.2.6 Sensitivity to the background noise and tumor detectability

In order to study the impact of the detector head geometry on the sensitivity to the background noise and thus, on small tumor detectability, simulations were done by adding a tumor uptake area in the tissue phantom described in Section 2.4.1.

The variation of the β sensitivity as a function of the tumor peak-to-valley ratio was estimated for increasing values of the energy threshold applied on the total output charge of detected events. The results presented on Figure 3.12 were simulated for a focal tumor of 5 mm and an uptake ratio of 1:2. Similar behaviour are obtained with the other clinical configurations. As expected, the 0.1 mm thick p-terphenyl scintillator provides the best tumor

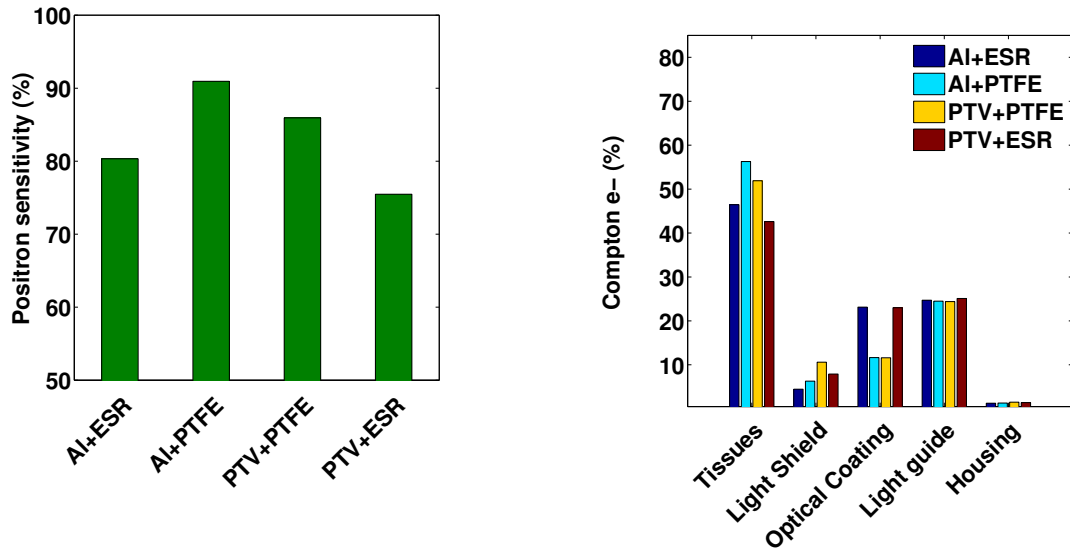


Figure 3.11 – Histogram comparing positron sensitivity for different combinations of light shieldings and optical coating, normalized by the sensitivity obtain without material interposing between the scintillator and the source (left). Intensity of the Compton electrons components of the background noise contamination as a function of the production volumes for different entrance window materials (right). All results are obtained for a 0.1 mm thick *p*-terphenyl scintillator coupled to a 2 mm thick light guide.

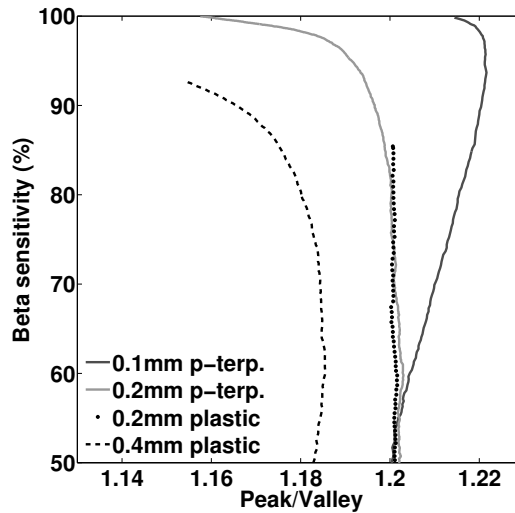


Figure 3.12 – Tumor peak-to-valley ratio as a function of the variation of the β sensitivity when applying an increasing energy threshold for the different detector head configurations. The radiotracer uptake ratio between the 5 mm diameter tumor and healthy tissue is set to 2. The relative β sensitivity is calculated from the ratio between the total number of positron events measured in a ROI placed over the tumor image normalized by the total number of events measured with the 0.2 mm thick *p*-terphenyl configuration and the minimal energy threshold. All detector heads are equipped with a 2 mm thick light guide, an ESR optical coating and an aluminum optical shielding.

peak-to-valley ratio whose optimal value (1.22) is reached for a low energy threshold (100 photoelectrons). This threshold induces a loss of β sensitivity of less than 3% compared to β detection with the minimal energy threshold (64 photoelectrons) corresponding to the charge threshold associated with the electronic trigger (see Section 3.2.5). Despite the low intrinsic sensitivity to γ radiation of this thin scintillator, the noise contamination (γ and Compton electrons components) represents 71% of the total detected events due to the large volume of background contamination. This noise reduces the Peak-to-Valley well below the ideal value of 2 obtained by considering only the positron signal. Increasing scintillator thickness implies a less effective trade-off between noise contamination and β sensitivity. For a 0.4 mm thick plastic scintillator, the γ noise contamination is multiplied by a factor of ~ 2 and the optimal Peak-Valley (1.18) is obtained for a higher energy threshold (350 photoelectrons) leading to a significant drop of the positron sensitivity (down to 64.2% of the β sensitivity achieved with the 0.2 mm thick p-terphenyl and the minimal energy threshold). Conversely, applying a low energy threshold in order to keep an high sensitivity degrades the peak-to-valley ratio (1.16 with the minimal energy threshold). Therefore, doubling the contamination noise when we pass from the 0.1 mm thick p-terphenyl scintillator to the 0.4 mm thick plastic scintillator causes a reduction of the Peak-Valley ratio of about 30% when the probe is used to detect a tumor of 5 mm diameter with a uptake ratio of 1:2 (the Peak-Valley decrease from 1.22 to 1.16). As shown by the experimental and simulation results obtained from the flood field irradiation of the detector with a ^{22}Na source (Table 3.1), p-terphenyl scintillators enable the highest simulated positron sensitivity, while the 0.2 mm plastic scintillator configuration, due to its poor light collection, presents the lowest value (85.4%). The differences in the relative simulated β sensitivities reported in Table 3.1 and Figure 3.12 are due to the different energy distribution of the ^{22}Na and ^{18}F emission spectra.

3.2.7 Focus on the optimal configuration

In light of the results presented above, the detection head composed of a 0.1 mm thick p-terphenyl scintillator covered by a specular reflector and a 10 μm layer of aluminium as light shielding, coupled to the SiPMs array through a 2 mm light guide appears to be the best candidate to achieve high spatial performances and good sensitivity while limiting the thickness of the sensitive detector and thus, minimizing the contamination from the γ rays background noise (see Sec. 2.4.2). Using a diffusing optical coating instead of a specular one allows a fine tuning between spatial performances and positron sensitivity. However, due to its mechanical properties allowing a much easier coupling with the other components of the detection head, the ESR was employed as optical coating for all the measurements presented in the following paragraphs.

3.2.7.1 Overvoltage optimization

A set of measurements was performed at 20°C for bias voltage of the SiPMs array ranging from 66.5 to 68.5 V, corresponding to an overvoltage variation from 0.8 to 3.2 V. The diagonal of the detector was scanned, from the center through the corner, with a collimated ^{204}Tl source (0.5 mm diameter) and a step of 1.6 mm along the x and y directions. The variation

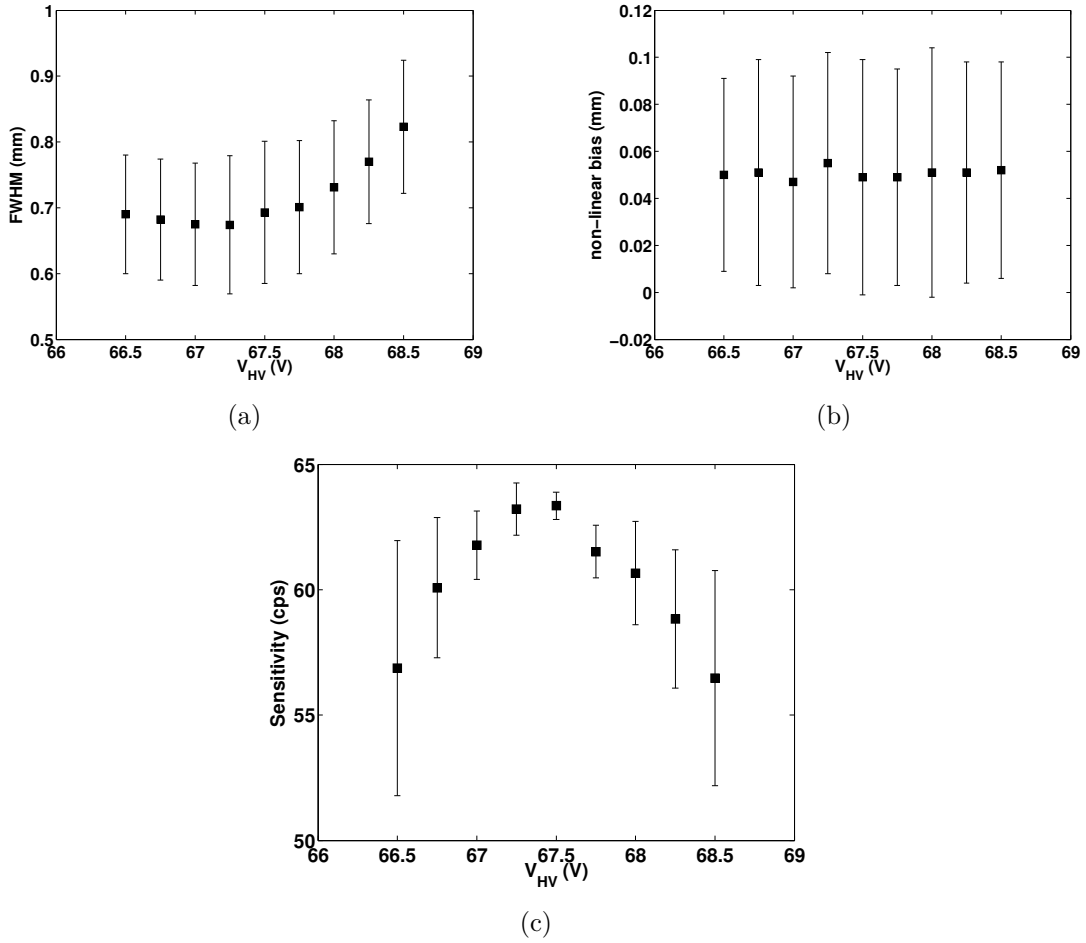


Figure 3.13 – (a) Average spatial resolution, bias (b) and β sensitivity (c) as a function of the supply voltage of the SiPMs array ($T = 20^\circ\text{C}$). The error bar represent the uniformity of the measured values over the all testing positions (diagonal scan from the center to 11.4 mm from the corner).

of spatial resolution (FWHM), spatial bias and β sensitivity as a function of the applied voltage is presented in Figure 3.13. The barycenter method after charge subtraction was used as a position reconstruction algorithm. The results relative to each supply voltage were analyzed by adjusting the charge subtraction in order to optimize the β sensitivity. This sensitivity is estimated as the average number of counts per seconds in all spots of the scan obtained after image reconstruction.

We can observe that the average spatial resolution, nearly constant for lower overvoltages, reaches a minimum values of 0.67 ± 0.11 mm at 67.25 V after which it increases with the applied voltage (0.82 ± 0.10 mm at 68.5 V) (Fig. 3.13a). On the other hand, the distortion is not influenced by the bias voltage (Fig. 3.13b). Rising too much the overvoltage increases of the photon detection efficiency (PDE) of the SiPMs but also the probability of crosstalk and afterpulses, and thus, enhances the weight of the charge distribution tails in the centroid calculation. When the charge distribution is too broad, the spatial resolution starts to degrade. This effect can be offset by increasing the charge subtraction before centroid calculation but at the expense of the β sensitivity. The subtraction in photoelectrons needed to reduce the

tail influence and to obtain the best spatial performances is minimal at 67.25 V and increases for higher overvoltage. Conversely, the sensitivity loss at lower overvoltage is due to a too low PDE. The detector sensitivity varies of about 11% between the maximum value obtained for 67.5 V and the minimum values obtained at the two extreme voltages (Fig. 3.13c). From these results, we can conclude that the optimal voltage giving the best trade-off between β sensitivity value and spatial performances is 67.5 V ($\Delta V=1.6$ V).

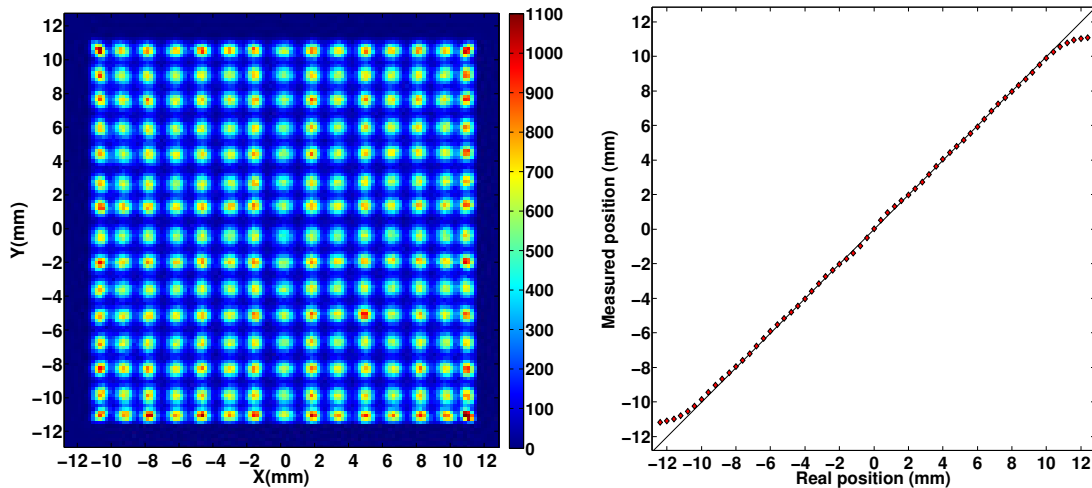


Figure 3.14 – Image of a scan of the ^{204}Tl source collimated by a 0.5 mm diameter hole. The spots are spaced 1.6 mm apart in both directions (left). Position linearity of the β imaging probe corresponding to the measured source positions versus the mechanical positions (right). Average positions measured along X direction are reported for all testing positions over the detection FoV. Similar position linearity was measured along Y direction. The error bars (standard deviation), representing the measured position uniformity for each mechanical position, are too small to be represented in the graph.

3.2.7.2 Spatial performances

An accurate characterization of the intrinsic spatial performances of the optimal configuration of the positron imaging probe was obtained by moving a 0.5 mm collimated ^{204}Tl source in 0.4 mm scanning steps over the whole FoV and within 0.45 mm from the detector edges. The scan was performed at a constant temperature of 20°C and optimal overvoltage of 1.6 V (67.5 V supply voltage). Figure 3.14 shows an example of the image of the scan with 1.6 mm pitch and the spatial linearity of the positron imaging probe measured from this scan. The linear compression effect in the central region is small with a position linearity coefficient of 0.98, obtained by the linear fit of the central peak positions. Small oscillations around this linear variation indicates the amplitude of the local bias in the central region (mean value of 0.10 ± 0.13 mm) due to the discretized nature of the photosensor. The mean distortion towards the center increases up to an average value 0.34 ± 0.31 mm on the edges. The intensity map of the local distortion on the whole FoV is represented in Figure 3.15. The color of each square region corresponds to the average value of the local bias vector in regions of 1.22×1.22 mm². An equivalent map represents the local average spatial resolution

on the whole FoV of the detector (Fig. 3.15). In the central region, the probe offers a mean spatial resolution of 0.74 ± 0.05 mm that degrades to an average value of 1.35 ± 0.38 mm on the detector edges.

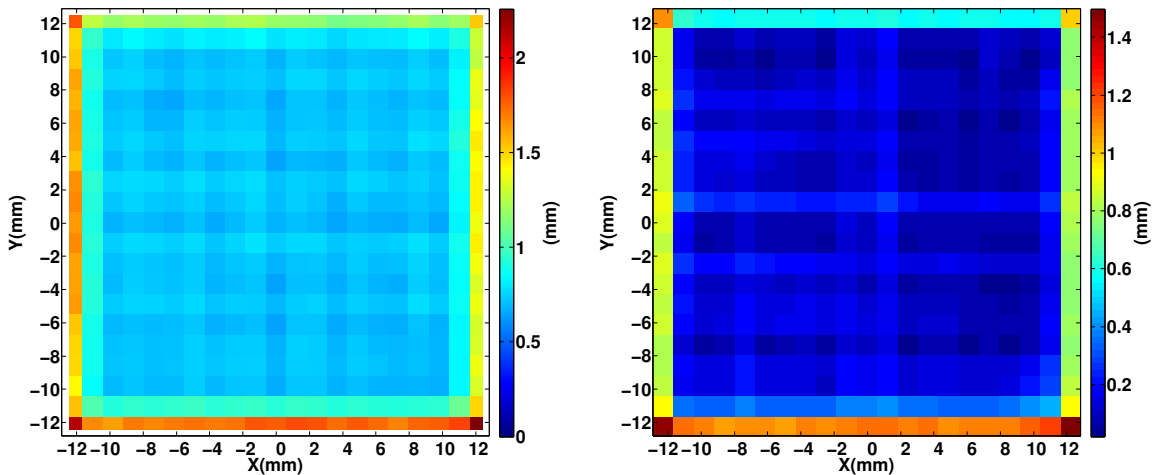


Figure 3.15 – Intensity maps representing the spatial resolution (left) and local distortion (right) on the whole FoV of the detector. The color in each square region represents the average parameter value on the corresponding region of 1.22×1.22 mm². The local distortion intensity is calculated as the module of the vector associated to the local bias.

3.2.7.3 Correction of temperature dependance

In order to quantify the temperature dependance of the positron imaging probe and to validate the efficiency of the gain correction, the detector performances were tested for temperatures ranging from 16 to 36°C (4°C step) with and without voltage adjustment. The reference bias voltage was set to 67.5 V at 20°C corresponding to the optimal overvoltage. The scan of the detector diagonal was performed following the same procedure that for the overvoltage optimization. The images were reconstructed with the barycenter method after application of the optimal threshold in terms of sensitivity for each set of measures (temperature and overvoltage). The average value of spatial resolution (FWHM), bias and sensitivity as a function of the temperature are presented in Figure 3.16. We can observe that the voltage adjustment allows to reduce the average bias. The spatial resolution presents the same behavior with and without voltage adjustment. Figure 3.16 shows that the response adjustment through overvoltage correction allows to maintain a constant signal sensitivity (mean value and homogeneity on the FoV). The maximum variation of the sensitivity with the overvoltage correction is 2.6% over a range of 20°C. Without correction, the sensitivity drops by 20% between 20°C and 38°C and becomes strongly inhomogeneous across the detector surface. This temperature correction can be easily implemented in the acquisition software to allow real time adjustment.

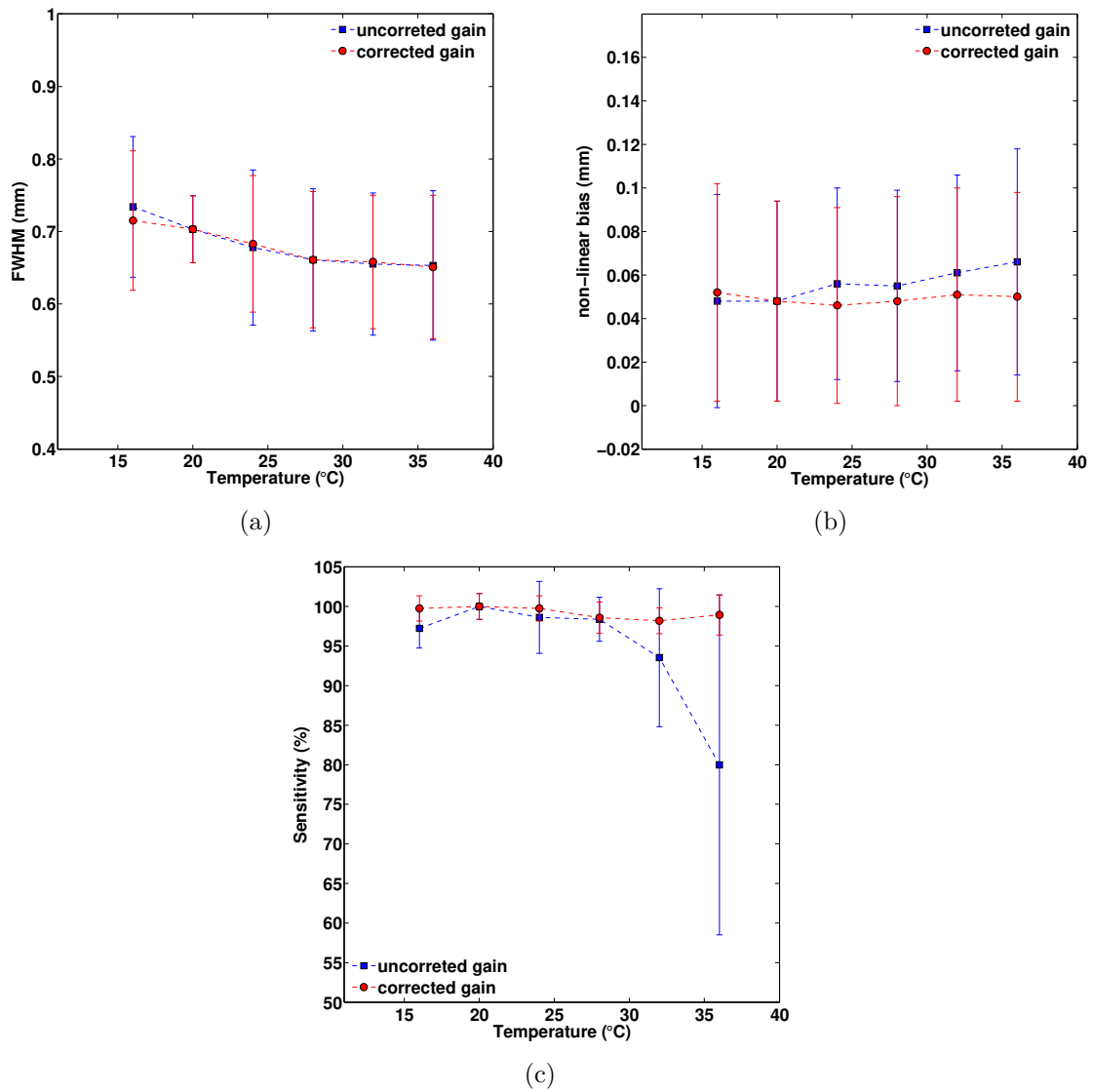


Figure 3.16 – Average spatial resolution (a), bias (b) and β sensitivity (c) as a function of the temperature without (bias voltage set at 67.5 V) and with gain correction. The error bars represent the uniformity of the measured values over all testing positions (diagonal from the center to 3 mm from the corner).

3.2.8 Comparison of reconstruction methods

The different position reconstruction algorithms described in Section 2.5.5 have been studied to improve the spatial resolution and distortion of the optimal configuration of the single scintillator probe: the barycenter method with charge subtraction, the iterative position weighted barycenter method, the analytical model fitting method and the neural networks. This comparison study was based on the experimental data relative to the scan with a step of $800 \mu\text{m}$ of the triangular region going from the center to within $850 \mu\text{m}$ of the detector edges (^{204}Tl source). The results of this study are summarized in the Table 3.5.

Reconstruction method	Spatial Res. (mm)		Bias (mm)		Reconstruction time (events/s)
	centre	edge	centre	edge	
Barycenter	0.64 ± 0.06	0.96 ± 0.35	0.05 ± 0.04	0.35 ± 0.34	7150
Iter. w. barycenter	0.69 ± 0.05	1.04 ± 0.36	0.06 ± 0.05	0.40 ± 0.36	450
Model fitting	0.69 ± 0.09	0.81 ± 0.26	0.06 ± 0.04	0.26 ± 0.16	680
Neural Network	0.64 ± 0.09	0.87 ± 0.23	0.05 ± 0.04	0.14 ± 0.08	13130

Table 3.5 – *Spatial performances obtained for the different reconstruction method tested. The barycenter method performances refer to the optimal subtraction value of 8 photoelectrons and the iterative weighted barycenter (Iter. w. barycenter) refers to optimal values obtained for a standard deviation of the Gaussian function of 7. The average and standard deviation of the spatial resolution (FWHM) and bias calculated over all testing positions with a ^{204}Tl source are given separately for the central and edges areas. The reconstruction time are calculated with a computer processor Intel Core i5 and 16 Gb RAM.*

3.2.8.1 Standard barycenter method

The barycenter method was evaluated for an increasing charge subtraction ranging from 4 to 16 photoelectrons. The results are presented in Figure 3.17. A position linearity coefficient of 0.98 is obtained in the central region for the lower subtraction, which increases up to 1 for a subtractions of 16 photoelectrons. The uniform charge subtraction applied on the charge distribution of each event allows to reduce the weight of the distribution tails on the barycenter calculation and therefore, slightly decreases the compression of the image in the center area and the spatial bias on the edges. However, at the same time, the large truncation of the light distribution tails slightly degrades the response uniformity in the central region as illustrated by the increasing mean bias values and standard deviations presented in Figure 3.17. Both spatial resolution and bias reach their minimum values for a charge subtraction of 8 photoelectrons (Table 3.5).

3.2.8.2 Iterative position weighted barycenter method

The implementation of the iterative position weighted barycenter method does not allow to improve the spatial performances compared to the standard barycenter method. The standard deviation of the Gaussian function of the weighting factor was tested for a value ranging from 4 to 9. The best spatial performances are obtained for a σ equal to 7. The

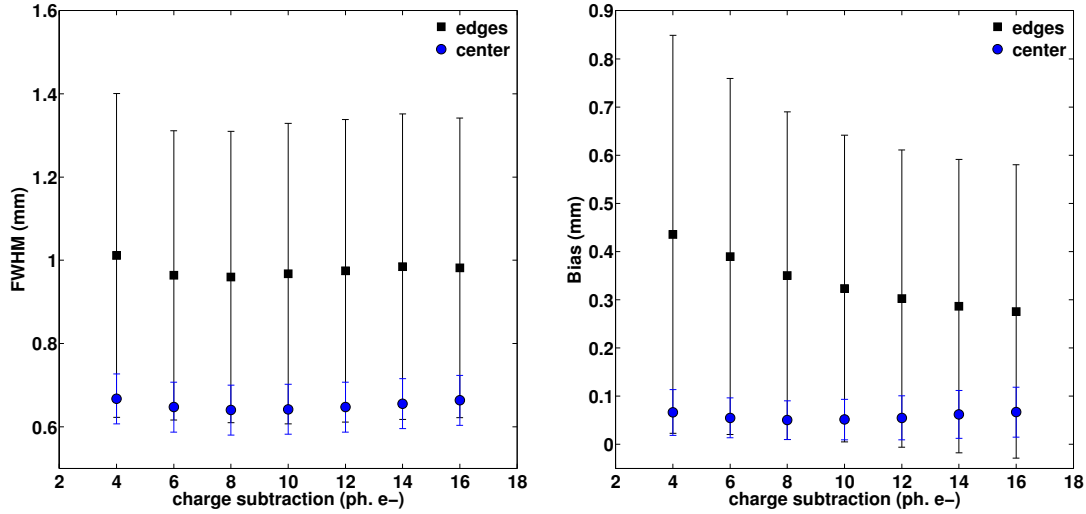


Figure 3.17 – Spatial performances obtained with standard barycenter method after application of a charge subtraction ranging from 4 to 16 photoelectrons. The average spatial resolution (left) and spatial bias (right) are reported separately for the central area and the detector periphery. The error bars represents the standard deviation of measured values in the two regions.

mean spatial resolution are 0.69 ± 0.05 mm and 1.04 ± 0.36 mm, and the spatial bias are 0.06 ± 0.05 mm and 0.40 ± 0.36 mm in the center and in the periphery of the detector, respectively (Fig. 3.18). Furthermore, the iterative process requires a computation time which is 17 times longer than the standard barycenter method.

3.2.8.3 Analytical model fitting method

The image of the scan of the detector surface reconstructed thanks to an iterative non-linear least squared method (Levenberg-Marquardt) fitting the Scrimger-Backer model (see Section 2.5.5) on the scintillation light distribution is shown in Figure 3.18. Due to the thin thickness of the p-terphenyl scintillator, the distance h between the point of scintillation light emission and the photodetector surface was fixed. The best spatial performances were found for $h = 2.5$ mm. This value corresponds roughly to the sum of the scintillator thickness (0.1 mm) plus the thickness of the light guide (2 mm) and the protective resin of our SiPMs array (0.2 mm). This method yields a position linearity coefficient close to the unity (0.999 ± 0.015) in the central region. Others spatial performances in the central area are very closed to that obtained with the barycenter method (0.69 ± 0.09 mm and 0.06 ± 0.04 mm for the spatial resolution and bias, respectively). The main advantage of this method is to reduce the distortion on the periphery region where the bias decreases from 0.35 ± 0.34 mm to 0.26 ± 0.16 mm and the spatial resolution decreases by 16% reaching 0.8 ± 0.26 mm (Table 3.5). The lack of accuracy in the reconstruction of the corner spots and more generally on the edges, is due to the fact that the Scrimger-Backer model no longers matches the real distribution of the light due to the truncation by the absorbing edges. More sophisticated models based on theory or measurements could probably improve further the performances near the edges. The analytical model fitting method requires a relatively long computational

time due to the fitting process, which limits its use for real time imaging when the acquisition frequency is high (more than 600 events/s) (Table 3.5).

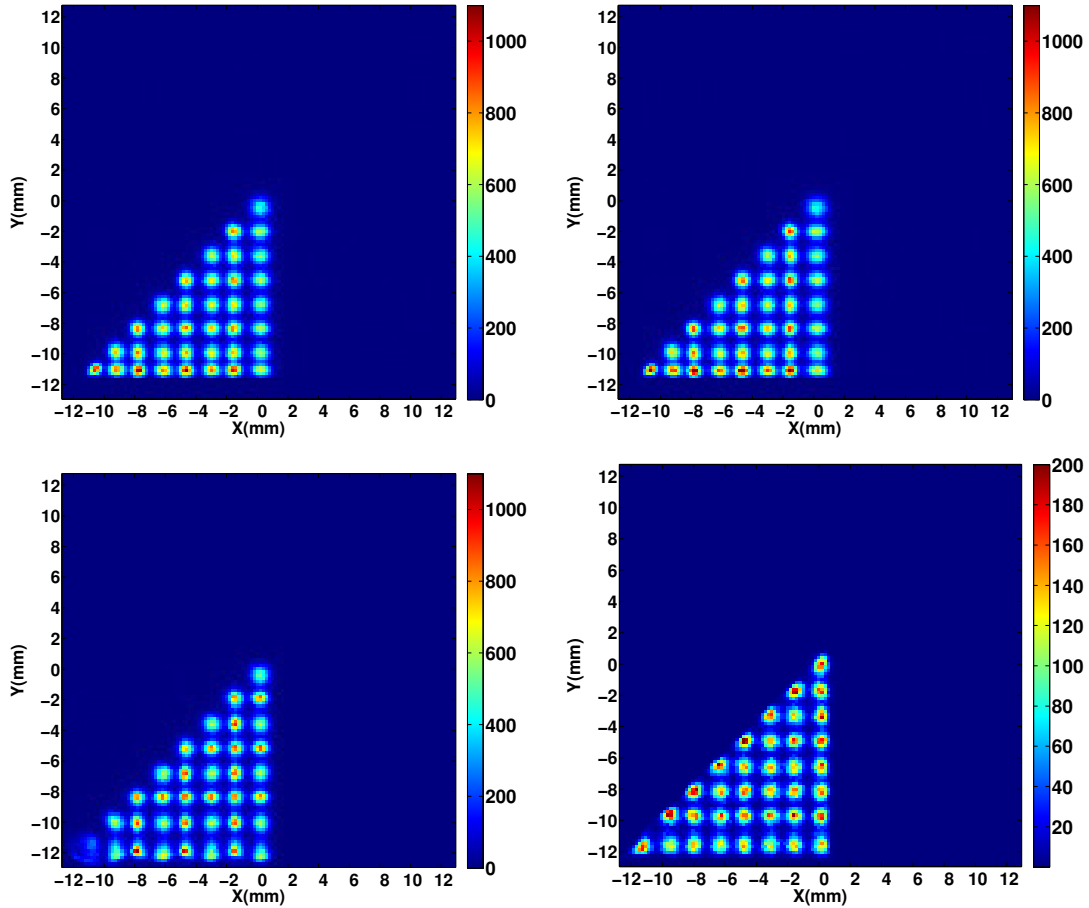


Figure 3.18 – Comparison of the images reconstructed with the barycentre method (top left), iterative position weighted barycenter method (top right), analytical model fitting method (bottom left) and the neural network method (bottom right). The points represented are spaced 1.6 mm apart in both directions.

3.2.8.4 Neural network method

In this section, we present some preliminary results of the image reconstruction performances obtained with a neural network method. The number of neurons in the hidden layer N was set to 16. For the training, we used a part of the acquisitions carried out for the fine characterization of the detector surface with a 0.5 mm collimated ^{204}Tl source and a pitch of 0.4 mm (see Paragraph 3.2.7.2). The number of events used in the training for each position was fixed at 300 and the number of epochs to 300. The optimization of the parameters and the training of the neural network have been made with the NeuralNetwork package implemented in Matlab on the basis of an optimization work performed on the MAGICS γ -camera.

Figure 3.18 presents an image of the scan reconstructed with trained neural network compared with a standard barycenter method after 8 photoelectron charge subtraction, the iterative position weighted barycenter and the analytical fitting method. The spatial resolution is comparable to that of the barycenter method in the central area (0.64 ± 0.09 mm compared to 0.64 ± 0.06 mm). However, the performances are strongly improved in the detector periphery since the spatial resolution decreases from 0.96 ± 0.35 mm to 0.87 ± 0.23 mm and the spatial bias from 0.53 ± 0.34 mm to 0.14 ± 0.08 mm compared to the barycentre method. Moreover, the computing time is perfectly suited to real time imaging display (Table 3.5). The only constraint of Neural networks is the need of an accurate spatial calibration for the learning process, which can be very time-consuming (about 55 hours for the 662 points scanning procedure).

In conclusion, Table 3.5 shows that the two methods allowing a real time image reconstruction of the interaction position with the best spatial performances are the barycenter method with the application of a charge subtraction and the neural networks. However, this last method needs to be further optimized. This is why the barycentre method was used for the preclinical evaluation of the positron imaging probe with radioactive phantoms (Chapter 4).

3.3 Optimization and performances of the dual scintillator probe

The single scintillator detection head presented above allows to obtain submillimetric spatial resolution and bias over its whole field of view. It was optimized to achieve an optimal trade-off between β sensitivity and minimization of the γ noise contamination. To move forward in the reduction of noise, we developed and characterized a dual scintillator detection head in order to estimate and then subtract the γ background noise contamination (Fig. 3.19). The estimation of this noise contamination is made by introducing a second

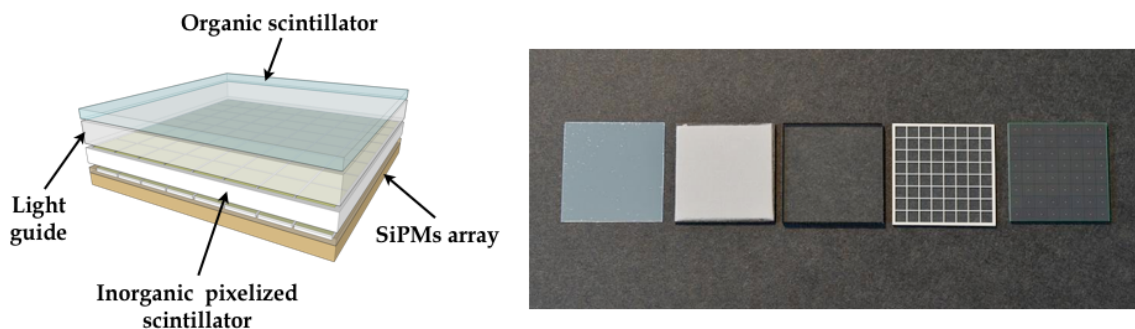


Figure 3.19 – Design of the dual scintillator configuration of the positron imaging probe (left). Components of the dual scintillator probe (right) and starting from the left to the right: ESR reflector coating, p-terphenyl scintillator, light guide, pixelized LYSO:Ce array (8×8 components of $3\times 3\times 0.5$ mm³) and 64-channels SiPMs array.

inorganic scintillator between the light guide and the SiPMs array. This bottom scintillator is shielded from the β particles thanks to the light guide and the top β -sensitive scintillator, allowing a quantification of the intensity of the photon flux incident on the detector surface. To maintain the compactness of the device and to not increase the number of electronic channels, both scintillators are readout by the same SiPMs array. The discrimination of the events interacting in the two scintillators is made on the basis of the spatial distribution of the scintillation light on the SiPM surface. Therefore, the lower β -shielded inorganic scintillator was pixelized to enhance the difference in light distributions, as previously discussed in Section 2.5. The different components used for this prototype are shown in Figure 3.19. A 0.2 mm thick polycrystalline p-terphenyl scintillator deposited on a 2 mm thick polyester light guide was used as β -sensitive scintillator. This scintillator was chosen to obtain the higher light production and compensates for light losses due to the addition of the β -shielded scintillator. The 8×8 LYSO:Ce array, composed of $3 \times 3 \times 0.5$ mm³ pixels, was optically coupled to the light guide and the SiPM array with a thin layers of optical grease. The pixels of the scintillator were accurately aligned to the SiPMs in order to efficiently collected the light produced in each pixel into the corresponding SiPM. The p-terphenyl scintillator was covered by an enhanced specular reflector (ESR, 65 μ m).

The 8×8 SiPMs array (S12642-0809PA, Hamamatsu) implemented for this dual scintillator configuration was characterized as described in Section 3.1 for the 4×4 SiPMs arrays. The application of SiPM uniformity correction by DAC tuning allows to reduce standard deviation between SiPMs gain by 70% at a bias voltage of 68.5 V. Other parameters of the readout electronics were set according to the data presented in Section 2.5.4.1. The optimal time constant of the slow shaper was set to 50 ns and delay of the HOLD to 68 ns using the same procedure described in the Section 2.5.4.1.

An efficient subtraction of the γ background noise is associated to a good discrimination between the signal generated from the β -sensitive and β -shielded scintillators. Therefore, the main focus of the optimization of this double detection head was its event discrimination ability. As described in Section 2.5, it strongly depends from the difference between the light distributions produced by the two scintillators. In order to improve event discrimination, two thicknesses of the light guide, 2 and 3 mm, were evaluated (see Section 3.3.1.4). Events discrimination was optimized as well as a function of the applied overvoltage and electronic gain (see Section 3.3.1.2).

The configurations with different light guide thicknesses were first characterized by performing flood field irradiations of the detector surface with uncollimated ²⁰⁴Tl and ²²Na sources. Acquisitions without source were performed to estimate the intrinsic background noise of the detector, produced by the natural activity of LYSO. An accurate characterization of the detector performances was obtained with scanning its whole field of view with a 0.5 mm collimated ²⁰⁴Tl source and a 0.8 mm scanning step. The images were reconstructed using the barycenter algorithm with a charge subtraction of 8 photoelectrons.

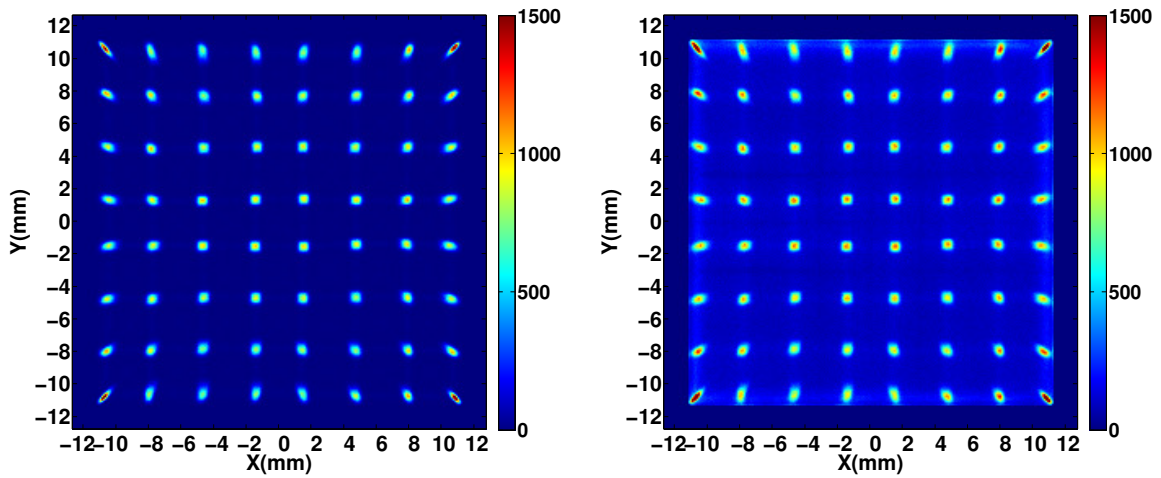


Figure 3.20 – Image produced from the background noise produce by the natural radioactivity of the pixelized LYSO:Ce scintillator (left). Image of the uniform irradiation of the detector surface with a ^{204}Tl source overlapped on the LYSO:Ce signal. Detector configuration composed of the 0.2 mm thick p-terphenyl scintillator coupled to the LYSO:Ce pixelized scintillator through a light guide of 2 mm and covered with the ESR. Measurements made with a low electronic gain (compensation capacitance of 300 fF) and a bias voltage of 70.2 V.

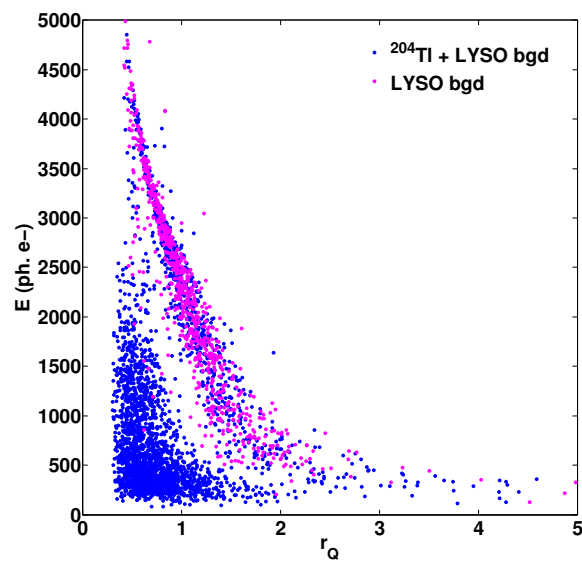


Figure 3.21 – Events total energy as a function of the r_Q parameter of events interacting in a central area of the detector surface. The events detected for an uniform irradiation with the ^{204}Tl source and LYSO noise are represented in blue and the noise events detected without source in magenta. The detection head is composed of the 0.2 mm thick p-terphenyl scintillator coupled to the LYSO:Ce through a 2 mm thick light guide. The measurements were made with a supply voltage of 70.2 V and an electronic gain corresponding to a compensation capacitance of 300 fF.

3.3.1 Scintillators discrimination

Figure 3.20 shows the image generated from the noise signal due to the natural radioactivity of the LYSO:Ce and the image obtained with a uniform irradiation of the detector surface with the a ^{204}Tl source. On this second image, we can observe the overlapping between the discretized image of the LYSO background and the uniform image of the ^{204}Tl source generated by the interaction of β particles in the p-terphenyl scintillator. The accumulations of counts at the center of each pixels is due to the pixelization of the LYSO scintillator, which focuses the scintillation light, resulting in a position reconstruction of the events created or generated in the LYSO at the center of each pixel.

The β -sensitive and β -shielded scintillators generate two distinguishable populations of events. Their differences can be characterized by many parameters such as the event total energy and the ratio r_Q between the charge of the pixel with the highest charge and the total charge of the surrounding pixels within a 3×3 pixels region (the size of this area was optimized for the discrimination), which gives a measure of the light distribution spread. Figure 3.21 shows the bi-dimensional plot of the event total energy as a function of the r_Q parameter for events interacting in the central area of both scintillators. The events detected after an uniform irradiation of the detector surface with a ^{204}Tl are represented in blue. Two populations are distinguishable. The first one relative to lower energy or/and lower r_Q values (wider light distributions) corresponds to the interaction of β particles coming from the ^{204}Tl source in the upper β -sensitive scintillator. The second cluster, with higher energy and r_Q values (thinner light distributions), corresponds the β noise events created in the lower pixelized LYSO:Ce. This second population is overlapped with the cluster of points corresponding to the LYSO radioactive noise obtained without source (magenta points in the Fig. 3.21). It is possible to associate the points belonging to the upper-right cluster to the events interacting in the β -shielded scintillator and the ones in the lower-left cluster to the events interacting in the β -sensitive scintillator. In order to optimize the scintillator discrimination ability of the detection heads, these two clusters have to be as splitted as possible. This can be obtained thanks to an adequate tuning of the SiPMs bias voltage and readout electronic gain (Section 3.3.1.2) as well as an accurate choice of the light guide thickness (Section 3.3.1.4).

We implemented an automatic method, based on a clustering algorithm, to discriminate the events without introducing any user bias. This method was used to confront the results obtained for the overvoltage and electronic gain optimization taking into consideration the energy and the light distribution parameter r_Q . However, the clustering method does not allow to achieve a real-time event discrimination. Therefore a second method based on an *ad hoc* separation of the events was implemented from the analysis of their total energy, light distribution parameter r_Q and number of fired pixels.

3.3.1.1 Automatic clustering

The automated clustering program was implemented in MATLAB. The program uses a k -means clustering algorithm to associate each observation to one of the two clusters. The k -mean clustering, or Lloyd's algorithm [Lloyd 1982], is an iterative data partition method that

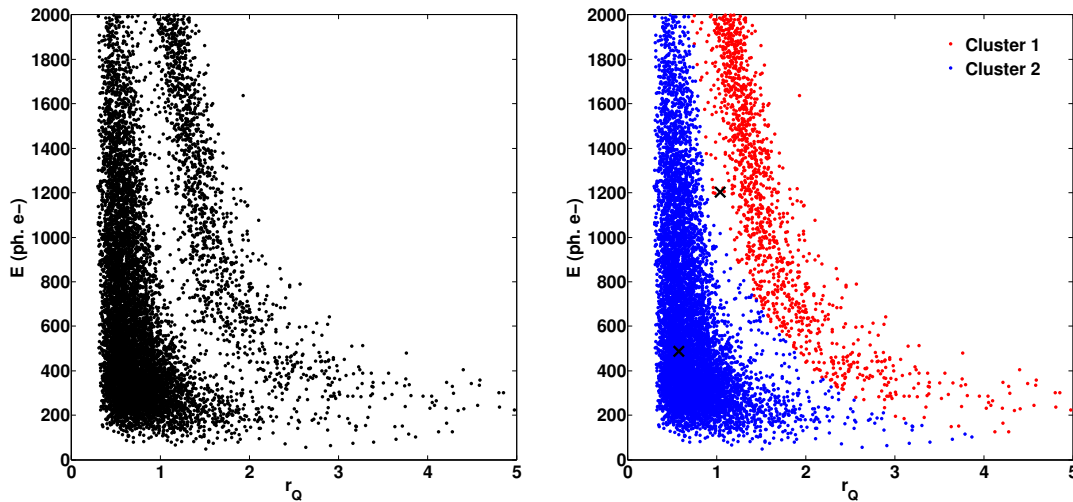


Figure 3.22 – Events total energy as a function of the r_Q parameter for an uniform irradiation with a ^{204}Tl source of the central ROI of the detector (left). The red and blues points represent the events assigned by the k -mean algorithm to the cluster created from the β -shielded scintillator (LYSO:Ce) and the one created from the β -sensitive scintillator (0.2 mm thick p -terphenyl). The black crosses represents the centroids of the two clusters (right). All events of the clusters are not represented in the image. The measurements were made with a supply voltage of 70.2 V and an electronic gain corresponding to a compensation capacitance of 300 pF.

treats observations as objects having a location and distance from each other. It separates objects into k clusters that are mutually exclusive, such that objects within each cluster are as close as possible to each other, and as far as possible from the object in the others clusters. The number of k clusters is chosen before the starting the algorithm. Each cluster is characterized by its member objects and its centroid. The centroid is defined as the point for which the sum of distances from all objects in the cluster is minimized. The algorithm first step consists in the random selection of k initial clusters centroids. Then it computes the point-to-cluster distance of all observations to each centroid (step 2) and assigns each observation to the cluster with the closest centroid (step 3). Finally, the average of the observations is calculated for each cluster to obtain k new centroid locations (step 4). Steps 2 to 4 are repeated until cluster assignment do not change, or the maximum number of iterations is reached.

For our application the number of clusters is equal to 2: one composed of the events interacting in the β -sensitive scintillator and the other composed from events interacting in the β -shielded one. The measured distance, chosen to compute the centroid clusters, was the sum of absolute differences along x and y directions. The clustering algorithm was used on ^{204}Tl data, since they present events interacting in both scintillators at once. The clustering was made for events interacting in the central region of the detector. The separation between the two clusters is estimated from the euclidian distance between clusters centroid in the E - r_Q plane. Figure 3.22 shows an example of the results obtained with the automated clustering. Cluster 2 regroups the event interacting in the β -sensitive scintillator while cluster 1 regroups the LYSO noise events.

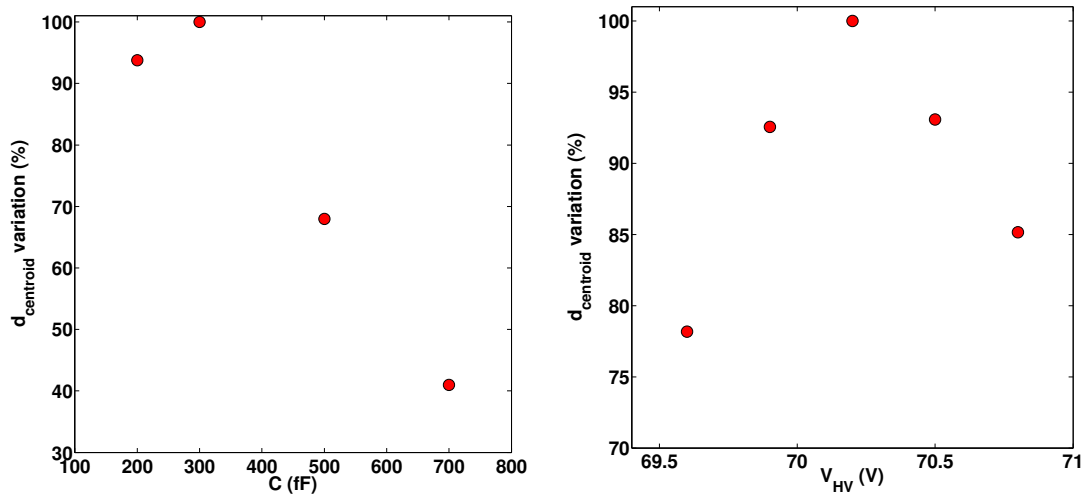


Figure 3.23 – Relative variation of the distance between the centroids of the clusters created by the events interacting in the β -shielded and β -sensitive scintillators as a function of the electronic gain capacitance (supply voltage of 69.9V) (left) and as a function of the supply voltage (electronic gain corresponding to a compensation capacitance of 300 fF) (right). The clustering algorithm was applied to the events interacting in the center of the detector. Both curves are normalized by their maximum value. The detection head is composed of a 0.2 mm thick *p*-terphenyl scintillator coupled to the pixelized LYSO array through a 2 mm thick light guide.

3.3.1.2 Overvoltage and electronic gain optimization

The influence of the electronic gain and supply voltage on population discrimination was tested for the configuration with a light guide of 2 mm thickness. The distance between the two clusters was evaluated for the events interacting in the central region of the detector. A greater distance between the centroids of the clusters associated to the two populations is associated to a better events discrimination.

Figure 3.23 represents the variation of the relative distance between the centroids of the clusters as a function of the capacitance of the low gain pre-amplifier and the applied supply voltage. The largest distances between the centroids is obtained for a capacitance of 300 fF. For this electronic gain, the optimal supply voltage is equal to 70.2 V. These optimal parameters were used for the following measurements.

3.3.1.3 Events discrimination method with cut

The clustering method cannot be used to perform real time discrimination of the events. Therefore, we developed a method based on the application of *ad hoc* cuts which allow to associate the events to the β -shielded or the β -sensitive scintillator on the basis of the total energy of the events, the parameter r_Q and the number of fired pixels. The distribution of the scintillation light and thus the total energy of the event depends on its point of interaction. The light distribution of the events interacting in the central area of the detector are wider. This is represented by a small r_Q ratio while the ones generated from the events interacting on the detector edges are thinner due to the light absorption. This effect impact as well the total energy collected and the number of fired pixel for each event. In order to take

into account those differences and accurately discriminate the events, different regions of the detector surface were analysed separately. We considered 9 regions of $6.4 \times 6.4 \text{ mm}^2$ within the central area of the detector and a region corresponding to the outermost pixels. For each of these regions, we first defined an *ad hoc* cut considering the relation between the total energy and the r_Q parameter (Fig. A.6, left). As shown in Figure A.6 (left), the function that better delimits the separation between the two distributions is an exponential. However, the application of the first cut do not allow to remove all the events interacting in the LYSO. We can indeed still observe the presence of a second population of points when the total energy of the events is represented as a function of the number of fired pixels. A second cut was therefore applied on the data selected by the first cut and associated to the β -sensitive scintillator by considering the relation between these two parameters (Fig. A.6, right). For the second cut it was chosen as a linear function, as represented in Figure A.6 (right). The parameters of these two cutting functions have been defined for each of the regions of the detector. The difference between the events distributions and the consequent adaptation of the *ad hoc* cuts for a central region and the frame region are shown in Figure A.6.

3.3.1.4 Influence of light guide thickness

The discrimination of the events interacting in the β -sensitive and β -shielded scintillators for the two detector configurations with 2 and 3 mm light guide was performed applying the cuts method. The values of the functions performing the event discrimination in the different regions was adapted for each configuration. The error made on the events discrimination was defined as the relative number of events assigned to the β -sensitive or β -shielded scintillator by the discrimination method whereas it has interacted in the other. This error was calculated as the difference between the number of events associated to the β -shielded scintillator when irradiating with the ^{204}Tl source and without source. The relative error is obtained by dividing this absolute error by the total number of β events coming from the ^{204}Tl and interacting in the detector. The error made on the events discrimination decreases from 5.3% to 0.8% when the light guide thickness increases from 2 to 3 mm. The thicker light guide increases the differences between light distributions of the two scintillators thanks to the larger spread of the scintillation light of events interacting in the β -sensitive scintillator.

3.3.1.5 Focus on the optimal configuration

The ability of the positron imaging probe to discriminate the signal coming from the β -shielded and β sensitive scintillators is illustrated in Figure 3.25 for the configuration with the 3 mm light guide. An aluminum collimator, with 10 holes of 0.5 mm diameter set in a triangular configuration and spaced 1.6 mm apart, was put in contact with the detector surface and irradiated with a ^{22}Na source placed at a distance of about 5 cm. This collimator allows to absorb the positrons incident on the detector surface and select the ones passing through the holes. In this way, we obtain an image of the collimated positron overlaid on a uniform background of γ rays corresponding to γ interacting in the β -sensitive scintillator and a pixelized image coming from β -shielded scintillator and corresponding to the intrinsic noise of LYSO and to the γ rays interacting inside it. Figure 3.25 left represents the image

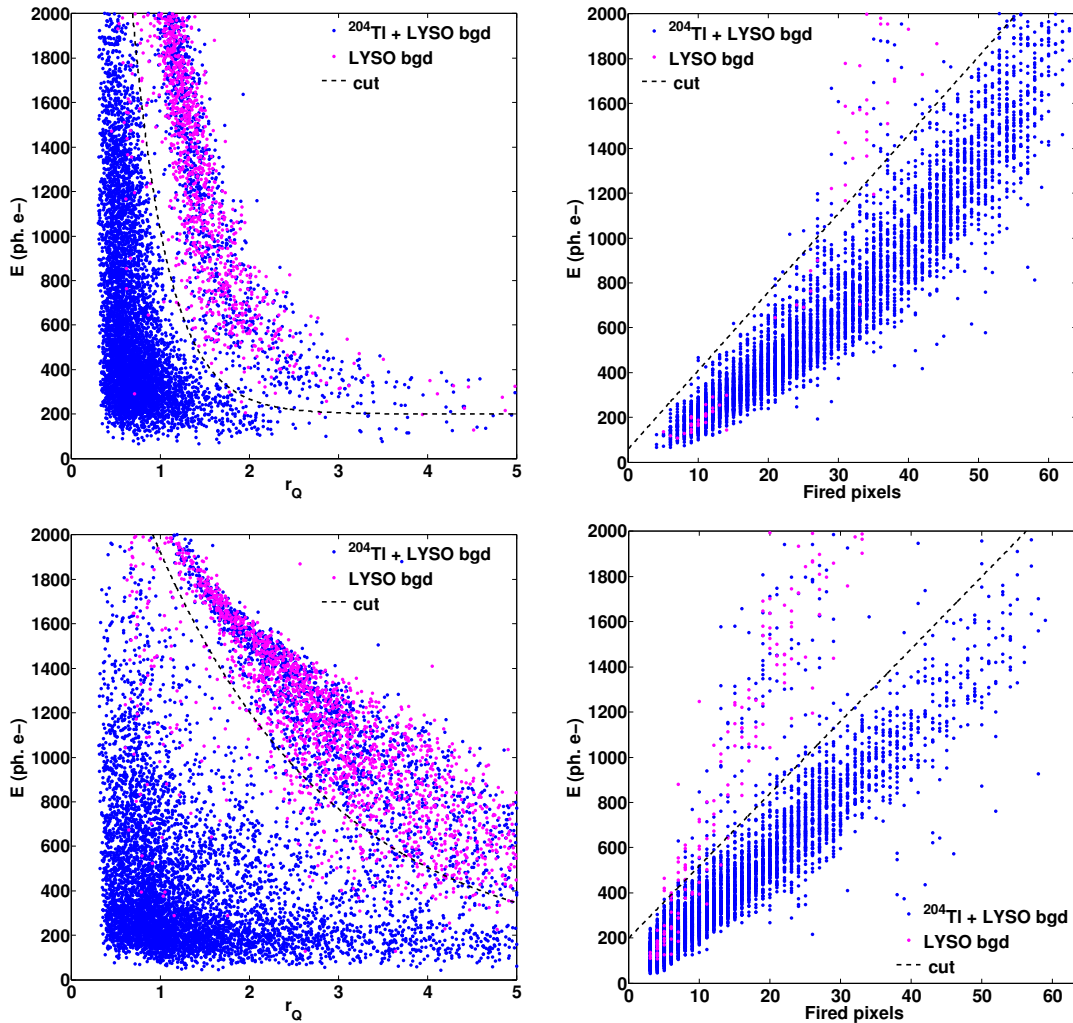


Figure 3.24 – Events total energy as a function of the r_Q parameter (left) or the number of fired pixels (right) for events interacting in a central region (top) and periphery region (bottom) of the detector surface. The events detected for an uniform irradiation with the ^{204}Tl source are represented in blue and the noise events detected without source in magenta. The detection head is composed of the 0.2 mm thick *p*-terphenyl scintillator coupled to the $\text{LYSO}:\text{Ce}$ through a 2 mm thick light guide. The measurements were made with a supply voltage of 70.2 V and an electronic gain corresponding to a compensation capacitance of 300 fF.

of the events detected in both scintillator, which was saturated to better visualize the image of the collimator and the pixelized signal from LYSO . The image corresponding to the β -sensitive scintillator after application of the cut method is represented on the right. We can clearly distinguish the spots created by the positron and the uniform background due to the annihilation γ rays interacting in the β -sensitive scintillator. However, a small contamination coming from the β -shielded detector, which is represented by the accumulations in the centers of the pixels, is still present on the β -sensitive scintillator. The mean number of events remaining in a spot corresponding to the LYSO accumulation points are less of 2%. Figure 3.26 shows the image of the β -sensitive scintillator obtained from a uniform

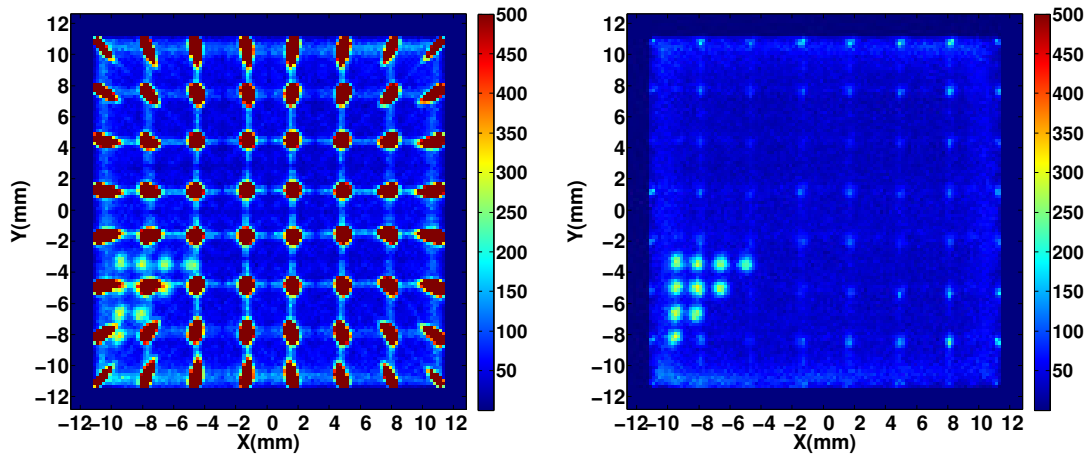


Figure 3.25 – Images of an aluminum collimator with 10 holes of 0.5 mm diameter set in a triangular configuration. The holes are spaced of 1.6 mm. The detector surface covered by this collimator was irradiated with a source of ^{22}Na placed at a distance of about 5 cm. The image is represented before (left) and after discrimination by selecting only events interacting in the β -sensitive scintillator (right). The detection head is composed of 0.2 mm thick *p*-terphenyl scintillator coupled to the LSYO:Ce through a 3 mm thick light guide.

irradiation of the detector surface with the ^{22}Na source (30 cm from the detector surface). The accumulation in the centers of the SiPMs due to the signals produced by the LYSO are still slightly visible on the edges of the detector.

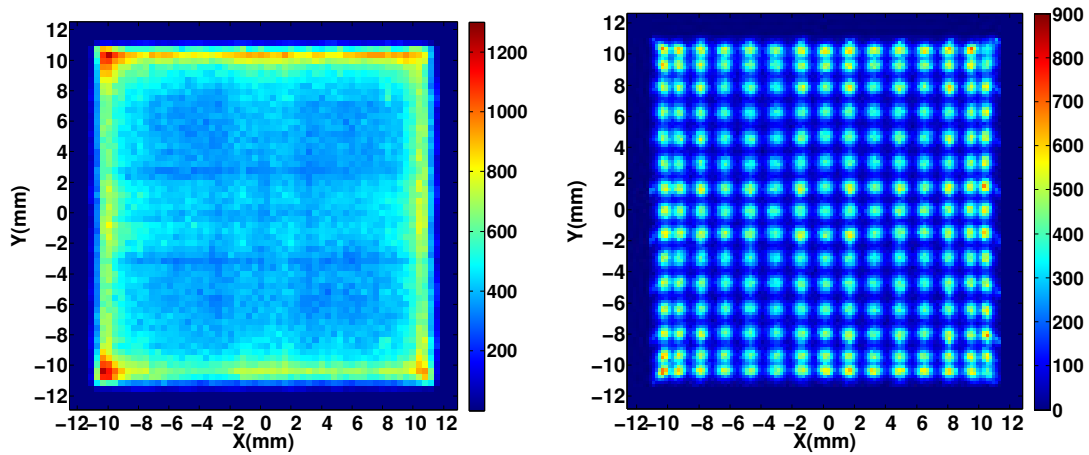


Figure 3.26 – Image of an uniform irradiation of the detector with a source of ^{22}Na (left). Image of a scan with the ^{204}Tl source collimated by a 0.5 mm diameter hole. The spots are spaced 1.6 mm apart in both directions (right). Both images correspond to events associated to the β -sensitive scintillator selected using the cuts method. The detection head is composed of the 0.2 mm thick *p*-terphenyl scintillator coupled to the LSYO:Ce through a 3 mm thick light guide.

The imaging performances of the optimal configuration of the dual scintillator probe with

the 3 mm thick light guide was evaluated on a scan performed with a 0.5 mm collimated ^{204}Tl source mounted on the motorized platform. The scanning step in the x and y directions was set to 0.8 mm. The image of the scan is reconstructed using only the events associated to the β -sensitive scintillator discriminated with the cuts method. This allows to remove the noise events of the LYSO from the image. The mean spatial resolution is 0.81 ± 0.09 mm and 1.11 ± 0.29 mm in the central and edges region, respectively. The mean spatial bias is 0.08 ± 0.08 mm and 0.40 ± 0.31 mm in the central and edges region, respectively. These results are in good agreement with the performances of the single scintillator configuration equipped with a 3 mm thick light guide, showing that the pixelised scintillator and the addition optical boundaries have low impact on the spatial performances (Table 3.3). The image of the scan performed with the ^{204}Tl source collimated with a 0.5 mm diameter hole is presented in Figure 3.26.

This dual detection head configuration allows to perform an estimation of the γ background noise thanks to the use of a second scintillator. We showed that optimization of the geometry of the detection head and of the photodetection system provides both good discrimination of events interacting in the two scintillators and submillimetric spatial resolution and bias on most of the field of view. Further improvements will include, for example, the optimization of the cutting functions on the whole field of view by dividing the detection surface in small area (more than the 10 regions used in this study). The use of neural networks to classify events coming from the two scintillators will be also investigated.

3.4 Towards the clinical prototype

The final instrument goal of this project was the development of a fully functional intraoperative β probe and its evaluation in a pre-clinical context. The necessity of contact detection, due to β short range, imposes strong constraint on the probe compactness. Furthermore, the probe should have low weight and be easy to handle in order to facilitate its use inside the operative wound. A dedicated miniaturized readout electronics and mechanical housing have been specifically design for this purpose.

3.4.1 Development of a new miniaturized readout electronics

In order to fulfill the requests of low weight, compactness and facility of handling, a new miniaturized electronic was designed in collaboration with the LAL laboratory (Fig. 3.27). The electronic board incorporates two 32-channels EASIROC ASIC's, whose characteristics have been described in details in Section 2.5.4. The board presents as well an FPGA (Altera Cyclone III), an USB protocol 2.0 high speed (FTDI FT2232H, 480Mbit/s), an USB mini-connector for to communicate with the PC interface, and a DC-to-DC converter to deliver the high voltage to the SiPMs array. The dimensions of the board is 11×2.5 cm² for a weight of 20 g. This size was chosen to fit the dimensions of the probe handle within which the electronics must be inserted (Fig. 3.28 and 3.29). An important effort has been done for minimizing these dimensions, while maintaining good performances of the full system in terms of noise, reduced cross-talk between analog channels, linearity and uniformity over all

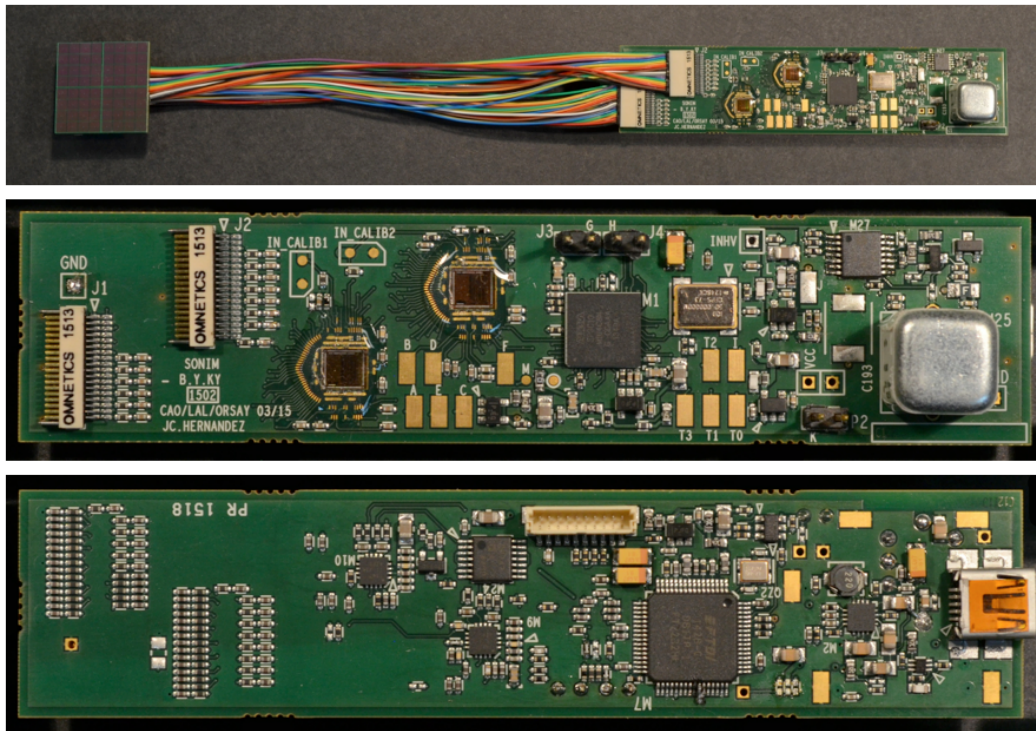


Figure 3.27 – Front side of the miniaturized electronic board connected to the four 4×4 SiPMs array (top), front side (center) and back side of the electronic board (bottom).

channels. This includes, for example, an accurate design of the path followed by the wires to avoid crosstalk, potential ground and parasitic noise or the appropriate choice of filter capacitances and board components to guarantee electromagnetic shielding compatibility, which is a necessary requirement to use the probe in the operative room.

3.4.2 Mechanical housing design

The mechanical housing developed for the single scintillator configuration is presented in Figure 3.29. It consists of two main components: the detection head and the handle. The housing of the detection head was design around the stack of the 0.1 mm thick scintillator and the 2 mm light guide coupled to the SiPMs array assembled on a PCB. Its external dimensions are $28.4 \times 28.4 \times 9.5 \text{ mm}^3$. A $10 \mu\text{m}$ aluminum sheet glued on the ESR covering the scintillator is used as optical shielding (Fig. 3.28). The overall dimensions of the intraoperative positron imaging probe is 20 cm length for a maximum diameter of 2.9 cm corresponding to the probe handle (Fig. 3.29). The total weight is 100 g.

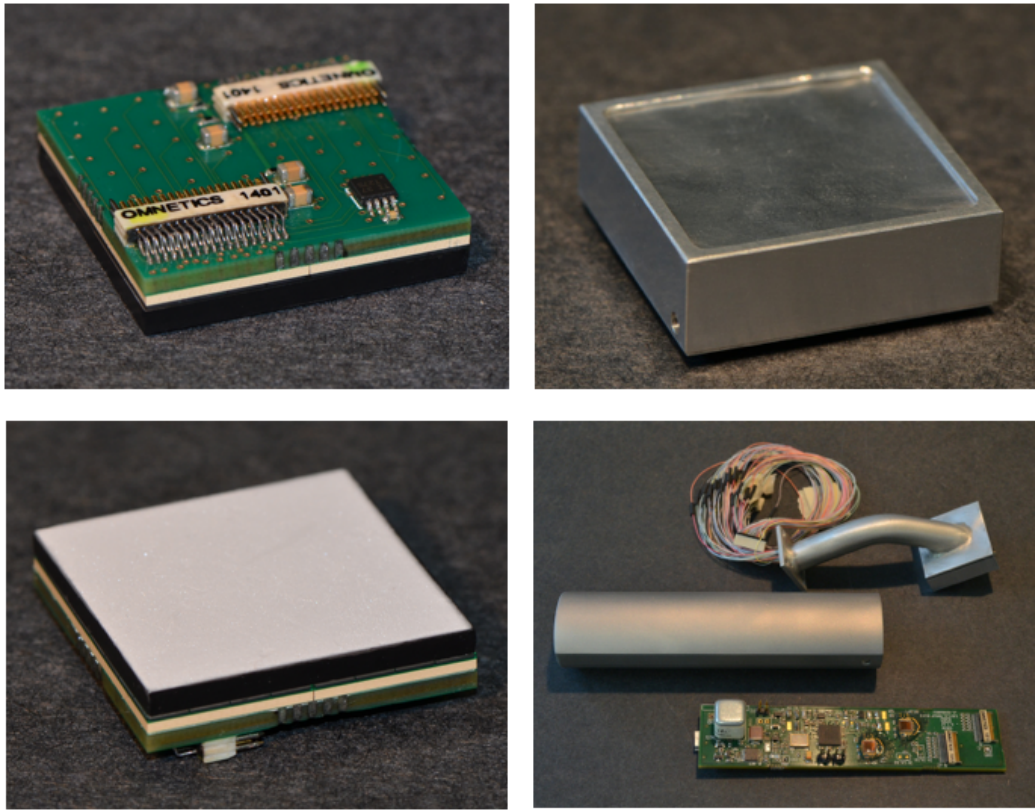


Figure 3.28 – Front side and back side of the detection module with the wire connector and the temperature sensors (left), mechanical housing of the detection head with the optical shielding (top right) and all components of the intraoperative positron imaging probe (bottom right).

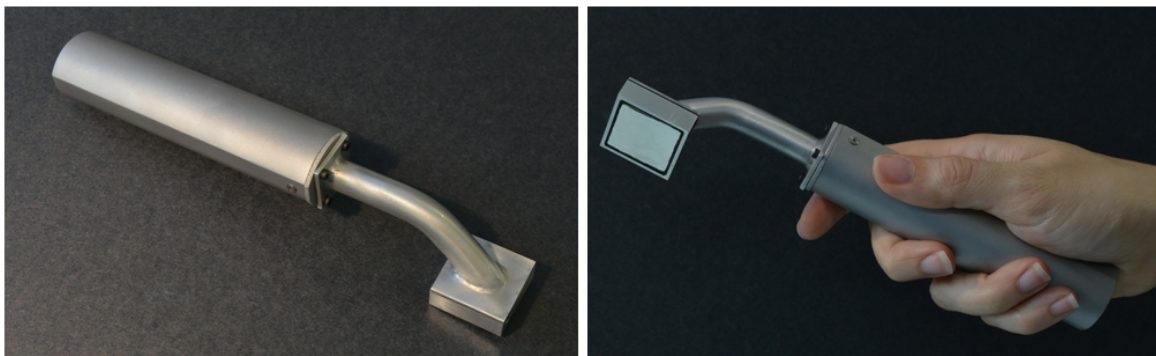


Figure 3.29 – Photographies of the complete intraoperative positron imaging probe.

Pre-clinical evaluation of the probe performances

The evaluation of the performances of the miniaturized detection probe, mounting the in a radioactive environment close to the clinical one is presented in this chapter. The intraoperative detection of small tumors depends on two major factors: the specificity of the administrated radiotracer and the intrinsic detection performances of the probe. The radiolabeled tumor focal areas and the non-specific radiotracer uptakes were simulated with phantoms filled with water in which were diluted different concentration of ^{18}F -FDG. In this preliminary study, we evaluated the detector β sensitivity as well as its spatial response for uncollimated radioactive sources. The ability of tumor discrimination was studied for a large set of variables such as tumor dimensions, uptake of the tracer in tumor tissues compared with its surrounding normal tissues, γ background noise intensity and acquisition time. To this purpose, different types of radioactive phantoms were customized.

4.1 Experimental protocol

All measurements presented in this Chapter have been performed with a non-sealed ^{18}F -FDG liquid source. Thanks to the mechanical housing and the light shielding of the probe, presented in section 3.4.2, it was possible to make the measurements without control of the ambient light. Measurements were performed at room temperature, around 21°C , which remained stable during all measurements. Only the performances of the single of the optimal design of the single scintillator configuration presented in Chapter 3 were evaluated. Its main components are a 0.1 mm thin p-terphenyl scintillator coupled through a 2 mm light guide to a 8×8 SiPMs array. The scintillator is covered with an ESR specular reflector and an aluminium sheet for light shielding. The overall field of view is 25.7×25.7 mm². The acquisition readout electronics with its related optimal setting have been presented and discussed in Chapter 2.

4.1.1 Estimation of positron sensitivity

The positron sensitivity, commonly expressed in counts per second per kBq (cps/kBq) or cps/(kBq/ml), represents the ratio between the count rate measured by the probe and the real activity or radioactive concentration of the source under evaluation. The sensitivity directly impacts the capability of the probe to identify small tumor uptakes and also the acquisition time needed for their detection. The positron sensitivity depends both on the photodetection efficiency of the detection device and the size of the sensitive area.

The sensitivity was estimated using a point source of ^{18}F -FDG, obtained by the evaporation of a $2\ \mu\text{l}$ drop of radioactive solution (2.7 kBq) on a $1\ \mu\text{m}$ thick layer of mylar. The surface of the probe was put in contact with the mylar so as to position the source in the central area of the field of view. The count rate was measured during several ^{18}F half-lives (110 minutes). Time evolution of the count rate was estimated from repeated acquisitions of 2 minutes. The number of detected events was estimated on a circular Region of Interest (ROI) centered on the source image, containing 99% of the overall detected events, and corrected for the γ noise contamination and the detector noise, mainly due to the DCR of the SiPM array. The γ noise contamination was estimated from an acquisition of the point source shielded by a $200\ \mu\text{m}$ thick tungsten layer, interposed between the detector entrance window and the source, that allows the complete absorption of the positrons.

A second ^{18}F point source obtained from a $0.2\ \mu\text{l}$ (2.42 kBq) evaporated drop was used to evaluate the β sensitivity of the probe as a function of the depth of the tumor in tissues. The interposing tissues are simulated by overlapping plastic sheets of $100\ \mu\text{m}$ thickness between the source and the entrance window of the detector. The acquisition time for each image was set to 6 minutes.

The lower detection limit of the probe, in the advantageous but unlikely case of absence of noise due to the non-specific uptake of the radiotracer, can be quantified knowing the probe sensitivity and the detection noise. The detection limit is the smallest mean count rate value (corrected by the background noise), which highlights the presence of a radioactive source, associated to an error probability to make the false assumption that the specimen under analysis do not contain any radioactivity, when it does. The detection limit L_d corresponding to a error probability of 2.5% is given by the formula:

$$L_d = 5.54 \cdot \frac{\sqrt{N}}{t} \quad (4.1)$$

where N is the average number of counts of the background noise measured during an acquisition time t [Prichard *et al.* 1992]. The detection limit is therefore a function of the acquisition time. The minimal detectable activity can be estimated from the sensitivity S using the equation:

$$A_d = 5.54 \cdot \frac{\sqrt{N}}{S \cdot t} \quad (4.2)$$

The number of background noise events is estimated, in absence of radioactivity sources, on a ROI of the same dimension as the one used to estimate the sensitivity with the point source.

4.1.2 Spatial resolution performances

Compared to the intrinsic spatial resolution measured with a collimated source, the overall spatial resolution of the imaging probe measured from a non-sealed source is degraded by the positron isotropic emission and by their scattered path through the neighboring tissues (average path length of approximately 1.5 mm for positrons at 242.8 keV, corresponding to the mean energy of ^{18}F). The global spatial resolution was estimated with the $0.2\ \mu\text{l}$ ^{18}F -FDG point source described in the section above. The resolution was calculated from the

average value of the full width half maximum (FWHM) of a bidimensional gaussian curve fit of the point source image. The influence on the spatial resolution of the source depth into tissues was as well evaluated. In the same way as for sensitivity, multiple plastic layers of $100\ \mu\text{m}$ were overlapped between the source and the entrance window of the detector to simulate the presence of interposing tissues.

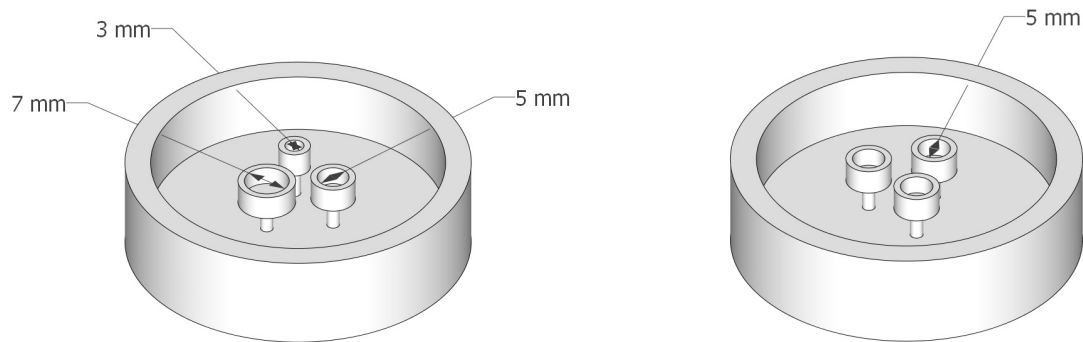


Figure 4.1 – Drawing of the plastic structures of the phantom designed to mimick three tumor focal areas of 3, 5 and 7 mm of diameter (left) and three tumor focal areas of 5 mm diameter (right), all of 3 mm height. The small wells simulating tumor uptake area are settle at the center of a 5 cm diameter and 1 cm height container simulating normal tissues uptake. The distance between the centers of each small wells was set to 1 cm.

4.1.3 Phantoms geometry and uptakes

Multiple phantom configurations were used to evaluate the ability of the probe to detect tumor uptakes of small dimensions for different background noise conditions. The phantoms were made with plastic containers filled with water in which were diluted the ^{18}F -FDG radiotracer. They were made with a 3D printer and designed to reproduce small tumoural uptake volumes embedded in a larger volume of healthy tissues with non-specific uptake of the radiotracer (Fig. 4.1). Water solutions with different ^{18}F -FDG concentrations were used to simulate various ratios between the radiotracer uptake in normal and tumoral tissues.

Three phantom configurations were realized: one simulating healthy tissues without tumor uptakes, a second simulating three tumor uptake areas of growing diameters and a third one simulating three equal tumor areas. Design of these last two phantoms is presented in Figure 4.1. For all phantoms, the normal tissue volume was modeled by a 1 cm height and 5 cm internal diameter cylindrical container, that was filled with 14 ml of water. For the second configuration (Fig. 4.1 left and Fig. 4.2), three cylindrical wells of 3, 5 and 7 mm inner diameters and 3 mm height were fixed on small support (6 mm high) and placed in the central area of the 14 ml container. The third phantom configuration was produced with an analogue structure but all tumors wells had a 5 mm inner diameters (Fig. 4.1 right). The distance between the center of each well was set to 1 cm. Due to the capillary effect, creating a meniscus on water surface, the small containers were not completely filled up. The water volumes of 14, 39 and $77\ \mu\text{l}$ for the 3, 5 and 7 mm diameter containers, respectively, were

chosen to obtain a 2 mm tumor high.

In order to simulate a larger γ background noise, closer to that encountered in realistic clinical environments, the phantoms previously described was placed just above a hemispherical volume of 15 cm diameter filled with 1.1 l of water with a radiotracer concentration equal to that used in the phantom container modeling healthy tissues (Fig. 4.2). For each phantom configuration, the entrance window of the imaging probe was placed at the same level as the upper part of the 5 cm diameter container. This corresponds to a mean distance of 2 mm from the water surface in the tumor wells.

The first phantom was used to quantify the background noise in the absence of tumors and also to obtain an uniform irradiation of the detector surface in order to evaluate the spatial uniformity of its response. The second and third phantoms were used to estimate the imager ability to detect tumor of decreasing dimensions. Three sets of measurements were realized with the second phantom corresponding to three uptake ratios between the radiotracer concentration in tumor area and healthy tissues: 2:1, 4:1 and 8:1. The different uptakes were obtained using water solution with appropriate concentrations of ^{18}F -FDG. For the third phantom, all containers were filled with different water concentrations to simulate the uptake ratios of 2:1, 4:1 and 8:1.

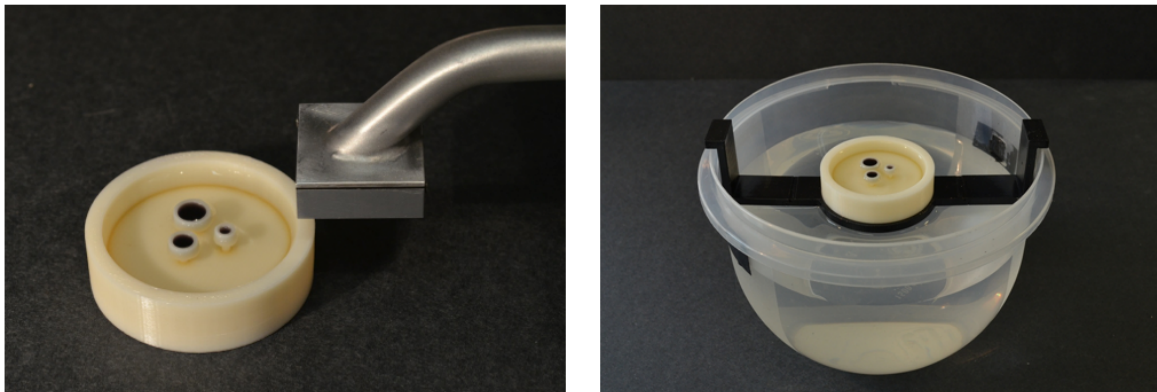


Figure 4.2 – Photography of the phantom filled with radioactive water explored with the positron imaging probe. The healthy tissues are modeled by a 5 cm diameter and 1 cm height cylinder and the tumor remnants by three wells with a diameter of 3, 5 and 7 mm and a height of 8 mm (left). The cylindrical container placed above the hemispherical volume modeling a large gamma background noise (right).

4.1.4 Evaluation of tumor detectability

The ability of an imaging system to detect small tumor uptake areas in a noisy environment can be evaluated thanks to the two following parameters: the Peak-to-Valley ratio (Peak-Valley) and the Tumor-to-Background Ratio (TBR). The Peak-Valley is defined as the ratio between the tumor signal (S_{tumor}) and the normal tissues signal (S_{normal}). The tumor signal is estimated as the number of counts detected inside a ROI over the tumor, with a diameter optimized in terms of TBR and Peak-Valley values for each tumor focal area.

S_{normal} is calculated as the number of counts detected in multiple ROIs over the normal tissues region and normalized by the area of the ROI used to estimate the tumor signal. This measure allows to take into account the variability of the background noise around the tumor. The TBR is calculated as the number of standard deviations in the difference between these two signals [Barber *et al.* 1989]:

$$TBR = \frac{S_{tumor} - S_{normal}}{\sqrt{\frac{1}{2}(\sigma_{S_{tumor}}^2 + \sigma_{S_{normal}}^2)}}, \quad (4.3)$$

where the standard deviation σ_S of the signal is equal to the square root of the signal itself assuming that radioactive detection follows a Poisson probability law.

The Peak-Valley parameter depends solely on the uptake ratio. Therefore, its value was calculated on a phantom image of 10 minutes acquisition time, in order to reduce the statistical fluctuations. By contrast, the TBR depends both on acquisition time and radiotracer uptake in tissues. The original pool of events was therefore resampled starting from a larger statistics to simulate acquisition times and/or radiotracers concentrations compatible with the length of a realistic surgery. Events are randomly resampled according to the probability needed to obtain the reduced-count image of wanted acquisition time and radiotracer uptake [White & Lawson 2015]. A total acquisition time of 10 minutes was obtained with repeated samples of 2 minutes, for each phantom. Due to the relatively short half life of ^{18}F (110 minutes), the radiative decay was considered as negligible during each two minutes acquisition, but was corrected between the samples during image resampling to correctly simulate the desired acquisition time and radiotracer uptake. We simulated acquisition times of 10, 30 and 60 s. The uptake parameters of three available clinical radiotracers were also simulated. They correspond to the uptake values in brain tumors reported in the literature for ^{18}F -FDG (tumor uptake of 25.9 kBq/ml, uptake ratio of 2:1), ^{18}F -FET (13.3 kBq/ml, 4:1) and ^{18}F -Choline (5.9 kBq/ml, 8:1) [DeGrado *et al.* 2001, Mertens *et al.* 2012, Wang *et al.* 2007, Pöpperl *et al.* 2006].

The tumor detectability was quantified as the TBR average and its standard deviation over 20 resampled images for each phantom configuration. The detectability threshold was defined as the minimum necessary TBR value for the surgeon to state that the differences observed on the image really corresponds to a tumor uptake surrounded by normal tissues. The threshold relative to the TBR was set to 4, corresponding to a Confidence Level of 99.5% of detecting a true positive tumor area [Barber *et al.* 1989, Dickerscheid *et al.* 2013].

All phantom images are presented after spatial uniformity correction to remove artifacts due to the discretized nature of the photodetector and the finite size of the scintillator. The image reconstructed from the flood field irradiation of the detector with the phantom configuration with no tumor uptake (activity concentration of 3.8 MBq/ml and acquisition time of 10 minutes) allows to evaluate the non-uniformity of the spatial response. Based on this image, 64×64 weighting factors, corresponding to the inverse of the counting in each area, were calculated. These factors were normalized by the minimum weighting factor value measured in the central region of the detector to build the uniformity correction matrix. The spatial uniformity correction is obtained by multiplying each image of the phantoms by the correction matrix. Finally, the image is blurred by convolution with a gaussian filter to reduce

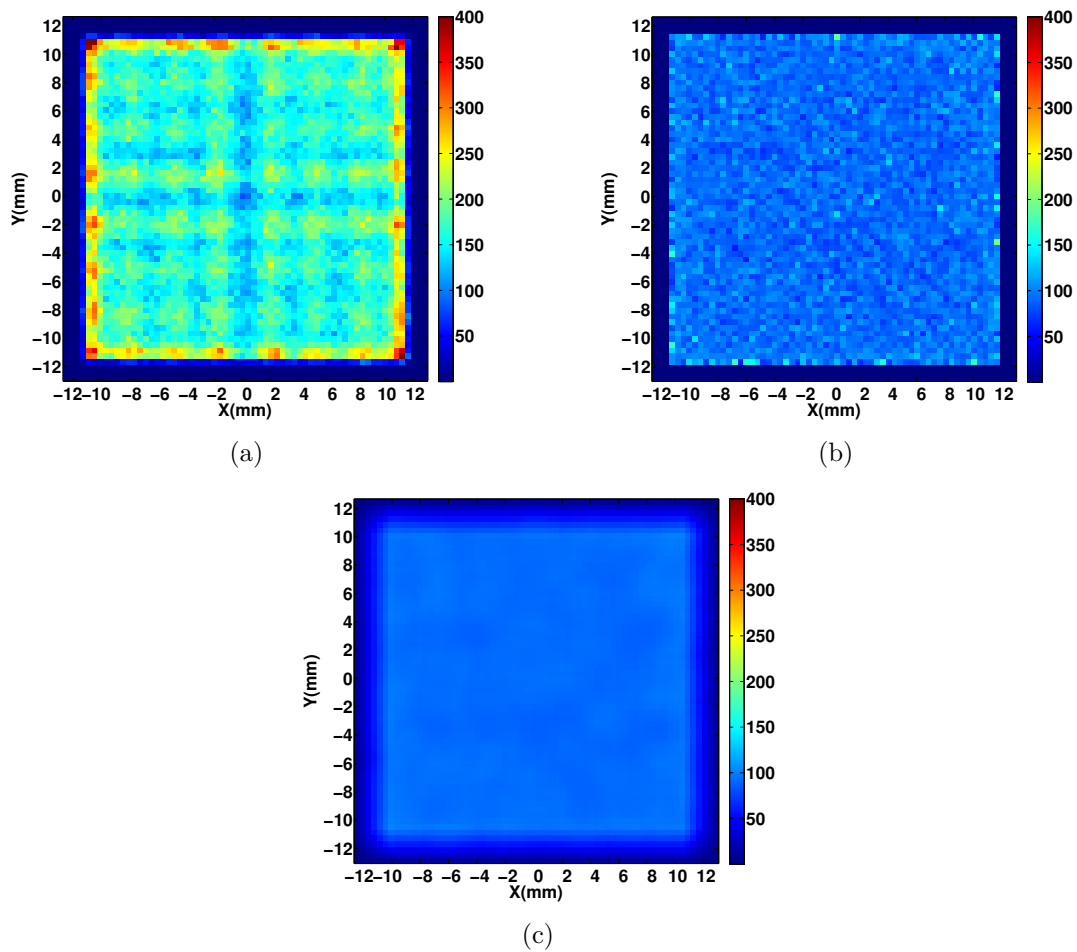


Figure 4.3 – (a) Flood field image obtained with the phantom with no tumor focal area (activity concentration of 3.8 MBq/ml and acquisition time of 10 minutes). (b) Flood image after uniformity correction and (c) application of a gaussian smoothing filter. The flat field image used to build the correction matrix was taken using the same set-up but at a different time than the image shown here.

the image noise and therefore improve tumor visualization. The effect of the uniformity correction and smoothing on the image is shown in Figure 4.3. The image obtained from the uniform irradiation with the phantom with no tumor focal area and reconstructed with the barycenter method after a charge subtraction of 8 photoelectrons is presented in Fig. 4.3a. The image inhomogeneity is associated to an integral uniformity of 36.8% and differential uniformity of 24.1% (see Section 3.2.1). The application of the uniformity correction allows to reduce these parameters to 15.4% and 12.8% respectively, as shown from the image in Fig. 4.3b. The small difference between IU and DU demonstrates that there is no systematic spatial variation across the field of view. The effect of the smoothing filter on the image is presented in Figure 4.3c.

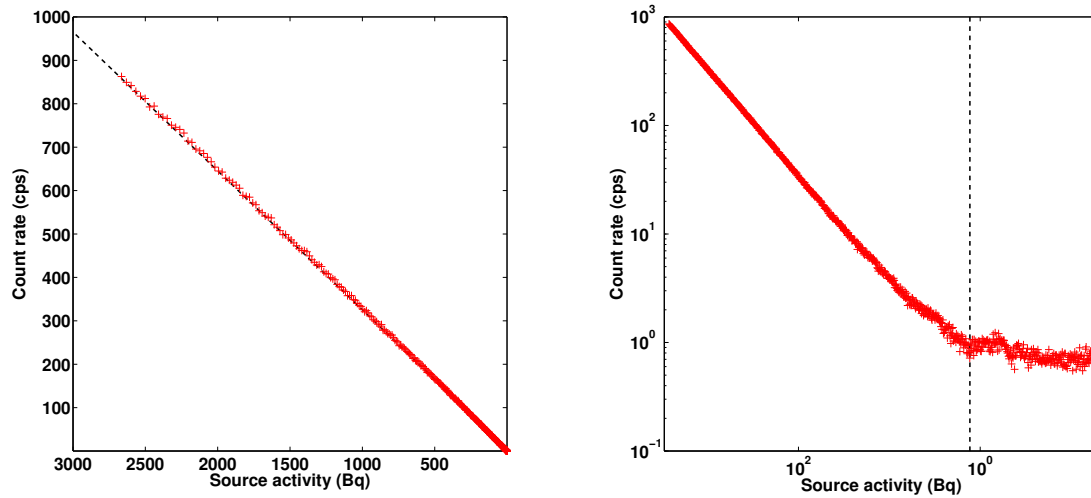


Figure 4.4 – Count rate measured by the imaging probe, with (left) or without (right) subtraction of γ contamination and detector noise, as a function of the activity of a $2 \mu\text{l}$ point source of ^{18}F -FDG. Each point corresponds to an acquisition time of 2 minutes. A linear fit allows to estimate the sensitivity as the slope of the line, represented with a dashed line (left). The vertical dashed line on the right graph represents the minimal detectable activity of 1.3 Bq. The error bars of each counting measurement are too small to be visible.

4.2 Spatial and sensitivity performances

4.2.1 Sensitivity and minimal detectable activity

The linear decay of the count rate measured by the probe, over a time lapse corresponding to 15 half-lives of the ^{18}F , is shown in Figure 4.4 as a function of the activity for the $2 \mu\text{l}$ point source. The slope of the line allows to estimate the counts detected per Bq of source activity and therefore the sensitivity of the probe (the measurement uncertainty of the activity of the $2 \mu\text{l}$ point source was considered to be negligible). The linear fit gives a slope value of $321 \pm 0.6 \text{ cps/kBq}$ for a threshold on the event total energy of 34 photoelectrons, corresponding to a detector noise of 10 Hz on the whole field of view. For an acquisition time of 2 minutes and the 34 photo-electrons energy threshold, the minimal detectable activity is equal to 1.3 Bq. However, this limit refers to the unlikely case of the absence of biological background noise due to the non-specific radiotracer uptake.

The variation of the β sensitivity as a function of the applied energy threshold is compared to the frequency of the detector noise on the whole FoV in Figure 4.5. The detector noise was measured without radioactive source at a temperature of 21°C . The sensitivity value remains constant (within 1% of variation) up to an energy threshold of 100 photoelectrons, which reduces the detector noise frequency down to 0.2 Hz. The slight influence of low energy threshold on β sensitivity is due both to absorption of low-energy particles in the optical coating and light shielding, to the shape of the emission energy spectrum of ^{18}F (see Section 3.2.3). The variation of the detector noise frequency as a function of the energy threshold illustrates its different components (Fig. 4.5). The main one, ranging from 0

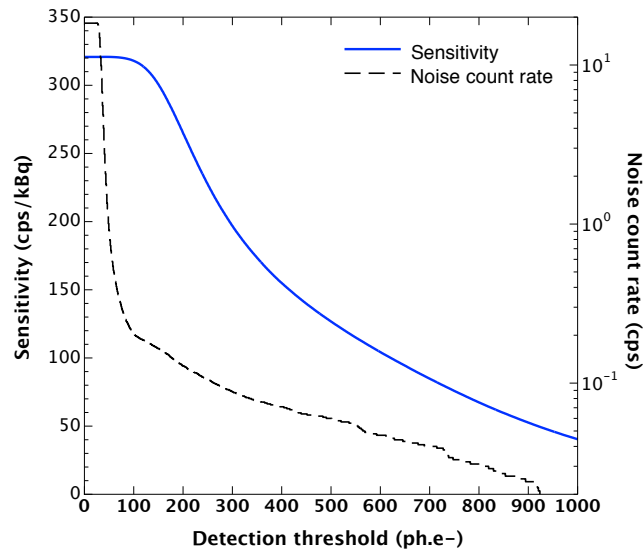


Figure 4.5 – Sensitivity and noise values as a function of the threshold applied on the event total energy. The measurements were done with a 2 μl point source of ^{18}F -FDG. The error bars of the sensitivity are too small to be visible and are not plotted for the noise to improve clarity.

to 100 photoelectrons, is the dark count noise of the SiPM array. Beyond 20 photoelectrons, the noise is dominated by the natural radioactivity (^{40}K , ^{238}U , etc . . .) and the cosmic rays whose total contribution in our detector is around 0.2 cps. The detector noise intensity defines in part the minimal activity that can be detected by the probe in the absence of biological background noise. For an acquisition time of 2 minutes and a 100 photoelectrons energy threshold, the minimal detectable activity is equal to 0.25 Bq.

The sensitivity measured from a point source in contact with the detector entrance window mainly depends on the detection efficiency of the probe. In the ideal case of a detector presenting a β detection efficiency of 100% and considering a geometrical efficiency of 50% (half of the events are emitted in the opposite hemisphere of the detector surface), the achievable sensitivity would be of nearly 500 cps/kBq. Considering the branching ratio of the positron emission of the ^{18}F , the maximum sensitivity would be 480 cps/kBq. The β sensitivity is also strongly impacted by the absorption of the positrons in the optical coating and light shielding materials. As discussed in Section 3.2.5, GATE simulations of the detector head placed in contact with a ^{18}F phantom allowed the estimation of this absorption. For a 10 μm thick aluminum layer coupled with a 65 μm thick ESR layer, 24% of the positron entering the detector do not reach the scintillator. Of these events, 2.6% are backscattered outside the detection head and 21.4% are absorbed, mainly in the optical coating materials. Therefore, even in the optimal case of detection of all particles interacting inside the scintillation volume, the β sensitivity of the probe would be limited to 365 cps/kBq. The additional loss of events observed experimentally is due to the detection efficiency of the detector that can be estimated to 88% for β particles emitted by a ^{18}F source. This detection efficiency is mainly influenced by the charge threshold associated to the electronic trigger that removes low-energy events. Therefore, the detection efficiency is indirectly dependent on the dark count

noise of the SiPMs array.

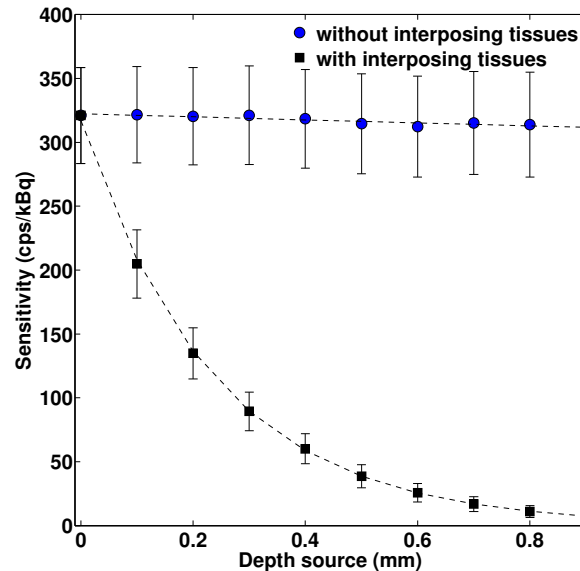


Figure 4.6 – Probe sensitivity as a function of the distance between the point source and the entrance window of the detector with and without interposing layers of plastic simulating the presence of tissues. The measurements were done with the $0.2 \mu\text{l}$ point source of ^{18}F -FDG. The curves are fitted with an exponential and linear function, respectively. Error bars represent the errors associated to the sensitivity measurements estimated by considering the statistical fluctuations of the counting rates and the 10% uncertainty of the activity of the $0.2 \mu\text{l}$ point source.

The presence of tissues between the source and the detector surface strongly affects the sensitivity, due to the short range of positrons in tissues. Figure 4.6 presents the values of the sensitivity as a function of the distance between the $0.2 \mu\text{l}$ point source of ^{18}F -FDG and the detector, with and without interposing plastic layers. One can see that the sensitivity exponentially decreases as a function of the increasing depth of the source in tissues with an absorption coefficient of 4.4 mm^{-1} . Its value drops to 38.6 cps/kBq when an interposing tissue layer of $500 \mu\text{m}$ is present, corresponding to a reduction of 87.9% compared to the sensitivity in contact. Without interposing tissues, the sensitivity slowly decreases with the distance with a loss of $7.5 \pm 1.8 \text{ cps/kBq per mm}$, estimated from the linear fit of the experimental results.

4.2.2 Spatial response

Figure 4.7 compares the variation of the spatial resolution of the positron probe as a function of the distance between the source and the detector with and without interposing tissues. The spatial resolution, evaluated with a non-sealed ^{18}F -FDG point source, degrades from 1.09 mm in contact to 1.44 mm when the source was set at $500 \mu\text{m}$ depth. The FWHM value increases by approximately 0.48 mm for each additional $100 \mu\text{m}$ layer of plastic. The

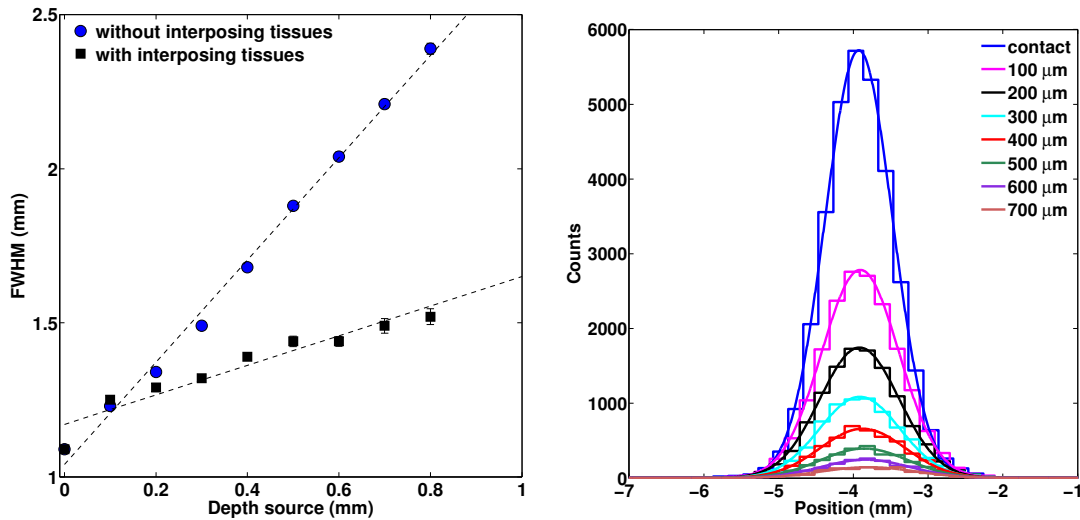


Figure 4.7 – Spatial resolution (FWHM) as a function of the source-detector distance with and without interposing tissues (left). Profile of the source ($0.2 \mu\text{l}$ dried drop of ^{18}F -FDG), for different depth in tissues (right). A Gaussian curve fitting is overlapped on each profile. For most of the points, the error bars, representing the fit goodness, are too small to be visible.

resolution degradation in presence of tissues is less important than in air due to absorption of β particles in the medium. Positrons emitted with large incident angles have longer paths to do before reaching the detector surface and therefore higher probability to be absorbed in tissues. This effect reduces the spread of the source image. The strong β absorption is clearly shown in Figure 4.7. The width of the gaussian function fitting the source profile quickly increases while the curve integral decreases according to the sensitivity drop shown in Figure 4.6.

4.3 Tumor detectability evaluation

The ability of the positron probe to detect small tumors depends on radiopharmaceutical uptake in tissues. Therefore, we studied the tumor detectability as a function of the radio-tracer uptake in tumor for different uptake ratio between the tumor and the healthy tissues. The influence of the intensity of the γ background noise was evaluated as well. Finally, we present the probe detection performances for small tumors and uptake parameters mimicking three available clinical radiotracers.

4.3.1 Influence of background noise

The 511 keV annihilation γ rays generate a background noise signal that overlaps to the positron one, deteriorating the signal-to-noise ratio and therefore the ability of tumor detection. The influence of the background noise on tumor detectability was studied using a set of phantoms where the volume simulating the non-specific uptake tissues was increased.

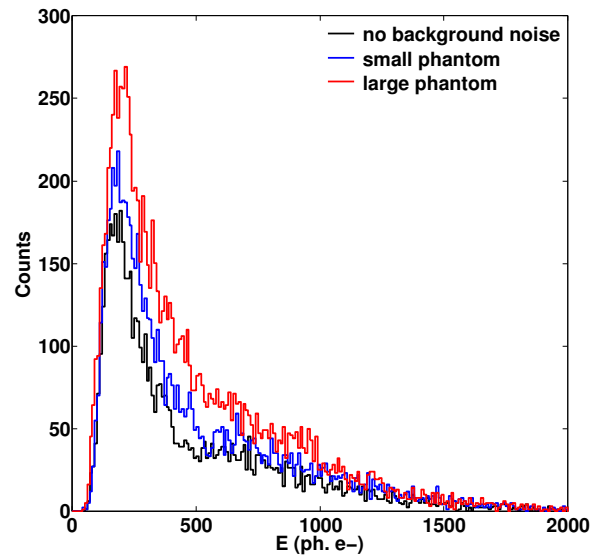


Figure 4.8 – Energy spectra of the detected particles obtained in the ideal case of radiotracer uptake only in tumor (black), with the phantom simulating small non-specific uptake volume (magenta) and the one simulating large non-specific uptake volume (red). All spectra are calculated on a ROI placed on the image of a 5 mm diameter tumor with 4:1 uptake ratio.

The ideal case, when the radiotracer targets only tumoral cells (absence of any biologic background noise) was simulated by filling only the tumor wells in the phantom. This acquisition allows to estimate the positron signal intensity. Figure 4.8 confronts the energy spectra obtained for the phantoms reproducing different background noise. The uptake in the 5 mm diameter tumor is 13.3 kBq/ml and the uptake ratio is 4:1, which correspond to the uptake parameter of ^{18}F -FET in brain tumors. The spectra relative to the positron signal is compared to that obtained in presence of a small (~ 46.6 kBq) and large ($\sim 3.7 \cdot 10^3$ kBq) non-specific uptake volume. All spectra were calculated on circular ROIs of equal area defined over the image of the 5 mm diameter tumor. Since the simulated radiotracer activity in tumor is unchanged from one phantom to the other, the variations between the spectra were mainly due to the increasing γ background noise generated by larger non-specific uptake volumes (the spatial selection with the ROI over the tumor image allows to remove most β contamination coming from the healthy tissues). The additional noise component represents 22.1% of the positron signal for the smaller noisy volume. For the larger one, simulating a more realistic clinical environment, 42.3% of the detected events are due to γ generated in non-specific uptake areas.

The background activity increases by a factor of 80, between the small and larger non-specific uptake volume phantoms. This induces a Peak-Valley reduction of nearly 69% for the 5 mm diameter tumor, from 2.52 ± 0.06 to 1.74 ± 0.05 . The TBR value progressively decreases going from 15.61 ± 1.06 to 11.06 ± 1.05 , for rising γ background noise and an acquisition time of 30 s. Figure 4.9 shows the effect of the increased noise contamination on images. It is clearly visible that the increasing background noise level of the larger non-specific uptake volume compromises the detectability of the 3 mm diameter tumor. Its TBR decreases from

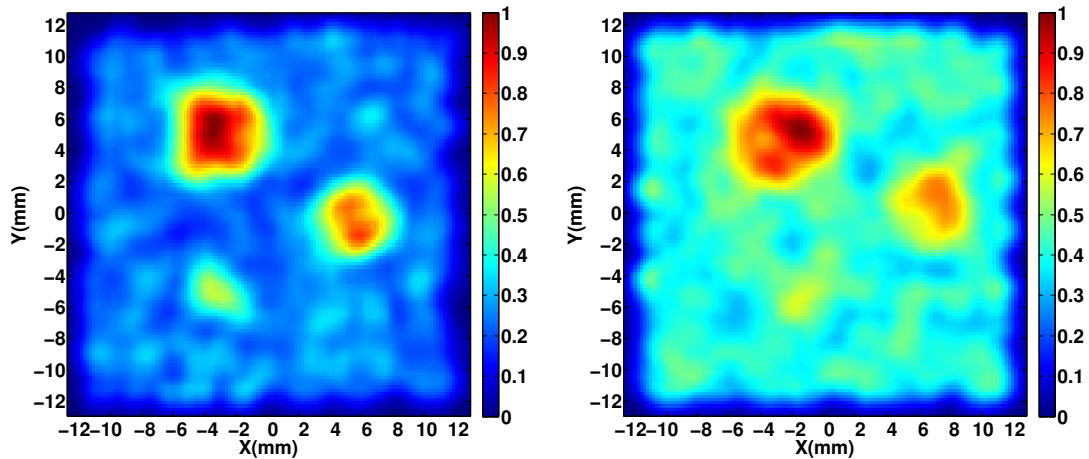


Figure 4.9 – Images of the phantom with the 3 mm, 5 mm and 7 mm diameter tumors filled with a concentration of 13.3 kBq/ml and an uptake ratio of 4:1. The acquisition time is 30 s. The images are obtained with the small non-specific uptake region phantom (14 ml, ~ 46.6 kBq) (left) and the large non-specific uptake volume (1.1 l, $\sim 3.7 \cdot 10^3$ kBq) (right). The TNR value for the 3, 5 and 7 mm tumors are 7.74, 15.72 and 24.42 for the small non-specific uptake region phantom and 4.43, 11.80 and 19.82 for the large one.

7.2 ± 1.01 to 4.45 ± 0.89 , just above the limit of the detectability threshold.

4.3.2 Influence of radiotracer uptake in tumor

Figure 4.10 represents the TBR as a function of the radiotracer uptake in a tumor of 5 mm diameter for uptake ratios of 8:1, 4:1 and 2:1. The tumors are embedded in the large non-specific uptake volume. All TBR values were calculated for an acquisition time of 30 s. Since the TBR depends on the difference between tumor and normal tissues signals on the square root of their sum, the TBR increases as the square root of the radiotracer uptake (solid lines in Fig. 4.10). As expected, the more advantageous uptake ratio allow to obtain higher TBR values for a equivalent uptake in the tumor: for a tumor uptake of 20 kBq/ml and uptake ratios of 8:1 and 4:1, we obtain a TBR nearly 5.9 and 3.7 times higher than the one obtained with the 2:1 ratio. On the other hand, equivalent values of TBR can be obtained for the 8:1 and 4:1 uptake ratios with different radiotracer uptake concentrations in tumor. This is the case of the clinical radiotracer ^{18}F -FET (13.3 kBq/ml uptake in tumor), for which the lower specificity (4:1), compared to ^{18}F -Choline (5.9 kBq/ml in tumor and ratio of 8:1), is balanced by an higher tumor sensitivity, allowing to obtain a comparable TBR value. The minimal activity in tumor necessary to reach the detection threshold (for a 30 s acquisition time) increases from ~ 1 kBq/ml for the 8:1 ratio to ~ 2 kBq/ml for the 4:1 ratio. For the most unfavorable ratio of 2:1, the minimum uptake is reached for values higher than 25 kBq/ml.

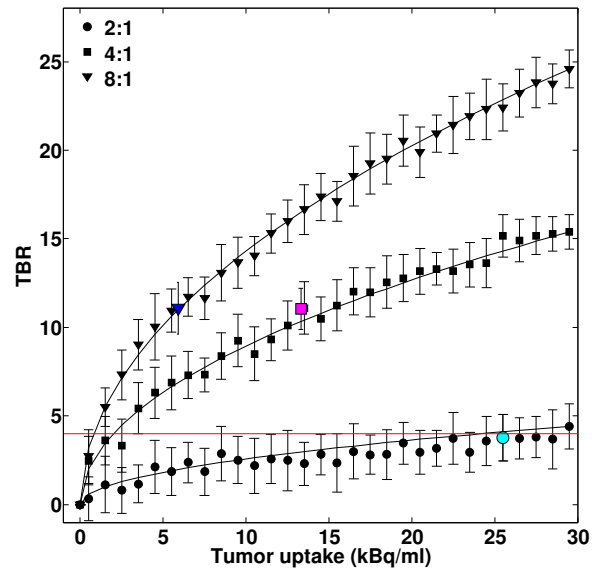


Figure 4.10 – TBR values relative to the 5 mm diameter tumor in the phantom configuration with large non-specific uptake volume, for a simulated acquisition time of 30 s. The mean values of the TBR and their standard deviations (error bars) are calculated over 20 resampled images. The three curves correspond to three uptake ratios between radiotracer concentration in healthy tissues and in tumor of 2:1, 4:1 and 8:1. The cyan, magenta and blue markers identify the TBR values obtained for an uptake in brain tumor obtained for ^{18}F -FDG, ^{18}F -FET and ^{18}F -Choline radiotracers, respectively. The theoretical trend of the TBR (square root of the tumor uptake) is adjusted on the experimental results and represented by the solid lines for each uptake ratio. The detectability threshold is represented by the red line.

Tumor \varnothing (mm)	^{18}F -FDG 2:1	^{18}F -FET 4:1	^{18}F -Chol 8:1
3	1.29 ± 1.04	2.61 ± 1.27	2.38 ± 0.80
5	1.43 ± 0.94	6.13 ± 1.37	6.01 ± 0.84
7	4.22 ± 1.42	10.21 ± 1.31	9.97 ± 0.76

Table 4.1 – TBR values are reported for the uptake ratio and concentration of the clinical radiotracers (^{18}F -FDG, ^{18}F -FET and ^{18}F -Choline) and three tumor focal areas of 3, 5 and 7 mm diameter embedded in the large non-specific uptake volume phantom. All values were calculated for an acquisition time of 10 s, compatible with the surgical use. The mean value of the TBR and its standard deviation are calculated over 20 resampled images.

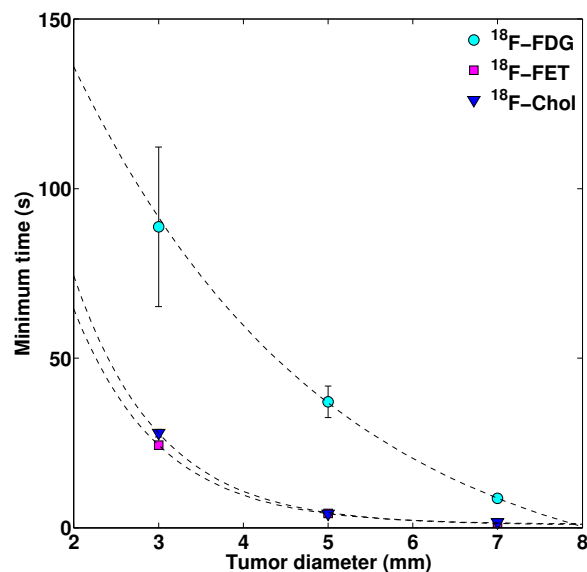


Figure 4.11 – Minimum time necessary to reach the tumor detectability threshold corresponding to a TBR of 4 for different tumor diameters and parameters of the radiotracer.

4.3.3 Detectability of small tumors

The influence of the dimension of the tumor and the characteristics of the radiotracers uptake on TBR is reported in Table 4.1 for phantoms reproducing realistic clinical uptake concentrations and environmental conditions (large non-specific uptake volume). The acquisition time was set to 10 s, compatible with the surgical procedures. Results show that for this short acquisition time, tumor with a diameter of 7 mm were detectable with all simulated radiotracers. The TBR of 4.22 was achievable with the lowest uptake ratio (2:1) thanks to the high uptake in tissues of $^{18}\text{F-FDG}$ (25.9 kBq/ml). However, for smaller tumors labelled with $^{18}\text{F-FDG}$, this acquisition time was too short to exceed the detectability threshold. On the other hand, $^{18}\text{F-FET}$ and $^{18}\text{F-Choline}$ allow both to detect 5 mm diameter tumors but none of the 3 mm tumors can be identified within a 10 s acquisition time. Figures 4.12 and show 4.13 the effect of increasing acquisition time, ranging from 10 to 60 s, on tumor visualization for three uptake configurations: $^{18}\text{F-FDG}$ (25.9 kBq/ml, 2:1), $^{18}\text{F-FET}$ (13.3 kBq/ml, 4:1) and $^{18}\text{F-Choline}$ (5.9 kBq/ml, 8:1). From these images sequences we can observe that the 5 mm diameter tumor labeled with $^{18}\text{F-FDG}$ and the 3 mm tumor diameter labeled with $^{18}\text{F-FET}$ emerge from the background noise for a 30 s acquisition time and get more visible for a 60 s. This is in agreement with the minimum acquisition time estimated at 37 s and 24 s, for the 3 mm and 5 mm diameter tumors, respectively (see Fig. 4.11). Tumors of 5 mm diameter (39 mg) can be detected in about 4 s with both $^{18}\text{F-FET}$ and $^{18}\text{F-Choline}$ radiotracers while less than 2 s are enough to identify a 7 mm diameter tumor (77 mg). Smallest tumor focal areas of 3 mm diameter (14 mg) are detectable starting from 24 and 28 s for $^{18}\text{F-FET}$ and $^{18}\text{F-Choline}$, respectively. These results demonstrate that the imaging positron probe is able to detect small tumor uptakes in a short time thanks to its high β sensitivity. This is perfectly suitable for surgery, allowing to perform a time-efficient

investigation of resection boundaries. Table 4.1 and Figure 4.12 re-emphasize the similar behavior of ^{18}F -FET and ^{18}F -Choline in term of tumor detectability, resulting from a balance between tumor uptake and uptake ratio. Tumors labels with ^{18}F -FDG, requires longer detection times not compatible with the surgery duration, especially for tumors smaller than 5 mm diameter.

4.4 Discussion and conclusions

The performances of our intraoperative positron imaging probe were evaluated during a preliminary study on ^{18}F -FDG phantoms. The optimization of the probe design and the materials choice has allowed us to reach a β detection sensitivity of 321 cps/kBq. This sensitivity value is comparable to that reported by [Heckathorne *et al.* 2008] obtained with a imaging probe based on a scintillation detector readout by a SiPM array. Their probe presents a sensitivity of 360 cps/kBq obtained without any light shielding material, which can significantly reduce the positron signal and a spatial resolution value more than doubled (2.1 mm) compared to the one obtained with our optimized prototype. Analogously, our sensitivity is about 28.3% greater than that (230 cps/kBq) reported by [Levin & Hoffman 1999] and more of the double than that (108 cps/kBq) reported by [Stolin *et al.* 2010] (see Section 1.2.2.4). Thanks to the high β sensitivity of our probe and its low intrinsic sensitivity to the background noise contamination due to the thin layer of p-terphenyl (0.1 mm), tumors of 5 mm diameters can be detected in less than 4 s for uptake parameters of available clinical radiotracers such as ^{18}F -FET (13.3 kBq/ml tumor uptake and uptake ratio of with 4:1) and ^{18}F -Choline (5.9 kBq/ml, 8:1), which perfectly fit the timing requirements of surgery. The ability to detect such small tumor uptake can be enhanced thanks to an improvement of the probe β sensitivity. As demonstrated in our study, this can be achieved by replacing the ESR optical coating with a less dense and/or thinner material, such as PTFEs as well as using a new generation of SiPM featuring a reduced thermal and correlated noise which permits to set a lower trigger lever for the readout electronic (see Sec. 3.2.3). However, the detection of small tumors labeled with low-specificity radiotracers such as ^{18}F -FDG is mainly hampered by the γ contamination. An active rejection needs to be implemented in order to further decrease this contamination. In that context, the dual scintillator configuration (see Section 3.3) should help to improve the performances of the positron imaging probe in very noisy environments. Its evaluation on radioactive phantoms in a pre-clinical context is on going. Another solution to eliminate the annihilation γ background noise would consist in the use of β^- radiotracers, as proposed by [Collamati *et al.* 2015c]. Our β imaging probe can be used with β^- emitters and its performances in terms of spatial resolution and sensitivity would be similar to the ones obtained for positrons with the same energy. However, at the moment, the number of β^- -emitting therapeutic radiotracers that could be used for radio-guided surgery is still very low (^{90}Y -DOTATATE or ^{90}Y -DOTATOC), which restricts the scope this application (brain tumors, neuroendocrine tumors).

All the above analysis were done for a given realistic geometry and activity of the tissue phantom. The background noise will roughly linearly increases with the radial dimension of the radiolabeled healthy volume around the tumor for an ideal uniform non-specific con-

centration of the radiotracer. The close proximity of high activity areas of normal uptake will also impact the intensity of the background noise and thus hamper further the detection of small tumor residues. On the other hand, some of the experimental conditions do not match a real exploration of the surgical cavity. During the phantom measurements, the distance between the entrance window of the probe and the tumor source was around 2 mm. First, this decreases the number of detected events due to the collimation effect by the wall of the tumor containers. This also degrades the spatial resolution of the detection system (Fig. 4.7) and thus, increases the partial volume effect which reduces the apparent tumor-to-background ratio. These two phenomena have more impact on small tumors and suggest that under optimal conditions, where the imaging probe is placed in direct contact with tumor tissues, smaller lesions could be detected or shorter acquisition times could be achieved.

Nowadays, only a few preliminary and not exhaustive studies have been reported concerning the preclinical evaluation of positron imaging probes on radioactive phantoms or animal models. Therefore, we compared the results obtained with our phantom study to those of the studies performed with clinical PET [Erdi 2012, Andersen *et al.* 2013, Metser *et al.* 2016]. These studies showed that tumor lesions diameter have to be at least of the order of 7 mm (200 mg) and the uptake ratio of the ^{18}F -FDG around 5:1 to be detected under clinical scanning condition using modern clinical PET scanners with a resolution limit of 4 mm. The detection ability is constraint by the limited PET sensitivity and the partial volume effect, causing an apparent loss of activity in small regions, due to the limited resolution of the tomography system. The positron imaging probe presented here has a much higher sensitivity than a standard PET system (32% compared to around 10%) and a better spatial resolution (1 mm compared to about 4 mm), which improve the ability to detect small radiolabeled tumors.

Finally, the phantom study also emphasizes the intrinsic advantages and constraints of β detection compared to γ detection. The short range of β particles allow to increase the spatial selectivity and sensitivity but prohibits the localization of tumors at a depth greater than 1 mm (Fig. 4.6). Depending on the clinical applications, β and γ detection can be associated, for example, to localize deep-seated tumors and control their surgical resection margins.

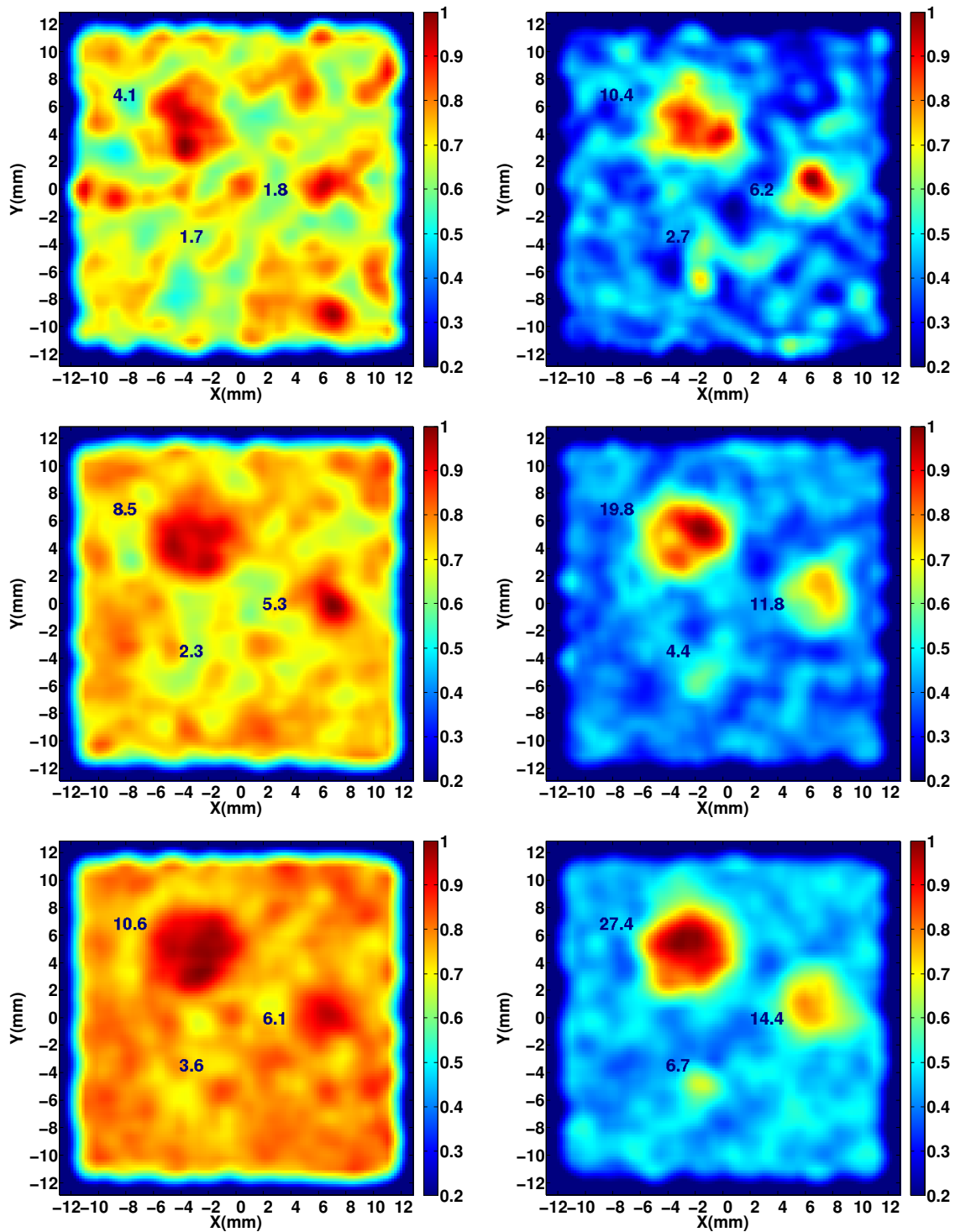


Figure 4.12 – Images of phantom for ^{18}F -FDG (left) and ^{18}F -FET uptake (right), for the increasing acquisition times of 10, 30 and 60 seconds (from top to bottom). The relative TBR values are reported on the images for each tumoral area. The images were selected in order to be representative of the mean TBR value calculated over 20 resampled images.

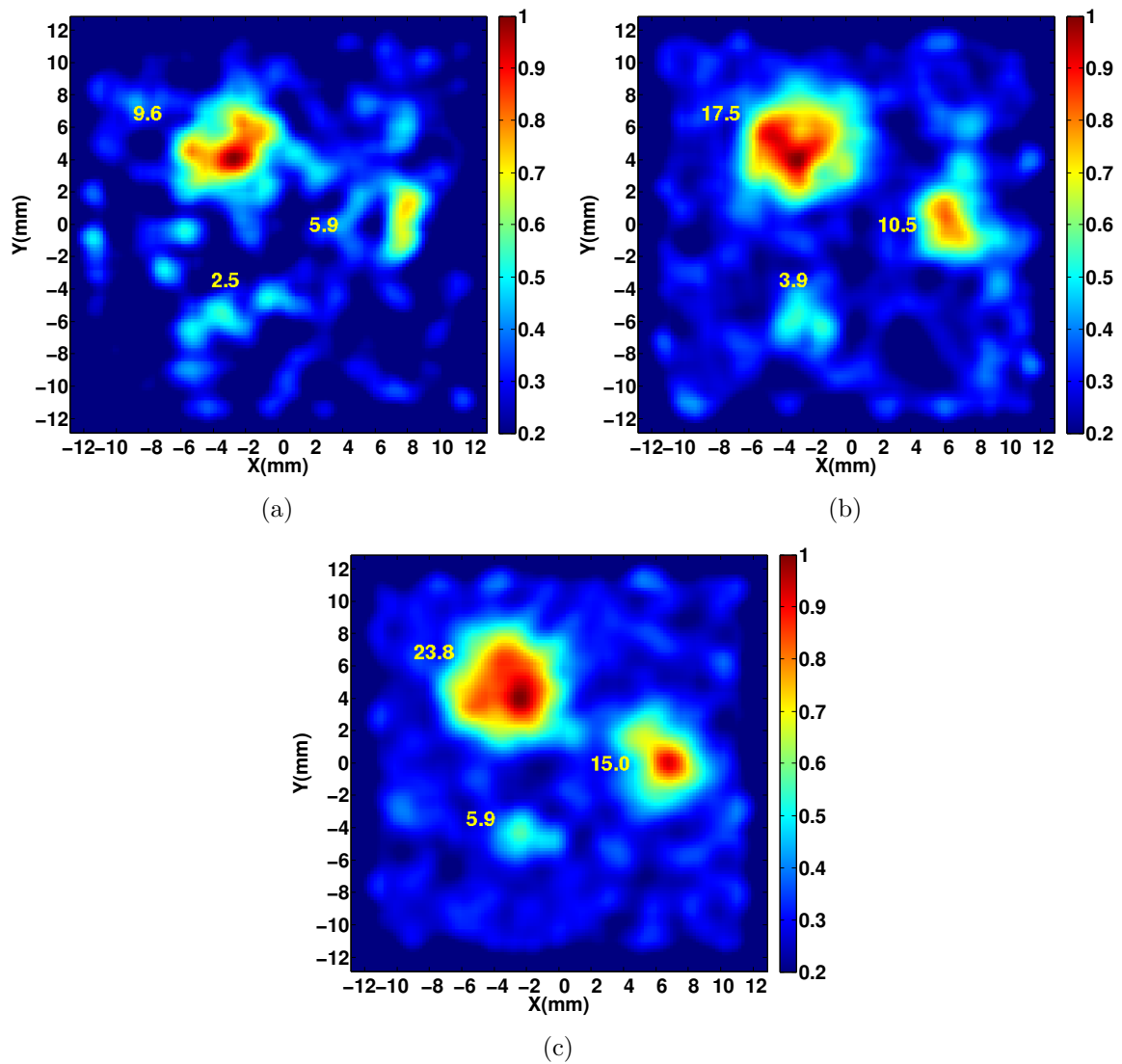


Figure 4.13 – Images of phantom for ^{18}F -Choline uptake for the increasing acquisition times of 10 (a), 30 (b) and 60 (c) seconds. The relative TBR values are reported on the images for each tumoral area. The images were selected in order to be representative of the mean TBR value calculated over 20 resampled images.

Conclusions

The accurate resection of tumor tissues is one of the main step in the therapy of solid tumors. In other to be effective the surgery has to remove as much tumoral tissues as possible while preserving the surrounding healthy tissues. The imaging technologies allow to guide the surgeon in the tumor localization and give information about its size, shape and stagis. Nowadays, alongside to the standard pre-operative imaging tools, intraoperative imagine techniques are getting higher importance thanks to their ability to provide real time information of the delineation of tumor boundaries. Among these techniques, the radioguided surgery is a promising field for accurate and sensitive tumor detection. Most available systems are based on the detection of γ radiations. The development of new tumor-seeking radiotracers labeled with β -emitters renewed the interest for intraoperative beta detection as a complementary tool. The β detection provides higher sensitivity and signal-to-noise ratio for shallow tumors making it particularly adapted to the delineation of the tumor margins and inspection of the surgical cavity for the research of small tumor remnants. However, the constraints imposed by the short range of β particles in tissues requires the development of extremely compact devices that can be directly introduced inside the surgical cavity in contact with the surveyed tissues. A new generation of photodetector, the SiPM, results nowadays as the most promising for the development of intraoperative β probes, thanks to their high compactness and their performances which are comparable to that of vacuum photomultipliers tube. In this context, this work aimed to the development and evaluation of two intraoperative miniaturized imaging probes based on the use of scintillators coupled to a SiPM array. The first prototype uses a reduced sensitive volume to minimize the γ background noise while the second one implements a discrimination methods allowing to subtract the noise contamination.

The single scintillator detection head was optimized in terms of β sensitivity, γ noise contamination influence, spatial performances and uniformity of response. This was done by evaluating, through Monte-Carlo simulation and systematic measurements, the influence of the geometry and material of its different components, including scintillator, light spreading window, optical coating and light shielding. Other optimization concerns the SiPM array, the readout electronics and the image reconstruction methods. As a results, we found that the detection head design allowing the best trade-off between spatial performances and minimization of the γ background noise contamination was the one coupling a 0.1 mm thick p-terphenyl scintillator with a light guide of 2 mm thickness. The second detection head is based on a stack of two scintillation material, one sensitive to β particles and γ rays (0.2 mm thick p-terphenyl scintillator) and the other only sensitive to the background γ noise (pixelized LYSO:Ce scintillator). The discrimination of the events coming from the two scintillator is made from the analysis of the distribution of the light readout from the SiPM array. This configuration was optimized to obtain the best event discrimination ability based on clustering methods. The optimal design of both imaging probes present submillimetric spatial performances and extremely low distortion on the whole field of view. These spatial performances and the β sensitivity were shown to be not sensitive to temperature

variation thanks to the development of a correction method which adjust in real time the supply voltage of the SiPM according to their temperature. Finally, we developed a fully operational probe by incorporating the single scintillator detection head into a mechanical housing where a new miniaturized readout electronic fits inside the probe handle.

The first prototype of the imaging probe was evaluated on a pre-clinical environment simulated with radioactive phantoms by using ^{18}F -FDG. The measured β sensitivity is 321 cps/kBq, which is comparable to that of the best β imaging system developed. This high sensitivity in association with the small scintillation volume which minimizes the γ background contamination allowed the detection of tumor as small as 14 mg for an acquisition time shorter than 30 s, compatible with the surgery duration, and uptake parameters of currently available clinical radiotracers, such as ^{18}F -FET and ^{18}F -Choline.

The results obtained during this work demonstrated the feasibility of the development of intraoperative imaging probes which can provide high sensitivity to weak β signals. However, further improved can be performed on both detection prototypes. The image distortion at the periphery of the detector due to the discretized dimension of the SiPM could be improve in order to increase the useable field of view of the imaging probes. A preliminary evaluation showed that the implementation of neural network method for the image reconstruction can efficiently reduce this distortion while maintaining a very short computing time. The neural network method could be also used to improve the events discrimination ability of the double scintillator detection head.

Aside from the technical improvements, the evaluation of both probes has to be further deepened. The efficiency of the γ subtraction method and β sensitivity of the double scintillator detection head has to be evaluated in a pre-clinical context simulating real tumor uptake and non-specific uptake volumes. These phantom studies, should be completed for both detection prototypes by a pre-clinical evaluation on an animal model (probably a rabbit) to observe the influence of *in vivo* parameters such as the blood circulation on the detection. It would be also interesting to test the performances of the single scintillator detection prototype for the use of β^- emitters to reduce the γ background noise. The final objective of these evaluation studies will be of course to test the best positron imaging probe into operation room. The first clinical trial could be focused on the *in situ* analysis of resection specimens and then directly into the surgical cavity for real time control of the resection margins.

A.1 Imagerie per-opératoire pour guider l'exérèse des tumeurs solides

L'efficacité du traitement du cancer est étroitement liée à la précision et à l'étendue de l'exérèse chirurgicale. La localisation précise des amas tumoraux après extraction de la masse tumorale est une information cruciale pour la survie et la qualité de vie du patient. La médecine nucléaire interventionnelle est utilisée dans ce but et peut s'appuyer sur un nombre croissant de traceurs tumoraux spécifiques, marqués avec des radionucléides émetteurs γ ou β^+ . Les compteurs ou les imageurs exploitant les informations issues de rayonnements γ de moyenne et haute énergie sont désormais bien implantés en routine clinique, en particulier pour la biopsie du ganglion lymphatique sentinelle. La détection *in situ* des particules chargées est également actuellement en cours de développement pour la définition en temps réel des marges de résection tumorale. Par rapport à la détection des rayonnements γ , le faible parcours des particules β^+ (environ 1 mm dans l'eau pour les positons du ^{18}F) permet une localisation plus précise de la tumeur et une meilleure sensibilité de détection, de 1 à 3 ordres de grandeur supérieure à celle des détecteurs γ . Comme aucune collimation n'est nécessaire, ce type de détecteur peut être très compact et léger. Ce faible parcours dans la matière permet également de réduire la contamination radioactive provenant de régions d'accumulation non-spécifique du radiotracer. Ces caractéristiques sont essentielles pour détecter de petites tumeurs dans des cavités chirurgicales étroites. En contrepartie, la détection per-opératoire des particules β^+ est superficielle et est perturbée par le bruit de fond provenant de l'annihilation des positons dans les tissus. Ce bruit provient de l'interaction directe ou indirect (après diffusion) des gammas d'annihilation dans le détecteur, mais également des électrons Compton générés dans l'environnement proche du détecteur et diffusés ensuite à l'intérieur de lui. Les détections per-opératoires γ et β sont donc complémentaires ; la détection γ permet une localisation des lésions occultes telles que les tumeurs profondes alors que les positons permettent une délimitation précise de l'étendue de la tumeur et un contrôle post-opératoire de la cavité chirurgicale. Dans ce contexte, l'objectif de ma thèse est de développer et d'évaluer les performances d'un prototype d'imageur β per-opératoire totalement opérationnel en bloc opératoire et permettant d'améliorer la chirurgie radio-guidée des tumeurs solides.

A.2 Les imageurs β per-opératoires

Deux configurations de détection basées sur des photomultiplicateurs silicium (SiPM) ont été développées. L'intérêt des SiPMs réside dans leur sensibilité à de bas niveaux de

lumière avec des performances comparables ou supérieures à celles des tubes photomultiplicateurs fonctionnant sur technologie du vide, mais combinées à une extrême compacité et une plus grande facilité d'utilisation (faible tension d'alimentation, robustesse, versatilité des géométries). Les deux configurations développées ont été conçues pour être les plus compactes possible tout en maintenant une grande sensibilité aux positons et en minimisant la contamination du bruit de fond γ .

A.2.1 Principe de détection des sondes β

Le premier prototype est constitué d'un scintillateur organique continu très fin couplé à une matrice de SiPMs à travers un guide de lumière (Fig. A.1, gauche). Celui-ci est utilisé pour optimiser l'étalement de la lumière de scintillation sur le photodétecteur, qui détermine partiellement la précision de la reconstruction du point d'impact de la particule incidente dans le scintillateur. Le faible volume de détection utilisé permet de réduire de manière passive l'intensité de la composante γ du bruit de fond. A l'inverse, le second prototype utilise un système de soustraction permettant de réduire de manière active l'influence de ce bruit en quantifiant sa contamination. Le détecteur est constitué d'un empilement de deux scintillateurs séparés par un guide de lumière (Fig. A.1, droite). La contamination γ est estimée à l'aide d'un scintillateur inorganique pixellisé protégé du rayonnement β^+ par un scintillateur organique placé juste au dessus de lui. Une image positon nettoyée du bruit γ peut être obtenue en soustrayant l'image de contamination obtenue avec le scintillateur organique de l'image mesurée avec le scintillateur inorganique après avoir appliqué un facteur de pondération adéquate. La lumière émise par les deux scintillateurs est lue par la même matrice de SiPMs. L'identification des événements interagissant dans les deux scintillateurs est obtenue grâce à l'analyse de la distribution spatiale de la lumière sur la matrice. La nature continue du scintillateur organique et la transmission de lumière à travers le guide de lumière permet en effet un large étalement de la lumière sur la surface des SiPMs, alors que la lumière créée par le scintillateur inorganique pixélisé placé directement au contact de la matrice présente une distribution très fine.

A.2.2 La tête de détection

L'optimisation du design des têtes de détection des deux configurations de la sonde a été focalisée sur le choix de la nature et de la géométrie du scintillateur, du guide de lumière, du revêtement optique du scintillateur et du blindage optique qui permet d'isoler le détecteur de la lumière ambiante.

Les performances des deux scintillateurs organiques, le plastique et le p-terphenyl, ont été comparées pour la première configuration de la sonde. Le p-terphenyl possède un rendement lumineux de 27 photons/keV, ce qui est 3,5 fois supérieur à celui d'un scintillateur plastique conventionnel (8 photons/keV) (Fig. A.2). Sa densité est également plus grande (1,23 g·cm³ vs. 1,032 pour le plastique). Ces propriétés doivent permettre de réduire l'épaisseur du scintillateur, diminuant ainsi le bruit de fond γ , sans compromettre la quantité de lumière collectée et donc la sensibilité de détection β et les performances spatiales. Afin de trouver un compromis optimal entre le taux d'énergie déposée dans le scintillateur par les particules

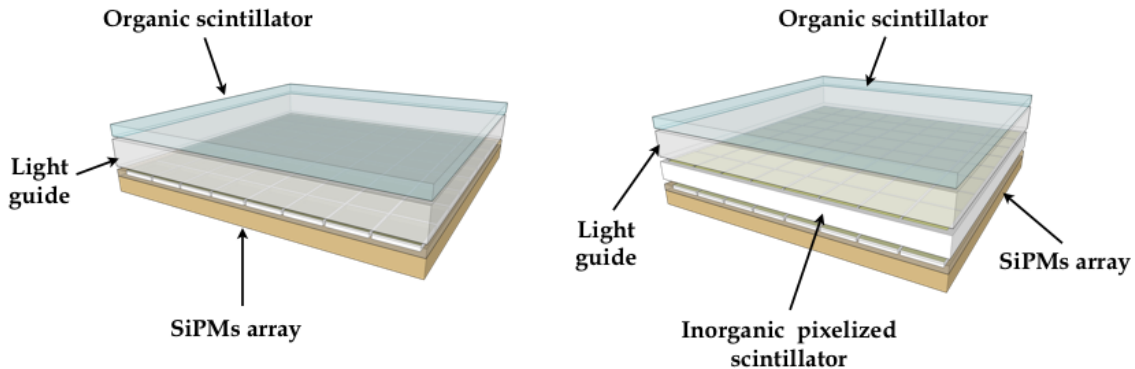


Figure A.1 – Représentation schématique du design de la sonde de détection de positons : la lumière de scintillation produite par un simple scintillateur (gauche) et double scintillateur (droite) est lue par une matrice unique de SiPMs.

β et la contamination γ , différentes épaisseurs de scintillateurs (0,1-0,4 mm) ont été testées. L'influence de l'étalement de la lumière de scintillation atteignant la matrice de SiPMs a également été quantifiée en utilisant un guide de lumière d'épaisseur variant de 1 à 3 mm.

Un scintillateur p-terphenyl de 0,2 mm d'épaisseur a été retenu pour le scintillateur organique du deuxième prototype afin d'optimiser la quantité de lumière collectée qui pourrait être impactée par les multiples interfaces optiques. Le scintillateur inorganique utilisé est un LYSO:Ce, qui présente le meilleur compromis entre une densité et un rendement lumineux élevés ($7,1 \text{ g}\cdot\text{cm}^3$ et 32 photons/keV), un temps de réponse rapide (40 ns), sa non-hygroscopicité et une transparence à la lumière produite par le p-terphenyl. Le LYSO a été pixelisé en une matrice de 8×8 pixels de $3\times 3\times 0,5 \text{ mm}^3$ séparés par un matériau diffusant de 0,2 mm afin de s'adapter à la géométrie de la matrice de SiPMs (Fig. A.2). L'influence de la diffusion de la lumière atteignant les SiPMs sur la discrimination des événements interagissant dans les deux scintillateurs a été étudiée en utilisant un guide de lumière de 2 ou 3 mm d'épaisseur. Deux types de revêtements optiques, déposés à la surface supérieure des scintillateurs, ont également été testés expérimentalement pour optimiser la collection de la lumière : un purement spéculaire (ESR, $65 \mu\text{m}$) et l'autre de type diffusant (PTFE, $75 \mu\text{m}$). Les bords des scintillateurs plastique et des guides de lumière sont non polis et recouvert d'une peinture noire absorbante pour réduire la distorsion du spot lumineux lorsque les particules interagissent à la périphérie du détecteur. Les scintillateurs sont couplés aux guides de lumière et aux matrices de SiPMs avec de la graisse optique.

A.2.3 Le photodétecteur et l'électronique d'acquisition

Les SiPMs sont des matrices de cellules élémentaires, composées d'une photodiode à avalanche fonctionnant en mode Geiger reliée en série à une résistance de décharge, connectées en parallèle sur un même substrat de silicium. Le photodétecteur utilisé pour les deux prototypes de l'imageur β est une matrice de 8×8 SiPMs de $3\times 3 \text{ mm}^2$ composés de cellules

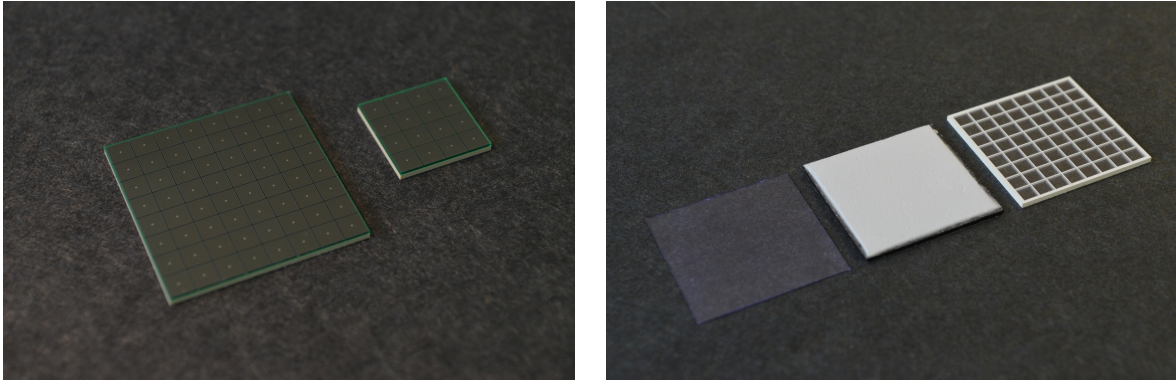


Figure A.2 – Gauche : matrice de SiPM TSV 8×8 (gauche) et 4×4 (droite) développées par Hamamatsu, avec de SiPMs $3 \times 3 \text{ mm}^2$ composés de 3600 cellules de $50 \mu\text{m}$ de dimension latérale. Droite : scintillateurs testés pendant l’optimisation de la tête de détection. De gauche à droite : le scintillateur plastique (EJ-212, Eljen Tech.), le scintillateur polycristalline p-terphenyl (Proteus Tech.) et le scintillateur inorganique de LYSO:Ce pixelisé en une matrice de 8×8 pixels de $3 \times 3 \times 0,5 \text{ mm}^3$ séparés par un matériau diffusant de $0,2 \text{ mm}$ (Hilger crystals).

élémentaire de $50 \times 50 \mu\text{m}^2$, offrant un champ de vue (FOV) d’environ $25 \times 25 \text{ mm}^2$ (Fig. A.2). Ces matrices sont développées par la société Hamamatsu selon la technologie TSV (Through Silicon Via) qui permet une réduction de la zone morte entre chaque SiPM ($0,2 \text{ mm}$) et donc l’optimisation de la compacité de la sonde. Les performances des SiPMs (efficacité de détection, gain, probabilité de crosstalk et d’afterpulses, bruit d’obscurité) sont directement liées à la surtension aux bornes du détecteur (différence entre la tension d’alimentation et la tension de seuil d’avalanche), mais dépendent également de la température, ce qui impose la mise en œuvre d’un système de compensation.

Les 64 voies de la matrice de SiPMs sont reliées à une électronique miniaturisée élaborée autour d’un circuit intégré (ASIC EASIROC développé par le pôle OMEGA, LAL) qui permet une mesure individuelle de la charge sur chaque pixel. Les signaux analogiques à la sortie des ASIC sont ensuite traités par un ensemble composé d’un Convertisseur Analogique Numérique (CAN), d’un circuit logique programmable (FPGA) et d’un contrôleur USB, qui réalise le contrôle de la numérisation, l’acquisition et le transfert des données vers l’ordinateur. Afin d’ajuster finement et individuellement la tension d’alimentation de chaque SiPM de la matrice, l’ASIC est équipé d’un CNA (Convertisseur Numérique Analogique) qui délivre sur 8 bits une tension continue programmable à l’anode du SiPM, permettant de réduire la différence entre les gains des SiPMs. Les différents paramètres de contrôle de la carte électronique d’acquisition (gain, constante de temps de mise en forme, trigger, ...) ont été optimisés en fonction des signaux issus des SiPMs.

A.3 Développement et optimisation des sondes positon

Chaque élément de la chaîne de détection de l’imageurs β présenté précédemment a été caractérisé et optimisé de manière à définir le design le plus adapté aux contraintes imposés par la finalité clinique visée.

A.3.1 Caractérisation du système de photodétection

L'uniformité de réponse de la matrice de SiPMs a été améliorée en ajustant la tension continue délivrée par le CNA. L'écart-type de la réponse relative aux 64 SiPMs est réduite de 70% par rapport à la réponse obtenue pour une même tension sur chaque SiPM. La surtension des SiPMs a été optimisée pour offrir le meilleur compromis entre performances spatiales et sensibilité et fixée à 1,6 V, ce qui correspond à un gain de $(7.5 \pm 0.1) \cdot 10^5$. La dépendance en température des SiPMs a également été étudiée puisque notre sonde d'imagerie conçue pour la détection *in situ*, au contact du corps humain du patient, pourra être soumise à des variations de températures. La réponse du détecteur a été évaluée en fonction de tension d'alimentation pour des températures allant de 16 à 38°C. La réponse en charge diminue avec la température en accord avec la diminution de la tension de seuil d'avalanche des SiPMs, et donc de la surtension, dont dépend directement le gain, l'efficacité de détection et les probabilités de crosstalk et d'afterpulses. Cependant cette variation peut être compensée en ajustant la tension d'alimentation en fonction de la température pour maintenir la surtension constante. La calibration en température du détecteur nous a permis de quantifier la dépendance en température de la surtension et donc de définir une méthode de compensation en temps réel basée sur l'ajustement de la tension d'alimentation de manière à maintenir une tension constante aux bornes des SiPMs quel que soit la température.

A.3.2 Optimisation et performances de l'imageur avec un scintillateur unique

Différents designs des deux configurations de l'imageur per-opérateur ont été étudiées expérimentalement et par simulation Monte Carlo. Leur impact sur les performances de la sonde a été optimisé en termes de sensibilité, de réponse spatiale et de sensibilité au bruit de fond gamma. Les effets de différents algorithmes de reconstruction sur les performances spatiales ont également été étudiés.

A.3.2.1 Mesures des performances d'imagerie

La position d'interaction de la particule β ou des rayonnements γ dans le scintillateur est calculée à partir du barycentre de la distribution de la charge totale fournie par la matrice de SiPMs, après l'application d'un seuil en charge sur le contenu des pixels pour diminuer l'influence des queues de la distribution et du bruit électronique. Le champ de vue des têtes de détection des deux prototypes a été analysé à l'aide d'une source de ^{204}Tl équipé d'un collimateur en tungstène de 0,5 mm de diamètre et monté sur une plateforme motorisée. La position de la source et la LMH (Largeur à Mi Hauteur) sont calculées à partir d'un ajustement gaussien sur la projection du pic de mesure le long des axes x et y . La distorsion spatiale est estimée par la différence absolue entre la position reconstruite, corrigée de la compression linéaire dans la région centrale du détecteur, et la position mécanique de la source. La résolution spatiale est estimée à partir de la LMH corrigée de la distorsion locale et déconvoluée par le diamètre du collimateur. Les uniformités intégrales (IU) et différentielles (DU) sont estimées à partir de l'irradiation uniforme de la surface du détecteur avec une source de ^{22}Na , tel que décrit dans les protocoles NEMA. La sensibilité β a également été estimée à partir de cette irradiation uniforme. Elle est définie comme le nombre d'événements

détectés dans la région centrale du FoV normalisé par le nombre d'évènements détecté avec la configuration de référence (scintillateur p-terphenyl de 0,2 mm d'épaisseur couplé avec un guide de lumière de 2 mm). Seuls les évènements dont l'énergie est supérieure à un seuil de 32 photoélectrons, correspondant au bruit d'obscurité total des SiPM de 1 Hz, sont prises en compte. Comme le bruit d'obscurité des SiPM et le gain intrinsèque sont extrêmement sensibles à la température, toutes les mesures ont été faite dans une chambre climatisée et la température a été maintenue à 20°C.

A.3.2.2 Etude par simulations Monte-Carlo

Afin d'estimer l'origine et l'intensité des différentes contributions du bruit de fond détecté par la sonde dans un contexte clinique, la géométrie des têtes de détection des deux prototypes a été modélisée par simulation Monte-Carlo (plateforme de simulation GATE). Tous les processus physiques impliquant des particules β telle que celle émise par le ^{18}F , ainsi que les rayonnements γ , ont été simulées avec une coupure sur le parcours minimal fixée à 0,01 mm. Les effets de création, transmission et diffusion de la lumière de scintillation n'étant pas pris en compte, la réponse en charge réelle du détecteur est obtenue en convoluant le dépôt en énergie obtenue à partir des simulations par les caractéristiques intrinsèques de la distribution en charge mesurée expérimentalement par la matrice de SiPMs pour chaque configuration de scintillateur (charge totale collectée et distribution moyenne). La sonde est placée au contact d'une tumeur de différents diamètres à l'intérieur d'une cavité chirurgicale. Différents rapports de fixation du traceur entre la tumeur et les tissus sains ont été simulés.

A.3.2.3 Choix de la configuration optimale

Les performances spatiales des différents prototypes sont présentées dans le Tableau A.1. Le scintillateur p-terphenyl montre des performances spatiales supérieures à celle du scintillateur plastique en raison de son rendement en lumière et de sa densité plus élevés que celle du scintillateur plastique qui augmentent ainsi la quantité de lumière de scintillation même pour des très faibles épaisseurs de scintillateur. La sensibilité β est également significativement augmentée avec le rendement lumineux plus important du p-terphenyl. Pour une même épaisseur de 0,2 mm, le p-terphenyl présente une sensibilité améliorée de plus de 36% par rapport au plastique grâce à une quantité de lumière collectée 3 fois plus importante. Pour un dépôt d'énergie moyen similaire, un scintillateur p-terphenyl de 0,1 mm d'épaisseur possède une sensibilité β toujours supérieure de 13,5% par rapport à celle d'un scintillateur plastique de 0,4 mm d'épaisseur. Ceci peut s'expliquer par la distribution spatiale plus fine de la lumière de scintillation obtenue avec le p-terphenyl qui rend la détection des particules β moins sensible au seuil en charge associé au seuil de déclenchement de l'électronique. Cet effet est bien reproduit par les simulations qui montrent le même classement de sensibilité entre les différentes configurations de détecteurs que celui obtenu expérimentalement. L'étude de l'influence de l'épaisseur du guide de lumière montre que le meilleur compromis en termes de performance spatiales est obtenue avec une fenêtre de diffusion de lumière de 2 mm d'épaisseur (pour un scintillateur fin couplé à une matrice avec des SiPMs de $3 \times 3 \text{ mm}^2$) (Tab. A.1). Un guide de lumière trop fin discrétise la réponse en lumière de la matrice des SiPM, ce qui a pour conséquence une forte distorsion spatiale et inhomogénéités.

Scintillateur (mm)	LG (mm)	Res. spatial (mm)		Bias (mm)		Unif.(%)		\bar{E} (ph. e-)	
		centre	péri.	centre	péri.	IU	DU		
p-terphenyl	0.1	2	0.64±0.06	0.96±0.35	0.05±0.04	0.35±0.34	40	25	422
	0.2	2	0.57±0.08	0.76±0.23	0.05±0.04	0.36±0.34	33	20	882
plastic	0.2	2	1.04±0.10	1.50±0.46	0.07±0.07	0.48±0.41	41	29	247
	0.4	2	0.82±0.12	1.21±0.40	0.07±0.07	0.50±0.44	31	16	424
p-terphenyl	0.1	1	0.66±0.09	0.97±0.37	0.22±0.15	0.30±0.27	80	65	465
		2	0.64±0.06	0.96±0.35	0.05±0.04	0.35±0.34	40	25	422
		3	0.94±0.12	1.43±0.53	0.07±0.07	0.48±0.40	30	18	319

Table A.1 – Performances spatiales des différentes têtes de détection. Les valeurs moyennes et écarts-types de la résolution spatiales (FWHM) et bias ont été calculées sur l'ensemble des positions testées, séparément dans la zone central et périphérique. L'uniformité intégrale (IU) et différentielle (DU) sont estimées à partir de l'irradiation uniforme de la surface du détecteur avec une source de ^{22}Na . Toutes les mesures ont été faites avec les scintillateurs couverts d'un revêtement spéculaire et couplés avec un guide de lumière (LG) de 2 mm d'épaisseur.

L'augmentation de l'épaisseur du guide de lumière améliore l'uniformité de réponse mais dégrade, en contrepartie, la résolution et la distorsion spatiale vers le centre à la périphérie de l'image, dû à un étalement plus important de la distribution de la lumière et à sa troncation plus importante par les bords absorbants.

La nature du revêtement optique qui couvre le scintillateur a également une légère influence sur les performances spatiales, mais la plus faible densité du PTFE permet par contre de détecter 10% d'évènements β supplémentaires par rapport à l'ESR. Les simulations ont permis d'étudier plus finement l'influence du revêtement et blindage optique sur la sensibilité β , mais également sur la composante du bruit de fond associée au électrons Compton diffusés. Parmi différentes combinaisons revêtement-blindage optique étudiés, l'association d'une couche d'aluminium de 10 μm et du PTFE offre le meilleur compromis entre sensibilité aux positons et minimisation du bruit issu des électrons diffusés. Le signal positon est seulement réduit de 9% alors que la contamination de bruit augmente de 8% comparés à la configuration sans blindage et revêtement optique.

De manière plus générale, les simulations Monte Carlo montrent que le choix d'un scintillateur organique mince permet de diminuer fortement la contamination du bruit de fond γ . Ainsi, le bruit est augmenté d'un facteur 2 entre un scintillateur plastique de 0,4 mm et un scintillateur p-terphényl de 0,1 mm (couplés à un guide de lumière de 2 mm et recouverts d'une revêtement optique ESR et d'un blindage optique en aluminium). Ceci implique une diminution du rapport signal-sur-bruit d'environ 30% lorsque l'imageur détecte une tumeur de 5 mm avec un rapport de fixation du traceur de 1:2 (le rapport tumeur-sur-fond passe de 1,22 à 1,16).

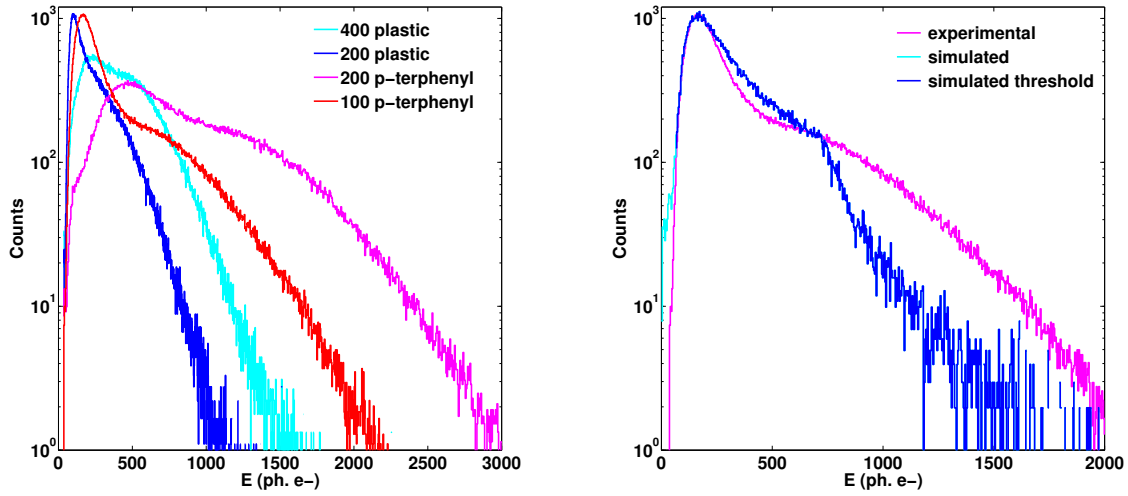


Figure A.3 – Spectres en énergie d’une source de ^{22}Na obtenu dans une région centrale du détecteur, pour différentes configurations de scintillateurs (gauche). Spectrum expérimental mesuré avec le scintillateur de *p*-terphenyl de 0,1 mm d’épaisseur superposé au spectre simulé après conversion en photoélectrons et application du seuil en charge associé au trigger de l’électronique et la soustraction de charge relative à la reconstruction de l’image.

A.3.2.4 Focus sur la configuration optimale

A la lumière de ces résultats, la tête de détection composée d’un scintillateur de *p*-terphenyl de 0,1 mm d’épaisseur recouvert d’un revêtement ESR et d’une couche d’aluminium de 10 μm et couplé d’une matrice de SiPM via un guide de lumière de 2 mm apparaît être le meilleur candidat pour notre application. Cette configuration permet d’assurer de bonnes performances spatiales tout en limitant l’épaisseur du volume sensible, et donc, limiter la contamination du bruit de fond γ . Le choix d’un revêtement optique PTFE permet une légère amélioration de la sensibilité au détriment de la réponse spatiale. Cette configuration permet d’obtenir une résolution spatiale moyenne de $0,74 \pm 0,05$ mm au centre du détecteur et $1,35 \pm 0,38$ mm à la périphérie pour une surtension optimale de 1,6V (Fig. A.4). La distorsion au centre est de $0,1 \pm 0,13$ mm et de $0,34 \pm 0,31$ mm à la périphérie. Grâce à la méthode de compensation en température, ces performances restent constantes pour des températures variant entre 16°C et 36°C. L’ajustement de la surtension en fonction de la température permet également de maintenir une sensibilité β constante. Sans correction, la sensibilité diminue de 20% entre 20°C et 36°C malgré l’optimisation de la soustraction en charge lors de la reconstruction. Avec correction, la variation maximale de la sensibilité est de 2,3%.

Afin d’aller plus loin dans l’amélioration des performances spatiales du système d’imagerie, différents algorithmes de reconstruction ont été testés. En plus de la méthode de barycentrage avec soustraction de charge, j’ai étudié un algorithme de reconstruction itératif par barycentrage pondéré, une méthode par ajustement d’un modèle analytique de la distribution de la lumière (Scrimber-Baker) et un réseau de neurones. Les méthodes de reconstruction

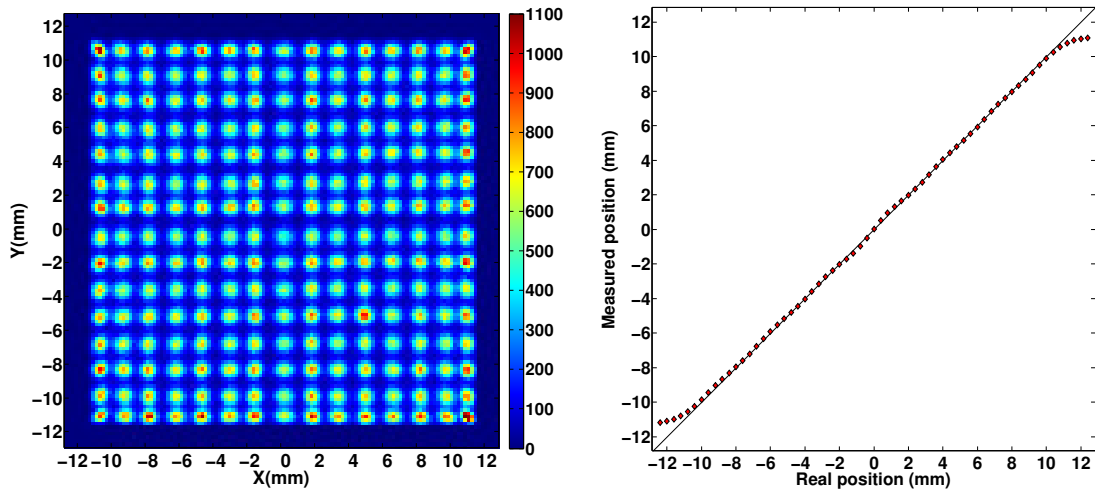


Figure A.4 – Image du scan de la surface du détecteur avec une source de ^{204}Tl collimatée avec un trou de 0.5 mm diamètre. Les spots sont espacés de 1.6 mm dans les deux directions (gauche). Linéarité de réponse de la sonde β correspondant à la position de la source mesurée versus sa position mécanique (droite). Moyenne des positions mesurées dans les directions pour toutes les positions testées sur la surface du détecteur. Les barres d'erreur (écart-types), représentant l'uniformité des positions mesurées pour chaque position mécanique, sont trop petites pour être affichées sur le graphique.

permettant une reconstruction en temps réel de la position de l'interaction avec les meilleures performances spatiales sont les méthodes du barycentre avec soustraction et le réseau de neurone (Fig. A.5). Cette dernière méthode améliore significativement les performances spatiales à la périphérie du détecteur et permet d'atteindre des taux d'acquisition très élevés (supérieur à 10 kHz).

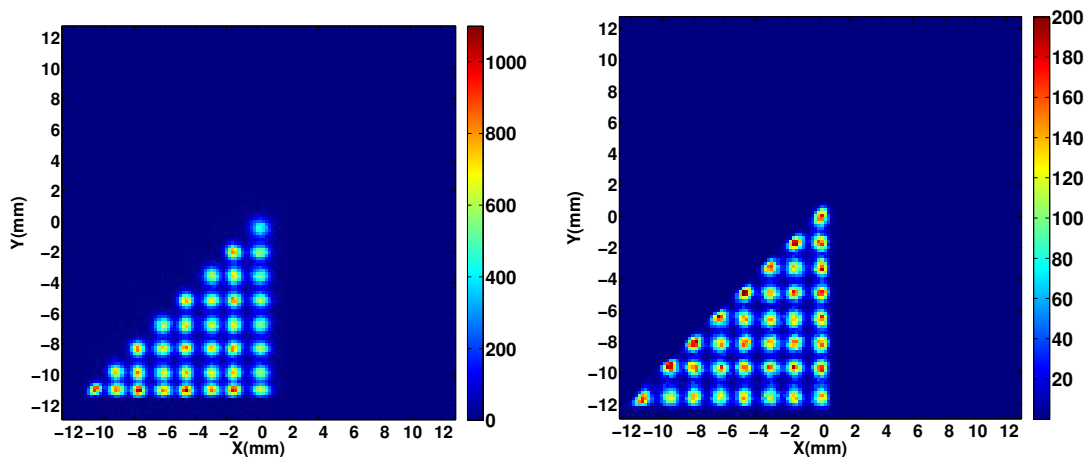


Figure A.5 – Comparaison entre l'image reconstruite avec le méthode de barycentrage avec soustraction de charge (gauche) et un réseau de neurones (droit). Les points sont espacés de 1.6 mm dans les deux directions.

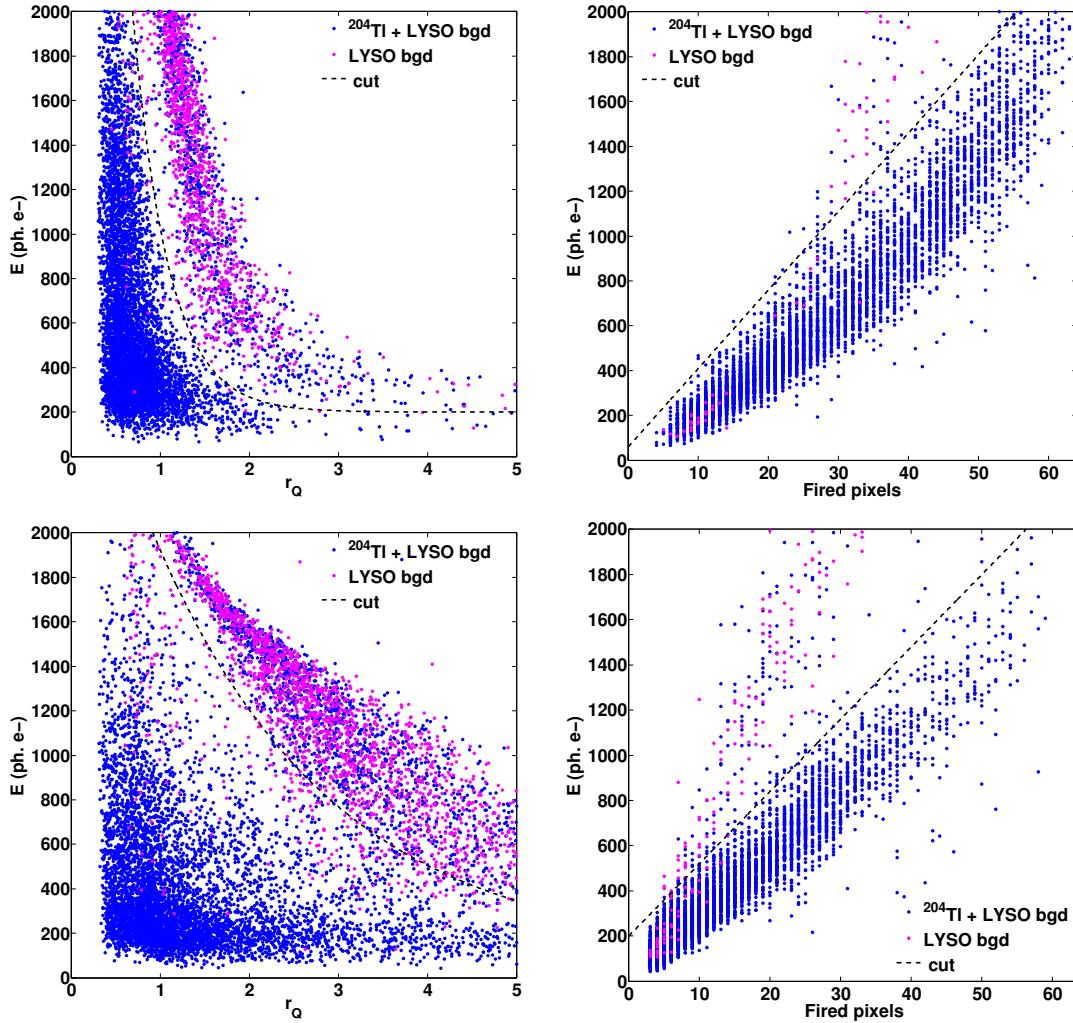


Figure A.6 – *Energie totale des évènements en fonction du paramètre r_Q (à gauche) ou le nombre de pixels activés (à droite) pour les évènements qui interagissent dans une région centrale (en haut) et la région périphérie (en bas) de la surface du détecteur. Les évènements détectés pour une irradiation uniforme avec la source de ^{204}Tl sont représentés en bleu et les évènements de bruit détectés sans source en magenta. La tête de détection est composé d'un scintillateur p-terphenyl de 0,2 mm d'épaisseur couplé au LYSO:Ce à travers un guide de lumière 2 mm d'épaisseur. Les mesures ont été faites avec une tension d'alimentation de 70,2 V et un gain électronique correspondant à une capacité de compensation de 300 fF.*

A.3.3 Optimisation et performances de l'imager avec deux scintillateurs

L'optimisation de la géométrie de la configuration de la sonde équipée de deux scintillateurs s'est principalement focalisée sur l'identification des évènements interagissant dans les scintillateurs afin d'obtenir une soustraction efficace du bruit de fond γ . Cette identification a été réalisée en analysant différents paramètres caractérisant les différences entre les distributions de lumière créées par un évènement interagissant dans le scintillateur organique continu ou le scintillateur inorganique pixelisé : énergie totale de l'évènement, nombre de pixels activés et rapport entre la charge du pixel avec la charge mesurée la plus importante

et la somme de la charge des pixels adjacents (r_Q), qui donne une mesure de la diffusion de la distribution lumineuse. La capacité de discrimination du scintillateur a été optimisée grâce à un paramétrage adéquate des tensions d'alimentation des SiPMs et du gain de l'électronique de lecture, mais également par le choix de l'épaisseur du guide de lumière entre les deux scintillateurs.

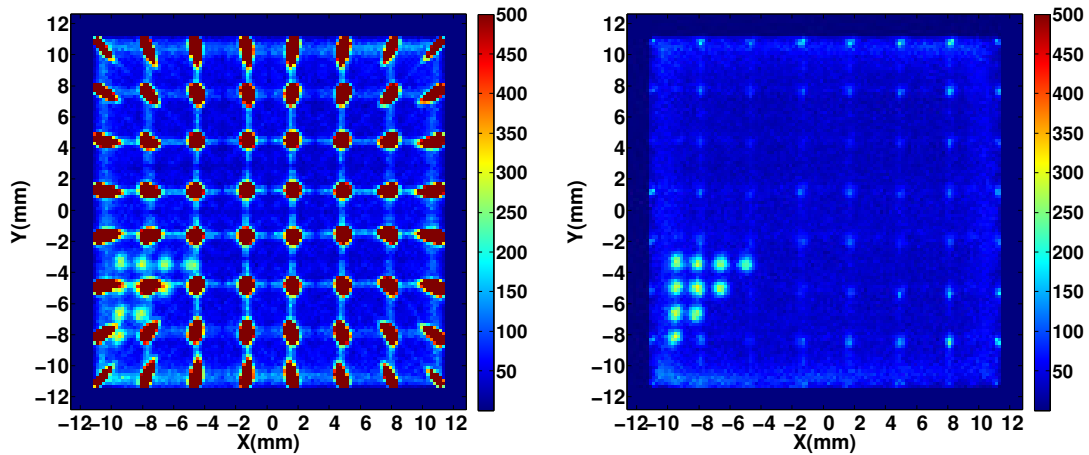


Figure A.7 – Images d'un collimateur en aluminium avec 10 trous des 0.5 mm de diamètre dans un configuration triangulaire. Les trous sont espacés de 1.6 mm. La surface du détecteur, couverte par le collimateur, a été irradiée avec une source de ^{22}Na placée à 5 mm de distance. L'image est représentée avant (gauche) et après identification des évènements qui ont interagi dans le scintillateur organique (droite). La tête de détection est composée du scintillateur en *p*-terphenyl de 0.2 mm d'épaisseur couplée au scintillateur LYSO grâce à un guide de lumière de 3 mm d'épaisseur.

Une méthode de partitionnement automatique, permettant de discriminer les évènements en fonction des différents paramètres caractérisant la distribution de la lumière sans introduire de dépendances liées à l'utilisateur, a été utilisée pour l'optimisation de la surtension et du gain électronique. Cependant, cette méthode ne permet pas de réaliser une discrimination en temps réel. C'est pourquoi, nous avons développé une méthode basée sur l'application de coupures *ad hoc* définies pour les différents paramètres. Cette méthode a été utilisée pour analyser les configurations de détecteurs avec 2 et 3 mm de guide de lumière. Comme la distribution de la lumière scintillante et donc l'énergie totale des évènements dépendent de leur point d'interaction. Les coupures ont été définies séparément pour différentes régions du détecteur. La Figure A.7 représente l'image avant et après identification des évènements qui ont interagi dans le scintillateur organique. L'erreur faite sur la discrimination des évènements entre les deux scintillateurs baisse de 5,3 à 0,8% avec l'augmentation de l'épaisseur du guide de lumière de 2 à 3 mm. Un guide plus épais augmente les différences des distributions lumineuses entre les deux scintillateurs grâce à une diffusion plus large de la lumière de scintillation des évènements interagissant dans le scintillateur le plus éloigné du photodétecteur. Les performances spatiales de la configuration optimale avec un guide de 3 mm d'épaisseur ont été évaluées sur l'image d'un scan obtenue avec une source collimatée de ^{204}Tl , reconstruite en utilisant seulement les évènements dans le scintillateur organique continu, discrim-

inés avec la méthode des coupures. La résolution spatiale moyenne est respectivement de $0,81\pm 0,09$ mm et $1,11\pm 0,29$ mm dans la région centrale et sur les bords de l'imageur. La distorsion spatiale moyenne est respectivement de $0,08\pm 0,08$ mm et $0,40\pm 0,31$ mm dans la région centrale et sur les bords.

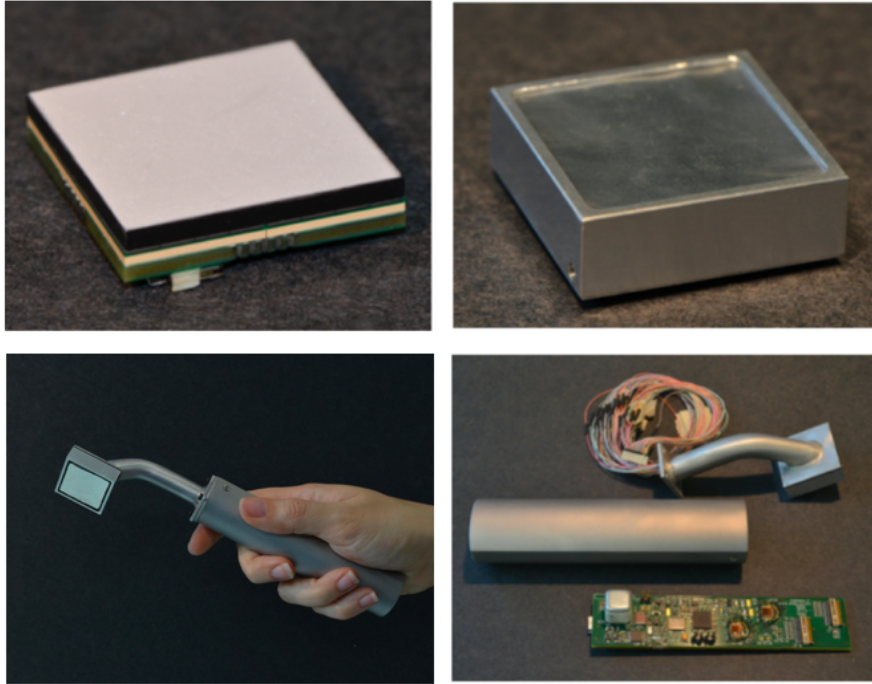


Figure A.8 – Face avant du module de detection (en haut à gauche), boîtier mécanique contenant la tête de détection couverte avec le revêtement optique (en haut à droite), photographie du prototype clinique de l'imageur β per-opérateur (en bas à gauche) et ensemble de composants de l'imageur positron (en bas à droite).

A.3.4 Présentation du prototype clinique

L'objectif instrumental final de ce projet a été le développement d'une sonde positron per-opérateur entièrement fonctionnelle. Une électronique de lecture miniaturisée dédiée et un boîtier mécanique ont ainsi été conçus fin de répondre aux contraintes de faible poids, de compacité et de facilité de manipulation. L'électronique miniaturisée a été conçue en collaboration avec le laboratoire LAL (Fig. A.8). Les dimensions de la carte sont de $11\times 2,5$ cm² (poids de 20 g), adapté aux dimensions de la poignée de la sonde dans lequel l'électronique doit être insérée. Un effort a été fait pour minimiser ces dimensions, tout en conservant de bonnes performances de l'ensemble du système en termes de bruit, diaphonie réduite entre les canaux analogiques, linéarité et uniformité sur tous les voies. Le boîtier mécanique développée pour la configuration avec un seul scintillateur est composée de deux éléments principaux (Fig. A.8) : la tête de détection contenant l'empilement du scintillateur et du guide de lumière 2 mm couplé à la matrice SiPMs monté sur un PCB ($28,4\times 28,4\times 9,5$ mm³ dimensions extérieures) et la poignée (20 cm de longueur pour un diamètre maximum de 2,9 cm). Le

poids total de l'imageur est de 100 g.

A.4 Evaluation préclinique des performances de la sonde

Les performances du premier prototype de la sonde équipé d'un seul scintillateur ont été évaluées en situation préclinique. Lors de cette étude préliminaire, nous avons évalué avec des sources non scellées la sensibilité β du détecteur, sa réponse spatiale et sa capacité de détecter de petits foyers tumoraux.

La sensibilité de la sonde, estimée à partir de la décroissance d'une source ponctuelle de ^{18}F -FDG, est de $321 \pm 0,6$ cps/kBq pour un seuil en l'énergie correspondant à un bruit thermique de détection de 10 Hz sur l'ensemble du champs de vue. Cette sensibilité correspond à une activité minimale détectable de 1,3 Bq (temps d'acquisition de 2 minutes). Lorsqu'une couche de tissu de 0,5 mm est interposée entre la source et le détecteur la sensibilité chute à 38,6 cps/kBq (87,9% de la sensibilité en contact) en raison du faible parcours des positons dans les tissus. La résolution spatiale, évaluée avec une source ponctuelle de ^{18}F -FDG, est de 1,09 mm au contact du détecteur et de à 1,44 mm lors que la source est placée à 0,5 mm de profondeur dans les tissus. La capacité de l'imageur à détecter de petites tumeurs a été étudié pour différent variables : la taille de la tumeur, le taux de fixation du radiotraceur entre le tissu tumoral et le tissu sain environnant et la durée d'acquisition. Dans ce but, plusieurs fantômes radioactifs ont été développés. Des puits cylindriques de 2 mm de profondeur et de différents diamètres (3, 5 et 7 mm) sont remplis d'une solution de ^{18}F -FDG pour simuler les résidus tumoraux. Ces puits sont positionnés au dessus d'un grand contenant cylindrique (1,1 litres) représentant les tissus sains et le bruit de fond lié à l'accumulation non-spécifique du traceur. La capacité du système d'imagerie à détecter une fixation tumorale de petite dimension dans un environnement bruité a été quantifiée en calculant le rapport Tumeur-sur-bruit (TBR) correspondant à la différence entre le signal mesuré au niveau de la tumeur et celui associée à une région saine, exprimée en nombre d'écart-type de ces signaux. Le TBR dépend non seulement de la durée d'acquisition mais également de la fixation du traceur dans le tissu. L'échantillon original d'évènements mesuré sa donc été ré-échantillonné à partir d'une large statistique afin de simuler différents temps d'acquisition (10, 30 et 60 secondes) et/ou concentrations du radiotraceur. Les paramètres de fixation de 3 radiotraceurs actuellement disponibles cliniquement ont été simulés: ^{18}F -FDG, (fixation tumorale de 25,9 kBq/ml, ratio de 2:1), ^{18}F -FET (13.3 kBq/ml, 4:1) et ^{18}F -Choline (5.9 kBq/ml, 8:1). Le seuil de détectabilité de la tumeur a été fixé à un TBR de 4 qui correspond à un niveau de confiance de 99.5%.

Pour un temps d'acquisition de 10 s, compatible avec une procédure chirurgicale, les résultats ont montré qu'une tumeur de 7 mm de diamètre était détectable pour les trois traceurs simulés (Table A.2). Pour de plus petites tumeurs marquées au FDG, ce temps d'acquisition était trop court pour dépasser le seuil de détection retenu, en raison de la faible spécificité du traceur. A l'inverse, le ^{18}F -FET et la ^{18}F -Choline permettent tous les deux de détecter des tumeurs de 5 mm de diamètre pour des temps d'acquisition d'environ 4 secondes, mais celles de 3 mm restent indétectables en dessous de 10 s de temps d'acquisition. Ces très petites tumeurs (14 mg) ne sont détectables qu'à partir d'un temps d'acquisition de 24, 28 et 80 s pour le FET, la choline et le FDG, respectivement.

Tumor \varnothing (mm)	^{18}F -FDG 2:1	^{18}F -FET 4:1	^{18}F -Chol 8:1
3	1.29 ± 1.04	2.61 ± 1.27	2.38 ± 0.80
5	1.43 ± 0.94	6.13 ± 1.37	6.01 ± 0.84
7	4.22 ± 1.42	10.21 ± 1.31	9.97 ± 0.76

Table A.2 – Valeurs du TBR en fonction des paramètres de fixation et de concentration du radiotracer pour des petits tumeurs des différents diamètres (3, 5 and 7 mm) situées dans un environnement bruité lié à l'accumulation non-spécifique du traceur. Toutes les valeurs ont été calculées pour un temps d'acquisition de 10 s compatible avec la durée d'un geste chirurgicale.

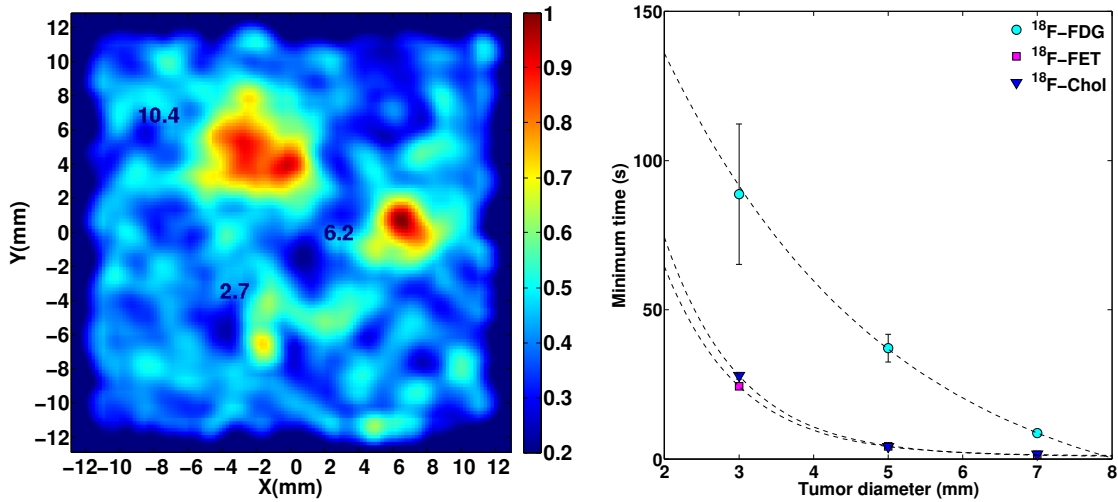


Figure A.9 – Image du fantôme marquée au ^{18}F -FET et un temps d'acquisition de 10 secondes (gauche); les valeurs du TBR relative aux différentes tumeurs sont reportées sur l'image. Temps minimum nécessaire pour atteindre le seuil de 4 pour le TBR en fonction de différents diamètres des tumeurs et paramètres du radiotracer (droite).

A.5 Conclusions

L'objectif de ma thèse était de développer et d'évaluer deux configurations d'imagerie β per-opératoire basées sur l'utilisation de scintillateurs couplés à des SiPMs. L'optimisation de la première configuration de la sonde a montré que le design offrant le meilleur compromis entre sensibilité, performances spatiales et diminution de la contamination du bruit de fond est celui qui associe un scintillateur p-terphenyl de 0,1 mm d'épaisseur avec le guide de lumière de 2 mm d'épaisseur. Le second prototype, basé sur l'utilisation de deux scintillateurs permettant de soustraire la contamination du bruit, a également été optimisé pour obtenir la meilleure capacité de discrimination des événements interagissant dans les deux scintillateurs. La configuration retenue associe un scintillateur p-terphenyl de 0,2 mm d'épaisseur couplé à un scintillateur pixelisé LYSO à travers un guide de lumière de 3 mm d'épaisseur. J'ai pu montrer que ces détecteurs optimisés offraient une résolution spatiale submillimétrique et

une distorsion très faible sur l'ensemble du champs de vue. La dépendance en température des performances spatiales et de la sensibilité β a été corrigée grâce au développement d'une méthode de correction qui ajuste en temps réel la tension d'alimentation des SiPM en fonction de la température. Une évaluation préliminaire des performances de la configuration de la sonde β avec un scintillateur unique a été réalisée à l'aide de fantômes radioactifs afin de simuler un environnement clinique réaliste. La haute sensibilité β de l'imageur associée à son faible volume de détection, qui minimise l'intensité de la contamination du bruit de fond γ , permet de détecter de très petites tumeurs (de l'ordre de 5 mm) pour un temps d'acquisition inférieur à 4 secondes et des paramètres de fixation du traceurs correspondants à des radiopharmaceutiques actuellement disponibles comme le ^{18}F -FET et la ^{18}F -Choline. Enfin, ce travail a également permis le développement du premier prototype d'une sonde totalement opérationnelle associant une électronique de lecture miniaturisée dans un boîtier mécanique compact.

Bibliography

- [Abo *et al.* 2015] T. Abo, A. Nanashima, S. Tobinaga, S. Hidaka, N. Taura, K. Takagi, J. Arai, H. Miyaaki, H. Shibata and T. Nagayasu. *Usefulness of intraoperative diagnosis of hepatic tumors located at the liver surface and hepatic segmental visualization using indocyanine green-photodynamic eye imaging*. *European Journal of Surgical Oncology*, vol. 41, no. 2, pages 257–264, 2015. 27
- [Acerbi *et al.* 2014] Francesco Acerbi, Morgan Broggi, Marica Eoli, Elena Anghileri, Claudio Cavallo, Carlo Boffano, Roberto Cordella, Lucia Cuppini, Bianca Pollo, Marco Schiariti, Sergio Visintini, Chiara Orsi, Emanuele La Corte, Giovanni Broggi and Paolo Ferroli. *Is fluorescein-guided technique able to help in resection of high-grade gliomas?* *Neurosurgical focus*, vol. 36, no. 2, page E5, 2014. 27, 28
- [Adams & Baum 2000] S Adams and RP Baum. *Intraoperative use of gamma-detecting probes to localize neuroendocrine tumors*. *The Quarterly Journal of Nuclear Medicine and Molecular Imaging*, vol. 44, no. 1, page 59, 2000. 54
- [Adams *et al.* 2001] Stefan Adams, Peter Acker, Matthias Lorenz, Elsbeth Staib-Sebler and Gustav Hör. *Radioisotope-guided surgery in patients with pheochromocytoma and recurrent medullary thyroid carcinoma*. *Cancer*, vol. 92, no. 2, pages 263–270, 2001. 53
- [Agnese *et al.* 2004] Doreen M Agnese, Shahab F Abdessalam, William E Burak, Mark W Arnold, Denise Soble, George H Hinkle, Donn Young, M B Khazaeli and Edward W Martin. *Pilot study using a humanized CC49 monoclonal antibody (HuCC49DeltaCH2) to localize recurrent colorectal carcinoma*. *Annals of surgical oncology*, vol. 11, no. 2, pages 197–202, 2004. 32
- [Agrawal *et al.* 2015] Amit Agrawal, Francisco J. Civantos, Kevin T. Brumund, Douglas B. Chepeha, Nathan C. Hall, William R. Carroll, Russell B. Smith, Robert P. Zitsch, Walter T. Lee, Yelizaveta Shnayder, David M. Cagnetti, Karen T. Pitman, Dennis W. King, Lori a. Christman and Stephen Y. Lai. *[99mTc]Tilmanocept Accurately Detects Sentinel Lymph Nodes and Predicts Node Pathology Status in Patients with Oral Squamous Cell Carcinoma of the Head and Neck: Results of a Phase III Multi-institutional Trial*. *Annals of Surgical Oncology*, pages 3708–3715, 2015. 32
- [Aitken *et al.* 1984] Delmar R Aitken, George H Hinkle, Marlin O Thurston, Steve E Tuttle, Daniel T Martin, John Olsen, Darrow E Haagensen Jr, David Houchens and Edward W Martin Jr. *A gamma-detecting probe for radioimmune detection of CEA-producing tumors*. *Diseases of the Colon & Rectum*, vol. 27, no. 5, pages 279–282, 1984. 53
- [Albertini *et al.* 1996] J J Albertini, C W Cruse, D Rapaport, K Wells, M Ross, R DeConti, C G Berman, K Jared, J Messina, G Lyman, F Glass, N Fenske and D S Reintgen. *Intraoperative radio-lympho-scintigraphy improves sentinel lymph node identification*

- for patients with melanoma.* *Annals of surgery*, vol. 223, no. 2, pages 217–24, 1996. 52
- [Alex *et al.* 1993] JC Alex, DL Weaver, JT Fairbank, BS Rankin and DN Krag. *Gamma-probe-guided lymph node localization in malignant melanoma.* *Surgical oncology*, vol. 2, no. 5, pages 303–308, 1993. 51
- [Andersen *et al.* 2013] Flemming Littrup Andersen, Thomas Levin Klausen, Annika Loft, Thomas Beyer and Søren Holm. *Clinical evaluation of PET image reconstruction using a spatial resolution model.* *European journal of radiology*, vol. 82, no. 5, pages 862–869, 2013. 158
- [Angarita *et al.* 2014] Fernando A. Angarita, Ashlie Nadler, Siham Zerhouni and Jaime Escallon. *Perioperative measures to optimize margin clearance in breast conserving surgery.* *Surgical Oncology*, vol. 23, no. 2, pages 81–91, 2014. 21
- [Angelone *et al.* 2014] M. Angelone, G. Battistoni, F. Bellini, V. Bocci, F. Collamati, E. De Lucia, R. Faccini, F. Ferroni, S. Fiore, M. Marafini, D. Materazzo, I. Mattei, S. Morganti, V. Patera, L. Piersanti, M. Pillon, L. Recchia, A. Russomando, A. Sarti, A. Sciubba, E.S. Camillocci and C. Voena. *Properties of para-Terphenyl as a Detector for α , β and γ Radiation.* *IEEE Transactions on Nuclear Science*, vol. 61, no. 3, pages 1483 – 1487, 2014. 70, 82
- [Anger 1958] Hal O Anger. *Scintillation camera.* *Review of scientific instruments*, vol. 29, no. 1, pages 27–33, 1958. 40, 102
- [Aoyama *et al.* 2011] Kei Aoyama, Takako Kamio, Tetsuya Ohchi, Masako Nishizawa and Shingo Kameoka. *Sentinel lymph node biopsy for breast cancer patients using fluorescence navigation with indocyanine green.* *World Journal of Surgical Oncology*, vol. 9, no. 1, page 157, 2011. 27
- [Arezzo *et al.* 2015] Alberto Arezzo, Roberto Passera, Alessandro Salvai, Simone Arolfo, Marco Ettore Allaix, Guido Schwarzer and Mario Morino. *Laparoscopy for rectal cancer is oncologically adequate: A systematic review and meta-analysis of the literature.* *Surgical Endoscopy and Other Interventional Techniques*, vol. 29, no. 2, pages 334–348, 2015. 16
- [Baker & Moallem 2007] KL Baker and MM Moallem. *Iteratively weighted centroiding for Shack-Hartmann wave-front sensors.* *Optics express*, vol. 15, no. 8, pages 5147–5159, 2007. 103
- [Barber *et al.* 1989] HB Barber, HH Barrett, JM Woolfenden, KJ Myers and TS Hickernell. *Comparison of in vivo scintillation probes and gamma cameras for detection of small, deep tumours.* *Physics in medicine and biology*, vol. 34, no. 6, page 727, 1989. 147
- [Barbosa *et al.* 2015] Breno J. A. P. Barbosa, Eric D. Mariano, Chary M. Batista, Suely K. N. Marie, Manoel J. Teixeira, Carlos U. Pereira, Marcos S. Tatagiba and Guilherme A. Lepski. *Intraoperative assistive technologies and extent of resection in*

- glioma surgery: a systematic review of prospective controlled studies*. Neurosurgical Review, vol. 38, no. 2, pages 217–227, 2015. 22
- [Barranger *et al.* 2005] Emmanuel Barranger, Khaldoun Kerrou, Yolande Petegnief, Emmanuel David-Montefiore, Annie Cortez and Emile Daraï. *Laparoscopic resection of occult metastasis using the combination of FDG-positron emission tomography/computed tomography image fusion with intraoperative probe guidance in a woman with recurrent ovarian cancer*. Gynecologic Oncology, vol. 96, no. 1, pages 241–244, 2005. 54
- [Bartolazzi *et al.* 2008] Armando Bartolazzi, Calogero D’Alessandria, Maria Gemma Parisella, Alberto Signore, Fabrizio Del Prete, Luca Lavra, Sten Braesch-Andersen, Roberto Massari, Carlo Trotta, Alessandro Soluri, Salvatore Sciacchitano and Francesco Scopinaro. *Thyroid cancer imaging in vivo by targeting the anti-apoptotic molecule galectin-3*. PLoS ONE, vol. 3, no. 11, 2008. 32
- [Barugola *et al.* 2009] Giuliano Barugola, Stefano Partelli, Stefano Marcucci, Nora Sartori, Paola Capelli, Claudio Bassi, Paolo Pederzoli and Massimo Falconi. *Resectable pancreatic cancer: who really benefits from resection?* Annals of surgical oncology, vol. 16, no. 12, pages 3316–3322, 2009. 22
- [Beekman & Schaart 2010] FJ Beekman and DR Schaart. *An improved nearest neighbor method for the estimation of the gamma photon entry point in monolithic scintillator detectors for PET*. . . . Record (NSS/MIC), . . . , pages 3088–3092, 2010. 105
- [Bhanot *et al.* 2007] Y Bhanot, S Rao and RV Parmeshwaran. *Radio-guided neurosurgery (RGNS): early experience with its use in brain tumour surgery*. British journal of neurosurgery, vol. 21, no. 4, pages 382–388, 2007. 54
- [Bilimoria *et al.* 2007] Karl Y Bilimoria, David J Bentrem, Clifford Y Ko, Andrew K Stewart, David P Winchester, Mark S Talamonti and Cord Sturgeon. *Extent of surgery affects survival for papillary thyroid cancer*. Annals of surgery, vol. 246, no. 3, pages 375–81; discussion 381–4, 2007. 23
- [Blanco *et al.* 2005] Roberto T. Blanco, Risto Ojala, Juho Kariniemi, Jukka Perälä, Jaakko Niinimäki and Osmo Tervonen. *Interventional and intraoperative MRI at low field scanner - A review*. European Journal of Radiology, vol. 56, pages 130–142, 2005. 25
- [Bogalhas *et al.* 2009] F Bogalhas, Y Charon, M-a Duval, F Lefebvre, S Palfi, L Pinot, R Siebert and L Ménard. *Development of a positron probe for localization and excision of brain tumours during surgery*. Physics in medicine and biology, vol. 54, pages 4439–4453, 2009. 47, 48, 49
- [Bricou *et al.* 2015] A Bricou, MA Duval, L Bardet, A Benbara, G Moreaux, F Lefebvre, L Menard, L Pinot, Y Charon, Barna I Tengheret *al.* *Is there a role for a handheld gamma camera (TReCam) in the SNOLL breast cancer procedure?* The quarterly journal of nuclear medicine and molecular imaging: official publication of the Italian Association of Nuclear Medicine (AIMN)[and] the International Association of Radiopharmacology (IAR),[and] Section of the Society of., 2015. 52

- [Buchs *et al.* 2010] Nicolas C Buchs, Michael Chilcott, Pierre-Alexandre Poletti, Leo H Buhler and Philippe Morel. *Vascular invasion in pancreatic cancer: Imaging modalities, preoperative diagnosis and surgical management*. World J Gastroenterol, vol. 16, no. 7, pages 818–31, 2010. 23
- [Bugby *et al.* 2014] S L Bugby, J E Lees, B S Bhatia and a C Perkins. *Characterisation of a high resolution small field of view portable gamma camera*. Physica medica : PM : an international journal devoted to the applications of physics to medicine and biology : official journal of the Italian Association of Biomedical Physics (AIFB), vol. 30, no. 3, pages 331–9, may 2014. 42
- [Busca *et al.* 2010] P Busca, R Peloso, C Fiorini, A Gola, R Eckhardt, K Hermenau, P Lechner, H Soltau and L Strüder. *Silicon drift photodetector arrays for the HICAM gamma camera*. Nuclear Instruments and Methods in Physics Research Section A: Accelerators, Spectrometers, Detectors and Associated Equipment, vol. 624, no. 2, pages 282–285, 2010. 42
- [Buzhan *et al.* 2001] P Buzhan, B Dolgoshein and a Ilyin. *An advanced study of Silicon Photomultiplier*. ICFA Inst. . . . , vol. 23, pages 28–41, 2001. 85, 88
- [Cabañas 1977] Ramon Cabañas. *an Approach for the Treatment of Penile*. Cancer, vol. 39, pages 456–466, 1977. 51
- [Caccia *et al.* 2004] M. Caccia, M. Alemi, C. Bianchi, A. Bulgheroni, C. Cappellini, L. Conte, W. Kucewicz, M. Prest, E. Vallazza and C. Sampietro. *Imaging of β particle sources used in medical applications with position sensitive Silicon sensors*. Nuclear Instruments and Methods in Physics Research, Section A: Accelerators, Spectrometers, Detectors and Associated Equipment, vol. 525, no. 1-2, pages 294–297, 2004. 47
- [Callier *et al.* 2012] Stéphane Callier, Christophe Dela Taille, Gisèle Martin-Chassard and Ludovic Raux. *Easiroc, an easy and versatile readout device for SiPM*. Physics Procedia, vol. 37, pages 1569–1576, 2012. 95, 97
- [Cals *et al.* 2015] Froukje LJ Cals, Tom C Bakker Schut, José A Hardillo, Robert J Baatenburg de Jong, Senada Koljenović and Gerwin J Puppels. *Investigation of the potential of Raman spectroscopy for oral cancer detection in surgical margins*. Laboratory Investigation, vol. 95, no. 10, pages 1186–1196, 2015. 26
- [Cappellini *et al.* 2008] C. Cappellini, a. Bulgheroni, M. Caccia, V. Chmill, M. Jastrzab, F. Risigo and P. Scopelliti. *Imaging of biological samples with silicon pixel detectors*. Nuclear Instruments and Methods in Physics Research Section A: Accelerators, Spectrometers, Detectors and Associated Equipment, vol. 591, no. 1, pages 34–37, 2008. 78
- [Carpentier 2008] a C Carpentier. *[Surgical resection of gliomas in 2008]*. Cancer radiothérapie : journal de la Société française de radiothérapie oncologique, vol. 12, no. 6-7, pages 676–86, nov 2008. 22

- [Casella *et al.* 2015] Claudio Casella, Pierluigi Rossini, Carlo Cappelli, Chiara Nessi, Riccardo Nascimbeni and Nazario Portolani. *Radioguided Parathyroidectomy with Portable Mini Gamma-Camera for the Treatment of Primary Hyperparathyroidism*. International Journal of Endocrinology, vol. 2015, pages 1–6, 2015. 55
- [Cassinotto *et al.* 2013] Christophe Cassinotto, Juliette Cortade, Geneviève Belleannée, Bruno Lapuyade, Eric Terrebonne, Véronique Vendrely, Christophe Laurent and Antonio Sa-Cunha. *An evaluation of the accuracy of CT when determining resectability of pancreatic head adenocarcinoma after neoadjuvant treatment*. European Journal of Radiology, vol. 82, no. 4, pages 589–593, 2013. 23
- [Chapuis *et al.* 2002] Alain Chapuis, Claude Janin and Michel Tararine. *Device and method for nuclear locating by iterative computing of barycenter, and application to gamma-cameras*. B1 Commissariat à l'énergie atomique, Paris (FR), feb 2002. 103
- [Cohn *et al.* 2008] David E. Cohn, Nathan C. Hall, Stephen P. Povoski, Leigh G. Seamon, William B. Farrar and Edward W. Martin. *Novel perioperative imaging with 18F-FDG PET/CT and intraoperative 18F-FDG detection using a handheld gamma probe in recurrent ovarian cancer*. Gynecologic Oncology, vol. 110, no. 2, pages 152–157, 2008. 54
- [Collamati *et al.* 2015a] F. Collamati, F. Bellini, V. Bocci, E. De Lucia, V. Ferri, F. Fioroni, E. Grassi, M. Iori, M. Marafini, S. Morganti, R. Paramatti, V. Patera, L. Recchia, A. Russomando, A. Sarti, A. Sciubba, M. Senzacqua, E. Solfaroli Camillocci, A. Versari, C. Voena and R. Faccini. *Time Evolution of DOTATOC Uptake in Neuroendocrine Tumors in View of a Possible Application of Radioguided Surgery with \hat{A} - Decay*. Journal of Nuclear Medicine, vol. 56, no. 10, pages 1501–1506, 2015. 28, 55, 56
- [Collamati *et al.* 2015b] F. Collamati, A. Pepe, F. Bellini, V. Bocci, G. Chiodi, M. Cremonesi, E. De Lucia, M. E. Ferrari, P. M. Frallicciardi, C. M. Grana, M. Marafini, I. Mattei, S. Morganti, V. Patera, L. Piersanti, L. Recchia, A. Russomando, A. Sarti, A. Sciubba, M. Senzacqua, E. Solfaroli Camillocci, C. Voena, D. Pinci and R. Faccini. *Toward Radioguided Surgery with \hat{A} - Decays: Uptake of a Somatostatin Analogue, DOTATOC, in Meningioma and High-Grade Glioma*. Journal of Nuclear Medicine, vol. 56, no. 1, pages 3–8, 2015. 31
- [Collamati *et al.* 2015c] Francesco Collamati, Alessandra Pepe, Fabio Bellini, Valerio Bocci, Giacomo Chiodi, Marta Cremonesi, Erika De Lucia, Mahila E Ferrari, Paola M Frallicciardi, Chiara M Grana *et al.* *Toward radioguided surgery with β - decays: uptake of a somatostatin analogue, DOTATOC, in meningioma and high-grade glioma*. Journal of Nuclear Medicine, vol. 56, no. 1, pages 3–8, 2015. 157
- [Collazuol *et al.* 2011] G. Collazuol, M. G. Bisogni, S. Marcatili, C. Piemonte and A. Del Guerra. *Studies of silicon photomultipliers at cryogenic temperatures*. Nuclear Instruments and Methods in Physics Research, Section A: Accelerators, Spectrometers, Detectors and Associated Equipment, vol. 628, no. 1, pages 389–392, 2011. 91, 92, 93

- [Collobert *et al.* 2012] Ronan Collobert, Koray Kavukcuoglu and Clément Farabet. *Implementing neural networks efficiently*. In *Neural Networks: Tricks of the Trade*, pages 537–557. Springer, 2012. 105
- [Colton & Hardy 1983] CL Colton and JG Hardy. *Evaluation of a sterilizable radiation probe as an aid to the surgical treatment of osteoid-osteoma*. *Journal of bone and joint surgery. American volume*, vol. 65, no. 7, pages 1019–1022, 1983. 31
- [Cornelio *et al.* 2011] a Cornelio, F Gasperini, S Lo Meo, N Lanconelli, S Moehrs, S Marcattili, M G Bisogni and a Del Guerra. *Comparison of different reconstruction methods for planar images in small gamma cameras*. *Journal of Instrumentation*, vol. 6, no. 01, pages C01030–C01030, 2011. 42
- [CrystalPhotonicsGermany 2016] CrystalPhotonicsGermany. *Crystal Gamma Probes*. <http://www.surgicalprobe.com/>, 2016. 34, 37
- [Daghighian *et al.* 1994] F Daghighian, J C Mazziotta, E J Hoffman, P Shenderov, B Eshaghian, S Siegel and M E Phelps. *Intraoperative beta probe: a device for detecting tissue labeled with positron or electron emitting isotopes during surgery*. *Medical physics*, vol. 21, no. 1, pages 153–157, 1994. 44, 45, 60, 79
- [Dammers *et al.* 2009] Ruben Dammers, Sanford PC Hsu and Ali F Krisht. *Radioguided improved resection of a cranial base meningioma*. *Neurosurgery*, vol. 64, no. 3, pages onsE84–onsE85, 2009. 54
- [Das *et al.* 2015] S. K. Das, M. E. Menezes, S. Bhatia, X.-Y. Wang, L. Emdad, D. Sarkar and P. B. Fisher. *Gene Therapies for Cancer: Strategies, Challenges and Successes*. *J Cell Physiology*, vol. 73, no. 4, pages 389–400, 2015. 18
- [De Witt Hamer *et al.* 2012] Philip C. De Witt Hamer, Santiago Gil Robles, Aeilko H. Zwinderman, Hugues Duffau and Mitchel S. Berger. *Impact of intraoperative stimulation brain mapping on glioma surgery outcome: A meta-analysis*. *Journal of Clinical Oncology*, vol. 30, no. 20, pages 2559–2565, 2012. 16
- [DeGrado *et al.* 2001] T R DeGrado, S W Baldwin, S Wang, M D Orr, R P Liao, H S Friedman, R Reiman, D T Price and R E Coleman. *Synthesis and evaluation of (18)F-labeled choline analogs as oncologic PET tracers*. *Journal of nuclear medicine : official publication, Society of Nuclear Medicine*, vol. 42, pages 1805–1814, 2001. 147
- [D’Errico *et al.* 2001] G D’Errico, MA Rosa, A Soluri, R Scafè, M Galli, S Chiarini, N Burgo, A Schiaratura, R Massa and F Scopinaro. *Radioguided biopsy of osteoid osteoma: usefulness of imaging probe*. *Tumori*, vol. 88, no. 3, pages S30–2, 2001. 55
- [DeVita 1983] V T DeVita. *Progress in cancer management. Keynote address*. *Cancer*, vol. 51, no. 12 Suppl, pages 2401–2409, 1983. 15
- [D’Hondt *et al.* 2011] Mathieu D’Hondt, Franck Vandenbroucke-Menu, Sébastien Prévillat-Ratelle, Simon Turcotte, Miguel Chagnon, Marylène Plasse, Richard Létourneau, Michel Dagenais, André Roy and Réal Lapointe. *Is intra-operative ultrasound still*

- useful for the detection of a hepatic tumour in the era of modern pre-operative imaging?* Hpb, vol. 13, no. 9, pages 665–669, 2011. 26
- [Dickerscheid *et al.* 2013] Dennis Dickerscheid, Jules Lavalaye, Leo Romijn and Jan Habraken. *Contrast-noise-ratio (CNR) analysis and optimisation of breast-specific gamma imaging (BSGI) acquisition protocols*. EJNMMI research, vol. 3, no. 1, page 1, 2013. 147
- [Dinu *et al.* 2009] N. Dinu, Z. Amara, C. Bazin, V. Chaumat, C. Cheikali, G. Guilhem, V. Puill, C. Sylvia and J. F. Vagnucci. *Electro-optical characterization of SiPM: A comparative study*. Nuclear Instruments and Methods in Physics Research, Section A: Accelerators, Spectrometers, Detectors and Associated Equipment, vol. 610, no. 1, pages 423–426, 2009. 84, 86
- [Dinu *et al.* 2015] N. Dinu, T. Ait Imando, a. Nagai, L. Pinot, V. Puill, S. Callier, B. Janvier, C. Esnault, M.-a. Verdier, L. Raux, V. Vandebussche, Y. Charon and L. Menard. *SiPM arrays and miniaturized readout electronics for compact gamma camera*. Nuclear Instruments and Methods in Physics Research Section A: Accelerators, Spectrometers, Detectors and Associated Equipment, vol. 787, no. August, pages 367–372, 2015. 42, 96, 97
- [Dinu 2013] Nicoleta Dinu. *Instrumentation on Silicon Detectors: from properties characterization to applications*. PhD thesis, 2013. 92, 94
- [Dolgoshein *et al.* 2006] B. Dolgoshein, V. Balagura, P. Buzhan, M. Danilov, L. Filatov, E. Garutti, M. Groll, A. Ilyin, V. Kantserov, V. Kaplin, A. Karakash, F. Kayumov, S. Klemin, V. Korbel, H. Meyer, R. Mizuk, V. Morgunov, E. Novikov, P. Pakhlov, E. Popova, V. Rusinov, F. Sefkow, E. Tarkovsky and I. Tikhomirov. *Status report on silicon photomultiplier development and its applications*. Nuclear Instruments and Methods in Physics Research, Section A: Accelerators, Spectrometers, Detectors and Associated Equipment, vol. 563, no. 2, pages 368–376, 2006. 74
- [Dooraghi *et al.* 2013] a a Dooraghi, N T Vu, R W Silverman, R Farrell, K S Shah, J Wang, J R Heath and a F Chatziioannou. *Betabox: a beta particle imaging system based on a position sensitive avalanche photodiode*. Physics in medicine and biology, vol. 58, no. 11, pages 3739–53, 2013. 47
- [Dothager *et al.* 2010] Robin S. Dothager, Reece J. Goiffon, Erin Jackson, Scott Harpstrite and David Piwnica-Worms. *Cerenkov radiation energy transfer (CRET) imaging: A novel method for optical imaging of PET isotopes in biological systems*. PLoS ONE, vol. 5, no. 10, pages 1–7, 2010. 36
- [Duarte *et al.* 2007] GM Duarte, C Cabello, RZ Torresan, M Alvarenga, GHQ Telles, ST Bianchessi, N Caserta, SR Segala, MCL de Lima, ECSC Etchebehere *et al.* *Radioguided Intraoperative Margins Evaluation (RIME): Preliminary results of a new technique to aid breast cancer resection*. European Journal of Surgical Oncology (EJSO), vol. 33, no. 10, pages 1150–1157, 2007. 53

- [Erdi 2012] Yusuf Emre Erdi. *Limits of tumor detectability in nuclear medicine and PET*. Molecular imaging and radionuclide therapy, vol. 21, no. 1, page 23, 2012. 158
- [España *et al.* 2010] Samuel España, LM Fraile, JL Herraiz, José Manuel Udías, Manuel Desco and Juan José Vaquero. *Performance evaluation of SiPM photodetectors for PET imaging in the presence of magnetic fields*. Nuclear Instruments and Methods in Physics Research Section A: Accelerators, Spectrometers, Detectors and Associated Equipment, vol. 613, no. 2, pages 308–316, 2010. 75
- [Esposito *et al.* 2008] Irene Esposito, Jörg Kleeff, Frank Bergmann, Caroline Reiser, Esther Herpel, Helmut Friess, Peter Schirmacher and Markus W Buehler. *Most pancreatic cancer resections are R1 resections*. Annals of surgical oncology, vol. 15, no. 6, pages 1651–1660, 2008. 23
- [Essner *et al.* 2001] R Essner, E C Hsueh, P I Haigh, E C Glass, Y Huynh and F Daghighian. *Application of an [(18)F]fluorodeoxyglucose-sensitive probe for the intraoperative detection of malignancy*. The Journal of surgical research, vol. 96, no. 1, pages 120–6, 2001. 54
- [Essner *et al.* 2002] Richard Essner, Farhad Daghighian and Armando E Giuliano. *Advances in FDG PET probes in surgical oncology*. The Cancer Journal, vol. 8, no. 2, pages 100–108, 2002. 56
- [Etchebehere *et al.* 2004] M Etchebehere, ECSC Etchebehere, LA Reganin, EMI Amstalden, A Cliquet Jr and EE Camargo. *Intraoperative localization of an osteoid-osteoma using a gamma probe*. International orthopaedics, vol. 28, no. 6, pages 379–383, 2004. 54
- [Etrych *et al.* 2016] Tomáš Etrych, Henrike Lucas, Olga Janoušková, Petr Chytil, Thomas Mueller and Karsten Mäder. *Fluorescence optical imaging in anticancer drug delivery*. Journal of Controlled Release, vol. 226, pages 168–181, 2016. 27
- [Fabbri *et al.* 2011] A Fabbri, P Bennati, V Orsolini Cencelli, MN Cinti, R Pellegrini, F Petullà, R Pani and F de Notaristefani. *A new iterative algorithm for pixilated and continuous scintillating crystal*. Nuclear Instruments and Methods in Physics Research Section A: Accelerators, Spectrometers, Detectors and Associated Equipment, vol. 648, pages S79–S84, 2011. 103
- [Ferlay *et al.* 2013] F Ferlay, I Soerjomataram, M Ervik, R Dirkschit, S Eser, C Mathers, M Rebelo, DM Parkin, D Forman and F Bray. *GLOBOCAN 2012 v1.0, Cancer Incidence and Mortality Worldwide: IARC CancerBase No. 11 [Internet]*. Lyon,France: International Agency for Research on Cancer, 2013. 13
- [Fernández *et al.* 2004] M. M. Fernández, J. M. Benlloch, J. Cerdá, B. Escat, E. N. Giménez, M. Giménez, Ch W. Lerche, J. Martínez, N. Pavón, F. Sánchez and A. Sebastià. *A flat-panel-based mini gamma camera for lymph nodes studies*. Nuclear Instruments and Methods in Physics Research, Section A: Accelerators, Spectrometers, Detectors and Associated Equipment, vol. 527, no. 1-2, pages 92–96, 2004. 42

- [Ficarra *et al.* 2007] Vincenzo Ficarra, Stefano Cavalleri, Giacomo Novara, Maurizio Aragona and Walter Artibani. *Evidence from robot-assisted laparoscopic radical prostatectomy: a systematic review*. *European urology*, vol. 51, no. 1, pages 45–56, 2007. 16
- [Fisher *et al.* 2002] Bernard Fisher, Stewart Anderson, John Bryant, Richard G Margoese, Melvin Deutsch, Edwin R Fisher, Jong-Hyeon Jeong and Norman Wolmark. *Twenty-year follow-up of a randomized trial comparing total mastectomy, lumpectomy, and lumpectomy plus irradiation for the treatment of invasive breast cancer*. *New England Journal of Medicine*, vol. 347, no. 16, pages 1233–1241, 2002. 21
- [Franc *et al.* 2005] Benjamin L Franc, Carina Mari, Denise Johnson and Stanley P Leong. *The role of a positron-and high-energy gamma photon probe in intraoperative localization of recurrent melanoma*. *Clinical nuclear medicine*, vol. 30, no. 12, pages 787–791, 2005. 54, 56
- [Fuccio *et al.* 2011] Chiara Fuccio, Domenico Rubello, Paolo Castellucci, Maria Cristina Marzola and Stefano Fanti. *Choline PET/CT for prostate cancer: Main clinical applications*. *European Journal of Radiology*, vol. 80, no. 2, pages 50–56, 2011. 32
- [Gamelin *et al.* 2009] John Gamelin, Yi Yang, Nrushingh Biswal, Yueli Chen, Shikui Yan, Xiaoguang Zhang, Mozafareddin Karemeddini, Molly Brewer and Quing Zhu. *A prototype hybrid intraoperative probe for ovarian cancer detection*. *Optics express*, vol. 17, no. 9, pages 7245–7258, 2009. 48, 49, 56
- [Ghelman *et al.* 1981] Bernard Ghelman, FRANCESCA M Thompson and WILLIAM D Arnold. *Intraoperative radioactive localization of an osteoid-osteoma. Case report*. *The Journal of Bone & Joint Surgery*, vol. 63, no. 5, pages 826–827, 1981. 53
- [Gil-Robles & Duffau 2010] Santiago Gil-Robles and Hugues Duffau. *Surgical management of World Health Organization Grade II gliomas in eloquent areas: the necessity of preserving a margin around functional structures*. *Neurosurgical Focus*, vol. 28, no. 2, page E8, 2010. 22
- [Goldberg *et al.* 2015] Gary Goldberg, Dennis Yi-Shin Kuo and Eric Liberman. *Robot-assisted surgery in gynecological oncology: a review*. *Robotic Surgery: Research and Reviews*, vol. 2, pages 81–94, 2015. 16
- [Gonzalez *et al.* 2011a] Lorena Gonzalez, Joyce Wong, Peter Brader, Maureen Zakowski, Mithat Gonen, Farhad Daghighian, Yuman Fong and Strong Vivian E. *An analysis of the utility of handheld PET probes for the intraoperative localization of malignant tissue*. *Journal of Gastrointestinal Surgery*, vol. 2, no. 15, pages 358–366, 2011. 55
- [Gonzalez *et al.* 2011b] Segundo Gonzalez, Joyce Wong, Lorena Gonzalez, Peter Brader, Maureen Zakowski, Mithat Gonen, Yuman Fong and Strong Vivian E. *Novel handheld PET probes provide intraoperative localization of PET-avid lymph nodes*. *Surg. Endosc.*, vol. 2, no. 25, pages 358–366, 2011. 55

- [Goto *et al.* 2005] Mariko Goto, Chio Okuyama, Takao Kubota, Yo Ushuima and Tsunehiko Nishimura. *Assessment of the solid-state gamma camera to depict axillary sentinel lymph nodes in breast cancer patients*. *Annals of Nuclear Medicine*, vol. 19, no. 7, pages 627–631, 2005. 52
- [Greif *et al.* 2010] Franklin Greif, David Aranovich, Veacheslav Zilbermints, Nisim Hannanel and Alexander Belenky. *Intraoperative hydrocolonic ultrasonography for localization of small colorectal tumors in laparoscopic surgery*. *Surgical Endoscopy and Other Interventional Techniques*, vol. 24, no. 12, pages 3144–3148, 2010. 26
- [Grootendorst & Purushotham 2015] MR Grootendorst and A Purushotham. *Clinical feasibility of intraoperative 18F-FDG Cerenkov Luminescence Imaging in breast cancer surgery*. *Journal of Nuclear Medicine*, vol. 56, no. supplement 3, pages 13–13, 2015. 50
- [Gruber *et al.* 1998] GJ Gruber, WW Moses, SE Derenzo, NW Wang, E Beuville and MH Ho. *A discrete scintillation camera module using silicon photodiode readout of CsI (TI) crystals for breast cancer imaging*. *Nuclear Science, IEEE Transactions on*, vol. 45, no. 3, pages 1063–1068, 1998. 42
- [Gudkov *et al.* 2016] Sergey V Gudkov, Natalya Yu Shilyagina, Vladimir A Vodeneev and Andrei V Zvyagin. *Targeted Radionuclide Therapy of Human Tumors*. *International journal of molecular sciences*, vol. 17, no. 1, page 33, 2016. 17
- [Gulec *et al.* 2006] Seza a Gulec, Farhad Daghighian and Richard Essner. *PET-Probe: Evaluation of Technical Performance and Clinical Utility of a Handheld High-Energy Gamma Probe in Oncologic Surgery*. *Annals of surgical oncology*, pages 1–8, 2006. 54
- [Gulec 2007] Seza A. Gulec. *PET Probe-Guided Surgery*. *Journal of surgical oncology*, vol. 95, no. 3, pages 148–155, 2007. 54
- [Hackert *et al.* 2009] T Hackert, MW Büchler and J Werner. *Surgical options in the management of pancreatic cancer*. *Minerva chirurgica*, vol. 64, no. 5, pages 465–476, 2009. 22
- [Haglund *et al.* 1996] Michael M Haglund, Mitchel S Berger and Daryl W Hochman. *Enhanced optical imaging of human gliomas and tumor margins*. *Neurosurgery*, vol. 38, no. 2, pages 308–317, 1996. 27
- [Haitz 1964] Roland H Haitz. *Model for the electrical behavior of a microplasma*. *Journal of Applied Physics*, vol. 35, no. 5, pages 1370–1376, 1964. 87
- [Hall & Truwit 2008] Walter A. Hall and Charles L. Truwit. *Intraoperative MR-guided neurosurgery*. *Journal of Magnetic Resonance Imaging*, vol. 27, no. 2, pages 368–375, 2008. 19
- [Hall *et al.* 2007] Nathan C Hall, Stephen P Povoski, Douglas a Murrey, Michael V Knopp and Edward W Martin. *Combined approach of perioperative 18F-FDG PET/CT*

- imaging and intraoperative 18F-FDG handheld gamma probe detection for tumor localization and verification of complete tumor resection in breast cancer*. World journal of surgical oncology, vol. 5, page 143, 2007. 31, 54
- [Hall *et al.* 2015] Nathan C. Hall, Shawnn D. Nichols, Stephen P. Povoski, Iyore A O James, Chadwick L. Wright, Randall Harris, Carl R. Schmidt, Peter Muscarella, Nicholas Latchana, Edward W. Martin and E. Christopher Ellison. *Intraoperative Use of a Portable Large Field of View Gamma Camera and Handheld Gamma Detection Probe for Radioguided Localization and Prediction of Complete Surgical Resection of Gastrinoma: Proof of Concept*. Journal of the American College of Surgeons, vol. 221, no. 2, pages 300–308, 2015. 31
- [Halsted 1907] W S Halsted. *I. The Results of Radical Operations for the Cure of Carcinoma of the Breast*. Annals of surgery, vol. 46, no. 1, pages 1–19, 1907. 15
- [Hamamatsu KK 2006] Photonics Hamamatsu KK. *Photomultiplier Tube Handbook*. Electron Tube Division,, 2006. 75
- [Hamamatsu KK 2014] Photonics Hamamatsu KK. *TSV MPPC array, 2014.03 KSX-150014-E S12642 Series (3mm - TSV - Array)*. Product Flyer, 2014. 85, 89, 95
- [Hamer *et al.* 2012] Philip C De Witt Hamer, Santiago Gil Robles, Aeilko H Zwinderman, Hugues Duffau and Mitchel S Berger. *Impact of intraoperative stimulation brain mapping on glioma surgery outcome: a meta-analysis*. Journal of Clinical Oncology, vol. 30, no. 20, pages 2559–2565, 2012. 22
- [Handgraaf *et al.* 2014] Henricus J. M. Handgraaf, Martin C. Boonstra, Arian R. Van Erkel, Bert A. Bonsing, Hein Putter, Cornelis J. H. Van De Velde, Alexander L. Vahrmeijer and J. Sven D. Mieog. *Current and Future Intraoperative Imaging Strategies to Increase Radical Resection Rates in Pancreatic Cancer Surgery*. BioMed Research International, vol. 2014, pages 1–8, 2014. 23
- [Harris *et al.* 1956] CC Harris, RR Bigelow, JE Francis, GG Kelley and PR Bell. *A CsI (Tl)-crystal surgical scintillation probe*. Nucleonics (US) Ceased publication, vol. 14, 1956. 53
- [Heckathorne *et al.* 2008] Elena Heckathorne, Lanny Tiefer, Farhad Daghighian and Magnus Dahlbom. *Evaluation of arrays of silicon photomultipliers for beta imaging*. In Nuclear Science Symposium Conference Record, 2008. NSS'08. IEEE, pages 1626–1631. IEEE, 2008. 49, 60, 157
- [Heller & Zanzonico 2011] Sherman Heller and Pat Zanzonico. *Nuclear probes and intraoperative gamma cameras*. Seminars in Nuclear Medicine, vol. 41, no. 3, pages 166–181, 2011. 36
- [Herweijer & Wolff 2003] H Herweijer and J A Wolff. *Progress and prospects: naked DNA gene transfer and therapy*. Gene therapy, vol. 10, no. 6, pages 453–8, 2003. 18

- [Hladik *et al.* 2001] P Hladik, J Vizda, J Bedrna, D Simkovic, L Strnad, K Smejkal and Z Voboril. *Immunoscintigraphy and intra-operative radioimmunodetection in the treatment of colorectal carcinoma*. *Colorectal Disease*, vol. 3, no. 6, pages 380–386, 2001. 54
- [Hoffman *et al.* 1998] E. J. Hoffman, M. P. Tornai, C. S. Levin, L. R. MacDonald and C. H. Holdsworth. *A dual detector β -ray imaging probe with γ -ray background suppression for use in intra-operative detection of radiolabeled tumors*. *Nuclear Instruments and Methods in Physics Research, Section A: Accelerators, Spectrometers, Detectors and Associated Equipment*, vol. 409, no. 1-3, pages 511–516, 1998. 45, 79
- [Hoffman *et al.* 1999] Edward J. Hoffman, Martin P. Tornai, Martin Janecek, Bradley E. Patt and Jan S. Iwanczyk. *Intraoperative probes and imaging probes*. *European Journal of Nuclear Medicine*, vol. 26, no. 8, pages 913–935, 1999. 44, 48, 49
- [Holl *et al.* 2009] G. Holl, R. Dorn, H. Wengenmair, D. Weckermann and J. Sciuk. *Validation of sentinel lymph node dissection in prostate cancer: Experience in more than 2,000 patients*. *European Journal of Nuclear Medicine and Molecular Imaging*, vol. 36, no. 9, pages 1377–1382, 2009. 51, 52
- [Holland *et al.* 2011] Jason P. Holland, Guillaume Normand, Alessandro Ruggiero, Jason S. Lewis and Jan Grimm. *Intraoperative imaging of positron emission tomographic radiotracers using cerenkov luminescence emissions*. *Molecular Imaging*, vol. 10, no. 3, pages 177–186, 2011. 35
- [Houssami *et al.* 2008] Nehmat Houssami, Stefano Ciatto, Petra Macaskill, Sarah J Lord, Ruth M Warren, J Michael Dixon and Les Irwig. *Accuracy and surgical impact of magnetic resonance imaging in breast cancer staging: systematic review and meta-analysis in detection of multifocal and multicentric cancer*. *Journal of Clinical Oncology*, vol. 26, no. 19, pages 3248–3258, 2008. 21
- [Hsieh *et al.* 2016] Chen-Hsi Hsieh, Pei-Wei Shueng, Li-Ying Wang, Yu-Chuen Huang, Li-Jen Liao, Wu-Chia Lo, Yu-Chin Lin, Le-Jung Wu and Hui-Ju Tien. *Impact of post-operative daily image-guided intensity-modulated radiotherapy on overall and local progression-free survival in patients with oral cavity cancer*. *BMC Cancer*, vol. 16, no. 1, page 139, 2016. 19
- [Hu *et al.* 2015] Hao Hu, Xin Cao, Fei Kang, Min Wang, Yenan Lin, Muhan Liu, Shujun Li, Liping Yao, Jie Liang, Jimin Liang, Yongzhan Nie, Xueli Chen, Jing Wang and Kaichun Wu. *Feasibility study of novel endoscopic Cerenkov luminescence imaging system in detecting and quantifying gastrointestinal disease: first human results*. *European Radiology*, vol. 25, no. 6, pages 1814–1822, 2015. 50
- [Hudin *et al.* 2012a] N Hudin, L Pinot, Y Charon, N Dinu, T Ait Imando, B Janvier, V Puill, D Benoit and M-a Duval. *Design and simulation of an intraoperative Positron Probe based on Silicon Photomultipliers*. *Proceeding of science*, 2012. 49, 60
- [Hudin *et al.* 2012b] N. Hudin, L. Pinot, N. Dinu and Y. Charon. *Characterization and Optimization of silicon photomultipliers for the development of intraoperative beta*

- probes*. Nuclear Instruments and . . . , vol. 695, pages 242–246, December 2012. 84, 87, 95, 117
- [Hudin 2013] N. Hudin. *Developpement de nouvelles sondes per-operatoires positron pour guider la chirurgie de tumeurs solides*. PhD thesis, Ecole Doctorale : Modelisation et Instrumentation en Physique, Energies, Geosciences et Environnement, 2013. 10, 57, 79, 92, 101
- [Huh *et al.* 2005] Sam S. Huh, D. Burdette, E. Chesi, K. Honscheid, H. Kagan, C. Lacasta, G. Llosa, M. Mikuz, S. J. Park, W. L. Rogers, a. Studen, P. Weilhammer and N. H. Clinthorne. *A pixelated silicon positron sensitive imaging probe*. IEEE Nuclear Science Symposium Conference Record, vol. 5, pages 2588–2591, 2005. 46
- [Hurkx *et al.* 1992] GAM Hurkx, HC De Graaff, WJ Kloosterman and MPG Knuvers. *A new analytical diode model including tunneling and avalanche breakdown*. Electron Devices, IEEE Transactions on, vol. 39, no. 9, pages 2090–2098, 1992. 92
- [Infante *et al.* 2015] JR Infante, R Lorente, JI Rayo, J Serrano, ML Domínguez, L García and M Moreno. *The use of radioguided surgery in the resection of osteoid osteoma*. Revista Española de Medicina Nuclear e Imagen Molecular (English Edition), vol. 34, no. 4, pages 225–229, 2015. 55
- [Ishiba *et al.* 2015] Toshiyuki Ishiba, Tsuyoshi Nakagawa, Takanobu Sato, Makoto Nagahara, Goshi Oda, Hitoshi Sugimoto, Mai Kasahara, Tokuko Hosoya, Kazunori Kubota, Tomoyuki Fujioka, Peter Danenberg, Kathleen Danenberg and Hiroyuki Uetake. *Efficiency of fluorodeoxyglucose positron emission tomography/computed tomography to predict prognosis in breast cancer patients received neoadjuvant chemotherapy*. SpringerPlus, vol. 4, page 817, 2015. 19
- [Ishikawa & Watanabe 2015] Norihiko Ishikawa and Go Watanabe. *Robot-Assisted Cardiac Surgery*. Annals of Thoracic and Cardiovascular Surgery, vol. 21, no. 4, pages 322–328, 2015. 16
- [Jarvis *et al.* 2014] Lesley A. Jarvis, Rongxiao Zhang, David J. Gladstone, Shudong Jiang, Whitney Hitchcock, Oscar D. Friedman, Adam K. Glaser, Michael Jermyn and Brian W. Pogue. *Cherenkov video imaging allows for the first visualization of radiation therapy in real time*. International Journal of Radiation Oncology Biology Physics, vol. 89, no. 3, pages 615–622, 2014. 49
- [Jewell *et al.* 2014] Elizabeth L. Jewell, Juan Juan Huang, Nadeem R. Abu-Rustum, Ginger J. Gardner, Carol L. Brown, Yukio Sonoda, Richard R. Barakat, Douglas A. Levine and Mario M. Leitao. *Detection of sentinel lymph nodes in minimally invasive surgery using indocyanine green and near-infrared fluorescence imaging for uterine and cervical malignancies*. Gynecologic Oncology, vol. 133, no. 2, pages 274–277, 2014. 27
- [Kaemmerer *et al.* 2012] Daniel Kaemmerer, Vikas Prasad, Wolfgang Daffner, Sven-Petter Haugvik, Stefan Senftleben, Richard P Baum and Merten Hommann. *Radioguided*

- surgery in neuroendocrine tumors using Ga-68-labeled somatostatin analogs: a pilot study.* *Clinical Nuclear Medicine*, vol. 37, no. 2, pages 142 – 147, 2012. 31
- [Kaschten *et al.* 1998] Bruno Kaschten, Achille Stevenaert, Bernard Sadzot, Manuel Deprezet *et al.* *Preoperative evaluation of 54 gliomas by PET with fluorine-18-fluorodeoxyglucose and/or carbon-11-methionine.* *The Journal of Nuclear Medicine*, vol. 39, no. 5, page 778, 1998. 22
- [Kebebew & Clark 2000] Electron Kebebew and Orlo H Clark. *Differentiated thyroid cancer: 'complete' rational approach.* *World journal of surgery*, vol. 24, no. 8, pages 942–951, 2000. 23
- [Keereweer *et al.* 2013] Stijn Keereweer, Pieter B A A Van Driel, Thomas J A Snoeks, Jeroen D F Kerrebijn, Robert J Baatenburg De Jong, Alexander L. Vahrmeijer, Henricus J C M Sterenberg and Clemens W G M Lowik. *Optical image-guided cancer surgery: Challenges and limitations.* *Clinical Cancer Research*, vol. 19, no. 14, pages 3745–3754, 2013. 19
- [Kerrou *et al.* 2011] Khaldoun Kerrou, Stéphanie Pitre, Charles Coutant, Roman Rouzier, Pierre-Yves Ancel, Cécile Lebeaux, Virginie Huchet, Françoise Montravers, Odile Pascal, Marie-Alix Duval, Françoise Lefebvre, Laurent Menard, Serge Uzan, Yves Charon and Emmanuel Barranger. *The Usefulness of a Preoperative Compact Imager, a Hand-Held {gamma}-Camera for Breast Cancer Sentinel Node Biopsy: Final Results of a Prospective Double-Blind, Clinical Study.* *Journal of nuclear medicine : official publication, Society of Nuclear Medicine*, vol. 52, no. 9, pages 1346–1353, 2011. 52
- [Kim *et al.* 2011] Wan Wook Kim, Jee Soo Kim, Sung Mo Hur, Sung Hoon Kim, Se Kyung Lee, Jae Hyuck Choi, Sangmin Kim, Joon Young Choi, Jeong Eon Lee, Jung Han Kim, Seok Jin Nam, Jung Hyun Yang and Jun Ho Choe. *Radioguided surgery using an intraoperative PET probe for tumor localization and verification of complete resection in differentiated thyroid cancer: A pilot study.* *Surgery*, vol. 149, no. 3, pages 416–424, 2011. 31
- [King *et al.* 2015] M. T. King, C. M. Carpenter, C. Sun, X. Ma, Q.-T. Le, J. B. Sunwoo, Z. Cheng, G. Prax and L. Xing. *À Radioluminescence Imaging: A Comparative Evaluation with Cerenkov Luminescence Imaging.* *Journal of Nuclear Medicine*, vol. 56, no. 9, pages 1458–1464, 2015. 35
- [Knoll 2010] Glenn F Knoll. *Radiation detection and measurement.* John Wiley & Sons, 2010. 61, 65, 68, 70, 71
- [Kovács *et al.* 2005] Adorján F Kovács, Constantin a Landes, Nadja Hamscho, Jörn H Risse, Uwe Berner and Christian Menzel. *Sentinel node biopsy as staging tool in a multimodality treatment approach to cancer of the oral cavity and the oropharynx.* *Otolaryngology–head and neck surgery : official journal of American Academy of Otolaryngology-Head and Neck Surgery*, vol. 132, pages 570–576, 2005. 52

- [Kraeber-Bodéré *et al.* 2005] Françoise Kraeber-Bodéré, Bertrand Cariou, Chantal Curtet, Boumediene Bridji, Caroline Rousseau, François Dravet, Bernard Charbonnel, Bruno Carnaille, Jean Claude Le Néel and Eric Mirallié. *Feasibility and benefit of fluorine 18-fluoro-2-deoxyglucose-guided surgery in the management of radioiodine-negative differentiated thyroid carcinoma metastases*. *Surgery*, vol. 138, no. 6, pages 1176–1182, 2005. 53
- [Krag *et al.* 1993] DN Krag, DL Weaver, JC Alex and JT et al Fairbank. *Surgical resection and radiolocalization of the sentinel lymph node in breast cancer using a gamma probe*. *Surgical oncology*, vol. 2, no. 6, pages 335–340, 1993. 51
- [Kubben *et al.* 2011] Pieter L Kubben, Karlien J ter Meulen, Olaf EMG Schijns, Mariel P ter Laak-Poort, Jacobus J van Overbeeke and Henk van Santbrink. *Intraoperative MRI-guided resection of glioblastoma multiforme: a systematic review*. *The Lancet Oncology*, vol. 12, no. 11, pages 1062–1070, 2011. 24
- [Lacaita *et al.* 1993] Andrea L Lacaita, Franco Zappa, Stefano Bigliardi and Manfredo Manfredi. *On the bremsstrahlung origin of hot-carrier-induced photons in silicon devices*. *Electron Devices, IEEE Transactions on*, vol. 40, no. 3, pages 577–582, 1993. 93
- [Lecoq *et al.* 2006] Paul Lecoq, Alexander Annenkov, Alexander Gektin, Mikhail Korzhik and Christian Pedrini. *Inorganic scintillators for detector systems: physical principles and crystal engineering*. Springer Science & Business Media, 2006. 68, 71
- [Lee *et al.* 2002] Wannoo Lee, Gyuseong Cho, Seung Wook Lee, Sungho Chang, Tae Hoon Lee and Jong Kyung Kim. *Simulation of maximum-likelihood position estimation in small gamma camera with position-sensitive photomultiplier tube (PSPMT)*. 2001 IEEE Nuclear Science Symposium Conference Record (Cat. No.01CH37310), vol. 4, pages 1915–1918, 2002. 42
- [Lehman *et al.* 2009] Constance D Lehman, Wendy DeMartini, Benjamin O Anderson and Stephen B Edge. *Indications for breast MRI in the patient with newly diagnosed breast cancer*. *Journal of the National Comprehensive Cancer Network*, vol. 7, no. 2, pages 193–201, 2009. 21
- [Leong *et al.* 2004] Carson Leong, John Boyages, Upali W Jayasinghe, Michael Bilous, Owen Ung, Boon Chua, Elizabeth Salisbury and Angela Y Wong. *Effect of margins on ipsilateral breast tumor recurrence after breast conservation therapy for lymph node-negative breast carcinoma*. *Cancer*, vol. 100, no. 9, pages 1823–1832, 2004. 21
- [Lerche *et al.* 2011] Christoph W Lerche, Torsten Solf, Peter Dueppenbecker, Benjamin Goldschmidt, Paul K Marsden and Volkmar Schulz. *Maximum likelihood based positioning and energy correction for pixelated solid state PET detectors*. In *Nuclear Science Symposium and Medical Imaging Conference (NSS/MIC)*, 2011 IEEE, pages 3610–3613. IEEE, 2011. 105
- [Levenback *et al.* 2009] Charles F Levenback, Ate GJ van der Zee, Lukas Rob, Marie Plante, Al Covens, Achim Schneider, Robert Coleman, Eugenio Solima, Hermann Hertel,

- Emmanuel Barranger *et al.* *Sentinel lymph node biopsy in patients with gynecologic cancers: expert panel statement from the International Sentinel Node Society Meeting, February 21, 2008.* *Gynecologic oncology*, vol. 114, no. 2, pages 151–156, 2009. 52
- [Levin & Hoffman 1999] C S Levin and E J Hoffman. *Calculation of positron range and its effect on the fundamental limit of positron emission tomography system spatial resolution.* *Physics in medicine and biology*, vol. 44, pages 781–799, 1999. 43, 157
- [Li *et al.* 2010a] Changqing Li, Gregory S Mitchell and Simon R Cherry. *Cerenkov luminescence tomography for small-animal imaging.* *Optics letters*, vol. 35, no. 7, pages 1109–1111, 2010. 35
- [Li *et al.* 2010b] Zhi Li, M Wedrowski, P Bruyndonckx and G Vandersteen. *Nonlinear least-squares modeling of 3D interaction position in a monolithic scintillator block.* *Physics in medicine and biology*, vol. 55, no. 21, page 6515, 2010. 104
- [Li *et al.* 2015] Joanne Li, Lawrence W Dobrucki, Marina Marjanovic, Eric J Chaney, Kenneth S Suslick and Stephen a Boppart. *Enhancement and wavelength-shifted emission of Cerenkov luminescence using multifunctional microspheres.* *Physics in medicine and biology*, vol. 60, no. 2, pages 727–39, 2015. 36
- [Ling *et al.* 2008] T Ling, TH Burnett, TK Lewellen and RS Miyaoka. *Parametric positioning of a continuous crystal PET detector with depth of interaction decoding.* *Physics in medicine and biology*, vol. 53, no. 7, page 1843, 2008. 103
- [Ling *et al.* 2014] Ted Ling, Jerry Slater, Prashanth Nookala, Rachel Mifflin, Roger Grove, Anh Ly, Baldev Patyal, Jerry Slater and Gary Yang. *Analysis of Intensity-Modulated Radiation Therapy (IMRT), Proton and 3D Conformal Radiotherapy (3D-CRT) for Reducing Perioperative Cardiopulmonary Complications in Esophageal Cancer Patients.* *Cancers*, vol. 6, no. 4, pages 2356–2368, 2014. 18
- [Liu & Goertzen 2013] Chen-Yi Liu and Andrew L Goertzen. *Improved event positioning in a gamma ray detector using an iterative position-weighted centre-of-gravity algorithm.* *Physics in medicine and biology*, vol. 58, no. 14, pages N189–200, jul 2013. 103
- [Liu *et al.* 2003] F. Liu, J.R. Saffer, G. M. Mayers, W. Kononenko, F. M. Newcomer, J. S. Karp and N. S. Lockyer. *Performance evaluation of a 64-pixel surgical probe for FDG imaging.* In *Nuclear Science Symposium Conference Record (NSS/MIC)*, 2003 IEEE, pages 645–649. IEEE, 2003. 48
- [Liu *et al.* 2010] Hongguang Liu, Gang Ren, Zheng Miao, Xiaofen Zhang, Xiaodong Tang, Peizhen Han and S Sanjiv. *Molecular Optical Imaging with Radioactive Probes.* *PLoS One*, vol. 5, no. 3, 2010. 35
- [Liu *et al.* 2012] H. Liu, C. M. Carpenter, H. Jiang, G. Pratz, C. Sun, M. P. Buchin, S. S. Gambhir, L. Xing and Z. Cheng. *Intraoperative Imaging of Tumors Using Cerenkov Luminescence Endoscopy: A Feasibility Experimental Study.* *Journal of Nuclear Medicine*, vol. 53, no. 10, pages 1579–1584, 2012. 35

- [Lloyd 1982] Stuart Lloyd. *Least squares quantization in PCM*. IEEE transactions on information theory, vol. 28, no. 2, pages 129–137, 1982. 134
- [Lodge *et al.* 2007] Mark Lodge, Madelon Pijls-Johannesma, Lisa Stirk, Alastair J Munro, Dirk De Ruyscher and Tom Jefferson. *A systematic literature review of the clinical and cost-effectiveness of hadron therapy in cancer*. Radiotherapy and Oncology, vol. 83, no. 2, pages 110–122, 2007. 17
- [Lovrics *et al.* 2011] P. J. Lovrics, S. D. Cornacchi, R. Vora, C. H. Goldsmith and K. Kahn moui. *Systematic review of radioguided surgery for non-palpable breast cancer*. European Journal of Surgical Oncology, vol. 37, no. 5, pages 388–397, 2011. 53
- [Majewski *et al.* 2011] S Majewski, J Proffitt and A Stolin. *Development of a mini gamma camera for prostate imaging*. In Nuclear Science Symposium and Medical Imaging Conference (NSS/MIC), 2011 IEEE, pages 4024–4029. IEEE, 2011. 42
- [Marcu 2012] Laura Marcu. *Fluorescence lifetime techniques in medical applications*. Annals of biomedical engineering, vol. 40, no. 2, pages 304–331, 2012. 27
- [Mariani *et al.* 2010] Giuliano Mariani, Armando E Giuliano and Harry William Strauss. Radioguided surgery. Springer, 2010. 36
- [Marone *et al.* 2009] A Marone, C Fiorini, P Baraldi, F Cadini, E Zio and F Camera. *Employing Neural Network to determine the position of interaction of medium-high energy gamma rays*. In Nuclear Science Symposium Conference Record (NSS/MIC), 2009 IEEE, pages 645–649. IEEE, 2009. 42, 104, 105
- [Martelli *et al.* 1998] Hélène Martelli, Marcel Ricard, Michèle Larroquet, Michel Wioland, François Paraf, Monique Fabre, Patrice Josset, Pierre G Helardot, Frédéric Gauthier, Marie-Josée Terrier-Lacombe *et al.* *Intraoperative localization of neuroblastoma in children with ^{123}I -or ^{125}I -radiolabeled metaiodobenzylguanidine*. Surgery, vol. 123, no. 1, pages 51–57, 1998. 54
- [Martin *et al.* 2000] A J Martin, W A Hall, H Liu, C H Pozza, E Michel, S O Casey, R E Maxwell and C L Truwit. *Brain tumor resection: intraoperative monitoring with high-field-strength MR imaging-initial results*. Radiology, vol. 215, no. 1, pages 221–8, 2000. 25
- [Martin *et al.* 2014] A. G R Martin, S. J. Thomas, S. V. Harden and N. G. Burnet. *Evaluating Competing and Emerging Technologies for Stereotactic Body Radiotherapy and Other Advanced Radiotherapy Techniques*. Clinical Oncology, vol. 27, no. 5, pages 251–259, 2014. 17
- [Mathelin *et al.* 2006a] C. Mathelin, I. Piqueras and J. L. Guyonnet. *Performances of a new prototype handheld scintillating probe for the search of sentinel lymph nodes in breast cancer*. European Journal of Surgical Oncology, vol. 32, no. 1, pages 24–28, 2006. 37, 42

- [Mathelin *et al.* 2006b] C Mathelin, I Piqueras and J-L Guyonnet. *Technologies en développement pour l'identification des ganglions sentinelles en chirurgie mammaire*. Gynécologie obstétrique & fertilité, vol. 34, no. 6, pages 521–525, 2006. 53
- [Mayer *et al.* 2000] a Mayer, E Tsiompanou, D O'Malley, Gm Boxer, J Bhatia, Aa Flynn, Ka Chester, Br Davidson, Aam Lewis, Mc Winslet, Ap Dhillon, Ajw Hilson and Rhj Begent. *Radioimmunoguided surgery in colorectal cancer using a genetically engineered anti-CEA single-chain Fv antibody*. Clinical Cancer Research, vol. 6, no. May, pages 1711–1719, 2000. 32
- [Mazzaferri & Kloos 2001] Ernest L Mazzaferri and Richard T Kloos. *Current approaches to primary therapy for papillary and follicular thyroid cancer*. The Journal of Clinical Endocrinology & Metabolism, vol. 86, no. 4, pages 1447–1463, 2001. 23
- [McNally & Golovin 2009] David McNally and Victor Golovin. *Review of solid state photomultiplier developments by CPTA and photonique SA*. Nuclear Instruments and Methods in Physics Research Section A: Accelerators, Spectrometers, Detectors and Associated Equipment, vol. 610, no. 1, pages 150–153, 2009. 93
- [Meads *et al.* 2014] C Meads, A J Sutton, A N Rosenthal, S MaÅysiak, M Kowalska, A Zapalska, E RogoziÅska, P Baldwin, R Ganesan, E Borowiack, P Barton, T Roberts, K Khan and S Sundar. *Sentinel lymph node biopsy in vulval cancer: systematic review and meta-analysis*. British journal of cancer, vol. 110, no. 12, pages 2837–2846, 2014. 51
- [Ménard *et al.* 1997] L Ménard, R Mastrippolito, Y Charon, P Laniece, L Pinot, L Ploux, A Saoudi, M Solal, M Ricard and L Valentin. *RITM: a mini γ camera for pre and per-operative radio guided cancer surgery evaluation for bone tumor localization in theater blocks*. Nuclear Science, IEEE Transactions on, vol. 44, no. 6, pages 2445–2449, 1997. 55
- [Mertens *et al.* 2012] Koen Mertens, Hamphrey Ham, Karel Deblaere, Jean-Pierre Okito Kalala, Caroline Van den Broecke, Dominique Slaets, Filip De Vos and Ingeborg Goethals. *Distribution Patterns of 18F-Labelled Fluoromethylcholine in Normal Structures and Tumors of the Head*. Clinical Nuclear Medicine, vol. 37, no. 8, pages e196–e203, 2012. 32, 147
- [Mester *et al.* 2011] C. Mester, C. Bruschini, P. Magro, N. Demartines, V. Dunet, E. Grigoriev, a. Konoplyannikov, V. Talanov, M. Matter, J. O. Prior and E. Charbon. *A handheld intra-operative ?? + sensing system*. Procedia Engineering, vol. 25, pages 988–991, 2011. 45
- [Metser *et al.* 2016] U Metser, R McVey, SE Ferguson, J Halankar and MQ Bernardini. *Intraoperative lymph node evaluation using 18F-FDG and a hand-held gamma probe in endometrial cancer surgery—a pilot study*. European journal of gynaecological oncology, vol. 37, no. 3, pages 362–366, 2016. 158
- [Mitchell *et al.* 2011] G S Mitchell, R K Gill, D L Boucher, C Li and S R Cherry. *In vivo Cerenkov luminescence imaging: a new tool for molecular imaging*. Philosophical

- transactions. Series A, Mathematical, physical, and engineering sciences, vol. 369, no. 1955, pages 4605–4619, 2011. 35
- [Moffatt-Bruce *et al.* 2008] Susan D Moffatt-Bruce, Stephen P Povoski, Suhail Sharif, Nathan C Hall, Patrick Ross, Morgan A Johnson and Edward W Martin. *A novel approach to positron emission tomography in lung cancer*. The Annals of thoracic surgery, vol. 86, no. 4, pages 1355–7, 2008. 54
- [Moncrieff *et al.* 2015] MD Moncrieff, AK Shah, L Igali and JJ Garioch. *False-negative rate of intraoperative frozen section margin analysis for complex head and neck nonmelanoma skin cancer excisions*. Clinical and experimental dermatology, vol. 40, no. 8, pages 834–838, 2015. 23
- [Monti *et al.* 2007] Simonetta Monti, Viviana Galimberti, Giuseppe Trifiro, Concetta De Cicco, Nicolas Peradze, Fabricio Brenelli, Julia Fernandez-Rodriguez, Nicole Rotmensz, Antuono Latronico, Anastasio Berrettini *et al.* *Occult breast lesion localization plus sentinel node biopsy (SNOLL): experience with 959 patients at the European Institute of Oncology*. Annals of Surgical Oncology, vol. 14, no. 10, pages 2928–2931, 2007. 53
- [Mortensen *et al.* 2011] Michael Bau Mortensen, Claus Frstrup, Alan Ainsworth, Henning Overgaard Nielsen, Torsten Pless and Claus Hovendal. *Combined pretherapeutic endoscopic and laparoscopic ultrasonography may predict survival of patients with upper gastrointestinal tract cancer*. Surgical endoscopy, vol. 25, no. 3, pages 804–812, 2011. 23
- [Motomura *et al.* 2005] Kazuyoshi Motomura, Atsushi Noguchi, Terumi Hashizume, Yoshihisa Hasegawa, Yoshifumi Komoike, Hideo Inaji, Toshihide Saida and Hiroki Koyama. *Usefulness of a solid-state gamma camera for sentinel node identification in patients with breast cancer*. Journal of Surgical Oncology, vol. 89, no. September 2004, pages 12–17, 2005. 53
- [Mullen *et al.* 2012] R Mullen, EJ Macaskill, A Khalil, E Elseedawy, DC Brown, AC Lee, CA Purdie, LB Jordan and AM Thompson. *Involved anterior margins after breast conserving surgery: is re-excision required?* European Journal of Surgical Oncology (EJSO), vol. 38, no. 4, pages 302–306, 2012. 21
- [Musienko 2009] Yuri Musienko. *Advances in multipixel Geiger-mode avalanche photodiodes (silicon photomultipliers)*. Nuclear Instruments and Methods in Physics Research, Section A: Accelerators, Spectrometers, Detectors and Associated Equipment, vol. 598, no. 1, pages 213–216, 2009. 90
- [Nakamura *et al.* 2014] Katsumasa Nakamura, Tomonari Sasaki, Saiji Ohga, Tadamasu Yoshitake, Kotaro Terashima, Kaori Asai, Keiji Matsumoto, Yoshiyuki Shioyama and Hiroshi Honda. *Recent advances in radiation oncology: Intensity-modulated radiotherapy, a clinical perspective*. International Journal of Clinical Oncology, vol. 19, no. 4, pages 564–569, 2014. 17

- [National Electrical Manufacturers Association 2012] Waszyngton. National Electrical Manufacturers Association. NEMA Standards Publication NU 1-2012: Performance Measurements of Gamma Cameras. National Electrical Manufacturers Association, 2012. 114
- [NCDB 2011] NCDB. *American College of Surgeon Commission on cancer, National Cancer Data Base, 2008 Data Submission*. Chicago, IL: American College of Surgeons, 2011. 23
- [Negele *et al.* 2006] T Negele, G Meisetschläger, T Brückner, K Scheidhauer, M Schwaiger and H Vogelsang. *Radio-guided surgery for persistent differentiated papillary thyroid cancer: case presentations and review of the literature*. Langenbeck's archives of surgery / Deutsche Gesellschaft für Chirurgie, vol. 391, no. 3, pages 178–86, 2006. 53
- [Nelson *et al.* 2013] Daniel W. Nelson, Terin H. Blanchard, Marlin W. Causey, Joseph F. Homann and Tommy A. Brown. *Examining the accuracy and clinical usefulness of intraoperative frozen section analysis in the management of pancreatic lesions*. American Journal of Surgery, vol. 205, no. 5, pages 613–617, 2013. 23
- [Netter *et al.* 2009] E Netter, L Pinot, L Menard, MA Duval, B Janvier, F Lefebvre, R Siebert and Y Charon. *The Tumor Resection Camera (TReCam), a multipixel imaging probe for radio-guided surgery*. In Nuclear Science Symposium Conference Record (NSS/MIC), 2009 IEEE, pages 2573–2576. IEEE, 2009. 42, 103
- [Niebling *et al.* 2016] M.G. Niebling, R.G. Pleijhuis, E. Bastiaannet, A.H. Brouwers, G.M. van Dam and H.J. Hoekstra. *A systematic review and meta-analyses of sentinel lymph node identification in breast cancer and melanoma, a plea for tracer mapping*. European Journal of Surgical Oncology (EJSO), 2016. 51
- [Ntziachristos *et al.* 2005] Vasilis Ntziachristos, Jorge Ripoll, Lihong V Wang and Ralph Weissleder. *Looking and listening to light: the evolution of whole-body photonic imaging*. Nature biotechnology, vol. 23, no. 3, pages 313–320, 2005. 27
- [Oppenlander & Porter 2014] M.E. Oppenlander and R.W. Porter. *Radiosurgery à Gamma Knife and Cyberknife*. Encyclopedia of the Neurological Sciences, vol. 3, pages 1050–1051, 2014. 17
- [Pani *et al.* 2002] R. Pani, R. Scafè, R. Pellegrini, A. Soluri, G. Trotta, L. Indovina, M. N. Cinti and G. De Vincentis. *Scintillation arrays characterization for photon emission imaging*. Nuclear Instruments and Methods in Physics Research, Section A: Accelerators, Spectrometers, Detectors and Associated Equipment, vol. 477, no. 1-3, pages 72–76, 2002. 41
- [Pani *et al.* 2004] R Pani, MN Cinti, F De Notaristefani, R Pellegrini, P Bennati, M Betti, G Trotta, A Karimian, Mauro Mattioli, F Garibaldiet *al.* *Imaging performances of LaCl 3: Ce scintillation crystals in SPECT*. In Nuclear Science Symposium Conference Record, 2004 IEEE, volume 4, pages 2283–2287. IEEE, 2004. 83

- [Pani *et al.* 2009] R. Pani, F. Vittorini, M. N. Cinti, P. Bennati, R. Pellegrini, S. Ridolfi, R. Scafé, S. Lo Meo, M. Mattioli, F. L. Navarra, G. Moschini, A. Fabbri, E. D'Abramo, V. Orsolini Cencelli and D. Sacco. *Revisited position arithmetics for $LaBr_3:Ce$ continuous crystals*. Nuclear Physics B - Proceedings Supplements, vol. 197, no. 1, pages 383–386, 2009. 42, 103
- [Pani *et al.* 2011] Roberto Pani, Maria Nerina Cinti, Paolo Bennati, Rosanna Pellegrini, Raffaele Scafé, Marco Bettiol, Chiara Marchioni, Sergio Lo Meo and Andrea Fabbri. *New position arithmetic for scintillation camera based on floating weight system*. In Nuclear Science Symposium and Medical Imaging Conference (NSS/MIC), 2011 IEEE, pages 3395–3398. IEEE, 2011. 103
- [Paredes *et al.* 2008] P. Paredes, S. Vidal-Sicart, G. Zanón, N. Roé, S. Rubí, S. Lafuente, J. Pavía and F. Pons. *Radioguided occult lesion localisation in breast cancer using an intraoperative portable gamma camera: First results*. European Journal of Nuclear Medicine and Molecular Imaging, vol. 35, pages 230–235, 2008. 54
- [Park *et al.* 2000] Catherine C Park, Michihide Mitsumori, Asa Nixon, Abram Recht, James Connolly, Rebecca Gelman, Barbara Silver, Stella Hetelekidis, Anthony Abner, Jay R Harris *et al.* *Outcome at 8 years after breast-conserving surgery and radiation therapy for invasive breast cancer: influence of margin status and systemic therapy on local recurrence*. Journal of Clinical Oncology, vol. 18, no. 8, pages 1668–1675, 2000. 21
- [Piemonte 2006] Claudio Piemonte. *A new Silicon Photomultiplier structure for blue light detection*. Nuclear Instruments and Methods in Physics Research, Section A: Accelerators, Spectrometers, Detectors and Associated Equipment, vol. 568, no. 1, pages 224–232, 2006. 86, 89
- [Piert *et al.* 2007] Morand Piert, Maria Burian, Günther Meisetschläger, Hubert J. Stein, Sibylle Ziegler, Jörg Nährig, Maria Picchio, Andreas Buck, Joerg R. Siewert and Markus Schwaiger. *Positron detection for the intraoperative localisation of cancer deposits*. European Journal of Nuclear Medicine and Molecular Imaging, vol. 34, no. 10, pages 1534–1544, 2007. 54, 56, 60
- [Piert *et al.* 2008] M Piert, J Carey and N Clinthorne. *Probe-guided localization of cancer deposits using [^{18}F] fluorodeoxyglucose*. The Quarterly Journal of Nuclear Medicine and Molecular Imaging, vol. 52, no. 1, page 37, 2008. 54
- [Pitre *et al.* 2003] Stéphanie Pitre, Laurent Ménard, Marcel Ricard, Maurice Solal, Jean-Rémi Garbay and Yves Charon. *A hand-held imaging probe for radio-guided surgery: physical performance and preliminary clinical experience*. European journal of nuclear medicine and molecular imaging, vol. 30, no. 3, pages 339–343, 2003. 42
- [Pöpperl *et al.* 2006] Gabriele Pöpperl, Friedrich W Kreth, Jochen Herms, Walter Koch, Jan H Mehrkens, Franz J Gildehaus, Hans a Kretzschmar, Jörg C Tonn and Klaus Tatsch. *Analysis of ^{18}F -FET PET for grading of recurrent gliomas: is evaluation of uptake kinetics superior to standard methods?* Journal of nuclear medicine : official publication, Society of Nuclear Medicine, vol. 47, no. 3, pages 393–403, 2006. 147

- [Povoski *et al.* 2008] Stephen P Povoski, Nathan C Hall, Edward W Martin and Michael J Walker. *Multimodality approach of perioperative 18F-FDG PET/CT imaging, intraoperative 18F-FDG handheld gamma probe detection, and intraoperative ultrasound for tumor localization and verification of resection of all sites of hypermetabolic activity in a case of occult recurrent metastatic melanoma*. World journal of surgical oncology, vol. 6, page 1, 2008. 31, 54
- [Povoski *et al.* 2009] Stephen P Povoski, Ryan L Neff, Cathy M Mojzisik, David M O'Malley, George H Hinkle, Nathan C Hall, Douglas a Murrey, Michael V Knopp and Edward W Martin. *A comprehensive overview of radioguided surgery using gamma detection probe technology*. World journal of surgical oncology, vol. 7, page 11, 2009. 19, 28, 52
- [Povoski *et al.* 2015] Stephen P Povoski, Nathan C Hall, Douglas A Murrey, Chadwick L Wright and Edward W Martin. *Feasibility of a multimodal (18)F-FDG-directed lymph node surgical excisional biopsy approach for appropriate diagnostic tissue sampling in patients with suspected lymphoma*. BMC cancer, vol. 15, page 378, 2015. 31
- [Prakash *et al.* 2009] Neal Prakash, Falk Uhlemann, Sameer A Sheth, Susan Bookheimer, Neil Martin and Arthur W Toga. *Current trends in intraoperative optical imaging for functional brain mapping and delineation of lesions of language cortex*. Neuroimage, vol. 47, pages T116–T126, 2009. 26
- [Prichard *et al.* 1992] HM Prichard, EA Venso and CL Dodson. *Liquid-scintillation analysis of {sup 222} Rn in water by alpha-beta discrimination*. Radioactivity and Radiochemistry, vol. 3, no. 1, 1992. 144
- [Puri *et al.* 2016] Rajesh Puri, Manish Manrai, Ragesh Babu Thandassery and Abdulrahman A Alfadda. *Endoscopic ultrasound in the diagnosis and management of carcinoma pancreas*. World journal of gastrointestinal endoscopy, vol. 8, no. 2, pages 67–76, 2016. 25, 26
- [Ramos *et al.* 2013] Manuel Ramos, Juan Carlos Díaz, Teresa Ramos, Ricardo Ruano, Martín Aparicio, Magdalena Sancho and José María González-Orús. *Ultrasound-guided excision combined with intraoperative assessment of gross macroscopic margins decreases the rate of reoperations for non-palpable invasive breast cancer*. Breast, vol. 22, no. 4, pages 520–524, 2013. 25
- [Raylman & Hyder 2004] Raymond R. Raylman and Asad Hyder. *A dual surface barrier detector unit for beta-sensitive endoscopic probes*. IEEE Transactions on Nuclear Science, vol. 51, no. 1 I, pages 117–122, 2004. 44, 45, 79
- [Raylman & Wahl 1994] R R Raylman and R L Wahl. *A fiber-optically coupled positron-sensitive surgical probe*. Journal of nuclear medicine : official publication, Society of Nuclear Medicine, vol. 35, no. 5, pages 909–913, 1994. 44
- [Raylman & Wahl 1996] Raymond R Raylman and Richard L Wahl. *Evaluation of ion-implanted-silicon detectors for use in intraoperative positron-sensitive probes*. Medical physics, vol. 23, no. 11, pages 1889–1895, 1996. 44

- [Rech *et al.* 2008] I Rech, A Ingargiola, R Spinelli, I Labanca, S Marangoni, M Ghioni and S Cova. *Optical crosstalk in single photon avalanche diode arrays: a new complete model*. Optics Express, vol. 16, no. 12, pages 8381–8393, 2008. 92, 93
- [Rettenbacher *et al.* 2000] Lukas Rettenbacher, Paul Sungler, Dietmar Gmeiner, Helmut Kässmann and Günther Galvan. *Detecting the sentinel lymph node in patients with differentiated thyroid carcinoma*. European journal of nuclear medicine, vol. 27, no. 9, pages 1399–1401, 2000. 52
- [Ribatti *et al.* 2006] D. Ribatti, G. Mangialardi and a. Vacca. *Stephen Paget and the 'seed and soil' theory of metastatic dissemination*. Clinical and Experimental Medicine, vol. 6, no. 4, pages 145–149, 2006. 15
- [Ricard *et al.* 1993] Marcel Ricard, Florence Tenenbaum, Martin Schlumberger, Jean-Paul Travagli, Jean Lumbroso, Yann Revillon and Claude Parmentier. *Intraoperative detection of pheochromocytoma with iodine-125 labelled meta-iodobenzylguanidine: a feasibility study*. European journal of nuclear medicine, vol. 20, no. 5, pages 426–430, 1993. 54
- [Robertson *et al.* 2009] R Robertson, M. S. Germanos, C. Li, G. S. Mitchell, S. R. Cherry and M. D. Silva. *Optical Imaging of Cerenkov light generation from positron-emitting radiotracers*. Phys Med Biol, vol. 54, no. 16, pages 1–12, 2009. 35
- [Roncali & Cherry 2011] Emilie Roncali and Simon R. Cherry. *Application of silicon photomultipliers to positron emission tomography*. Annals of Biomedical Engineering, vol. 39, no. 4, pages 1358–1377, 2011. 90, 91
- [Rössler *et al.* 2005] Karl Rössler, M Donat, R Lanzenberger, K Novak, A Geissler, A Gartus, AR Tahamtan, D Milakara, T Czech, M Barthet *et al.* *Evaluation of preoperative high magnetic field motor functional MRI (3 Tesla) in glioma patients by navigated electrocortical stimulation and postoperative outcome*. Journal of Neurology, Neurosurgery & Psychiatry, vol. 76, no. 8, pages 1152–1157, 2005. 22
- [Rubello *et al.* 2006] Domenico Rubello, Maria Rosa Pelizzo, Dario Casara, Andrea Piotto, Antonio Toniato, Lorraine Fig and Milton Gross. *Radio-guided surgery for non-131I-avid thyroid cancer*. Thyroid, vol. 16, no. 11, pages 1105–1111, 2006. 53
- [Rubello *et al.* 2007] D Rubello, M Salvatori, G Ardito, G Mariani, A Al-Nahhas, MD Gross, PC Muzzio and MR Pelizzo. *Iodine-131 radio-guided surgery in differentiated thyroid cancer: outcome on 31 patients and review of the literature*. Biomedicine & Pharmacotherapy, vol. 61, no. 8, pages 477–481, 2007. 53
- [Russo *et al.* 2008] P Russo, a Lauria, G Mettivier, M C Montesi, M Marotta, L Aloj and S Lastoria. *18F-FDG positron autoradiography with a particle counting silicon pixel detector*. Physics in medicine and biology, vol. 53, no. 21, pages 6227–6243, 2008. 46
- [Rygh *et al.* 2008] Ola Morten Rygh, Tormod Selbekk, Sverre Helge Torp, Stian Lydersen, Toril Anita Nagelhus Hernes and Geirmund Unsgaard. *Comparison of navigated 3D*

- ultrasound findings with histopathology in subsequent phases of glioblastoma resection.* Acta Neurochirurgica, vol. 150, no. 10, pages 1033–1041, 2008. 26
- [Sabet *et al.* 2015] Hamid Sabet, Brendan C Stack Jr and Vivek V Nagarkar. *A Hand-Held , Intra-Operative Positron Imaging Probe for Surgical Applications.* IEEE Transaction on Nuclear Science, vol. 62, no. 5, pages 1927–1934, 2015. 48, 49, 56, 61, 79
- [Sadeghi 2015] R. Sadeghi. *Sentinel node biopsy for lymph nodal staging of uterine cervix cancer: a systematic review and meta-analysis of the pertinent literature.* European journal of surgical oncology : the journal of the European Society of Surgical Oncology and the British Association of Surgical Oncology, vol. 41, no. 1, pages 1–20, 2015. 51
- [Salvador *et al.* 2007] S Salvador, V Bekaert, C Mathelin, JL Guyonnet and D Huss. *An operative gamma camera for sentinel lymph node procedure in case of breast cancer.* Journal of Instrumentation, vol. 2, no. 07, page P07003, 2007. 42
- [Sanai & Berger 2008] Nader Sanai and Mitchel S Berger. *Glioma extent of resection and its impact on patient outcome.* Neurosurgery, vol. 62, no. 4, pages 753–766, 2008. 22
- [Sansovini *et al.* 2013] M Sansovini, S Severi, A Ambrosetti, M Monti, O Nanni, A Sarnelli, L Bodei, L Garaboldi, M Bartolomei and G Paganelli. *Treatment with the Radiolabelled Somatostatin Analog ¹⁷⁷Lu-DOTATATE for Advanced Pancreatic Neuroendocrine Tumors.* Neuroendocrinology, vol. 97, pages 347–354, 2013. 31
- [Sarikaya *et al.* 2007] Ismet Sarikaya, Stephen P Povoski, Osama H Al-Saif, Ergun Kocak, Mark Bloomston, Steven Marsh, Zongjian Cao, Douglas a Murrey, Jun Zhang, Nathan C Hall, Michael V Knopp and Edward W Martin. *Combined use of preoperative ¹⁸F FDG-PET imaging and intraoperative gamma probe detection for accurate assessment of tumor recurrence in patients with colorectal cancer.* World journal of surgical oncology, vol. 5, page 80, 2007. 54
- [Scatliff & Morris 2014] James H Scatliff and Peter J Morris. *From roentgen to magnetic resonance imaging: the history of medical imaging.* North Carolina medical journal, vol. 75, no. 2, pages 111–3, 2014. 16
- [Scollard *et al.* 2011] Deborah A. Scollard, Conrad Chan, Claire M B Holloway and Raymond M. Reilly. *A kit to prepare ¹¹¹In-DTPA-trastuzumab (Herceptin) Fab fragments injection under GMP conditions for imaging or radioimmunoguided surgery of HER2-positive breast cancer.* Nuclear Medicine and Biology, vol. 38, no. 1, pages 129–136, 2011. 32
- [Scrimger & Baker 1967] JW Scrimger and RG Baker. *Investigation of light distribution from scintillations in a gamma camera crystal.* Physics in medicine and biology, vol. 12, no. 1, page 101, 1967. 104
- [SEER 2014] SEER. *Surveillance, Epidemiology, and End Results Program.* SEER Cancer Statistics Review, 1975-2012, National Cancer Institute, 2014. 23

- [Selverstone *et al.* 1949] Bertram Selverstone, H. William Sweet and Charles V Robinson. *The Clinical Use of Radioactive Phosphorus in the Surgery of Brain Tumors*. *Annals of Surgery*, pages 643–650, 1949. 28
- [Senft *et al.* 2011] Christian Senft, Andrea Bink, Kea Franz, Hartmut Vatter, Thomas Gasser and Volker Seifert. *Intraoperative MRI guidance and extent of resection in glioma surgery: A randomised, controlled trial*. *The Lancet Oncology*, vol. 12, no. 11, pages 997–1003, 2011. 24, 25
- [Senkus *et al.* 2013] E Senkus, S Kyriakides, F Penault-Llorca, P Poortmans, A Thompson, Sophia Zackrisson and F Cardoso. *Primary breast cancer: ESMO Clinical Practice Guidelines for diagnosis, treatment and follow-up*. *Annals of Oncology*, page mdt284, 2013. 21
- [Serrano *et al.* 2005] J Serrano, JI Rayo, JR Infante, ML Domínguez, L Lorenzana, JL Porras, JM Cabezudo, L García-Bernardo and R Sánchez-Sánchez. *Radioguided neurosurgery: a novel application of nuclear medicine*. *Revista española de medicina nuclear*, vol. 25, no. 3, pages 184–187, 2005. 54
- [Shestakova *et al.* 2006] Irina Shestakova, Vivek V Nagarkar, Valeriy Gaysinskiy, Gerald Entine, Brendan C Stack and Brian Miller. *Feasibility Studies of an EMCCD-based Beta Imaging Probe for Radioguided Thyroid Surgery*. *Physics*, vol. 6319, no. August 2015, pages 1–9, 2006. 31
- [Shimazoe *et al.* 2011] Kenji Shimazoe, Hiroyuki Takahashi, Kaoru Fujita, Hiroshi Mori and Toshimitsu Momose. *Development of positron sensor for multi-modal endoscopy*. *Nuclear Instruments and Methods in Physics Research Section A: Accelerators, Spectrometers, Detectors and Associated Equipment*, vol. 648, pages S116–S118, 2011. 43
- [Shimotake *et al.* 2005] Takashi Shimotake, Tomoki Tsuda, Shigeyoshi Aoi, Shigehisa Fumino and Naomi Iwai. *Iodine 123 metaiodobenzylguanidine radio-guided navigation surgery for recurrent medullary thyroid carcinoma in a girl with multiple endocrine neoplasia type 2B*. *Journal of Pediatric Surgery*, vol. 40, no. 10, pages 1643–1646, 2005. 32
- [Shoaib *et al.* 2001] T Shoaib, D S Soutar, D G MacDonald, I G Camilleri, D J Dunaway, H W Gray, G M McCurrach, R G Bessent, T I MacLeod and a G Robertson. *The accuracy of head and neck carcinoma sentinel lymph node biopsy in the clinically N0 neck*. *Cancer*, vol. 91, no. 11, pages 2077–83, 2001. 51
- [Sieira-Gil *et al.* 2015] Ramón Sieira-Gil, Pilar Paredes, Carles Martí-Pagès, Ada Ferrer-Fuertes, Eloy García-Díez, Gui Youn Cho-Lee, Andres Tapias, Maria Mayoral and Sergi Vidal-Sicart. *SPECT-CT and intraoperative portable gamma-camera detection protocol for sentinel lymph node biopsy in oral cavity squamous cell carcinoma*. *Journal of Cranio-Maxillofacial Surgery*, vol. 43, no. 10, pages 2205–2213, 2015. 52
- [Sim *et al.* 1986] F. H. Sim, W. F. Taylor, D. J. Pritchard and E. H. Soule. *Lymphadenectomy in the management of stage I malignant melanoma: a prospective randomized study*. In *Mayo Clinic Proceedings*, volume 61, pages 697–705. Elsevier, 1986. 52

- [Singh *et al.* 2009] Bipin Singh, Brendan Stack, Samta Thacker, Valeriy Gaysinskiy, Steven Cool, Gerald Entine and Vivek Nagarkar. *In vivo imaging of lingual cancer in a rabbit model using a hand-held imaging beta probe*. In Nuclear Science Symposium Conference Record (NSS/MIC), 2009 IEEE, pages 3038–3041. IEEE, 2009. 49, 56
- [Singh *et al.* 2013] Bipin Singh, Brendan C Stack Jr, Samta Thacker, Valeriy Gaysinskiy, Twyla Bartel, Val Lowe, Steven Cool, Gerald Entine and Vivek Nagarkar. *A hand-held beta imaging probe for FDG*. Annals of nuclear medicine, vol. 27, no. 3, pages 203–208, 2013. 48
- [Solfaroli Camillocci *et al.* 2014] E Solfaroli Camillocci, G Baroni, F Bellini, V Bocci, F Collamati, M Cremonesi, E De Lucia, P Ferroli, S Fiore, C M Grana, M Marafini, I Mattei, S Morganti, G Paganelli, V Patera, L Piersanti, L Recchia, a Russomando, M Schiariti, a Sarti, a Sciubba, C Voena and R Faccini. *A novel radioguided surgery technique exploiting $\beta(-)$ decays*. Scientific reports, vol. 4, page 4401, jan 2014. 46, 56, 57
- [Solfaroli Camillocci *et al.* 2016] E Solfaroli Camillocci, V Bocci, G Chiodi, F Collamati, R Donnarumma, R Faccini, C Mancini Terracciano, M Marafini, I Mattei, S Muraro *et al.* *Intraoperative probe detecting β - decays in brain tumour radio-guided surgery*. Nuclear Instruments and Methods in Physics Research Section A: Accelerators, Spectrometers, Detectors and Associated Equipment, 2016. 45, 55, 56
- [Soluri *et al.* 2006] A. Soluri, R. Massari, C. Trotta, A. Tofani, G. Di Santo, B. Di Pietro, M. L. Di Paolo, A. Roncacci, C. Amanti and F. Scopinaro. *Small field of view, high-resolution, portable γ -camera for axillary sentinel node detection*. Nuclear Instruments and Methods in Physics Research, Section A: Accelerators, Spectrometers, Detectors and Associated Equipment, vol. 569, no. 2 SPEC. ISS., pages 273–276, 2006. 73
- [Song *et al.* 2015] Tianming Song, Xia Liu, Yawei Qu, Haixiao Liu, Chengpeng Bao, Chengcai Leng, Zhenhua Hu and Kun Wang. *A Novel Endoscopic Cerenkov Luminescence Imaging System for Intraoperative Surgical Navigation*. Molecular Imaging, vol. 14, no. August, pages 443–452, 2015. 35
- [Spinelli *et al.* 2011] Antonello E Spinelli, Chaincy Kuo, Brad W Rice, Riccardo Calandrino, Pasquina Marzola, Andrea Sbarbati and Federico Boschi. *Multispectral Cerenkov luminescence tomography for small animal optical imaging*. Optics express, vol. 19, no. 13, pages 12605–12618, 2011. 35
- [Spinelli *et al.* 2013] Antonello Enrico Spinelli, Marco Ferdeghini, Carlo Cavedon, Emanuele Zivelonghi, Riccardo Calandrino, Alberto Fenzi, Andrea Sbarbati and Federico Boschi. *First human Cerenkography*. Journal of Biomedical Optics, vol. 18, no. 2, pages 020502–020502, 2013. 49, 50
- [Stoffels *et al.* 2012] I. Stoffels, T. Poeppel, C. Boy, S. Mueller, F. Wichmann, J. Dissemond, D. Schadendorf, S. Rosenbaum-Krumme and J. Klode. *Radio-guided surgery: Advantages of a new portable γ -camera (Sentinella®) for intraoperative real time imaging*

- and detection of sentinel lymph nodes in cutaneous malignancies.* Journal of the European Academy of Dermatology and Venereology, vol. 26, no. 3, pages 308–313, 2012. 52
- [Stolin *et al.* 2010] AV Stolin, S Majewski, RR Raylman and HW Hazard. *Fingertip beta imager based on the SiPM technology.* In Nuclear Science Symposium Conference Record (NSS/MIC), 2010 IEEE, pages 2595–2597. IEEE, 2010. 49, 60, 157
- [Strong *et al.* 2008] Vivian E. Strong, John Humm, Paul Russo, Achim Jungbluth, W. Douglas Wong, Farhad Daghighian, Lloyd Old, Yuman Fong and Steven M. Larson. *A novel method to localize antibody-targeted cancer deposits intraoperatively using handheld PET beta and gamma probes.* Surgical Endoscopy and Other Interventional Techniques, vol. 22, no. 2, pages 386–391, 2008. 32
- [Strong *et al.* 2009] Vivian Strong, Charles Galanis, Christopher Riedl, Valerie Longo, Farhad Daghighian, John Humm, Steven Larson and Yuman Fong. *Portable PET probes are a novel tool for intraoperative localization of tumor deposits.* Annals of Surgical Innovation and Research, vol. 3, no. 1, page 2, 2009. 55
- [Stummer *et al.* 2006] Walter Stummer, Uwe Pichlmeier, Thomas Meinel, Otmar Dieter Wiestler, Friedhelm Zanella and Hans-Jürgen Reulen. *Fluorescence-guided surgery with 5-aminolevulinic acid for resection of malignant glioma: a randomised controlled multicentre phase III trial.* The lancet oncology, vol. 7, no. 5, pages 392–401, may 2006. 27
- [Sudhakar 2010] a Sudhakar. *History of Cancer, Ancient and Modern Treatment Methods Akulapalli.* J Cancer Sci Ther., vol. 1, no. 2, pages 1–4, 2010. 13
- [Sweet 1951] William H Sweet. *The uses of nuclear disintegration in the diagnosis and treatment of brain tumor.* New England Journal of Medicine, vol. 245, no. 23, pages 875–878, 1951. 53
- [Szelényi *et al.* 2010] Andrea Szelényi, Lorenzo Bello, Hugues Duffau, Enrica Fava, Guenther C Feigl, Miroslav Galanda, Georg Neuloh, Francesco Signorelli and Francesco Sala. *Intraoperative electrical stimulation in awake craniotomy: methodological aspects of current practice.* Neurosurgical focus, vol. 28, no. 2, page E7, 2010. 22
- [Thacker *et al.* 2008] Samta C Thacker, Brendan C Stack, Val Lowe, Valeriy Gaysinskiy, Steven Cool, Vivek V Nagarkar and Gerald Entine. *A novel imaging beta probe for radio-guided surgery.* In Nuclear Science Symposium Conference Record, 2008. NSS’08. IEEE, pages 3875–3878. IEEE, 2008. 49
- [Thorek *et al.* 2013a] D. L. J. Thorek, C. C. Riedl and J. Grimm. *Clinical Cerenkov Luminescence Imaging of 18F-FDG.* Journal of Nuclear Medicine, vol. 55, no. 1, pages 95–98, 2013. 49
- [Thorek *et al.* 2013b] Daniel L J Thorek, Anuja Ogirala, Bradley J Beattie and Jan Grimm. *Quantitative imaging of disease signatures through radioactive decay signal conversion.* Nature medicine, vol. 19, no. 10, pages 1345–50, 2013. 36

- [Tiernan *et al.* 2012] J. P. Tiernan, I. Ansari, N. A. Hirst, P. A. Millner, T. A. Hughes and D. G. Jayne. *Intra-operative tumour detection and staging in colorectal cancer surgery*. *Colorectal Disease*, vol. 14, no. 9, pages 510–521, 2012. 54
- [Tipnis *et al.* 2004] SV Tipnis, VV Nagarkar, I Shestakova, V Gaysinskiy, G Entine, MP Tornai and BC Stack Jr. *Feasibility of a beta-gamma digital imaging probe for radioguided surgery*. *Nuclear Science, IEEE Transactions on*, vol. 51, no. 1, pages 110–116, 2004. 60
- [Tornai *et al.* 1996] Martin P. Tornai, Lawrence R. MacDonald, Craig S. Levin, Stefan Siegel and Edward J. Hoffman. *Design considerations and initial performance of a 1.2 cm² beta imaging intra-operative probe*. *IEEE Transactions on Nuclear Science*, vol. 43, no. 4 PART 1, pages 2326–2335, 1996. 60
- [Tornai *et al.* 2001] M. P. Tornai, C. N. Archer, A. G. Weisenberger, R. Wojcik, V. Popov, S. Majewski, C. E. Keppel, C. S. Levin, S. V. Tipnis and V. V. Nagarkar. *Investigation of microcolumnar scintillators on an optical fiber coupled compact imaging system*. *IEEE Transactions on Nuclear Science*, vol. 48, no. 3 II, pages 637–644, 2001. 48
- [Tornai *et al.* 2002] Martin P Tornai, Bradley E Patt, Jan S Iwanczyk, Carolyn R Tull, Lawrence R MacDonald and Edward J Hoffman. *A novel silicon array designed for intraoperative charged particle imaging*. *Medical physics*, vol. 29, no. 11, pages 2529–2540, 2002. 46
- [Trotta *et al.* 2007] C. Trotta, R. Massari, N. Palermo, F. Scopinaro and A. Soluri. *New high spatial resolution portable camera in medical imaging*. *Nuclear Instruments and Methods in Physics Research, Section A: Accelerators, Spectrometers, Detectors and Associated Equipment*, vol. 577, no. 3, pages 604–610, 2007. 42
- [Trotta *et al.* 2008] C. Trotta, R. Massari, G. Trinci, N. Palermo, S. Boccalini, F. Scopinaro and A. Soluri. *High-Resolution Imaging System (HiRIS) based on H9500 PSPMT*. *Nuclear Instruments and Methods in Physics Research, Section A: Accelerators, Spectrometers, Detectors and Associated Equipment*, vol. 593, no. 3, pages 454–458, 2008. 42
- [Tsuchimochi & Hayama 2013] Makoto Tsuchimochi and Kazuhide Hayama. *Intraoperative gamma cameras for radioguided surgery: Technical characteristics, performance parameters, and clinical applications*. *Physica Medica*, vol. 29, no. 2, pages 126–138, 2013. 28, 35, 40
- [Ubhi *et al.* 1984] CS Ubhi, JG Hardy and CAS Pegg. *Mediastinal parathyroid adenoma: a new method of localization*. *British journal of surgery*, vol. 71, no. 11, pages 859–860, 1984. 53
- [Unsgaard *et al.* 2006] G Unsgaard, O M Rygh, T Selbekk, T B Muller, F Kolstad, F Lindseth and T A Hernes. *Intra-operative 3D ultrasound in neurosurgery*. *Acta Neurochir (Wien)*, vol. 148, no. 3, pages 235–53; discussion 253, 2006. 25

- [Van Dam *et al.* 2010] Herman T Van Dam, Stefan Seifert, Ruud Vinke, Peter Dendooven, Herbert Löhner, Freek J Beekman and Dennis R Schaart. *A comprehensive model of the response of silicon photomultipliers*. Nuclear Science, IEEE Transactions on, vol. 57, no. 4, pages 2254–2266, 2010. 91
- [van de Watering *et al.* 2014] Floor C. J. van de Watering, Mark Rijpkema, Marc Robillard, Wim J. G. Oyen and Otto C. Boerman. *Pretargeted Imaging and Radioimmunotherapy of Cancer Using Antibodies and Bioorthogonal Chemistry*. Frontiers in Medicine, vol. 1, no. November, pages 1–11, 2014. 33
- [Varadhachary *et al.* 2006] Gauri R Varadhachary, Eric P Tamm, James L Abbruzzese, Henry Q Xiong, Christopher H Crane, Huamin Wang, Jeffrey E Lee, Peter WT Pisters, Douglas B Evans and Robert A Wolff. *Borderline resectable pancreatic cancer: definitions, management, and role of preoperative therapy*. Annals of surgical oncology, vol. 13, no. 8, pages 1035–1046, 2006. 22
- [Vargo & Beriwal 2014] John a Vargo and Sushil Beriwal. *Image-based brachytherapy for cervical cancer*. World journal of clinical oncology, vol. 5, no. 5, pages 921–30, 2014. 19
- [Verbeek *et al.* 2014] Floris P R Verbeek, Susan L Troyan, J Sven D Mieog, Gerrit-Jan Liefers, Lorissa A Moffitt, Mireille Rosenberg, Judith Hirshfield-Bartek, Sylvain Gioux, Cornelis J H van de Velde, Alexander L Vahrmeijer and John V Frangioni. *Near-infrared fluorescence sentinel lymph node mapping in breast cancer: a multicenter experience*. Breast cancer research and treatment, vol. 143, no. 2, pages 333–42, 2014. 27
- [Verbeke *et al.* 2006] CS Verbeke, D Leitch, KV Menon, MJ McMahon, PJ Guillou and A Anthoney. *Redefining the R1 resection in pancreatic cancer*. British Journal of Surgery, vol. 93, no. 10, pages 1232–1237, 2006. 23
- [Vermeeren *et al.* 2009] L Vermeeren, RA Valdés Olmos, W Meinhardt, A Bex, HG Van der Poel, WV Vogel, F Sivro, CA Hoefnagel and S Horenblas. *Intraoperative radioguidance with a portable gamma camera: a novel technique for laparoscopic sentinel node localisation in urological malignancies*. European journal of nuclear medicine and molecular imaging, vol. 36, no. 7, pages 1029–1036, 2009. 52
- [Vermeeren *et al.* 2011] Lenka Vermeeren, Renato A Valdés Olmos, Willem Meinhardt and Simon Horenblas. *Intraoperative imaging for sentinel node identification in prostate carcinoma: its use in combination with other techniques*. Journal of Nuclear Medicine, vol. 52, no. 5, pages 741–744, 2011. 52
- [Veronesi *et al.* 1999] U Veronesi, G Paganelli, G Viale, V Galimberti, a Luini, S Zurrada, C Robertson, V Sacchini, P Veronesi, E Orvieto, C De Cicco, M Intra, G Tosi and D Scarpa. *Sentinel lymph node biopsy and axillary dissection in breast cancer: results in a large series*. Journal of the National Cancer Institute, vol. 91, no. 4, pages 368–373, 1999. 51, 52

- [Veronesi *et al.* 2006] Umberto Veronesi, Giovanni Paganelli, Giuseppe Viale, Alberto Luini, Stefano Zurrada, Viviana Galimberti, Mattia Intra, Paolo Veronesi, Patrick Maisonneuve, Giovanna Gatti, Giovanni Mazzarol, Concetta De Cicco, Gianfranco Manfredi and Julia Rodriguez Fernandez. *Sentinel lymph node biopsy as a staging procedure in breast cancer: update of a randomised controlled study*. *Lancet Oncology*, vol. 7, no. 12, pages 983–990, 2006. 51
- [Vidal-Sicart *et al.* 2010] Sergi Vidal-Sicart, Pilar Paredes, Gabriel Zanón, Jaume Pahisa, Sergio Martinez-Román, Xavier Caparrós, Antoni Vilalta, Ramon Rull and Francesca Pons. *Added value of intraoperative real-time imaging in searches for difficult-to-locate sentinel nodes*. *J Nucl Med Technol*, vol. 51, no. 8, pages 1219–1225, 2010. 53
- [Vidal-Sicart *et al.* 2011] Sergi Vidal-Sicart, Lenka Vermeeren, Oriol Solà, Pilar Paredes and Renato A. Valdés-Olmos. *The use of a portable gamma camera for preoperative lymphatic mapping: A comparison with a conventional gamma camera*. *European Journal of Nuclear Medicine and Molecular Imaging*, vol. 38, no. 4, pages 636–641, 2011. 52
- [Visvikis & MacDonald 1998] D Visvikis and JH MacDonald. *A solid state detector for intraoperative imaging*. In *Nuclear Science Symposium, 1998. Conference Record. 1998 IEEE*, volume 2, pages 1295–1299. IEEE, 1998. 46, 49
- [Volders & Haloua 2016] José H Volders and Max H Haloua. *Current status of ultrasound-guided surgery in the treatment of breast cancer*. *World journal of clinical oncology*, vol. 15, no. 4, pages 469–476, 2016. 19
- [Wallace *et al.* 2013] Anne M Wallace, Linda K Han, Stephen P Povoski, Kenneth Deck, Schlomo Schneebaum, Nathan C Hall, Carl K Hoh, Karl K Limmer, Helen Krontiras, Thomas G Frazier, Charles Cox, Eli Avisar, Mark Faries, Dennis W King, Lori Christman and David R Vera. *Comparative evaluation of ^{99m}Tc -tilmanocept for sentinel lymph node mapping in breast cancer patients: results of two phase 3 trials*. *Annals of surgical oncology*, vol. 20, no. 8, pages 2590–9, 2013. 32
- [Wang *et al.* 2007] Yingbing Wang, Edison Chiu, Jarrett Rosenberg and Sanjiv Sam Gambhir. *Standardized uptake value atlas: Characterization of physiological 2-Deoxy-2-[18F]fluoro-d-glucose uptake in normal tissues*. *Molecular Imaging and Biology*, vol. 9, no. 2, pages 83–90, 2007. 147
- [Wang *et al.* 2015] Shuanhu Wang, Zongbing Zhang, Mulin Liu, Shiqing Li and Congqiao Jiang. *Endoscopic Resection Compared with Gastrectomy to Treat Early Gastric Cancer: A Systematic Review and Meta-Analysis*. *PloS one*, vol. 10, no. 12, page e0144774, 2015. 16
- [White & Lawson 2015] Duncan White and Richard S Lawson. *A Poisson resampling method for simulating reduced counts in nuclear medicine images*. *Physics in Medicine & Biology*, vol. 60, page N167, 2015. 147
- [Wilhelm *et al.* 1999] Abraham J. Wilhelm, G. Sophie Mijnhout and E. J F Franssen. *Radio-pharmaceuticals in sentinel lymph-node detection - An overview*. *European Journal of Nuclear Medicine*, vol. 26, no. SUPPL., 1999. 31

- [Wurz *et al.* 2015] G. T. Wurz, C.-J. Kao and M. W. DeGregorio. *Novel cancer antigens for personalized immunotherapies: latest evidence and clinical potential*. Therapeutic Advances in Medical Oncology, vol. 8, no. 1, pages 4–31, 2015. 18
- [Xiong *et al.* 2014] L. Xiong, E. Gazyakan, W. Yang, H. Engel, M. Hünnerbein, U. Kneser and C. Hirche. *Indocyanine green fluorescence-guided sentinel node biopsy: A meta-analysis on detection rate and diagnostic performance*. European Journal of Surgical Oncology, vol. 40, no. 7, pages 843–849, 2014. 27
- [Yamamoto *et al.* 1997] S Yamamoto, C Seki, K Kashikura, H Fujita, T Matsuda, R Ban and I Kanno. *Development of a high resolution beta camera for a direct measurement of positron distribution on brain surface*. Nuclear Science, IEEE Transactions on, vol. 44, no. 4, pages 1538–1542, 1997. 48
- [Yamamoto *et al.* 2004] Seiichi Yamamoto, Kenichi Matsumoto and Michio Senda. *Optimum threshold setting for a positron-sensitive probe with background rejection capability*. Annals of nuclear medicine, vol. 18, no. 3, pages 251–256, 2004. 45, 79
- [Yamamoto *et al.* 2005] Seiichi Yamamoto, Keiichi Matsumoto, Setsu Sakamoto, Kazumasa Tarutani, Kotaro Minato and Michio Senda. *An intra-operative positron probe with background rejection capability for FDG-guided surgery*. Annals of nuclear medicine, vol. 19, no. 1, pages 23–28, 2005. 45, 60, 79
- [Yamamoto *et al.* 2011] Seiichi Yamamoto, Hiroshi Watabe, Yasukazu Kanai, Masao Imaizumi, Tadashi Watabe, Eku Shimosegawa and Jun Hatazawa. *Development of a high-resolution Si-PM-based gamma camera system*. Physics in medicine and biology, vol. 56, no. 23, page 7555, 2011. 42
- [Yang *et al.* 2011] Yi Yang, Nrusingh C Biswal, Tianheng Wang, Patrick D Kumavor, Mozafareddin Karimeddini, John Vento, Melinda Sanders, Molly Brewer and Quing Zhu. *Potential role of a hybrid intraoperative probe based on OCT and positron detection for ovarian cancer detection and characterization*. Biomedical optics express, vol. 2, no. 7, pages 1918–1930, 2011. 56
- [Yeh *et al.* 2015] Michael W Yeh, Andrew J Bauer, Victor A Bernet, Robert L Ferris, Laurie A Loevner, Susan J Mandel, Lisa A Orloff, Gregory W Randolph and David L Steward. *American Thyroid Association statement on preoperative imaging for thyroid cancer surgery*. Thyroid, vol. 25, no. 1, pages 3–14, 2015. 23
- [Zaniboni *et al.* 2015] Alberto Zaniboni, Giordano Savelli, Claudio Pizzocaro, Pietro Basile and Valentina Massetti. *Positron Emission Tomography for the Response Evaluation following Treatment with Chemotherapy in Patients Affected by Colorectal Liver Metastases: A Selected Review*. Gastroenterology research and practice, vol. 2015, pages 706–808, 2015. 19
- [Zavagno *et al.* 2008] G Zavagno, G. L. De Salvo, G. Scalco, F. Bozza, L. Barutta, P. Del Bianco, M. Renier, C. Racano, P. Carraro, D Nitti and GIVOM Trialists. *A Randomized clinical trial on sentinel lymph node biopsy versus axillary lymph node dissection in*

breast cancer: results of the Sentinella/GIVOM trial. Annals of Surgery, vol. 247, pages 207–213, 2008. 52

[Zhou *et al.* 2013] Yang Zhou, Kwamena E. Baidoo and Martin W. Brechbiel. *Mapping biological behaviors by application of longer-lived positron emitting radionuclides.* Advanced Drug Delivery Reviews, vol. 65, no. 8, pages 1098–1111, 2013. 29

Title : Development and evaluation of an intraoperative beta imaging probe for radio-guided solid tumor surgery

Keywords : imaging, radioguided surgery, tumor and SiPM

Abstract : Extent and accuracy of surgical resection is a crucial step in the therapy of operable solid tumors. The recent availability of specific tumor-seeking agents, positron labeled, renewed the interest for radioguided surgery. The detection of beta particles, due to their short range, allows a more sensitive and accurate tumor localization. Since no mechanical collimation is necessary, it is possible to design probes with a sensitivity increased by one to three orders of magnitude compared to gamma detectors. The beta particle short range also reduces the contamination from distal non-specific radiotracers uptake region, which results in a increased signal-to-noise-ratio. Conversely, beta detection requires sensors to be extremely compact in order to operate in contact with the surveyed tissues in narrow surgical cavities. This thesis takes place in that context. Its aim was to develop an intraoperative positron imaging probe based on the silicon photomultiplier technology (SiPM) and to evaluate its ability to perform in real time tumor localization and post-operative control of the surgical cavity.

During this work, two prototypes of intraoperative positron imaging probe were developed. The first detector design is based on the use of a single organic scintillator coupled to an array of SiPMs. This configuration uses a small sensitive volume to reduce the contamination noise coming from the annihilation gamma rays. The second version of the probe implements a subtraction method allowing to improve gamma rejection efficiency. This configuration uses a stack of two scintillators separated by a light guide. The events interacting in the top and the bottom scintillator are discriminated by the analysis of the different light distributions on the SiPM array.

Different designs of the positron imaging probes, including scintillator material and thickness, light spreading window and optical reflector, were investigated with Montecarlo simulations and measurements. Their impact on the probes performances were optimized in terms of positron sensitivity, gamma ray rejection efficiency, spatial resolution and bias and uniformity of response. The effect of different reconstruction algorithm on spatial performances was also studied. Finally, the objective of developing an intraoperative probe fully operationnal in the operating room has been achieved by the design of dedicated miniaturized electronic readouts and mechanical housing.

In the last part of my thesis, the evaluation of the single scintillator configuration in a realistic clinical environment was performed with ^{18}F -FDG phantoms. We showed that the low intrinsic sensitivity of this probe to gamma radiations allows to detect tumor volumes as small as 14 mg for uptake properties corresponding to currently available radiotracers and acquisition times compatible with the surgery duration.

Titre : Développement et évaluation d'un imageur beta per-opérateur pour guider la chirurgie des tumeurs solides (en français)

Mots clés : imagerie, tumeurs, SiPM et radiotraceur

Résumé : La précision de l'ablation chirurgicale des tissus tumoraux est l'une des étapes essentielles dans la stratégie thérapeutique contre les cancers solides. Le développement récent de traceurs tumoraux spécifiques émetteurs de positons a relancé l'intérêt de la chirurgie radioguidée pour améliorer la qualité de l'exérèse. L'avantage des particules beta est leur faible parcours dans les tissus mous, de quelques millimètres, qui permet une détection plus sensible et précise. Il permet en effet de développer des systèmes de détection avec une sensibilité de un à trois ordres de grandeur plus élevée que celle des dispositifs utilisant les rayonnements gamma, car aucune collimation mécanique ou électronique n'est nécessaire. Le faible parcours des particules chargées permet également de réduire la contamination provenant de zones d'accumulation non-spécifique du radiotraceur. A l'inverse, la détection beta impose de développer des sondes extrêmement compactes capables d'être utilisées au contact des tissus opérés dans des cavités chirurgicales étroites. Ma thèse s'inscrit dans ce contexte. L'objectif était de développer un imageur beta per-opérateur basé sur la technologie des photomultiplicateurs silicium (SiPM) et d'évaluer sa capacité à localiser en temps réels de petites lésions tumorales radio-marquées dans la cavité opératoire.

Durant ce projet, deux prototypes d'imageur per-opérateur ont été développés. La tête de détection du premier prototype est basée sur l'association d'un scintillateur organique avec une matrice de SiPMs. Cette configuration minimise la taille du volume de détection pour réduire la contamination provenant des gammas d'annihilation. La seconde configuration met en œuvre une méthode de soustraction permettant de réduire l'influence du bruit gamma. Pour ce faire, un assemblage de deux scintillateurs séparés par un guide de lumière est utilisé. Les événements interagissant dans le scintillateur supérieur et inférieur sont discriminés par l'analyse des différentes distributions de la lumière sur la matrice de SiPMs.

Différents designs des deux sondes beta, incluant le choix du matériau et l'épaisseur du scintillateur, le guide de lumière et le revêtement optique, ont été étudiés expérimentalement ou par simulation Monte Carlo. Ces paramètres ont été optimisés en termes de sensibilité aux positons, de discrimination du bruit de fond gamma, de résolution spatiale, de distorsion et d'uniformité de réponse. L'influence de différents algorithmes de reconstruction sur les performances spatiales de l'imageur a également été étudiée. Finalement, l'objectif de développer une sonde per-opérateur totalement opérationnelle en bloc opératoire, a été atteint grâce à la conception d'une électronique et d'une mécanique miniaturisées dédiées.

La dernière partie de ma thèse a été consacrée à l'évaluation de la configuration de l'imageur per-opérateur basée sur un seul scintillateur à l'aide de fantômes marqués au ^{18}F -FDG reproduisant un environnement clinique réaliste. Nous avons pu montrer que la faible sensibilité intrinsèque de la sonde au bruit de fond gamma permettait de détecter des volumes tumoraux inférieurs à 14 mg pour des propriétés de fixation correspondant à des radiotraceurs actuellement disponibles et des temps d'acquisition compatible avec la pratique chirurgicale.

